Dipolarizations in Mercury's Magnetotail: Characteristics and Consequences in a Miniature Magnetosphere

by

Ryan M. Dewey

A dissertation submitted in partial fulfillment
of the requirements for the degree of
Doctor of Philosophy
(Climate and Space Sciences and Engineering)
in the University of Michigan
2020

Doctoral Committee:

Associate Research Scientist Jim M. Raines, Co-Chair
Professor James A. Slavin, Co-Chair
Assistant Professor Yang Chen
Associate Professor Xianzhe Jia

Ryan M. Dewey

rmdewey@umich.edu

ORCID iD: 0000-0003-4437-0698

DEDICATION

To my parents, siblings, partner, and cat.

Thank you for being my biggest supporters and most steadfast companions.

ACKNOWLEDGEMENTS

There is not enough space here to express the gratitude I feel to everyone who has supported me through this program. While this thesis focuses on the culmination of five years of research, behind every word is an incredible ensemble of people that made this journey possible.

I would like to start by thanking my advisors, Jim Slavin and Jim Raines. I could not have asked for better mentors, colleagues, and friends. Jim and Jim knew how to support my growth as a budding scientist, giving me room to explore and investigate independently, but also knowing when to nudge me back to the path when I wandered too far into the weeds. They provided me the opportunity to share my work throughout the country and around the world, helping me to build a network and a name for myself within the community. Both Jims are enthusiastic about science, and their enthusiasm is contagious. During the roughest, most self-doubting times of this journey, their passion reminded me of why I was here. Jim Slavin always found ways of slipping mentoring into each of our conversations, often under the guise of a story as a break from talking about science. Jim Raines coached me on balance, and although I will probably always struggle with it, the advice and tools Jim taught me will be invaluable. I am honored to have Jim and Jim guide my journey.

I will always be thankful to Dan Baker who helped me to start this journey. Dan introduced me to Mercury and the MESSENGER mission as an undergrad when he graciously let me join his research group. It was through Dan that I met Jim and Jim and realized the type of science I enjoy so much. Thank you Dan for your enduring support, collaboration, and belief in me.

Thank you Xianzhe Jia and Yang Chen for joining my dissertation committee. The guidance and feedback through this process is greatly appreciated, and I look forward to continuing to work closely together in the future.

A serious shout-out to Abby Azari and Camilla Harris. Abby and I have shared a similar research path, investigating the dynamics of a planetary magnetosphere using statistical and data science techniques to bolster single-spacecraft observations. Although the planets we work on could not be more different (Saturn and Mercury), I have learned so much from Abby and our mutual frustrations. Abby is also from Colorado and likes cats, so I think it was always destined we would be friends. Camilla is my best tea-buddy, my fellow Santa Fe enthusiast, and a rockstar of the planetary community within the department (and another cat lover). I always enjoy Camilla's perspective on science, and on life. Dynamos, dynamite, sleep all day, and Bayeswatch all night!

I would not have survived my PhD without my fellow graduate students and post-docs (past and current) providing sage wisdom, hearty laughs, and close council. Thank you to Mojtaba Akhavan-Tafti, Doga Ozturk, Weijie Sun, Jamie Jasinski, Yash Sarkango, Nithin Sivadas, Suzanne Smith, Ashley Greeley, Matt Cooper, Willi Exner, Sae Aizawa, and Gangkai Poh in particular.

My time in graduate school would not have been half as entertaining and enjoyable without Alexandra Mierzwa, Marcus Berger, Jim Antonaglia, Parker Koch, Connor Campbell, William Dean, Max Dubrinsky, Ryan Sharrar, Harrison Ball, and Chris Altheim. Whether out at the Renaissance Festival, eating (debating about) dumplings, or playing cardboard games, I could not have asked for better company here in Michigan.

Outside of Michigan, my family has provided me with incredible support and encouragement. From a young age, my parents have taught me to be inquisitive, aim high with my aspirations, and find joy around me. Returning home during breaks in undergrad, I would be greeted by their warm embrace and space-related news articles they clipped out of the daily paper for me. My family has always supported my path down mathematics and science, and I know I can always rely on them. To my family I dedicate this thesis.

I am also thankful to two much newer members of my family. Paul (the cat) has been a fantastic sounding board and a wonderful distraction from work. Writing this thesis, he often wanted to contribute as well, with such actual quotes as:

"G UIinquisitibe ve, zs"

and

"kj…………………………………………………………….."

During the most difficult times, he reminded me of the importance of sleeping, eating, and cuddling.

Finally, I could not have survived this journey without my partner in crime, Chris Brown. Chris celebrated my successes (no matter how small) and spoke words of encouragement during times of failure. He always listened when I needed to clear my mind, or accompany me on a stroll to get away from work. In the last few months of the thesis writing and stressing, Chris was my rock. Chris has been an essential part of my success, and I am still wondering how lucky I am to have him along for the journey.

TABLE OF CONTENTS

CHAPTER

LIST OF FIGURES

FIGURE

LIST OF TABLES

TABLE

LIST OF APPENDICES

APPENDIX

ABSTRACT

Mercury's global magnetic field forms a terrestrial-like magnetosphere with its interaction with the upstream solar wind. While Mercury and Earth's magnetospheres share similar structure and many similar dynamics, the weaker planetary field, stronger solar wind forcing, and lack of ionosphere at Mercury result in smaller spatiotemporal scales and stronger effects from magnetic reconnection. These magnetospheric differences influence substorm dynamics at the two planets, including magnetotail dipolarizations. Dipolarizations result from intense magnetic reconnection in the magnetotail, and at Earth, are important for magnetic flux transport, particle energization, and substorm current wedge formation. We use in situ observations of Mercury's space environment from the MESSENGER spacecraft to identify the characteristics and consequences of dipolarizations to Mercury's magnetosphere. In the pursuit to improve our understanding of dipolarizations at Mercury, we develop new techniques to determine plasma flow from limited observations, identify energetic electron bursts from indirect measurements, and select dipolarizations from a magnetic field time series.

Employing statistical analysis on Mercury's dipolarizations, we find that they share many similar features to those at Earth. Dipolarizations at Mercury are characterized by a rapid (~2 s) increase in the northward field ($\Delta B_z \sim 30$ nT) that persists for ~10 s, accompanied by a depletion ($\Delta n/n \sim -0.3$) and heating ($\Delta T/T \sim 0.2$) of thermal plasma, rapid sunward flow ($v_x \sim 200$ km/s), strong cross-tail electric field ($E_y \sim 11$ mV/m), and enhancement of energetic electron flux. We find that dipolarizations typically transport ~0.06 MWb of magnetic flux. Although a single

dipolarizations transports substantially less flux than a typical substorm loads into the magnetotail (~0.7 MWb), we find that dipolarizations are typically observed in series with others, allowing dipolarizations to transport the majority of magnetic flux during a substorm. As they transport magnetic flux from the reconnection site to Mercury's inner magnetosphere, dipolarizations can energize electrons to ~120 keV via betatron and Fermi acceleration mechanisms. The frequency of dipolarizations in Mercury's magnetotail (~1 min^{-1}) indicates that dipolarizations may be the dominant source of Mercury's energetic electron environment. Finite gyroradius effects prevent ions from experiencing the same degree of acceleration. Finally, we find that despite Mercury's relatively weak planetary magnetic field and the small spatial distance from the nightside reconnection site to the planetary surface, Mercury's dipole field is strong enough to cause dipolarizations to brake before reaching the planet's nightside. Braking typically occurs within a region ~500 km in thickness, located ~900 km in altitude above Mercury's nightside surface and is evidenced by strong decreases in dipolarization frequency and in sunward flow speed. As dipolarizations brake, their transported magnetic flux accumulates and allow for the possibility of a current wedge to develop. Dipolarizations, therefore, share similar characteristics and consequences in Mercury's magnetosphere as Earth's, informing our understanding of the substorm process at terrestrial-like planets.

CHAPTER I. Introduction

Mercury and its three nearest neighboring planets are the only four rocky planets within our solar system, and they each share distinctive characteristics. Venus, while comparable in size to Earth, possesses a thicker, denser atmosphere while Mercury, miniature in size to Earth, possesses no appreciable atmosphere at all. Mercury, however, possesses a global planetary magnetic field like Earth that both Venus and Mars lack. The unique connections we can draw between any two of these terrestrial planets allow for rich investigations of comparative planetology, and for comparisons with Earth's space environment, Mercury pairs the closest. The global magnetic fields of both planets interact with the upstream solar wind to form magnetospheres similar in general structure and magnetic field topology. However, Mercury's magnetosphere contains several critical differences from Earth's that make it an ideal laboratory for understanding the space physics dynamics common to both of these systems. While the two magnetospheres share similar structure and dynamics, Mercury lacks an ionosphere, endures stronger upstream solar wind forcing, and possesses a weaker planetary magnetic field. Investigating the dynamics of Mercury's magnetosphere, therefore, not only advances our understanding of Mercury's space environment, but also enriches our understanding of our own space environment and allows us to begin generalizing these space physics processes outside of our solar system. For extensive reviews of Mercury and its space environment, we refer readers to Solomon et al. (2018).

1.1 Mercury and its Orbit

Mercury is both the smallest planet within the solar system and the closest to orbit the Sun. Mercury's mean radius is 2,440 km (1 R_M), approximately a third the size of Earth's (6,371 km = 1 R_E), resulting in a mass only ~5% that of Earth. Despite Mercury's small mass, it has the greatest uncompressed density of planets within the solar system, due in large part to its metallic core. The planet is comprised of a large (~2,000 km) core surrounded by a thin layer (~440 km) of crust. Dynamo action within the core produces Mercury's global planetary magnetic field (see Chapter 1.3). The crust consists of a resistive regolith with high abundances of Si, Mg, O, Na, Al, and Ca. The surface is heavily cratered and heavily space weathered. Above the surface, Mercury lacks any appreciable atmosphere, but possesses a tenuous exosphere.

In addition to these unique characteristics about Mercury, the planet also holds a unique place within the solar system as both the planet closest to the Sun and the planet with the most eccentric orbit. Mercury orbits between 0.308 AU at perihelion to 0.467 AU at aphelion corresponding to an eccentricity of 0.206. By contrast, Earth orbits the Sun with an eccentricity of 0.017 causing only a small difference in the Sun-Earth distance during an Earth orbit (ranging from 0.983 to 1.017 AU). The high eccentricity of Mercury's orbit results in a unique 3:2 spin-orbit resonance in which the planet rotates three times during every two revolutions about the Sun. A Mercury year is equivalent to 88.0 Earth days while a sidereal Mercury day equals 58.7 Earth days. The long rotation period of Mercury results in a large difference in temperature between the planet's dayside (~700 K) and nightside (~100 K) surfaces. Another consequence of Mercury's high orbital eccentricity is the substantial variation of solar wind conditions Mercury experiences over the course of its orbit.

1.2 Solar Wind at Mercury

The solar wind is the plasma from the Sun's upper atmosphere (corona) that expands to fill the solar system. Typical solar wind parameters (e.g., density and temperature) evolve as a function of distance from the Sun. Table 1.1 lists average solar wind parameters at each terrestrial planet. To first order, solar wind density, proton temperature, electron temperature, and interplanetary magnetic field (IMF) strength decrease with increasing distance from the Sun while the solar wind speed remains approximately constant. Mercury, orbiting much closer to the Sun than Earth, therefore experiences different typical conditions. At Mercury's mean distance from the Sun (0.40 AU), the solar wind at Mercury's orbital location is typically ~6 times more dense, ~2 times hotter, and with an IMF magnitude ~5 times stronger than at Earth. These more intense solar wind conditions result in a stronger upstream dynamic pressure (ρv_{sw}^2) and a weaker upstream Alfvén Mach number ($M_A = v_{sw}/v_A$), where v_{sw} is the solar wind speed, $v_A = B/\sqrt{\mu_0 \rho}$ is the Alfvén speed, B is the magnetic field strength, μ_0 is the permeability of free space, and ρ is the mass density. Furthermore, Mercury experiences substantial variation of solar wind conditions over the course of its orbit due to the orbit's high eccentricity. At perihelion, the solar wind density is ~2 times greater and the IMF magnitude is ~2 times stronger than at aphelion. Finally, while the IMF magnitude varies along Mercury's orbit and is substantially stronger at Mercury than at Earth for nominal conditions, the orientation of the IMF also displays dramatic variation. A result of the Sun's spin and the "frozen-in" condition of the magnetic field lines to the solar wind plasma (see Chapter 1.3), the IMF is more radial at Mercury (~17° angle from the Sun-Mercury line at perihelion, ~25° at aphelion) compared to Earth (~45° angle from the Sun-Earth line).

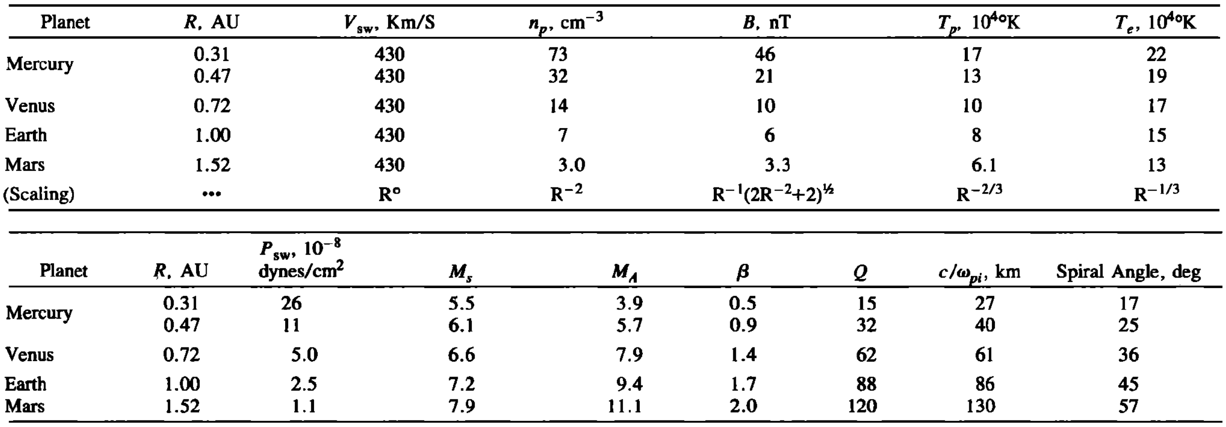

Planet	R, AU	V_{sw}, Km/S	n_p, cm^{-3}	B, nT	T_p, 10^4°K	T_e, 10^4°K
Mercury	0.31 0.47	430 430	73 32	46 21	17 13	22 19
Venus	0.72	430	14	10	10	17
Earth	1.00	430	7	6	8	15
Mars	1.52	430	3.0	3.3	6.1	13
(Scaling)	•••	R°	R^{-2}	$R^{-1}(2R^{-2}+2)^{1/2}$	$R^{-2/3}$	$R^{-1/3}$

Planet	R, AU	P_{sw}, 10^{-8} dynes/cm^2	M_s	M_A	β	Q	c/ω_{pi}, km	Spiral Angle, deg
Mercury	0.31 0.47	26 11	5.5 6.1	3.9 5.7	0.5 0.9	15 32	27 40	17 25
Venus	0.72	5.0	6.6	7.9	1.4	62	61	36
Earth	1.00	2.5	7.2	9.4	1.7	88	86	45
Mars	1.52	1.1	7.9	11.1	2.0	120	130	57

Table 1.1. Typical solar wind conditions at each of the terrestrial planets as scaled from observations at Earth (1 AU). Adapted from Slavin & Holzer (1981).

In addition to the slowly evolving solar wind conditions at Mercury due to the planet's eccentric orbit, transient phenomena in the solar wind can substantially change these conditions on much shorter timescales. For example, coronal mass ejections (CMEs) discharged from the Sun can result in dynamically evolving conditions at Mercury's orbital location on the timescales of hours to days. CMEs typically travel faster than the surrounding ambient solar wind, causing a standing shock wave to form at the leading edge of these events. As ambient plasma is overtaken by the CME, the shock heats and compresses the plasma and enhances the magnetic field strength. Following the shocked solar wind is the CME structure that is typically depleted in thermal plasma and enhanced in magnetic field with helical magnetic field topology. We do not focus on these events in our investigation in particular, but they can have substantial effects on Mercury's magnetosphere (see Slavin et al., 2014; Slavin et al., 2019) and represent intervals of substantial, rapid changes in upstream solar wind conditions.

Unfortunately, the Mercury, Surface, Space ENvironment, GEochemistry, and Ranging (MESSEGNER) spacecraft that we use in our investigation cannot simultaneously sample the solar wind and Mercury's magnetosphere (see Chapter 2). To provide solar wind context to spacecraft observations, multiple techniques have been used. Some studies (e.g., Gershman et al., 2013; Gershman et al., 2014) use observations of the solar wind from the spacecraft and assume they are approximately constant during the spacecraft's pass into the magnetosphere, while others have focused on modeling the solar wind at Mercury's orbital location (Baker et al., 2009; Baker et al., 2011; Baker et al., 2013; Dewey et al., 2015). An example of such a model is the WSA-ENLIL+Cone model that simulates both the ambient solar wind and solar wind transients (e.g., CMEs) as depicted in Figure 1.1.

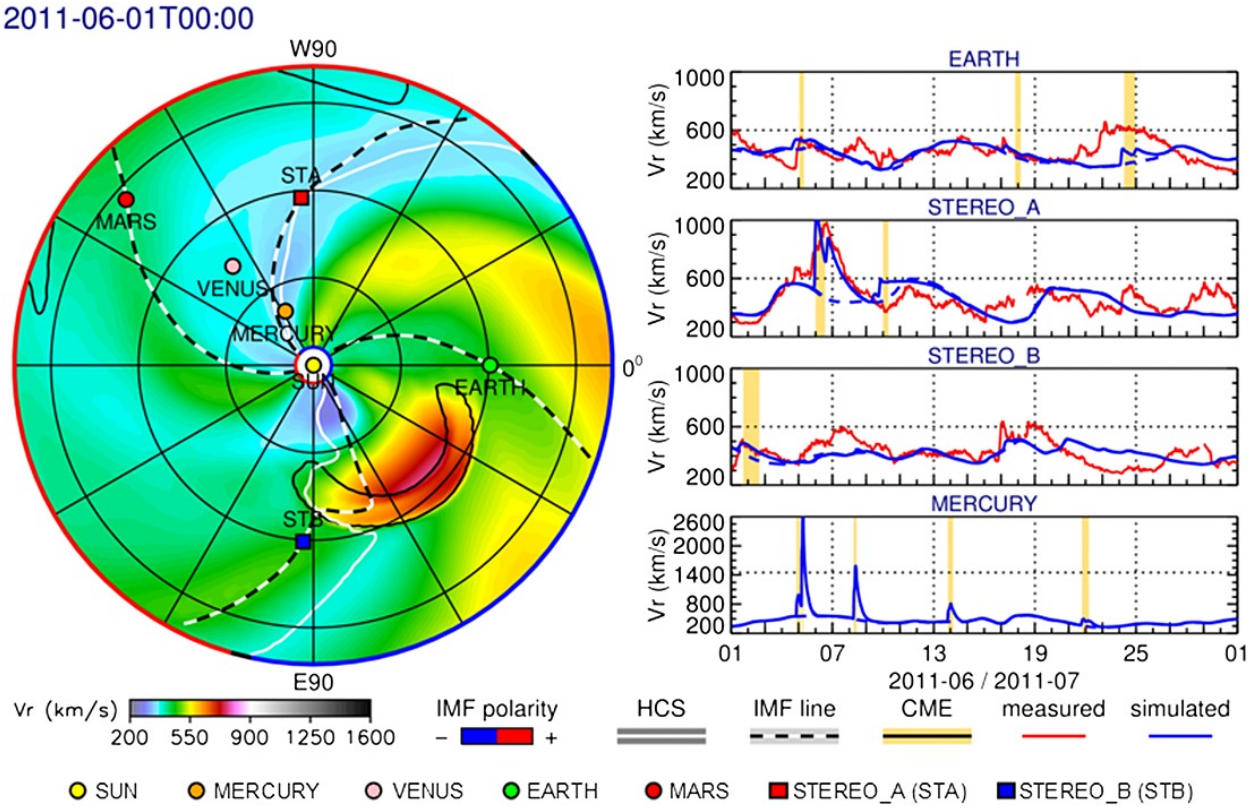

Figure 1.1. (left) Modeled radial solar wind speed in the ecliptic plane from the WSA-ENLIL+Cone model for 1 June 2011 and (right) comparison with spacecraft observations throughout the heliosphere for June 2011. Figure from Dewey et al. (2015).

1.3 Mercury's Magnetosphere

The upstream solar wind plays a critical role in the formation and dynamics of both Mercury and Earth's magnetospheres. In the absence of the solar wind, Mercury's magnetic field is described well as a dipole magnetic field offset northward from the planet's geographic equator. This magnetic field was first discovered by the Mariner 10 flybys in 1974 and 1975 (Ness et al., 1974; Ness et al., 1975) and refined later by MESSENGER observations (Aleexev et al., 2010; Anderson et al., 2011; Johnson et al., 2012). The dipole moment of the planet is aligned with the rotation axis (<1°), is centered northward of the planetary barycenter (~484 km or ~0.2 R_M), is directed southward (similar as Earth), and has a strength of ~190 nT R_M^3. This dipole orientation is the same as Earth's, however, Earth's planetary magnetic field is ~150 times stronger (~31,000 nT R_E^3).

The solar wind compresses Mercury's dayside magnetic field and stretches the nightside field into an elongated magnetotail, as depicted in Figure 1.2. Mercury's magnetosphere shares many of the same regions as Earth's, including this dayside magnetosphere and magnetotail. However, Mercury's weaker planetary magnetic field and the stronger upstream solar wind it endures cause Mercury's magnetosphere to be smaller than Earth's by both relative and absolute scales. The width of Mercury's magnetotail, for example, is ~4 R_M = 10,000 km compared to Earth's of ~40 R_E = 255,000 km (Slavin et al., 2012; Kaymaz et al., 1992). The smaller spatial scales at Mercury result in the planet occupying a larger fraction of its magnetosphere than Earth. Therefore, while Mercury's magnetosphere shares many similar regions as Earth's, it lacks a substantial inner magnetosphere. The inner magnetosphere, for example, is where Earth's radiation belts reside; the equivalent location in Mercury's magnetosphere would be inside the planet (Ogilvie et al., 1997).

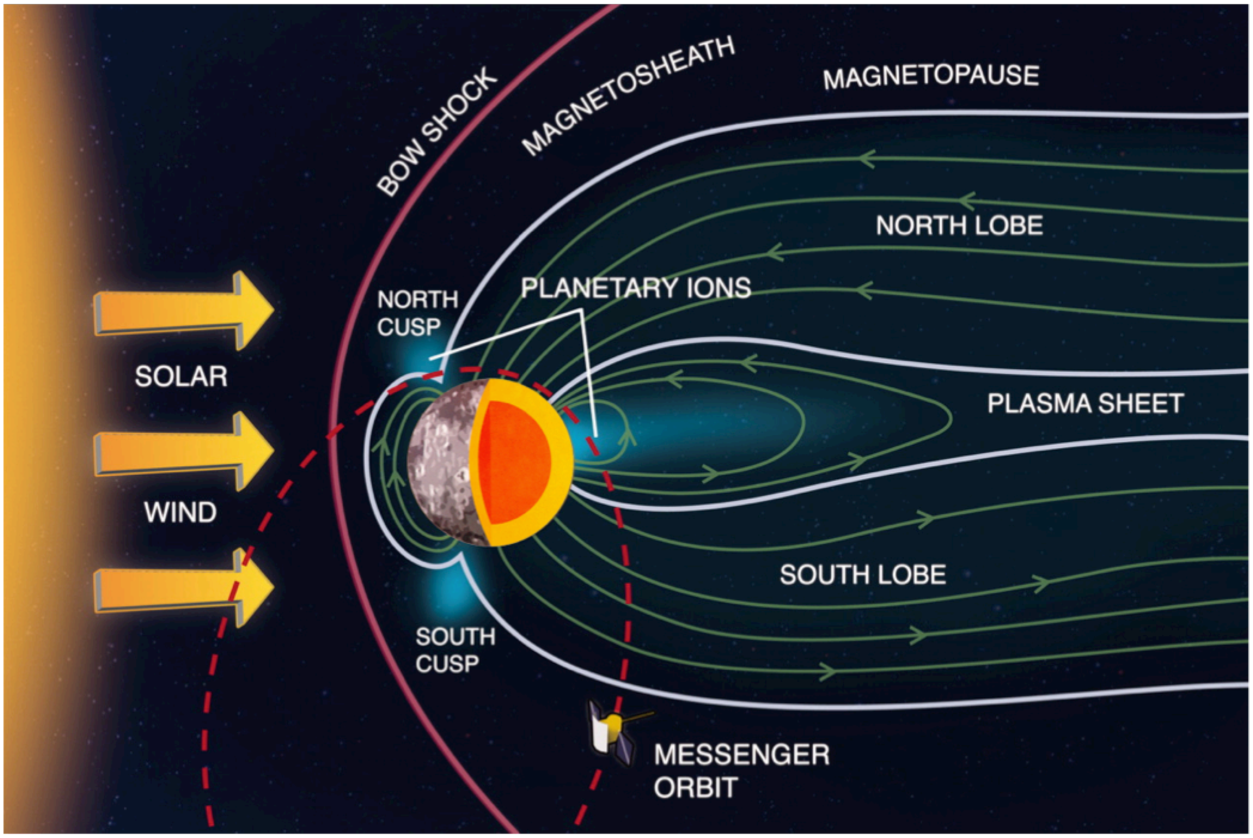

Figure 1.2. Schematic of Mercury's magnetosphere in the noon-midnight plane. Regions of the magnetosphere are labeled. The planetary core (dark orange), MESSENGER orbit (dashed red), and magnetospheric boundaries (solid while and solid red) are shown to scale with regards to the planet. Green lines indicate magnetic field lines with arrows indicating field line direction. Adapted from Zurbuchen et al. (2011).

Similar to at Earth, Mercury's magnetic field acts as an obstacle to the supersonic solar wind flow, so to communicate the presence of this obstacle, a bow shocks stands in front of the planet to slow the solar wind to subsonic speeds. The bow shock compresses and heats the plasma that passes through it, similar to the shocks associated with CMEs (see Chapter 1.2). Across the shock, the flow speed decreases while the magnetic field intensity increases. A statistical study of bow shock observations from the first three Mercury years of MESSENGER's orbital mission revealed a typical standoff distance of ~1.96 R_M from Mercury's dipole center (Winslow et al., 2013). Planetward of the bow shock, the shocked solar wind continues to flow antisunward and around Mercury's magnetosphere within the magnetosheath region.

The magnetopause separates Mercury's planetary magnetic field (i.e., the magnetosphere) from the magnetosheath. The magnetopause location is determined at first order by the pressure balance between the dayside magnetosphere and the shocked solar wind in the magnetosheath. The combined plasma and magnetic field pressures balance across the magnetopause, where plasma pressure dominates within the magnetosheath and magnetic pressure dominates within the dayside magnetosphere. A consequence of the lower upstream Alfvén Mach number at Mercury is the formation of thick plasma depletion layers on the magnetosheath side of the magnetopause (Gershman et al., 2013). These depletion layers, so named because of their reduced plasma density compared to the surrounding magnetosheath, contain a stronger magnetic field, resulting in a pressure balance across the magnetopause at Mercury that is more sensitive to magnetic field strength of the IMF. In other words, the magnetic pressure in the magnetosheath plays a larger role in pressure balance across the magnetopause at Mercury than at Earth. The typical subsolar magnetopause standoff distance from Mercury's dipole center is ~1.45 R_M (Winslow et al., 2013), however, this distance can vary substantially as a function of upstream solar wind conditions. Increases in solar wind dynamic pressure act to compress Mercury's dayside magnetosphere and move the magnetopause closer to the planet. Mercury's large metallic core resists these changes. As Mercury lacks an atmosphere (and therefore an ionosphere as well), the inner conductive boundary to its magnetosphere is its large conducting core. Changes in magnetopause location induce currents on the surface of the core that resist these changes by effectively increasing Mercury's magnetic moment (i.e., increase the magnetic pressure inside the magnetosphere) (Slavin et al., 2014; Jia et al., 2015; Johnson et al., 2016; Jia et al., 2019). While similar responsive currents may also be induced on the surface of Earth's core, these currents are substantially stronger at Mercury due to Mercury's relatively larger core and the core's close proximity to the magnetopause.

In addition to changes in dynamic pressure, magnetic reconnection can modify the location of the magnetopause as well. Magnetic reconnection is a fundamental physical process that occurs in laboratory, astrophysical, and space plasmas. Magnetic reconnection, or often just termed reconnection, transfers energy and momentum from the magnetic field to the local plasma by changing the magnetic field topology to a lower energy state. For a detailed review, see Zweibel & Yamada (2016). Definitions of reconnection begin with the generalized Ohm's law. For a collisionless plasma:

$$\boldsymbol{E} + \boldsymbol{v} \times \boldsymbol{B} = \eta \boldsymbol{j} + \frac{1}{ne}\boldsymbol{j} \times \boldsymbol{B} - \frac{1}{ne}\nabla \boldsymbol{P}_e + \frac{m_e}{ne^2}\frac{\partial \boldsymbol{j}}{\partial t}$$

where $\boldsymbol{E}$ is the electric field, $\boldsymbol{j}$ is the current density, $\boldsymbol{v}$ is the plasma velocity, $\boldsymbol{B}$ is the magnetic field, η is the resistivity of the plasma, $\boldsymbol{P}_e$ is the electron pressure tensor, m_e is the electron mass, e is the fundamental charge (i.e., proton charge), and n is the plasma density. In the ideal fluid treatment of the plasma, the right-hand side equals zero, i.e., $\boldsymbol{E} + \boldsymbol{v} \times \boldsymbol{B} = 0$. This is the statement of the "frozen-in" condition mentioned in Chapter 1.2; the magnetic field lines move with the plasma. Magnetic reconnection occurs when the terms on the right-hand side are non-negligible on the order of ion and electron inertial lengths. This typically occurs near thin, intense current sheets that support opposing magnetic field line geometries. A schematic of reconnection is shown in Figure 1.3. As the thickness of the current sheet decreases below the ion inertial length (defined as $d_i = c/\omega_i$ where c is the speed of light and ω_i is the ion plasma frequency), the ions become de-magnetized. In other words, the identity of which field line an ion belongs to becomes lost. This region is known as the ion diffusion region. Electrons have smaller inertial lengths and gyroradii than ions so they maintain clear identity of field lines until within the electron diffusion region. Here, the electrons become de-coupled from magnetic field lines. With no particles maintaining the identity of field lines within the electron diffusion region, the field lines break and reconnect at the neutral point. Electric fields associated with the separation of ions and electrons within the ion diffusion region and the tension ($\boldsymbol{j} \times \boldsymbol{B}$) of the newly-reconnected field lines carry these field lines out of the ion diffusion region where they travel at the local Alfvén speed (i.e., fast reconnection exhaust). The newly reconnected field lines relax, transferring energy from the magnetic field to the local plasma. The frequency and intensity (i.e., rate) of magnetic reconnection depends on local plasma and magnetic field conditions (see, e.g., Shay & Swisdak, 2004).

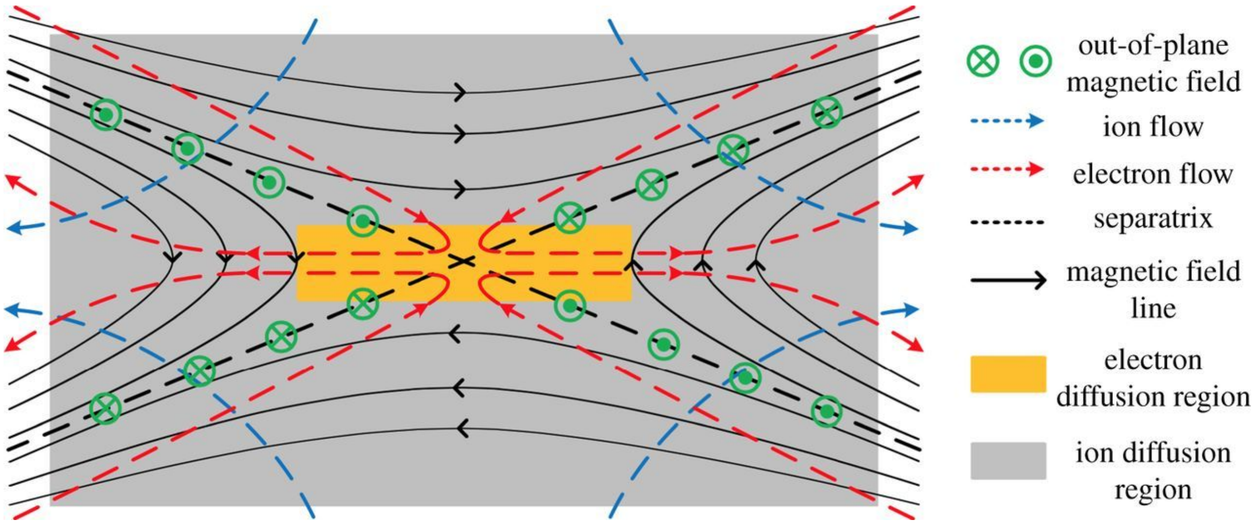

Figure 1.3. Schematic of magnetic reconnection from Zweibel & Yamada (2016).

Magnetic reconnection at the dayside magnetopause can erode it to lower altitudes. A result of the lower upstream solar wind M_A and the thick plasma depletion layers in the magnetosheath, magnetic reconnection at Mercury's magnetopause is more frequent, stronger, and less sensitive to the direction of the IMF than dayside magnetopause reconnection at Earth. At Earth, intense subsolar reconnection typically occurs only when the IMF is southward ($-B_{z,IMF}$), oppositely directed from Earth's northward magnetic field at the magnetopause (Burton et al., 1975). Magnetopause reconnection at both planets transfers magnetic flux from the dayside magnetosphere into the magnetotail. Reconnection occurs between an IMF field line and a closed planetary field line (i.e., a magnetic field line that has both ends anchored to the conducting inner boundary of the magnetosphere). The newly reconnected field lines will each be "open" in topology: have one end connected to the planet and the other embedded within the solar wind. As the solar wind continues to flow past the planet, it drags these open field lines over the poles and into the magnetotail. As reconnection continues, the dayside magnetosphere loses magnetic flux, causing the magnetopause to decrease in altitude. At Mercury, dayside reconnection can be so intense that the magnetopause is eroded to the planet's surface (Slavin et al., 2019; Winslow et al., 2020). These instances are uncommon and typically occur in conjunction with extreme forcing conditions from solar wind transients (e.g., CMEs). Nevertheless, the erosion of Mercury's magnetopause to the planet's surface illustrates the dynamic impacts of reconnection within Mercury's magnetosphere.

To return magnetic flux to the dayside, the convection cycle continues with field line motion in the magnetotail. The magnetotail consists of two oppositely directed magnetic lobes separated by a current-carrying plasma sheet. The lobes are characterized by a low plasma density and by a strong magnetic field that is directed sunward (antisunward) in the northern (southern) hemisphere, resulting in a plasma beta $\beta \ll 1$ where $\beta = P_{th}/P_{mag}$ is the ratio of the plasma pressure (P_{th}) to the magnetic pressure (P_{mag}). The plasma sheet separates the two lobes and is characterized by hot, dense plasma with $\beta \gg 1$. Embedded within the plasma sheet is the central current sheet that supports the opposing field line geometry of the lobes. At Mercury, the lobe field strength is ~50 nT and the lobe ion densities are < 1 cm^{-3} (Rong et al., 2018). The plasma sheet at Mercury consists predominately of protons (~75% by number density) with temperatures between 10-30 MK and densities between 1-10 cm^{-3} (Gershman et al. 2014). The current sheet has typical current densities of ~100 nA/m^2 and a thickness of ~0.4 R$_M$ (Poh et al., 2017a). As the open field lines from the dayside are dragged by the solar wind over the polar caps and into the magnetotail, they convect within the magnetotail lobes towards the plasma sheet by the $\boldsymbol{E} \times \boldsymbol{B}$ drift. Magnetic reconnection between the two lobes within the central current sheet creates two new field lines: one with both ends connected to the solar wind that returns to the IMF and the other that is newly closed. The closed field line is embedded within sunward reconnection outflow that carries the field line back to the dayside magnetosphere where it can reconnect again and begin this cycle anew. Reconnection in Mercury's magnetotail typically occurs between ~2–3 R$_M$ antisunward of the terminator (Slavin et al., 2009; DiBraccio et al., 2015; Poh et al., 2017a).

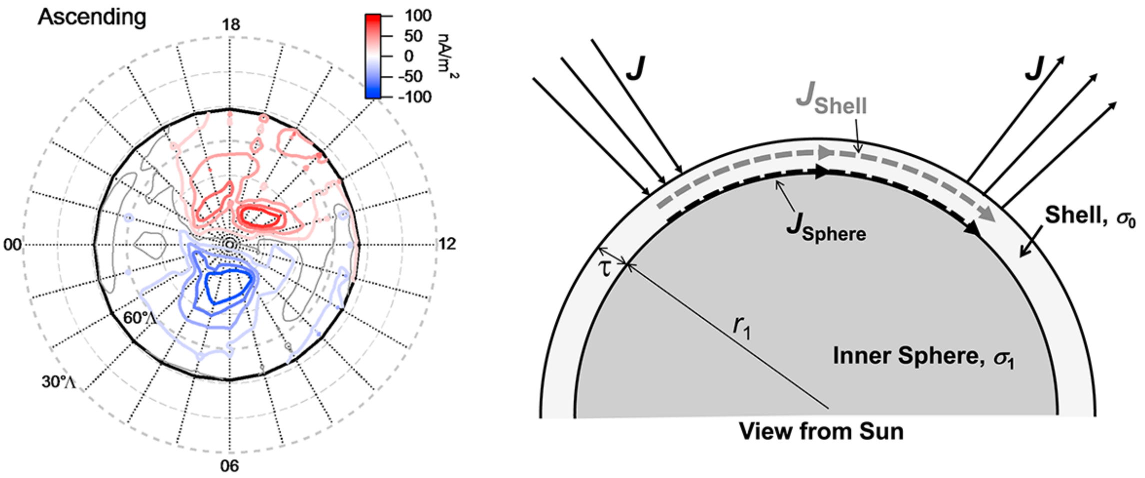

Figure 1.4. (left) Contours of radial current density determined from MESSENGER observations as a function of local time and invariant latitude (Λ). Red and blue contours correspond to upward and downward current, respectively. (right) Schematic of radial current closure via Mercury's large conducting core (dark grey). Figure adapted from Anderson et al. (2014).

Field-aligned currents over the planet's poles capture this motion of magnetic field lines as they cycle through the magnetosphere. Figure 1.4 depicts these currents at Mercury. Over

Mercury's northern pole, the magnetic field points nearly radially into the planet so the antisunward motion from dayside-reconnected field lines being dragged into the magnetotail generates a duskward electric field. These field lines reconnect again in the magnetotail and are dragged about the planet to the dayside. The return motion is sunward, generating a dawnward electric field near the polar cap. As the return motion occurs at lower latitudes than the motion over the poles, the dawnward electric field straddles the duskward field on either side. To satisfy the momentum equation, the convergence (divergence) of the electric fields produces a current parallel (antiparallel) to the magnetic field. This current system is known as the Region 1 current and is observed at both Mercury and Earth. At Earth, the Region 1 current closes through the ionosphere close to the planet and to the magnetopause far from the planet. At Mercury, the current is expected to close through the planet's conducting core. As depicted in Figure 1.4, the current passes radially through Mercury's resistive regolith to close over the surface of the core, illustrating an additional role of Mercury's core to the magnetosphere system.

This flux circulation, which involves dayside and nightside reconnection as well as field-aligned currents over the poles, is known as the Dungey cycle (Dungey, 1961). It describes the general steady-state configuration of Mercury's magnetosphere. For Earth, this description applies to southward IMF conditions when dayside, subsolar reconnection is expected. At Earth, the Dungey cycle is ~1-3 hours in duration, while it is ~1-3 min at Mercury due to Mercury's weaker planetary magnetic field and the stronger solar wind forcing it experiences (Tanskanen, 2009; Slavin et al. 2010). The Dungey cycle describes a state of balance between dayside and nightside reconnection. To maintain steady state, the flux transported by dayside reconnection to the magnetotail balances the flux transported by nightside reconnection to the dayside magnetosphere. However, these reconnection rates infrequently balance exactly. When the dayside reconnection rate is substantially greater than the nightside rate, magnetospheric substorms begin.

1.4 Substorm Dynamics at Earth

Substorms have been a subject of considerable interest and research since their initial observation by Akasofu (1964) who noticed consistent patterns of auroral activity in Earth's ionosphere. Since this initial discovery, spacecraft have expanded our understanding of substorms by connecting auroral features to their corresponding magnetospheric phenomena. Our understanding of Earth's substorm process continues to evolve but several features are well agreed upon (for a review, see Haerendel, 2015). Substorms are described by three phases: growth, expansion, and recovery. During the growth phase, the dayside reconnection rate exceeds the nightside rate causing a net transport of magnetic flux to the magnetotail, stored within the lobes. This process is known as magnetotail loading. As dayside reconnection continues, the lobes flare while pressure gradients across the terminator evacuate magnetic flux from the near-magnetotail to the dayside. The increased magnetic pressure within the lobes and forces associated with flux evacuation thin the central current sheet. The current sheet thins until intense magnetic reconnection between the low-β lobes initiates, marking the end of the growth phase and the onset of the expansion phase. During the expansion phase, the increased magnetotail reconnection rate unloads magnetic flux of the lobes. The recovery phase begins as the magnetotail reconnection rate decreases from the reduction in lobe magnetic flux content. During the recovery phase, substorm activity settles and the magnetosphere returns to (approximately) steady state. Substorms typically last ~2-3 hours during which the magnetotail lobes are loaded and unloaded by ~10% of their magnetic flux content (Forsyth et al., 2015; Hsu & McPherron, 2000).

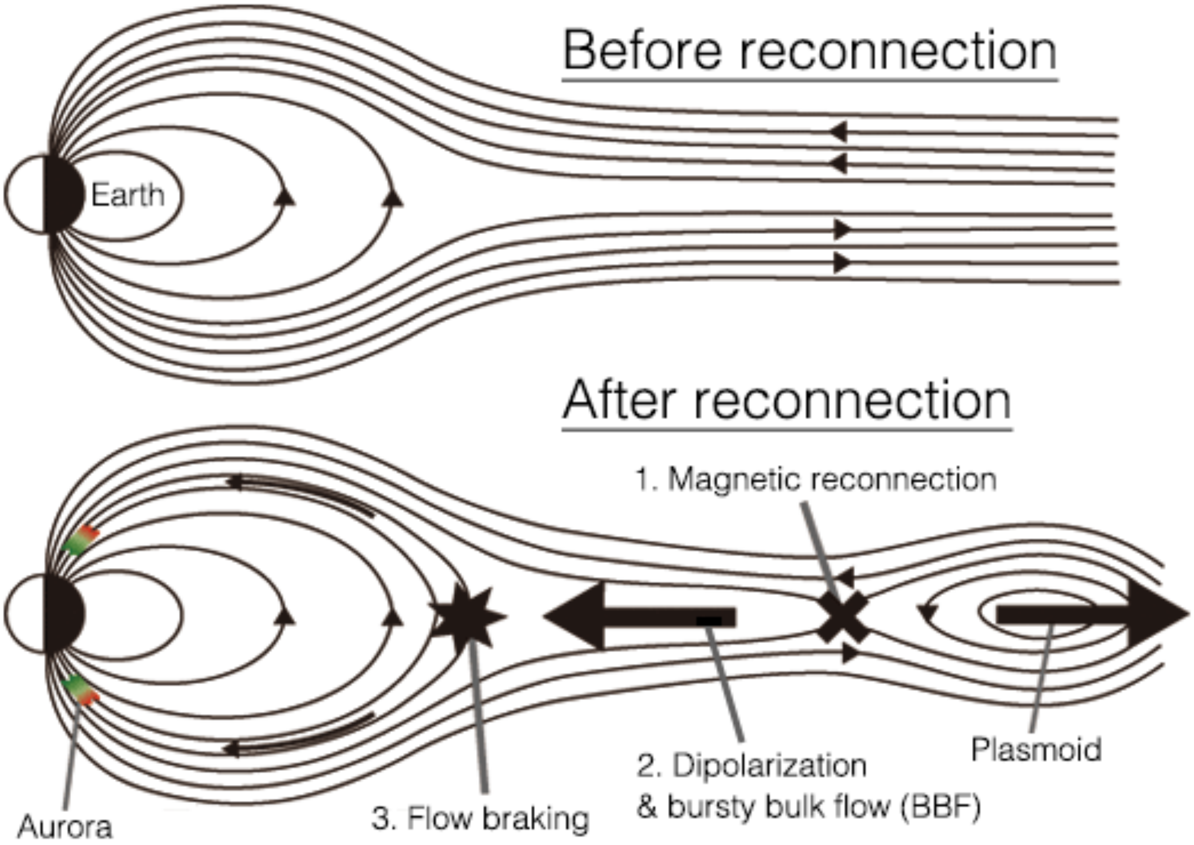

Figure 1.5. Schematic of magnetotail reconnection producing a dipolarization at Earth. Adapted from Miyashita (2010).

The expansion phase generates magnetic structures known as dipolarizations. Dipolarizations are the newly reconnected, closed flux tubes produced by intense nightside reconnection and correspond to the collapse of the near-tail region from a stretched configuration to a more dipolar configuration (see Figure 1.5). Dipolarizations contain a stronger northward magnetic field component than the surrounding plasma sheet, such that currents are required to separate these distinct plasma populations. The leading edge of the dipolarization is known as the dipolarization front while the magnetic structure behind the front is known as the dipolarizing flux bundle. A strong duskward current separates the dipolarization front from the plasma sheet in front of it. While some of this current connects around the dipolarization, the majority of it connects to the ionosphere in a Region 1-sense. Created from magnetic reconnection, dipolarizations are embedded within fast reconnection outflows, also known as bursty bulk flows, and are depleted in thermal plasma while enhanced in superthermal or even energetic plasma compared to the ambient plasma. Consistent with the enhanced sunward flow and enhanced northward magnetic field, dipolarizations possess strong duskward electric fields. Despite dipolarizations being localized in cross-tail width (~1-3 R_E compared to ~40 R_E with of Earth's magnetotail), they are responsible for the majority of flux transport within the plasma sheet during substorm expansion phases (Liu et al., 2014). An example of in situ observations of a dipolarization is shown in Figure 1.6.

As dipolarizations travel from the reconnection site toward Earth, they are responsible for additional substorm dynamics. Dipolarizations accelerate particles as the structures travel closer towards Earth's dipole center (Ashour-Abdalla et al., 2011; Gabrielse et al., 2016). The typical magnetic field strength near the reconnection site in Earth's magnetotail is ~10 nT so as dipolarizations travel closer to Earth, they encounter regions of stronger magnetic field strength. Plasma trapped by the strong magnetic field gradients about the dipolarization structure (e.g., Ukhorskiy et al., 2018) experience this increase in field strength and energize accordingly (i.e., betatron acceleration from the conservation of the first adiabatic invariant). As the dipolarizations travel Earthward, their field lines shorten, which allow for Fermi acceleration (i.e., conservation of the second adiabatic invariant). As plasma is energized, their gyroradii can increase beyond the scale size of the dipolarization, causing the energized plasma to escape the structure. Particles do not need to be trapped to experience energization from the dipolarization (e.g., Birn et al., 2013). Electrons, for example, traveling dawnward across the magnetotail can drift across the dipolarization. Since the dipolarization contains a strong duskward electric field, electrons are energized as they move across the magnetic structure. Plasma energization from dipolarizations can be an important seed population to Earth's radiation belts (Gkioulidou et al., 2015; Turner et al., 2015).

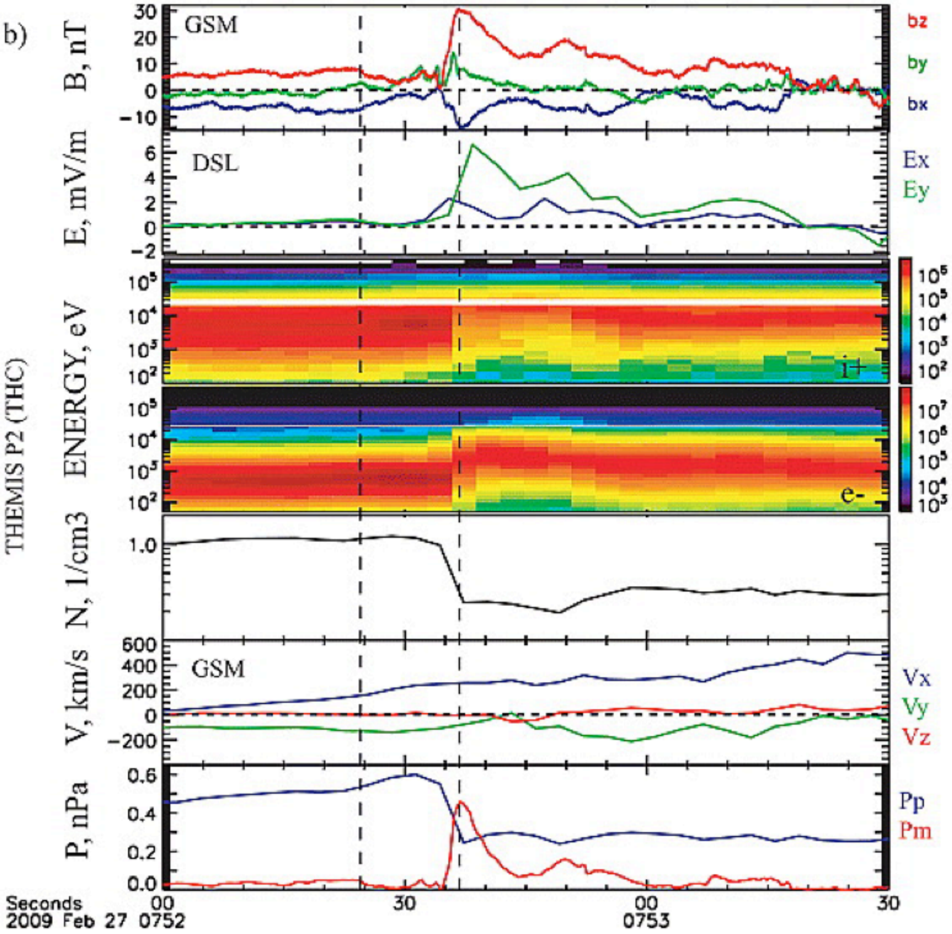

Figure 1.6. Example dipolarization observed in situ by a THEMIS spacecraft at Earth. Panels, from top to bottom, correspond to: vector magnetic field, vector electric field, ion flux spectrogram, electron flux spectrogram, plasma density, vector ion flow, and pressure (plasma and magnetic). Adapted from Runov et al. (2009).

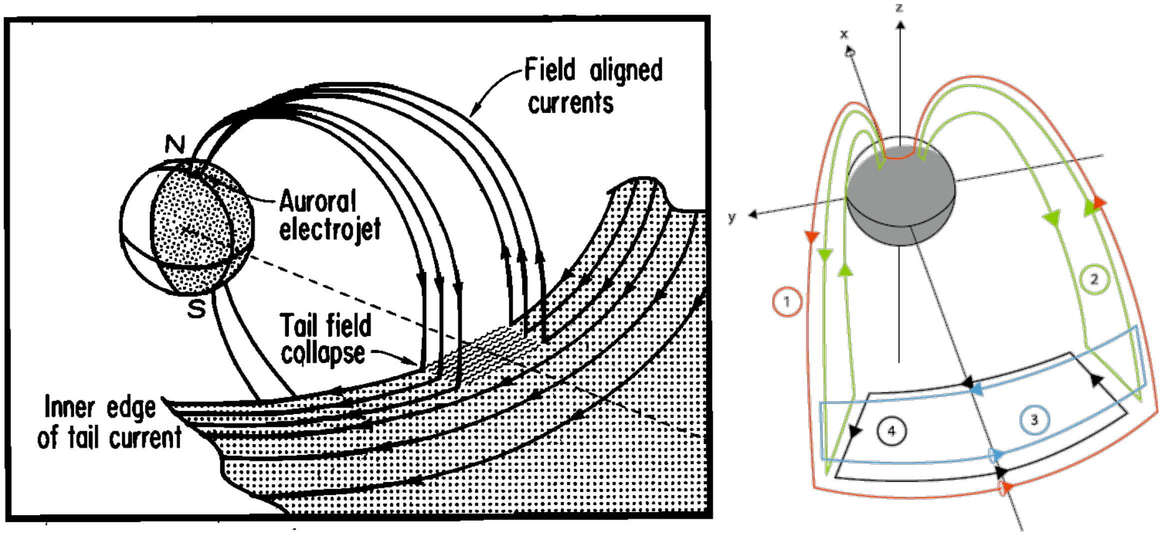

Figure 1.7. (left) Early schematic of the substorm current wedge from McPherron et al. (1973). (right) Updated schematic with additional current loops from Kepko et al. (2015). These additional loops are suggested by simulations of magnetotail collapse (Birn et al., 1999).

In addition to plasma energization and magnetic flux transport, dipolarizations at Earth are also responsible for the formation of the substorm current wedge. The substorm current wedge (SCW), depicted in Figure 1.7, is a large-scale current system that forms during the expansion/recovery phases of substorms. The SCW diverts the duskward plasma sheet current into the ionosphere along magnetic field lines (see, e.g., Kepko et al., 2015). This current structure is associated with an enhancement of the northward component in the near-tail region, which is supplied by dipolarizations. Dipolarizations infrequently reach Earth's inner magnetosphere, instead braking near the inner edge of the plasma sheet due to the steep increase in magnetic pressure located there (Shiokawa et al., 1997; Liu et al., 2016). As dipolarizations and their associated fast flows brake, the magnetic flux contained within the structure accumulates (i.e., piles up) at this region (Birn et al., 2011). The enhanced northward component of the magnetic field at this pileup region initiates the SCW. As dipolarizations travel from the magnetotail reconnection site to the braking region, they communicate changes in their field line geometry to the ionosphere via Alfvén waves (Southwood & Kivelson, 1991). Alfvén waves propagate along the field line and carry field-aligned current. As the dipolarization brakes these Alfvén waves become standing waves, allowing for the formation of a static field-aligned current system like the SCW. In the leading "wedgelet" conceptual model for SCW formation, multiple dipolarizations braking and contributing their magnetic flux and field-aligned currents to the pileup region establish the current wedge (Liu et al., 2013; Birn et al., 2019). As additional individual dipolarizations brake and pile up, the pileup region expands azimuthally and further downtail (e.g., Merkin et al., 2019). The pileup of magnetic flux near the inner edge of the plasma sheet and the associated increased of the northward component of the magnetic field there is often considered as a "large-scale dipolarization" since the enhancement spans a region larger than a typical (small-scale) dipolarization.

1.5 Substorm Dynamics at Mercury

While the concept of a magnetospheric substorm originated from and has been most thoroughly studied with regards to Earth, Mercury's magnetosphere exhibits similar dynamics. An example of a substorm observed by MESSENGER is shown in Figure 1.8 (Sun et al., 2015). The MESSENGER spacecraft observed the characteristic signatures of tail loading, unloading, and dipolarization within the plasma sheet. The first two vertical dashed lines mark the growth phase. During this interval, the sunward component of the magnetic field (B_x) increases while the total field strength decreases, indicative of plasma sheet thinning under the enhanced pressure from loaded magnetotail lobes that is consistent with the growth phase. Between the second and third dashed lines (the expansion phase), the sunward field decreases while the northward field

(B_z) increases, consistent with unloading and dipolarization. These substorm components at Mercury have also received the attention of dedicated investigations.

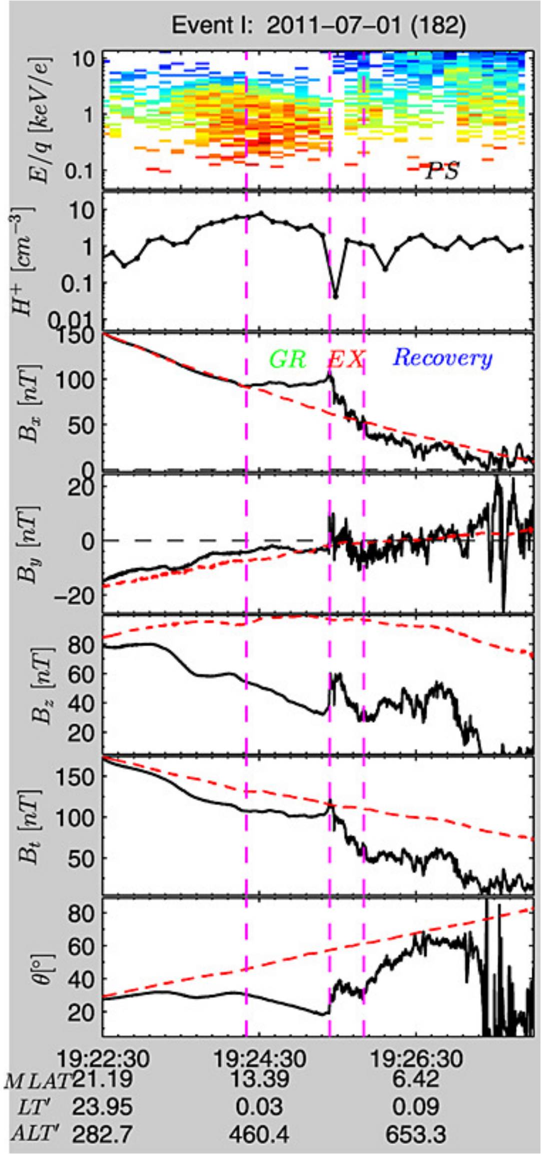

Figure 1.8. An example of a substorm observed by MESSENGER at Mercury. Panels, from top to bottom, correspond to: proton flux spectrogram, proton density, northward magnetic field (B_z), duskward magnetic field (B_y), sunward magnetic field (B_x), total magnetic field strength, and magnetic elevation angle. Time and spacecraft location are listed below the bottom panel.

Mercury's magnetotail experiences intervals of clear loading and unloading (e.g., Slavin et al., 2010). Three such loading-unloading events in Mercury's southern magnetotail lobe are shown in Figure 1.9. During this ~30 min interval, the spacecraft observes three intervals consistent with lobe loading and unloading (shaded in green). Within each event, the magnetic field strength increases and the magnetotail flares (loading) followed by a decrease in both field strength and elevation angle (unloading). Examining 438 loading-unloading events in Mercury's magnetotail, Imber & Slavin (2017) found that loading-unloading events are relatively shorter and more intense at Mercury than at Earth. Loading increases the lobe field by ~25% at Mercury over ~1-3 min compared to ~10% at Earth over ~1-3 hours. Typically, loading of Mercury's magnetotail increases its magnetic flux content by ~0.69 ± 0.38 MWb, which corresponds to a dayside reconnection rate ~7 kV greater than the nightside rate. Mercury's magnetosphere has a total magnetic flux content of ~7.5 MWb, so the magnetic flux stored within Mercury's lobes during the substorm growth phase is a meaningful fraction of the total flux of the system.

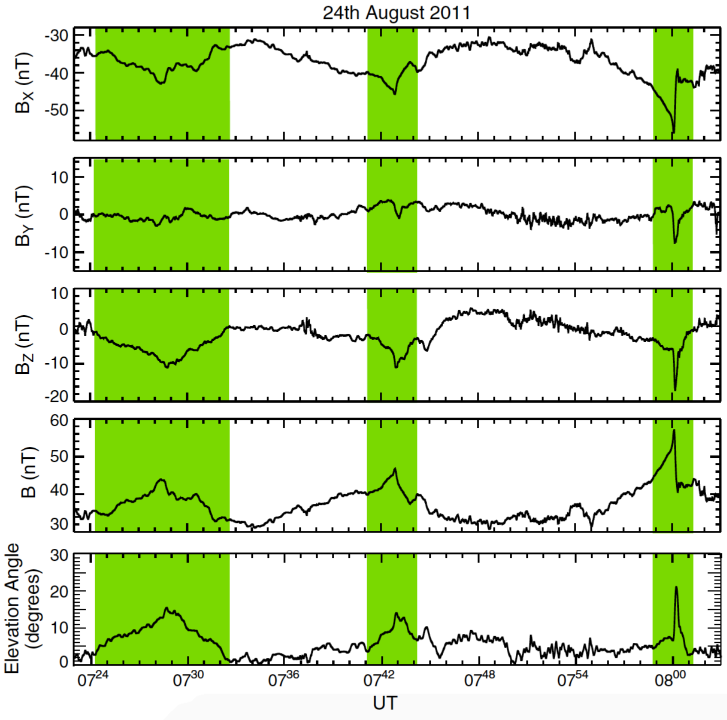

Figure 1.9. Examples of magnetotail loading and unloading (shaded green) observed by MESSENGER in Mercury's southern magnetotail lobe. Adapted from Imber & Slavin (2017).

Dipolarizations in Mercury’s plasma sheet have also been identified. Observations from the Mariner 10 flybys first suggested their presence within Mercury’s plasma sheet, which was later confirmed by MESSENGER observations. A series of dipolarizations identified by MESSENGER is shown in Figure 1.10. A statistical analysis of a small sample of dipolarizations (24 events) by Sundberg et al. (2012) reveal dipolarization fronts last ~1.6 s over which the magnetic field increases to ~40-50 nT and persists for ~10 s (dipolarizing flux bundle duration). Sun et al. (2016) used an automated detection technique to expand the survey of dipolarizations in Mercury’s magnetotail and discovered that dipolarizations at Mercury are more frequent to the post-midnight (i.e., dawnside) magnetotail, opposite to that of Earth. In addition to insights into the characteristic magnetic structure and event location, some studies have loosely connected dipolarizations to energetic electron acceleration and injection. Two dipolarizations from the Mariner 10 flybys (Christon et al., 1987) and an additional event during MESSENGER’s orbital mission (Baker et al., 2016) have identified energetic electrons coincident with a dipolarization. Since Mercury occupies a large fraction of its magnetosphere (see Chapter 1.3), Mercury’s magnetosphere does not host permanent radiation belts like Earth but does possess bursts of energetic electrons (e.g., Ho et al., 2012; Lawrence et al., 2015; Ho et al., 2016). These bursts are typically observed on the dawnside of the magnetosphere, suggesting they may originate in the magnetotail and drift towards the dayside. Baker et al. (2016) proposed dipolarizations may energize and inject these electrons, however, this hypothesis remains an open question. Similarly, many other open questions concerning dipolarizations persist, spanning from their contribution to magnetic flux transport to their association with fast sunward flows.

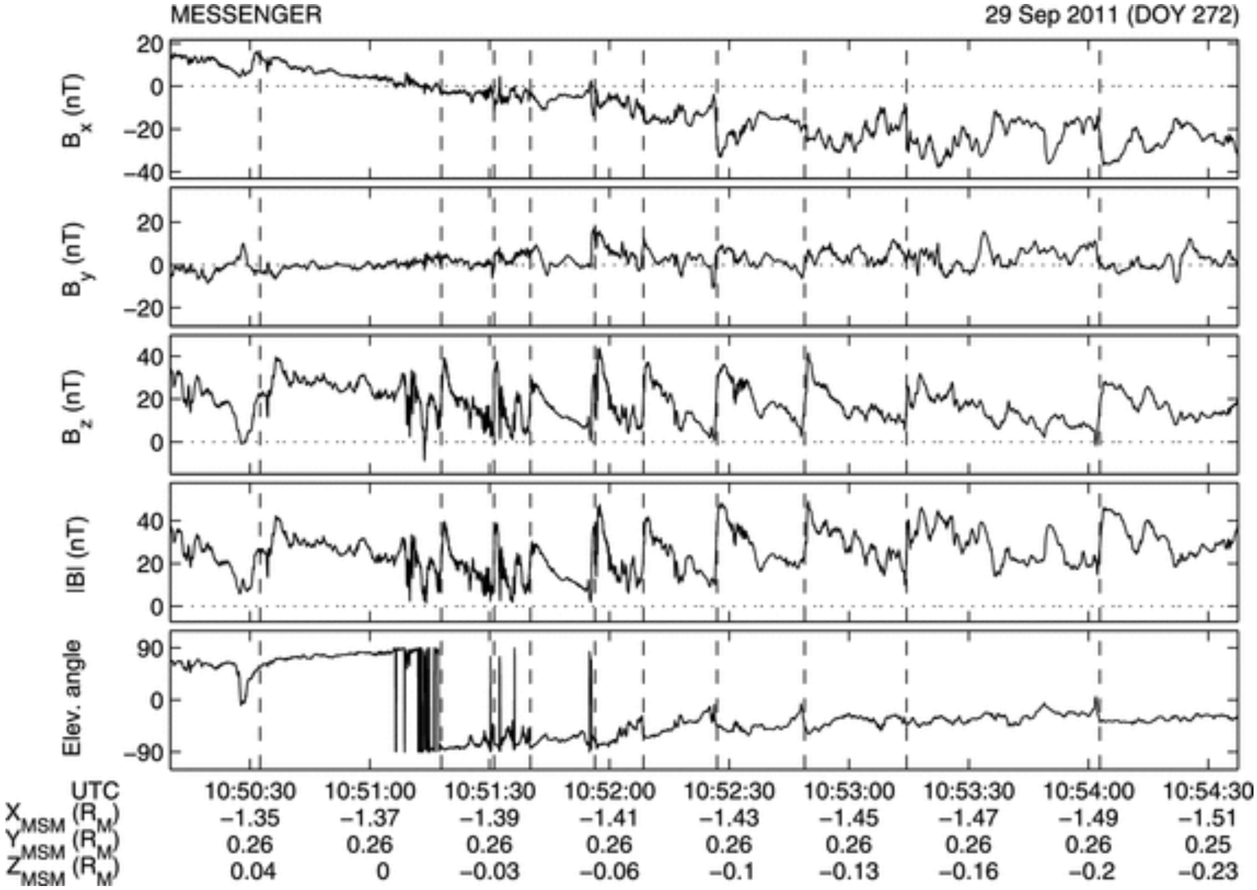

Figure 1.10. A series of magnetotail dipolarizations (dipolarization fronts indicated by vertical dashed lines) observed by MESSENGER in Mercury's magnetotail. Figure from Sundberg et al. (2012).

1.6 Guiding Science Questions

Mercury possesses an intrinsic global magnetic field that with its interaction with the solar wind forms a terrestrial-like magnetosphere. However, different from Earth's magnetosphere, Mercury's operates at substantially smaller spatiotemporal scales, experiences stronger effects from magnetic reconnection, and displays intricate coupling with the planetary interior. These differences manifest as a result from Mercury's weaker planetary field strength, lack of atmosphere, and stronger upstream solar wind forcing. Despite the differences between the magnetospheres, both share similar substorm dynamics, particularly magnetotail loading/unloading and dipolarization. While these dynamics have been investigated at Earth for over 50 years using both ground- and space-based observations, the study of Mercury's substorm dynamics has benefitted from only six spacecraft flybys and 4 years of orbital observations. It is not surprising, therefore, that as open questions about Earth's substorm process remain that even more persist for Mercury's magnetosphere. We seek to enhance our understanding of Mercury's substorm dynamics by investigating the nature of dipolarizations within the planet's magnetotail. Given the similarities between Earth and Mercury's magnetospheres, improving our understanding of dipolarizations at Mercury not only help us to learn more about the smallest planet's dynamics, but enrich our understanding of Earth's dynamics as well, opening the door to begin generalizing the substorm process outside of our solar system. We focus our investigation about the following three scientific questions:

1. **How characteristically similar are dipolarizations in Mercury's magnetotail to those at Earth?**

   Dipolarizations at both Earth and Mercury share similar magnetic structure: the sharp, step-like increase of the northward component of the magnetic field (dipolarization front) that persists for some time (dipolarizing flux bundle). In addition to this structure, Earth's dipolarizations also exhibit depletion and heating of thermal plasma, enhancement of energetic plasma, a strong sunward flow, and (self-consistently) a strong duskward electric field. Do Mercury's dipolarizations exhibit similar signatures and how do they compare both relatively and absolutely?

2. **What are the consequences of dipolarizations at Mercury?**

Dipolarizations in Earth's magnetotail are important for magnetic flux and mass transport, energization of plasma, and substorm current wedge formation. At Mercury, dipolarizations have been suspected to play similarly important roles (e.g., energetic electron acceleration) but have not been thoroughly investigated.

3. **How do differences between Earth and Mercury's magnetospheres manifest in dipolarizations?**

    Initial studies of dipolarizations at Mercury have already indicated some difference with those at Earth. Namely, dipolarizations at Mercury occur more commonly in the post-midnight magnetotail, while dipolarizations at Earth occur more commonly in the pre-midnight magnetotail. What other differences, in both dipolarizations' characteristics and consequences, exist and what do they reveal about the substorm process?

To address these questions, we use observations from the MESSENGER spacecraft. Chapter 2 discusses the spacecraft mission in more detail, describes the instruments and data we utilize, and summarizes the philosophy of our methodology. Chapters 3-5 investigate facets of dipolarizations at Mercury, beginning with the association with energetic electrons in Chapter 3, association with fast flows in Chapter 4, and occurrence of flow braking and flux pileup in Chapter 5. Chapter 6 summarizes the results and conclusions from each of these investigative chapters in reference to our science questions, with an eye towards the future. In support of our analysis, we include three appendices that describe in detail some of the techniques we apply during our investigations.

1.7 References

Akasofu, S. I. (1964). The development of the auroral substorm. *Planetary and Space Science*, **12**(4), 273-282.

Alexeev, I. I., Belenkaya, E. S., Slavin, J. A., Korth, H., Anderson, B. J., Baker, D. N., … Solomon, S. C. (2010). Mercury's magnetospheric magnetic field after the first two MESSENGER flybys. *Icarus*, **209**(1), 23–39. https://doi.org/10.1016/j.icarus.2010.01.024

Anderson, B. J., Johnson, C. L., Korth, H., Purucker, M. E., Winslow, R. M., Slavin, J. A., … Zurbuchen, T. H. (2011). The global magnetic field of Mercury from MESSENGER orbital observations. *Science*, **333**, 1859–1862. https://doi.org/10.1126/science.1211001

Anderson, B. J., Johnson, C. L., Korth, H., Slavin, J. A., Winslow, R. M., Phillips, R. J., Solomon, S. C., & McNutt Jr., R. L. (2014). Steady-state field-aligned currents at Mercury. *Geophysical Research Letters,* **41**, 7444–7452. https://doi.org/10.1002/2014GL061677

Ashour-Abdalla, M., El-Alaoui, M., Goldstein, M. L., Zhou, M., Schriver, D., Richard, R., …Hwang, K.-J. (2011). Observations and simulations of non-local acceleration of electrons in magnetotail magnetic reconnection events. *Nature Physics,* **7**, 360 365. https://doi.org/10.1038/nphys1903

Baker, D. N., Odstrčil, D., Anderson, B. J., Arge, C. N., Benna, M., Gloeckler, G., … Zurbuchen, T. H.(2009). Space environment of mercury at the time of the first MESSENGER flyby: Solar wind and interplanetary magnetic field modeling of upstream conditions. *Journal of Geophysical Research*, **114**, A10101. https://doi.org/10.1029/2009JA014287

Baker, D. N., Odstrčil, D., Anderson, B. J., Arge, C. N., Benna, M., Gloeckler, G., & Zurbuchen, T. H.(2011). The space environment of Mercury at the times of the second and third MESSENGER flybys. *Planetary and Space Science*, **59**(15), 2066–2074. https://doi.org/10.1016/j.pss.2011.01.018

Baker, D. N., Poh, G., Odstrčil, D., Arge, C. N., Benna, M., Johnson, C. L., … Zurbuchen, T. H. (2013). Solar wind forcing at Mercury: WSA-ENLIL model results. *Journal of Geophysical Research: Space Physics*, **118**, 45–57. https://doi.org/10.1029/2012JA018064

Baker, D. N., Dewey, R. M., Lawrence, D. J., Goldsten, J. O., Peplowski, P. N., Korth, H., … Solomon, S. C. (2016). Intense energetic electron flux enhancements in Mercury's magnetosphere: An integrated view with high-resolution observations from MESSENGER. *Journal of Geophysical Research: Space Physics*, **121**, 2171–2184. https://doi.org/10.1002/2015JA021778

Birn, J., Hesse, M., Haerendel, G., Aumjohann, W. B., & Shiokawa, K. (1999). Flow braking and the substorm current wedge. *Journal of Geophysical Research: Space Physics,* **114**(A), 19895–19904.

Birn, J., Nakamura, R., Panov, E., & Hesse, M. (2011). Bursty bulk flows and dipolarization in MHD simulations of magnetotail reconnection. *Journal of Geophysical Research*, **116**, A01210. https://doi.org/10.1029/2010JA016083

Birn, J., Hesse, M., Nakamura, R., & Zaharia, S. (2013). Particle acceleration in dipolarization events. *Journal of Geophysical Research: Space Physics,* **118**, 1960–1971. https://doi.org/10.1002/jgra.50132

Birn, J., Liu, J., Runov, A., Kepko, L., & Angelopoulos, V. (2019). On the contribution of dipolarizing flux bundles to the substorm current wedge and to flux and energy transport. *Journal of Geophysical Research: Space Physics,* **124**, 5408–5420. https://doi.org/10.1029/2019JA026658

Burton, R. K., McPherron, R. L., & Russell, C. T. (1975). The terrestrial magnetosphere: A half-wave rectifier of the interplanetary electric field. *Science*, **189**(4204), 717–718. https://doi.org/10.1126/science.189.4204.717

Christon, S. P., Feynman, J., & Slavin, J. A. (1987). Dynamic substorm injections — Similar magnetospheric phenomena at Earth and Mercury. In A. T. Y. Lui (Ed.), *Magnetotail physics* (pp. 393–400). Baltimore, MD: Johns Hopkins University Press.

Dewey, R. M., Baker, D. N., Anderson, B. J., Benna, M., Johnson, C. L., & Korth, H. (2015). Improving solar wind modeling at Mercury: Incorporating transient solar phenomena into the WSA-ENLIL model with the CONE extension. *Journal of Geophysical Research: Space Physics*, **120**, 5667–5685. https://doi.org/10.1002/2015JA021194

DiBraccio, G. A., Slavin, J. A., Imber, S. M., Gershman, D. J., Raines, J. M., Jackman, C. M., et al. (2015). MESSENGER observations of flux ropes in Mercury's magnetotail. *Planetary and Space Science,* **115**, 77–89. https://doi.org/10.1016/j.pss.2014.12.016

Dungey, J. W. (1961). Interplanetary magnetic field and the auroral zones. *Physical Review Letters*, **6**, 47–48. https://doi.org/10.1103/PhysRevLett.6.47

Forsyth, C., Rae, I. J., Coxon, J. C., Freeman, M. P., Jackman, C. M., Gjerloev, J., & Fazakerley, A. N. (2015). A new technique for determining substorm onsets and phases from indices of the electrojet (SOPHIE). *Journal of Geophysical Research: Space Physics*, **120**, 10,592–10,606. https://doi.org/10.1002/2015JA021343

Gabrielse, C., Harris, C., Angelopoulos, V., Artemyev, A., & Runov, A. (2016). The role of localized inductive electric fields in electron injections around dipolarizing flux bundles.

Journal of Geophysical Research: Space Physics, **121**, 9560–9585. https://doi.org/10.1002/2016JA023061

Gershman, D. J., Slavin, J. A., Raines, J. M., Zurbuchen, T. H., Anderson, B. J., Korth, H., … Solomon, S. C. (2013). Magnetic flux pile-up and plasma depletion in Mercury's subsolar magnetosheath. *Journal of Geophysical Research: Space Physics*, **118**, 7181–7199. https://doi.org/10.1002/2013JA019244

Gershman, D. J., Slavin, J. A., Raines, J. M., Zurbuchen, T. H., Anderson, B. J., Korth, H., et al. (2014). Ion kinetic properties in Mercury's premidnight plasma sheet. *Geophysical Research Letters*, **41**, 5740–5747. https://doi.org/10.1002/2014GL060468

Gkioulidou, M., Ohtani, S., Mitchell, D. G., Ukhorskiy, A. Y., Reeves, G. D., Turner, D. L., Gjerloev, J. W., Nosé, M., Koga, K., Rodriguez, J. V., & Lanzerotti, L. J. (2015). Spatial structure and temporal evolution of energetic particle injections in the inner magnetosphere during the 14 July 2013 substorm event. *Journal of Geophysical Research: Space Physics*, **120**, 1924–1938. https://doi.org/10.1002/2014JA020872

Haerendel, G. (2015). Substorms: Plasma and Magnetic Flux Transport from Magnetic Tail into Magnetosphere. In A. Keiling, C. M. Jackman, & P. A. Delamere (Eds.), *Magnetotails in the solar system*. Hoboken, NJ: John Wiley. https://doi.org/10.1002/9781118842324.ch18

Ho, G. C., Krimigis, S. M., Gold, R. E., Baker, D. N., Anderson, B. J., Korth, H., … Solomon, S. C. (2012). Spatial distribution and spectral characteristics of energetic electrons in Mercury's magnetosphere. *Journal of Geophysical Research*, **117**, A00M04. https://doi.org/10.1029/2012JA017983

Ho, G. C., Starr, R. D., Krimigis, S. M., Vandegriff, J. D., Baker, D. N., Gold, R. E., … Solomon, S. C. (2016). MESSENGER observations of suprathermal electrons in Mercury's magnetosphere. *Geophysical Research Letters*, **43**, 550–555. https://doi.org/10.1002/2015GL066850

Hsu, T.-S., & McPherron, R. L. (2000). The characteristics of storm-time substorms and non-storm substorms, Proceedings of the International Conference on Substorms (ICS-5), Eur. Space Agency, Spec. Publ., ESA SP-443, 439.

Imber, S. M., & Slavin, J. A. (2017). MESSENGER observations of magnetotail loading and unloading: Implications for substorms at Mercury. *Journal of Geophysical Research: Space Physics*, **122**, 11,402–11,412. https://doi.org/10.1002/2017JA024332

Jia, X., Slavin, J. A., Gombosi, T. I., Daldorff, L. K. S., Toth, G., & van der Holst, B. (2015). Global MHD simulations of Mercury's magnetosphere with coupled planetary interior: Induction effect of the planetary conducting core on the global interaction. *Journal of Geophysical Research: Space Physics,* **120**, 4763–4775. https://doi.org/10.1002/2015JA021143

Jia, X., Slavin, J. A., Poh, G., DiBraccio, G. A., Toth, G., Chen, Y., et al. (2019). MESSENGER observations and global simulations of highly compressed magnetosphere events at Mercury. *Journal of Geophysical Research: Space Physics,* **124**, 229–247. https://doi.org/10.1029/2018JA026166

Johnson, C. L., Purucker, M. E., Korth, H., Anderson, B. J., Winslow, R. M., Al Asad, M. M. H., Slavin, J. A., Alexeev, I. I., Phillips, R. J., Zuber, M. T., & Solomon, S. C. (2012). MESSENGER observations of Mercury's magnetic field structure. *Journal of Geophysical Research*, **117**, E00L14. https://doi.org/10.1029/2012JE004217

Johnson, C. L., Philpott, L. C., Anderson, B. J., Korth, H., Hauck, S. A. II, Heyner, D., et al. (2016). Messenger Observations Of Induced Magnetic Fields In Mercury's Core. *Geophysical Research Letters,* **43**, 2436–2444. https://doi.org/10.1002/2015GL067370

Kaymaz, Z., Siscoe, G. L., & Luhmann, J. G. (1992). IMF draping around the Geotail: IMP 8 observations. *Journal of Geophysical Research*, **19**, 829– 832.

Kepko, L., McPherron, R., Amm, O., Apatenkov, S., Baumjohann, W., Birn, J., & Sergeev, V. (2015). Substorm current wedge revisited. *Space Science Reviews,* **190**, 1–46. https://doi.org/10.1007/s11214-014-0124-9

Lawrence, D. J., Anderson, B. J., Baker, D. N., Feldman, W. C., Ho, G. C., Korth, H., … Winslow, R. M. (2015). Comprehensive survey of energetic electron events in Mercury’s magnetosphere with data from the MESSENGER gamma-ray and neutron spectrometer. *Journal of Geophysical Research: Space Physics*, **120**, 2851–2876. https://doi.org/10.1002/2014JA020792

Liu, J., Angelopoulos, V., Runov, A., & Zhou, X.-Z. (2013). On the current sheets surrounding dipolarizing flux bundles in the magnetotail: The case for wedgelets. *Journal of Geophysical Research: Space Physics,* **118**, 2000–2020. https://doi.org/10.1002/jgra.50092

Liu, J., Angelopoulos, V., Zhou, X.-Z., & Runov, A. (2014). Magnetic flux transport by dipolarizing flux bundles. *Journal of Geophysical Research: Space Physics,* **119**, 909–926. https://doi.org/10.1002/2013JA019395

Liu, J., Angelopoulos, V., Zhang, X.-J., Turner, D. L., Gabrielse, C., Runov, A., Li, J., Funsten, H. O., & Spence, H. E. (2016). Dipolarizing flux bundles in the cis-geosynchronous magnetosphere: Relationship between electric fields and energetic particle injections. *Journal of Geophysical Research: Space Physics*, **121**, 1362–1376. https://doi.org/10.1002/2015JA021691

McPherron, R. L., Russell, C. T., & Aubry, M. A. (1973). Satellite studies of magnetospheric substorms on August 15, 1968, 9, Phenomenological model for substorms. *Journal of Geophysical Research,* **78**, 3131.

Merkin, V. G., Panov, E. V., Sorathia, K., & Ukhorskiy, A. Y. (2019). Contribution of bursty bulk flows to the global dipolarization of the magnetotail during an isolated substorm. *Journal of Geophysical Research: Space Physics,* **124**, 8647–8668. https://doi.org/10.1029/2019JA026872

Miyashita, Y. (2010). Mysterious Auroral Events ~ To be Explored by GEOTAIL Satellite. Japanese Aerospace Exploration Agency, accessed via http://www.isas.jaxa.jp/e/forefront/2010/miyashita/02.shtml

Ness, N. F., Behannon, K. W., Lepping, R. P., Whang, Y. C., & Schatten, K. H. (1974). Magnetic field observations near Mercury: Preliminary results from Mariner 10. *Science*, **185**(4146), 151– 160. https://doi.org/10.1126/science.185.4146.151

Ness, N. F., Behannon, K. W., Lepping, R. P., and Whang, Y. C. (1975). Magnetic field of Mercury confirmed. *Nature*, **255**, 204–205. https://doi.org/10.1038/255204a0

Ogilvie, K. W., Scudder, J. D., Vasyliunas, V. M., Hartle, R. E., & Siscoe, G. L. (1977). Observations at the planet Mercury by the plasma electron experiment, Mariner 10. *Journal of Geophysical Research,* **82**(13), 1807–1824. https://doi.org/10.1029/JA082i013p01807

Poh, G., Slavin, J. A., Jia, X., Raines, J. M., Imber, S. M., Sun, W.-J., et al. (2017a). Mercury's cross-tail current sheet: Structure, X-line location and stress balance. *Geophysical Research Letters,* **44**, 678–686. https://doi.org/10.1002/2016GL071612

Rong, Z. J., Ding, Y., Slavin, J. A., Zhong, J., Poh, G., Sun, W. J., … Shen, C. (2018). The magnetic field structure of Mercury's magnetotail. *Journal of Geophysical Research: Space Physics,* **123**, 548–566. https://doi.org/10.1002/2017JA024923

Runov, A., Angelopoulos, V., Sitnov, M. I., Sergeev, V. A., Bonnell, J., McFadden, J. P., … Auster, U. (2009). THEMIS observations of an earthward-propagating dipolarization front. *Geophysical Research Letters,* **36**, L14106. https://doi.org/10.1029/2009GL038980

Shay, M. A., & Swisdak M. (2004). Three-species collisionless reconnection: Effect of O+ on magnetotail reconnection. *Physical Review Letters,* **93**, 175001. https://doi.org/10.1103/PhysRevLett.93.175001

Shiokawa, K., Baumjohann, W., & Haerendel, G. (1997). Braking of high-speed flows in the near-Earth tail. *Geophysical Research Letters,* **24**, 1179–1182. https://doi.org/10.1029/97GL01062

Slavin, J. A., & Holzer R. E. (1981). Solar wind flow about the terrestrial planets, 1. Modeling bow shock position and shape. *Journal of Geophysical Research*, **86**, 11,401–11,418. doi:10.1029/JA086iA13p11401.

Slavin, J. A., Acuna, M. H., Anderson, B. J., Baker, D. N., Benna, M., Boardsen, S. A., et al. (2009). MESSENGER observations of magnetic reconnection in Mercury's magnetosphere. *Science,* **324**(5927), 606–610. https://doi.org/10.1126/science.1172011

Slavin, J. A., Anderson, B. J., Baker, D. N., Benna, M., Boardsen, S. A., Gloeckler, G., … Zurbuchen, T. H. (2010). MESSENGER observations of extreme loading and unloading of Mercury's magnetic tail. *Science*, **329**(5992), 665–668. https://doi.org/10.1126/science.1188067

Slavin, J. A., Anderson, B. J., Baker, D. N., Benna, M., Boardsen, S. A., Gold, R. E., … Zurbuchen, T. H. (2012). MESSENGER and Mariner 10 flyby observations of magnetotail structure and dynamics at Mercury. *Journal of Geophysical Research*, **117**, A01215. https://doi.org/10.1029/2011JA016900

Slavin, J. A., DiBraccio, G. A., Gershman, D. J., Imber, S., Poh, G. K., Raines, J., et al. (2014). MESSENGER observations of Mercury's dayside magnetosphere under extreme solar wind conditions. *Journal of Geophysical Research: Space Physics,* **119**, 8087–8116. https://doi.org/10.1002/2014JA020319

Slavin, J. A., Middleton, H. R., Raines, J. M., Jia, X., Zhong, J., Sun, W.-J., Livi, S., Imber, S. M., Poh, G.-K., Akhavan-Tafti, M., Jasinski, J. M., DiBraccio, G. A., Dong, C., Dewey, R. M., & Mays, M. L. (2019). MESSENGER observations of disappearing dayside magnetosphere events at Mercury. *Journal of Geophysical Research: Space Physics*, **124**, 6613– 6635. https://doi.org/10.1029/2019ja026892

Solomon, S. C., Nittler, L. R., & Anderson, B. J. (2018). *Mercury: The view after MESSENGER*. London: Cambridge Univ. Press. ISBN: 978-1107154452

Southwood, D. J., & Kivelson, M. G. (1991). An approximate description of field-aligned currents in a planetary magnetic field. *Journal of Geophysical Research*, **96**(A1), 67–75. https://doi.org/10.1029/90JA01806

Sun, W.-J., Slavin, J. A., Fu, S., Raines, J. M., Zong, Q. G., Imber, S. M., et al. (2015). MESSENGER observations of magnetospheric substorm activity in Mercury's near magnetotail. *Geophysical Research Letters*, **42**, 3692–3699. https://doi.org/10.1002/2015GL064052

Sun, W. J., Fu, S. Y., Slavin, J. A., Raines, J. M., Zong, Q. G., Poh, G. K., & Zurbuchen, T. H. (2016). Spatial distribution of Mercury's flux ropes and reconnection fronts: MESSENGER observations. *Journal of Geophysical Research: Space Physics*, **121**, 7590–7607. https://doi.org/10.1002/2016JA022787

Sundberg, T., Slavin, J. A., Boardsen, S. A., Anderson, B. J., Korth, H., Ho, G. C., et al. (2012). MESSENGER observations of dipolarization events in Mercury's magnetotail. *Journal of Geophysical Research*, **117**, A00M03. https://doi.org/10.1029/2012JA017756

Tanskanen, E. I. (2009). A comprehensive high-throughput analysis of substorms observed by IMAGE magnetometer network: Years 1993–2003 examined. *Journal of Geophysical Research*, **114**, A05204. https://doi.org/10.1029/2008JA013682

Turner, D. L., Claudepierre, S. G., Fennell, J. F., O'Brien, T. P., Blake, J. B., Lemon, C., Gkioulidou, M., Takahashi, K., Reeves, G. D., Thaller, S., Breneman, A., Wygant, J. R., Li, W., Runov, A., & Angelopoulos, V. (2015). Energetic electron injections deep into the inner magnetosphere associated with substorm activity. *Geophysical Research Letters*, **42**, 2079–2087. https://doi.org/10.1002/2015GL063225

Ukhorskiy, A. Y., Sorathia, K. A., Merkin, V. G., Sitnov, M. I., Mitchell, D. G., & Gkioulidou, M. (2018). Ion trapping and acceleration at dipolarization fronts: High-resolution MHD and test-particle simulations. *Journal of Geophysical Research: Space Physics,* **123***,* 5580–5589. https://doi.org/10.1029/2018JA025370

Winslow, R. M., Anderson, B. J., Johnson, C. L., Slavin, J. A., Korth, H., Purucker, M. E., … Solomon, S. C. (2013). Mercury's magnetopause and bow shock from MESSENGER Magnetometer observations. *Journal of Geophysical Research: Space Physics,* **118**, 2213–2227. https://doi.org/10.1002/jgra.50237

Winslow, R. M., Lugaz, N., Philpott, L., Farrugia, C. J., Johnson, C. L., Anderson, B. J., Paty, C. S., Schwadron, N. A., & Al Asad, M. (2020). Observations of Extreme ICME Ram Pressure Compressing Mercury's Dayside Magnetosphere to the Surface. *The Astrophysical Journal*, **889**, 2, (184). https://doi.org/10.3847/1538-4357/ab6170

Zurbuchen, T. H., Raines, J. M., Slavin, J. A., Gershman, D. J., Gilbert, J. A., Gloeckler, G., Anderson, B. J., Baker, D. N., Korth, H., Krimigis, S. M., Sarantos, M., Schriver, D., McNutt Jr., R. L., & Solomon, S. C. (2011). MESSENGER observations of the spatial distribution of planetary ions near Mercury. *Science*, **333**, 1862–1865, htpps://doi.org/10.1126/science.1211302

Zweibel, E. G., & Yamada, M. (2016). Perspectives on magnetic reconnection. *Proceedings of the Royal Society A.*, **472**(2196), 20160479. https://doi.org/10.1098/rspa.2016.0479

CHAPTER II. MESSENGER Spacecraft and Instrumentation

2.1 MESSENGER Mission to Mercury

To investigate the science questions outlined in Chapter 1, we utilize observations from the MErcury Surface, Space ENvironment, GEochemistry, and Ranging (MESSENGER) spacecraft. For extensive discussion of MESSENGER's orbit and instrumentation, we refer readers to Solomon et al. (2007) and Solomon & Anderson (2018).

Launched in 2004, MESSENGER executed flybys of Earth, Venus, and Mercury before orbital insertion about Mercury on 18 March 2011. The spacecraft entered orbit about the planet with a highly inclined eccentric orbit. Initially, MESSENGER orbited Mercury with a 12 hour orbit, ~85° inclined from Mercury's equatorial plane (i.e., nearly polar), with periapsis of ~200 km and apoapsis of ~15,000 km. An example spacecraft orbit about Mercury is shown in Figure 2.1. After the first Earth year in orbit, spacecraft maneuvers on 16 and 20 April 2012 reduced apoapsis to ~10,000 km while keeping periapsis altitude fixed, resulting in a new 8 hour orbital period. MESSENGER continued in this orbit until near the end of the mission, when between August and October 2014, a series of maneuvers lowered the spacecraft's periapsis to within ~50 km of the surface. This "low altitude campaign" continued until the spacecraft exhausted its fuel and impacted Mercury's surface on 30 April 2015. While the three MESSENGER flybys of Mercury in 2008 and 2009 provide the first in situ measurements of Mercury's space environment since the initial Mariner 10 flybys in 1974 and 1975, we focus on the orbital phase of MESSENGER's mission to prevent overstated influence from the unique flyby geometries in our statistical analysis (see Chapter 2.6).

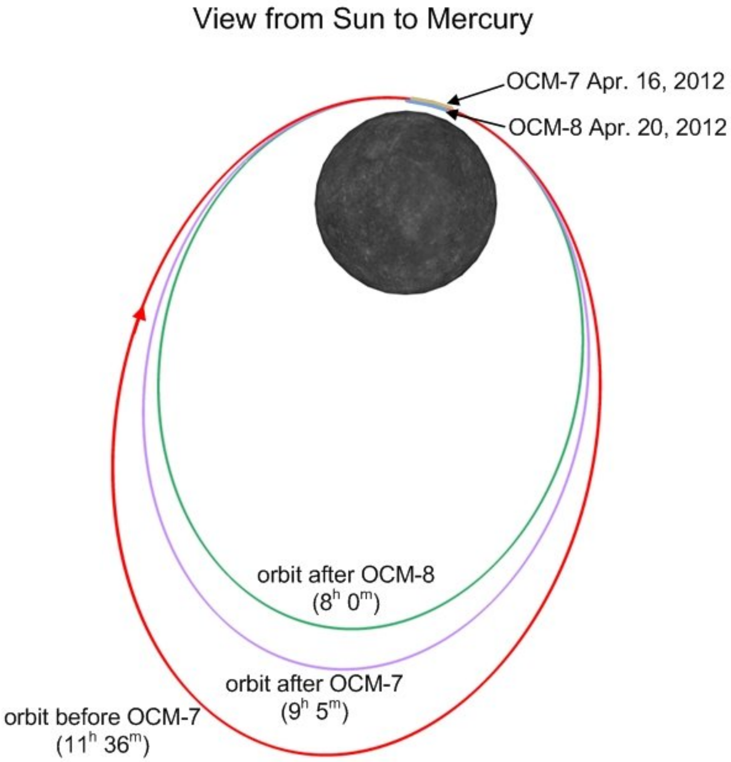

Figure 2.1. MESSENGER's orbit prior to (red) the orbit-correction maneuvers that reduced the spacecraft's orbit to 8 hours (green). North is up. From McAdams et al. (2014).

During the orbital lifetime of the MESSENGER mission, it executed 4,105 orbits of the planet spanning a little more than 4 Earth years (more than 16 Mercury years) and conducted its science collection continuously. Tasked with advancing our understanding of Mercury's magnetic field, exosphere, surface, and interior, MESSENGER was equipped with a variety of instruments. For our investigations, we focus on the Magnetometer (MAG), Fast Imaging Plasma Spectrometer (FIPS), and Gamma-Ray Spectrometer (GRS), which correspond to measurements of the magnetic field, thermal ion plasma, and energetic electron plasma respectively.

2.2 MAG Instrument

MESSENGER's Magnetometer (MAG) instrument (Anderson et al., 2007) provided observations of the local magnetic field. The instrument consists of a low noise, tri-axial fluxgate magnetometer mounted at the end of a 3.6 m boom. The boom is oriented along the +Y spacecraft direction (see Figure 2.2) so the MAG instrument was typically located directly antisunward of the spacecraft. MAG provided vector measurements of the magnetic field at variable magnitude and temporal resolution. For our investigation, we use the highest temporal (20 Hz resolution) observations, which correspond to a measurement range of ±1,530 nT with resolution of 0.047 nT along each of its axes.

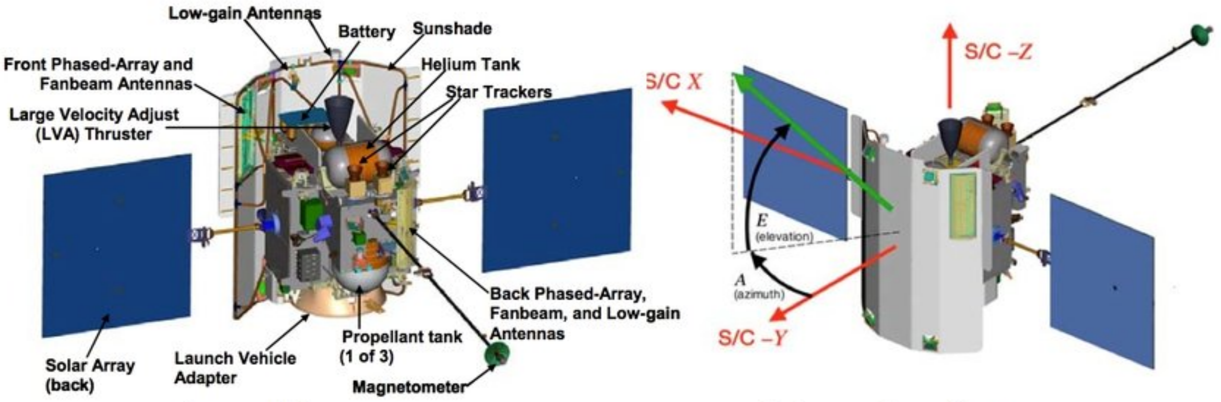

a. Spacecraft Components

b. Spacecraft coordinate axes

Figure 2.2. (a) The MESSENGER spacecraft and (b) its local coordinate system. From Vaughan et al. (2006).

2.3 FIPS Instrument

The Fast Imaging Plasma Spectrometer (FIPS) sensor measured thermal and low-energy ions with resolution of ion species (Andrews et al., 2007). A cross-sectional diagram of the sensor is included as Figure 2.3. During a complete measurement (~10 s in "burst" mode), FIPS would measure ions of different energy-per-charge (E/q) by stepping down 60 logarithmically spaced energy steps that span the instrument's energy range (46 eV/e to 13 keV/e). At each energy step, voltages applied to the deflection plates allow ions of only that corresponding energy-per-charge to pass through the electrostatic analyzer (i.e., ions following the curved, solid trajectories). This allowed FIPS to filter ions' incident energy; ions of too low or too high E/q would impact the instrument walls. At the entrance to the time of flight chamber, ions are accelerated by a large (12-15 kV) voltage so that they can pass through a thin carbon foil. Interacting with the foil, the ion is neutralized and secondary electrons are ejected. The now-neutralized ion travels ballistically to the micro-channel plate (MCP) located at the end of the TOF chamber, while the mirror-harp assembly guides secondary electrons to the MCP located at the bottom of the chamber. The electrons travel faster than the heavier neutralized ion, triggering a "start" signal at the bottom MCP; the neutralized ion provides the "stop" signal on the second MCP. From the two signals, the time of flight is determined, which along with knowing the ion's initial energy-per-charge allow for the determination of the ion's mass-per-charge. FIPS can therefore detect ions of mass-per-change (m/q) between 1 and 40 amu/e. In addition to its species resolution capability, FIPS also has imaging capabilities. The stop MCP consists of an array of 64 by 64 pixels, each of which map to a location in the FIPS field of view (FOV), enabling an ion's incident direction to be determined. Combined, the MCP pixels allow for an instantaneous FOV imaging of ~1.4π sr about FIPS's boresight direction (the central axis of the ~70° FOV cone), although spacecraft obstructions reduce this to an effective ~1.15π sr. The position-sensing capability of the MCP allows construction of three-dimensional velocity space distributions from which bulk flows can be estimated (see Appendix B). For our investigations, we focus on the "burst" mode, proton (m/q = 1) observations from FIPS.

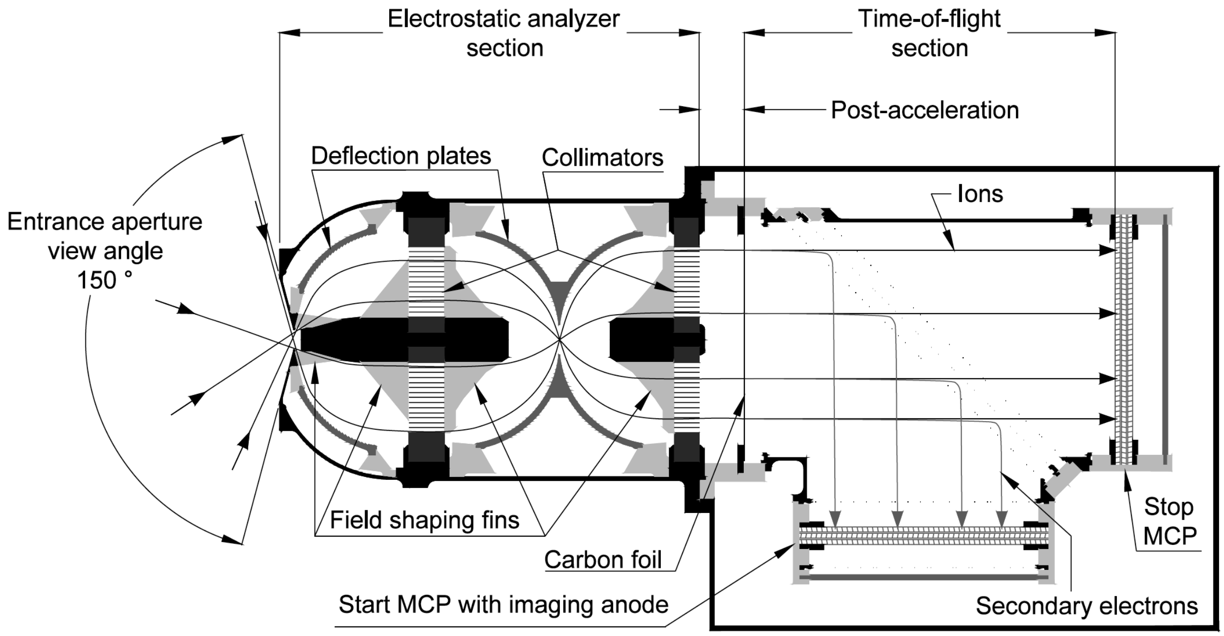

Figure 2.3. Cross-section of the FIPS instrument, including the major sensor components and typical ion trajectories. From Andrews et al. (2007).

2.4 GRS Instrument

Multiple instruments on MESSENGER recorded observations of energetic electrons. The Energetic Particle Spectrometer (EPS; Andrews et al., 2007) made dedicated observations of this plasma population, however, the X-Ray Spectrometer (XRS; Schlemm et al., 2007), Neutron Spectrometer (NS; Goldsten et al., 2007), and Gamma-Ray Spectrometer (GRS; Goldsten et al., 2007) also responded to energetic electrons as these particles would induce fluorescence or bremsstrahlung emissions within these instruments. XRS, NS, and GRS were each designed to determine Mercury’s surface composition; measurements of energetic electrons were not their intended scientific focus. In this sense, investigations focusing on Mercury’s surface consider these energetic electron observations to be noise in their signal while we consider them as a valuable signal itself. For our investigation, we focus on observations from the GRS instrument. While these observations are noisy (see Appendix A), the faster time resolution and larger geometric factor of GRS make it more suitable than EPS for investigating electric electrons associated with dipolarizations. From March 2013 to the end of the mission, GRS provided 100 Hz observations of energetic electrons, compared to the 0.3 Hz of EPS, 0.05 Hz of NS, and 0.025 Hz of XRS. We provide a brief description of the GRS energetic electron observations below, and refer readers to Chapter 3.2 for additional information.

The GRS sensor was designed to map Mercury's surface composition, but after the end-of-life of one of its components, it was updated to provide high-time-resolution observations of energetic electrons. GRS consists of a cryo-cooled, high-purity germanium crystal detector surrounded by a plastic scintillator anticoincidence shield (ACS) (Goldsten et al., 2007). To achieve its primary science, the detector would record signals of nuclear fluorescence from Mercury's surface allowing composition to be determined. However, the detector is sensitive to other gamma-rays, including those produced by galactic cosmic rays (GCRs), planetary neutrons (Peplowski et al., 2015), and energetic electrons (Lawrence et al., 2015) impinging on the sensor's casing as well as gamma-rays emanating from the spacecraft itself. To remove these false positive signals, the detector was surrounded by an ACS along all sides expect for the planet-pointing face. To determine surface composition, signals recorded by both the detector and ACS within a narrow time window are filtered, while signals recorded only by the detector are kept. The cryo-cooling system that enabled the detector to make these low-noise observations of the surface reached its expected end-of-life in June 2012, making measurements of surface fluorescence impossible. On 25 February 2013, the GRS telemetry was redistributed to the ACS count rate in order to make high-time-resolution (100 Hz) measurements of the local radiation environment available for science. The ACS count rate corresponds to the rate of pulse-height analyzed photons within the ACS generated by impinging particles, which are listed above

(Peplowski et al., 2015). Planetary neutrons and Mercury-originating gamma-rays dominate the ACS count rate at low altitudes and for nadir boresight pointing, while GCRs and spacecraft-originating gamma-rays dominate the count rate at high altitudes and for off-planet boresight pointing. However, on the timescales of seconds, energetic electrons (energies above approximately 10 keV) dominate the ACS count rate and appear as localized peaks superposed on the GCR/neutron background (Lawrence et al., 2015). While the precise field of view, response function, and energy threshold of the ACS are not well known, the GRS sensor possess a large geometric factor and is expected to behave nearly omnidirectionally (see Lawrence et al., 2015). In short, the count rate is derived from the ACS's response integrated over its omnidirectional field of view, large geometric factor, particle species (energetic electrons, GCRs, planetary neutrons), and particle energy. For simplicity, we use "GRS" to refer to the high-time-resolution ACS measurements except where noted otherwise.

2.5 Coordinate Systems

To organize the observations from MESSENGER's instruments, we take advantage of several local and global coordinate systems. In the spacecraft's rest frame, the local spacecraft (SC) coordinates are +Y_{SC} in the direction of the magnetometer boom, +Z_{SC} in the direction of the adapter ring, and +X_{SC} along the solar arrays, which completes the right-handed system (see Figure 2.2b). For coordinates about Mercury, we use Mercury solar orbital (MSO) coordinates, Mercury solar magnetospheric (MSM) coordinates, and aberrated Mercury solar magnetospheric (MSM') coordinates. In MSO coordinates, +X_{MSO} is directed sunward, +Z_{MSO} is directed northward parallel to the planet's rotation axis, and +Y_{MSO} completes the right-handed system. The MSO coordinate system is centered at the geographic center of the planet. MSM coordinates possess the same unit vector directions as MSO coordinates, but with the origin at Mercury's dipole center ($Z_{MSM} = 0$ corresponds to $Z_{MSO} = 484$ km). MSM and MSM' share the same origin, however, MSM' unit vectors are MSM vectors rotated in the X_{MSM}–Y_{MSM} plane to correct for Mercury's orbital motion about the Sun. In the MSM' system, $+X_{MSM'}$ is antiparallel to the upstream solar wind, $+Z_{MSM'}$ is directed northward parallel to the planet's rotation axis, and $+Y_{MSM'}$ completes the right-handed coordinate system. Without a dedicated solar wind monitor, the solar wind vector is typically unknown for each MESSENGER orbit, so a radial (with respect to the Sun) solar wind is assumed with speeds ~400 km/s. Mercury orbits the Sun perpendicular to the Mercury-Sun line at speeds ~40 km/s so the typical aberration angle is ~6°.

2.6 MESSENGER Instrumentation, Spacecraft, and Orbit Considerations

MESSENGER's orbital mission provided a wealth of data for scientific studies of Mercury's interior, surface, and space environment. Compared to Mariner 10, MESSENGER's observations are both wider in scope and greater in data volume. For studies of Mercury's magnetosphere, MESSENGER provided observations of the local magnetic field (MAG), thermal ion plasma (FIPS), and energetic electron plasma (GRS). For our investigations (Chapters 3-5), the data from these three instruments over MESSENGER's orbital campaign corresponds to ~250 GB of in situ observations, compared to the $\lesssim$1 MB of closest-equivalent Mariner 10 observations accumulated over its three flybys.

The MESSENGER mission has revolutionized our understanding of the innermost planet and its environment (see, e.g., Solomon et al., 2018), however, the mission and the data it collected are not without its limitations. Within the context of our investigations, we find it valuable to discuss limitations of the spacecraft, its instruments, and its orbit as well as how these limitations shape our investigations. Foremost, MESSENGER's expansive scientific focus combined with payload restrictions in cost, size, weight, and power, limit the instruments MESSENGER is equipped with to investigate Mercury's magnetosphere. Compared with dedicated magnetospheric missions (e.g., the Magnetospheric Multiscale mission), MESSENGER lacks dedicated observations of the local electric field, plasma and magnetic waves, thermal electrons, and low (photoelectron) energy plasma. Additionally, restrictions on spacecraft pointing and spin limit the capability of the FIPS instrument to resolve plasma flows. To withstand the intense solar irradiation at Mercury's orbital location, MESSENGER is equipped with a ceramic cloth sunshade that must continuously point sunward. For the sunshade to point sunward while allowing remote sensing instruments to image the planet requires the spacecraft to be three-axis stabilized. This stabilization prevents the FIPS instrument from determining bulk plasma flows directly as the resulting spacecraft rotation is slow compared to the timescales of magnetospheric dynamics (see Appendix B). Furthermore, MESSENGER is a single spacecraft, so its in situ magnetospheric measurements are locally constrained. Lacking multiple probes, we do not observe the magnetosphere synoptically and simultaneously. For example, MESSENGER cannot simultaneously measure the solar wind and the plasma sheet, and conditions within either region are expected to have changed during the time it takes for the spacecraft to move from one of those regions to the other (e.g., James et al., 2017). Single spacecraft observations also limit our understanding of temporal versus spatial variations. Finally, MESSENGER's orbital configuration limits our understanding of seasonal versus local time variations. Depicted in Figure 2.4, MESSENGER's orbital plane is fixed in inertial space, i.e., with respect to the Sun and stars. As Mercury orbits the Sun, MESSENGER is able to sample different local time sectors of the magnetosphere. This geometry prevents MESSENGER from sampling all locations of the magnetosphere at all points in Mercury's orbit about the Sun. Therefore, trends in season, such as those caused from the variable distance of Mercury to the Sun, are difficult to diagnose and correct for in MESSENGER observations.

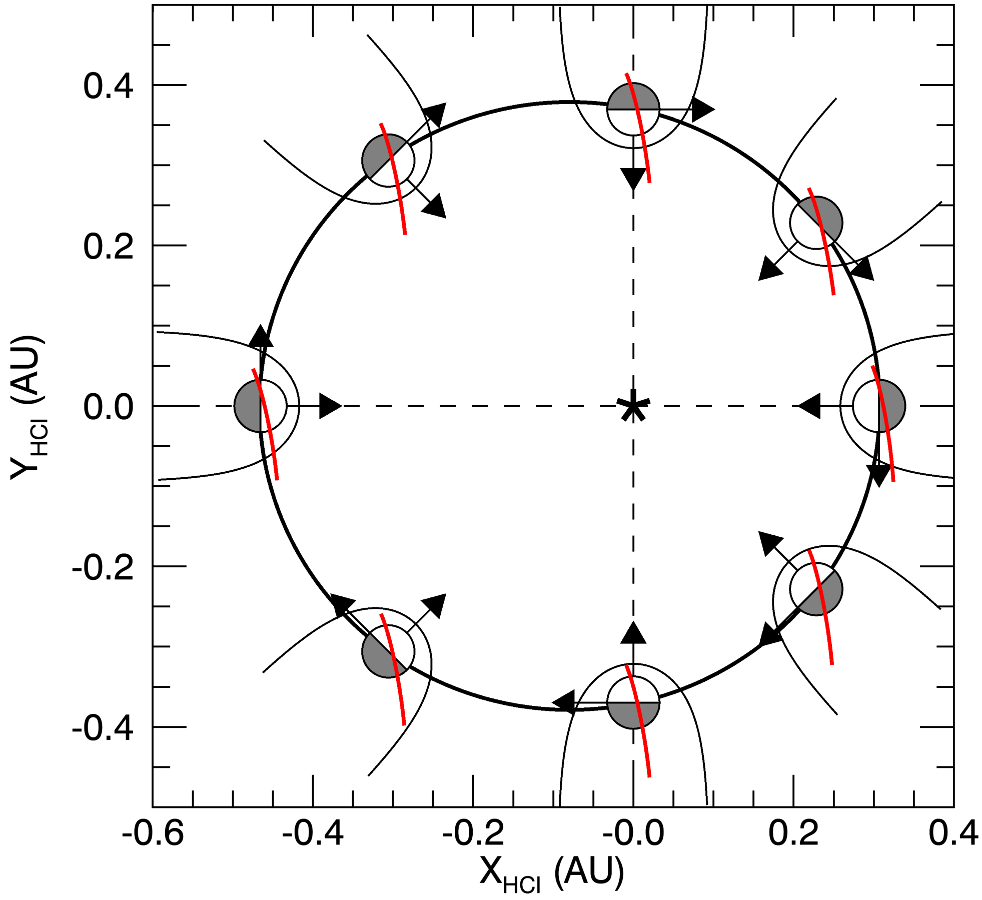

Figure 2.4. The sunlit (white) and nightside (grey) hemispheres of Mercury at different positions in its orbit about the Sun (star) in Heliocentric Inertial (HCI) coordinates. To scale with the planet, the magnetopause (black parabola) and northern ($Z_{MSO} > 0$) component of MESSENGER's orbit (red) about Mercury. The arrows at each location indicate the X_{MSO} (sunwards) and Y_{MSO} directions. MESSENGER's orbital plane is fixed with respect to inertial space so it samples different regions of Mercury's magnetosphere as the planet orbits the Sun.

To mitigate limitations of the spacecraft, its orbit, and its instrumentation, we focus on statistical approaches to our investigations. For example, although MESSENGER cannot sample every location of Mercury's central current sheet simultaneously, we can use a statistical description to provide this synoptic depiction. Furthermore, while FIPS cannot measure flows for individual intervals unambiguously, we can supplement the instrument's capability by combining many FIPS observations together statistically (see Appendix B). Finally, we use statistical techniques to identify events, such as energetic electron bursts recorded by GRS (see Appendix A) and dipolarizations recorded by MAG (see Appendix C). While these statistical approaches enrich and empower our observational capabilities, they are not without their own limitations. Most importantly, since there is no robust description of the seasonal trends in Mercury's magnetosphere, we must assume that the characteristics and dynamics of dipolarizations in Mercury's magnetotail do not depend substantially on Mercury's season. To help ensure our statistical results are not artifacts of our statistical approach, we ground these results in spacecraft observations by providing examples and case studies where relevant. Finally, while we focus on utilizing statistical techniques to provide synoptic description of Mercury's magnetotail, there are alternative approaches. Global modeling, for example, can provide global context to spacecraft observations (e.g., Jia et al., 2015; Jia et al., 2019; Chen et al., 2019).

2.7 References

Anderson, B. J., Acuña, M. H., Lohr, D. A., Scheifele, J., Raval, A., Korth, H., & Slavin, J. A. (2007). The magnetometer instrument on MESSENGER. *Space Science Reviews*, **131**, 417–450. https://doi.org/10.1007/s11214-007-9246-7

Andrews, G. B., Zurbuchen, T. H., Mauk, B. H., Malcom, H., Fisk, L. A., Gloeckler, G., … Raines, J. M. (2007). The energetic particle and plasma spectrometer instrument on the MESSENGER spacecraft. *Space Science Reviews*, **131**(1–4), 523–556. https://doi.org/10.1007/s11214-007-9272-5

Baker, D. N., Dewey, R. M., Lawrence, D. J., Goldsten, J. O., Peplowski, P. N., Korth, H., … Solomon, S. C. (2016). Intense energetic electron flux enhancements in Mercury's magnetosphere: An integrated view with high-resolution observations from

MESSENGER. *Journal of Geophysical Research: Space Physics*, **121**, 2171–2184. https://doi.org/10.1002/2015JA021778

Chen, Y., Tóth, G., Jia, X., Slavin, J. A., Sun, W., Markidis, S., et al. (2019). Studying dawn-dusk asymmetries of Mercury's magnetotail using MHD-EPIC simulations. *Journal of Geophysical Research: Space Physics*, **124**, 8954–8973. https://doi.org/10.1029/2019JA026840

Goldsten, J. O., Rhodes, E. A., Boynton, W. V., Feldman,W. C., Lawrence, D. J., Trombka, J. I., … Witte, M. C. (2007). The MESSENGER gamma-ray and neutron spectrometer. *Space Science Reviews*, **131**(1–4), 339–391. https://doi.org/10.1007/s11214-007-9262-7

James, M. K., Yeoman, T. K., Mager, P. N., & Klimushkin, D. Y. (2013). The spatio-temporal characteristics of ULF waves driven by substorm injected particles. *Journal of Geophysical Research: Space Physics*, **118**, 1737–1749. https://doi.org/10.1002/jgra.50131

Jia, X., Slavin, J. A., Gombosi, T. I., Daldorff, L. K. S., Toth, G., & van der Holst, B. (2015). Global MHD simulations of Mercury's magnetosphere with coupled planetary interior: Induction effect of the planetary conducting core on the global interaction. *Journal of Geophysical Research: Space Physics*, **120**, 4763–4775. https://doi.org/10.1002/2015JA021143

Jia, X., Slavin, J. A., Poh, G., DiBraccio, G. A., Toth, G., Chen, Y., . . . Gombosi, T. I. (2019). MESSENGER observations and global simulations of highly compressed magnetosphere events at Mercury. *Journal of Geophysical Research: Space Physics*, **124** (1), 229-247. https://doi.org/10.1029/2018JA026166

Lawrence, D. J., Anderson, B. J., Baker, D. N., Feldman, W. C., Ho, G. C., Korth, H., … Winslow, R. M. (2015). Comprehensive survey of energetic electron events in Mercury's magnetosphere with data from the MESSENGER gamma-ray and neutron spectrometer. *Journal of Geophysical Research: Space Physics*, **120**, 2851–2876. https://doi.org/10.1002/2014JA020792

McAdams, J. V., Bryan, C. G., Moessner, D. P., Page, B. R., Stanbridge, D. R., & Williams, K. E. (2014). Orbit design and navigation through the end of MESSENGER's extended mission at Mercury. *24th Space Flight Mechanics Meeting, American Astronautical Society/American Institute of Aeronautics and Astronautics*, paper AAS 14-369.

Peplowski, P. N., Lawrence, D. J., Feldman, W. C., Goldsten, J. O., Bazell, D., Evans, L. G., … Weider, S. Z. (2015). Geochemical terranes of Mercury's northern hemisphere revealed by MESSENGER neutron measurements. *Icarus*, **253**, 346–363. https://doi.org/10.1016/j.icarus.2015.02.002

Schlemm, C. E. II, Starr, R. D., Ho, G. C., Bechtold, K. E., Hamilton, S. A., Boldt, J. D., … Williams, B. D. (2007). The X-ray spectrometer on the MESSENGER spacecraft. *Space Science Reviews*, **131**(1–4), 393–415. https://doi.org/10.1007/s11214-007-9248-5

Solomon, S. C., McNutt, R. L., Gold, R. E., & Domingue, D. L. (2007). MESSENGER mission overview. *Space Science Reviews*, **131**, 3– 39. https://doi.org/10.1007/s11214-007-9247-6

Solomon, S. C., & Anderson, B. J. (2018). The MESSENGER Mission: Science and Implementation Overview. In S. C. L. R. Nittler, & B. J. Anderson (Eds.), *Mercury: The view after MESSENGER* (Chapter 17, pp. 461–496). London: Cambridge Univ. Press. ISBN: 978-1107154452

Solomon, S. C., Nittler, L. R., & Anderson, B. J. (2018). *Mercury: The view after MESSENGER*. London: Cambridge Univ. Press. ISBN: 978-1107154452

Vaughan, R. M., Leary, J. C., Conde, R. F., Dakermanji, G., Ercol, C. J., Fielhauer, K. B., Grant, D. G., Hartka, T. J., Hill, T. A., Jaskulek, S. E., McAdams, J. V., Mirantes, M. A., Persons, D. F., & Srinivasan, D.K. (2006). Return to Mercury: the MESSENGER spacecraft and mission. *Institute of Electrical and Electronics Engineers (IEEE) Aerospace Conference*, Big Sky, MT, 15.

CHAPTER III. Energetic Electron Acceleration and Injection During Dipolarization Events in Mercury's Magnetotail

This chapter is taken from Dewey, R. M., Slavin, J. A., Raines, J. M., Baker, D. N., & Lawrence, D. J. (2017). Energetic electron acceleration and injection during dipolarization events in Mercury's magnetotail. *Journal of Geophysical Research: Space Physics,* 122, 12,170–12,188. https://doi.org/10.1002/2017JA024617. We have performed minor edits for formatting consistency with the other chapters.

3.1 Abstract

Energetic particle bursts associated with dipolarization events within Mercury's magnetosphere were first observed by Mariner 10. The events appear analogous to particle injections accompanying dipolarization events at Earth. The Energetic Particle Spectrometer (3 s resolution) aboard MESSENGER determined the particle bursts are composed entirely of electrons with energies $\gtrsim 300$ keV. Here we use the Gamma-Ray Spectrometer high-time-resolution (10 ms) energetic electron measurements to examine the relationship between energetic electron injections and magnetic field dipolarization in Mercury's magnetotail. Between March 2013 and April 2015, we identify 2,976 electron burst events within Mercury's magnetotail, 538 of which are closely associated with dipolarization events. These dipolarizations are detected on the basis of their rapid (~2 s) increase in the northward component of the tail magnetic field (ΔB_z ~30 nT), which typically persists for ~10 s. Similar to

those at Earth, we find that these dipolarizations appear to be low-entropy, depleted flux tubes convecting planetward following the collapse of the inner magnetotail. We find that electrons experience brief, yet intense, betatron and Fermi acceleration during these dipolarizations, reaching energies ~130 keV and contributing to nightside precipitation. Thermal protons experience only modest betatron acceleration. While only ~25% of energetic electron events in Mercury's magnetotail are directly associated with dipolarization, the remaining events are consistent with the Near-Mercury Neutral Line model of magnetotail injection and eastward drift about Mercury, finding that electrons may participate in Shabansky-like closed drifts about the planet. Magnetotail dipolarization may be the dominant source of energetic electron acceleration in Mercury's magnetosphere.

3.2 Introduction

MESSENGER frequently observed energetic electrons ($E \gtrsim 10$ keV) within Mercury's magnetosphere (Baker et al., 2016; Ho, Krimigis, et al., 2011; Ho, Starr, et al., 2011; Ho et al., 2012, 2016; Lawrence et al., 2015). However, particle acceleration in this miniature magnetosphere has remained a topic of curiosity and controversy. While Mercury's intrinsic magnetic field forms a terrestrial-like magnetosphere when it interacts with the solar wind (e.g., Alexeev et al., 2010; Anderson et al., 2011), its magnetospheric dynamics operate on significantly smaller spatial scales and shorter temporal scales than the Earth's due to the many differences between the two magnetospheres (see, e.g., Slavin et al., 2007, 2009, 2012). The small physical scales limit the time an energetic particle can gain energy in Mercury's magnetosphere before being lost to surface precipitation or magnetopause shadowing, leaving little possibility for trapped radiation belts (Slavin et al., 2007) and constraining possible acceleration mechanisms (Zelenyi et al., 2007). While electrons behave adiabatically, the magnetosphere's small size can result in nonadiabatic ion behavior and strong finite gyroradius effects (Delcourt et al., 2010). First detected by Mariner 10 (e.g., Simpson et al., 1974), the presence of energetic particle bursts therefore raised questions about how such a small magnetosphere can rapidly accelerate particles to suprathermal and relativistic energies (e.g., Baker et al., 2016).

Surveys of MESSENGER and Mariner 10 energetic particle bursts in Mercury's magnetotail suggest connection between particle acceleration and magnetic reconnection. Two of the Mariner 10 events during its first flyby appeared analogous to magnetic field dipolarization and particle injection events at Earth (Christon et al., 1987). A MESSENGER examination of the most intense energetic electron events detected by the Gamma-Ray Spectrometer revealed an additional example of simultaneous magnetic field dipolarization and energetic electron injection (Baker et al., 2016). At Earth, dipolarization events are rapid reconfigurations of the magnetotail into a more dipolar state, that is, the collapse of the near-tail region due to explosive nightside reconnection (e.g., Runov et al., 2012). The intense reconnection drives bursty bulk flows (e.g., Angelopoulos et al., 1992) that carry the newly reconnected dipolarizing flux bundle (DFB) (e.g., Liu et al., 2013) toward the nightside inner magnetosphere. These flux bundles are interpreted as low entropy, depleted flux tubes created by the reconnection of low-β flux tubes between the north and south lobes of the magnetotail (e.g., Sergeev et al., 1996). As the flows brake near the inner magnetosphere, the magnetic field at the leading edge of the flux bundle steepens and forms a discontinuity (the dipolarization front or DF) (e.g., Runov et al., 2009). Dipolarization events are a powerful source of particle acceleration, responsible for transporting energetic particles into the inner magnetosphere, where they are termed injection events (e.g., Baker et al., 1978; Birn et al., 2011; Deng et al., 2010). The planetward motion/braking of the dipolarization front energizes and heats the local plasma, while the bulk motion and collapse of the near-tail field transport particles into the inner magnetosphere (e.g., Ashour-Abdalla et al., 2011; Birn et al., 2013; Gabrielse et al., 2016). Magnetic field dipolarization associated with energetic particle injection often occurs during substorms at Earth (e.g., Baker et al., 1996).

The MESSENGER spacecraft has observed brief, yet intense, substorm-like events and characteristic substorm features. In contrast to the Earth's several-hour process, Mercury's substorm-like events last only minutes (Sun et al., 2015) but share common dipolarization (Sun et al., 2016; Sundberg et al., 2012) and tail loading/unloading (Slavin et al., 2010) signatures with substorms at Earth. While a few examples of energetic electron events coincident with magnetic field dipolarization (here termed dipolarization-injection events) have been presented at Mercury (Baker et al., 2016; Christon et al., 1987), previous studies of energetic electron bursts with MESSENGER data have focused on the electrons and not the associated magnetospheric activity (e.g., Ho, Krimigis, et al., 2011; Ho, Starr, et al., 2011; Ho et al., 2016; Lawrence et al., 2015).

Here we seek to expand upon the previous analyses of MESSENGER energetic electron bursts to discover the relationship between dipolarizations and injections at Mercury. As dipolarizations and injections relate to both magnetospheric and particle dynamics, in this study, we focus on topics related to particle acceleration. In a companion study we focus on the magnetospheric dynamics and substorm characteristics of the dipolarization-injection events. The questions to be addressed in this study include the following:

1. Where and how frequently do dipolarization-injection events occur at Mercury?

2. What processes are responsible for energizing particles during these events at Mercury?
3. How responsible are these events for the energetic particle environment about Mercury?

We present statistical observations of injection events associated with magnetic field dipolarizations, suggesting frequent occurrence of rapid, intense electron acceleration associated with mechanisms similar to those operating during dipolarization events at Earth. Our investigation is organized as follows: in section 3.3 we describe our data sources and event identification methodology; in section 3.4 we present statistical analysis of the identified dipolarization-injection events; in section 3.5 we discuss the results in context to previous Mercury studies and phenomena at Earth; and finally, in section 3.6, we summarize our work and present avenues for future investigation.

3.3 Data Sources and Event Identification

3.3.1 MESSENGER Instruments

MESSENGER entered orbit about Mercury on 18 March 2011 and, after providing over 4 years of continuous observations of the planet's surface and space environment, impacted the planet on 30 April 2015. For this investigation, we rely on the Magnetometer (MAG) (Anderson et al., 2007), Fast Imaging Plasma Spectrometer (FIPS) (Andrews et al., 2007), and Gamma-Ray Spectrometer (GRS) instruments (Goldsten et al., 2007). The MAG instrument measures the in situ vector magnetic field at 20 Hz (50 ms) time resolution. The FIPS sensor measures thermal and low-energy ions with energy per charge ratio (E/q) between <50 eV/q and 13 keV/q, completing a scan at 0.1 Hz (10 s) nominally.

After a telemetry update on 25 February 2013, the GRS sensor provides a high-time-resolution proxy for energetic electron (E $\gtrsim$ 10 keV) flux at 100 Hz (10 ms) resolution (see, e.g., Baker et al., 2016). Prior to the telemetry update, the GRS sensor mapped Mercury's surface composition by recording planetary nuclear fluorescence emissions (Goldsten et al., 2007). Its plastic scintillator anticoincidence shield (ACS) was designed to remove false positives recorded by the high-purity germanium crystal detector. The ACS responds to galactic cosmic rays (GCRs), planetary neutrons (Peplowski et al., 2015), and energetic electrons (Lawrence et al., 2015) impinging on the sensor's casing as well as gamma rays emanating from the planetary surface and from the spacecraft. On 25 February 2013, the GRS telemetry was updated to send the 100 Hz ACS count rate data to the ground. The count rate consists of pulse-height analysis of photons in the ACS generated by the particles listed above (Peplowski et al., 2015). Planetary neutrons and Mercury-originating gamma rays dominate the ACS count rate at low altitudes and for nadir boresight pointing, while GCRs and spacecraft-originating gamma rays dominate the count rate at high altitudes and for off-planet boresight pointing. However, on the time scales of seconds, energetic electrons dominate the ACS count rate and appear as localized peaks superposed on the GCR/neutron background (Lawrence et al., 2015). While the precise field of view, response function, and energy threshold of the ACS are not well known, the GRS sensor possesses a large geometric factor and is expected to behave nearly omnidirectionally (see Lawrence et al., 2015). In short, the count rate is derived from the ACS's response integrated over its omnidirectional field of view, large geometric factor, particle species (energetic electrons, GCRs, and planetary neutrons), and particle energy. While the Energetic Particle Spectrometer (3 s resolution) (Andrews et al., 2007), X-Ray Spectrometer (XRS, 40 s resolution) (Schlemm et al., 2007), and Neutron Spectrometer (NS, 20 s resolution) (Goldsten et al., 2007) instruments also observe energetic electrons, we focus on GRS observations because of the sensor's superior time resolution and its high sensitivity from its nearly omnidirectional response and large geometric factor. For simplicity, we use "GRS" to refer to the high-time-resolution ACS measurements except where noted otherwise.

In addition to the 10 ms count rate, the GRS sensor also provides an energy-resolved count rate, but at a substantially lower time resolution (20 s). The energy-resolved count rate is derived from 20 s accumulations of individual pulse-height analysis events in the ACS. Similar to the 10 ms count rate, the spectral accumulations possess a background spectra dominated by planetary neutrons and GCRs; rapid enhancements above the background spectra are due to energetic electrons (Peplowski et al., 2015). The ACS has 1,024 energy channels, each separated by approximately 3 keV. The instrument behaves nonlinearly at lower (<50 keV) energies and has an estimated threshold of ~10 keV (Lawrence et al., 2015). The electron energy recorded in the 20 s spectral accumulations is the energy of the Bremsstrahlung radiation produced by impinging elections; it is not the impinging electrons' kinetic energy, although the two are closely related (see Goldsten et al., 2007; Lawrence et al., 2015). Assuming electrons deposit their entire kinetic energy in a single Bremsstrahlung photon, we can estimate the electron energy spectra.

Our study uses the GRS high-time-resolution count rates and spectral accumulations collected between 1 March 2013 and 30 April 2015, corresponding to the interval between GRS telemetry update and planetary impact. During this interval, MESSENGER orbited the planet in a near-polar (~80° inclination) 8 h orbit. While MAG and FIPS operated continuously during this period of study, GRS only recorded the high-time-resolution count rate continuously when MESSENGER was within ~6,600 km (i.e., 2.7 R_M, where R_M = 2,440 km is Mercury's radius) of the planet's center. During the final months of the mission, there are additional gaps in the high-time-resolution GRS coverage associated with MESSENGER's final low-altitude campaign.

We use the Mercury solar magnetospheric (MSM) coordinate system to organize and display the spacecraft location, charged particle measurements, and vector magnetometer data. This right-handed coordinate system is centered at the origin of Mercury's magnetic dipole, which is offset ~484 km (~0.2 R_M) north of the planetary center (Alexeev et al., 2010; Anderson et al., 2011). In this system, the X_{MSM} axis points toward the Sun, the Y_{MSM} axis lies in Mercury's orbital plane and points in the direction opposite to planetary motion, and the Z_{MSM} axis completes the right-handed system (i.e., positive toward the north, which is parallel to the planetary rotation axis).

3.3.2 Dipolarization-Injection Event Identification

We developed an automated algorithm to identify energetic electron events within the high-time-resolution GRS data (Baker et al., 2016). The algorithm, described in detail in Appendix A, uses a sliding window to determine the background GRS count rate and identifies electron events as points that fall significantly above the background. Over the 1 March 2013 to 30 April 2015 period of our study, the algorithm identified 10,566 energetic electron events over 2,139 orbits. The spatial distribution of these events about the planet as a function of local time (LT) and Z_{MSM} is shown in Figure 3.1. Figure 3.1 displays the number of electron events distributed about the planet corrected for MESSENGER's observation time, i.e., event frequency. The spatial distribution shares many similarities with previous studies of GRS (Baker et al., 2016), XRS (Ho et al., 2016), and NS (Lawrence et al., 2015) electron events. We find the greatest frequency of electron events ~1 $(2\text{ min})^{-1}$ near the magnetic equator in the postmidnight sector. At postdawn, prenoon local times, the electron events migrate to higher Z_{MSM}, before the frequency of events falls off sharply with local time in the postnoon and premidnight sectors. Few events are observed in the premidnight sector despite the almost uniform local time coverage of the MESSENGER spacecraft during the period of study. More events are observed north of Mercury's geographic equator ($Z_{MSM} \geq -0.2\ R_M$) due to MESSNGER's highly inclined orbit with periapsis near the planet's northern pole.

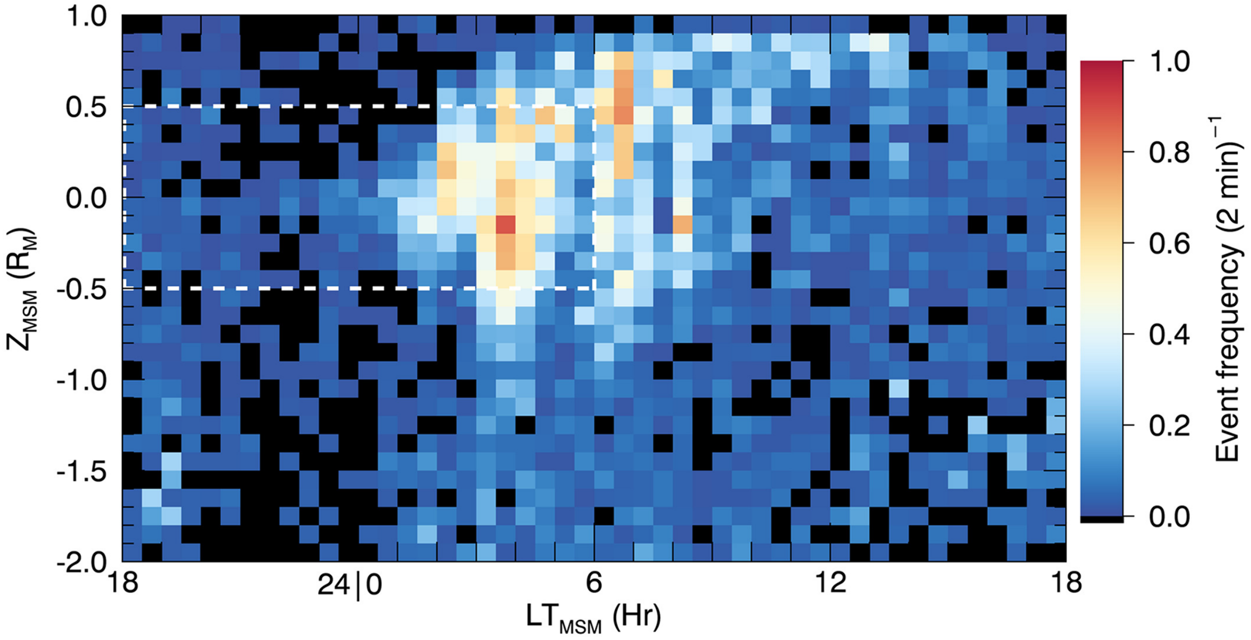

Figure 3.1. Spatial distribution of GRS electron events identified by the automated algorithm. The color bar indicates the event frequency within each bin of local time (LT, hours) and Z_{MSM} (R_M). The black color indicates no identified electron events. The regions enclosed by the dashed white lines correspond to the survey region used to identify dipolarization events.

To identify dipolarization-injection events, we analyzed all electron events near the nightside plasma sheet for dipolarization signatures. We selected all electron events located behind the nightside of the planet ($X_{MSM} < 0\ R_M$) and within 0.5 R_M of the magnetic equator ($|Z_{MSM}| \leq 0.5\ R_M$), corresponding to the region outlined by the white dashed lines in Figure 3.1. Of the 10,566 electron events, 2,976 events (~30%) fall within this survey region. While dipolarizations at Earth are frequently associated with bursty bulk flows, characterized by high-speed flows of 400 km/s or faster (e.g., Angelopoulos et al., 1992), the FIPS sensor cannot directly observe sunward or antisunward flow in Mercury's magnetotail due to the obstruction of its field of view by the spacecraft's sunshade. As a result, we must rely on magnetic field observations to identify dipolarization events. Using similar criteria to Sundberg et al. (2012), we visually identified dipolarization fronts in the magnetic field for each electron event located within the survey region by (1) a sharp, step-like increase in B_z that (2) reaches a local maximum and is (3) followed by a gradual relaxation. For each dipolarization event, we define the dipolarization front (DF) Δt_{DF} to last from the minimum B_z prior to the step-like increase to the local maximum B_z at the end of the increase, the dipolarizing flux bundle (DFB) to last from the end of the DF to the minimum B_z following the event, and the dipolarization event Δt_{DIP} to last from the start of the DF to the end of the DFB. We use the term "dipolarization-injection event" to denote a dipolarization event coincident with an energetic electron event within the survey region. We refer to "injection events," in general, as the 2,976 electron events within the survey region.

3.4 Dipolarization-Injection Event Observations and Analysis

3.4.1 Example Dipolarization-Injection Events

Of the 2,976 electron events within the survey region, we identified 538 dipolarization-injection events. Figures 3.2 and 3.3 detail four sample MESSENGER dipolarization-injection events for comparison with the Mariner 10 events. We selected these four events to demonstrate the variability of magnetic field and particle signatures associated with dipolarization-injections at Mercury. Characteristic parameters from these examples are listed in Table 3.1.

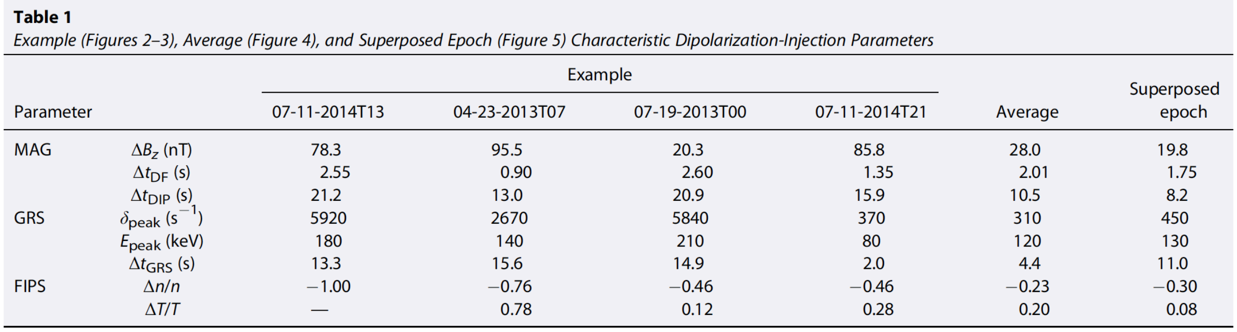

Table 1
Example (Figures 2–3), Average (Figure 4), and Superposed Epoch (Figure 5) Characteristic Dipolarization-Injection Parameters

Parameter		Example				Average	Superposed epoch
		07-11-2014T13	04-23-2013T07	07-19-2013T00	07-11-2014T21		
MAG	ΔB_z (nT)	78.3	95.5	20.3	85.8	28.0	19.8
	Δt_{DF} (s)	2.55	0.90	2.60	1.35	2.01	1.75
	Δt_{DIP} (s)	21.2	13.0	20.9	15.9	10.5	8.2
GRS	δ_{peak} (s^{-1})	5920	2670	5840	370	310	450
	E_{peak} (keV)	180	140	210	80	120	130
	Δt_{GRS} (s)	13.3	15.6	14.9	2.0	4.4	11.0
FIPS	$\Delta n/n$	−1.00	−0.76	−0.46	−0.46	−0.23	−0.30
	$\Delta T/T$	—	0.78	0.12	0.28	0.20	0.08

Table 3.1. Example (Figures 3.2–3.3), Average (Figure 3.4), and Superposed Epoch (Figure 3.5) Characteristic Dipolarization-Injection Parameters

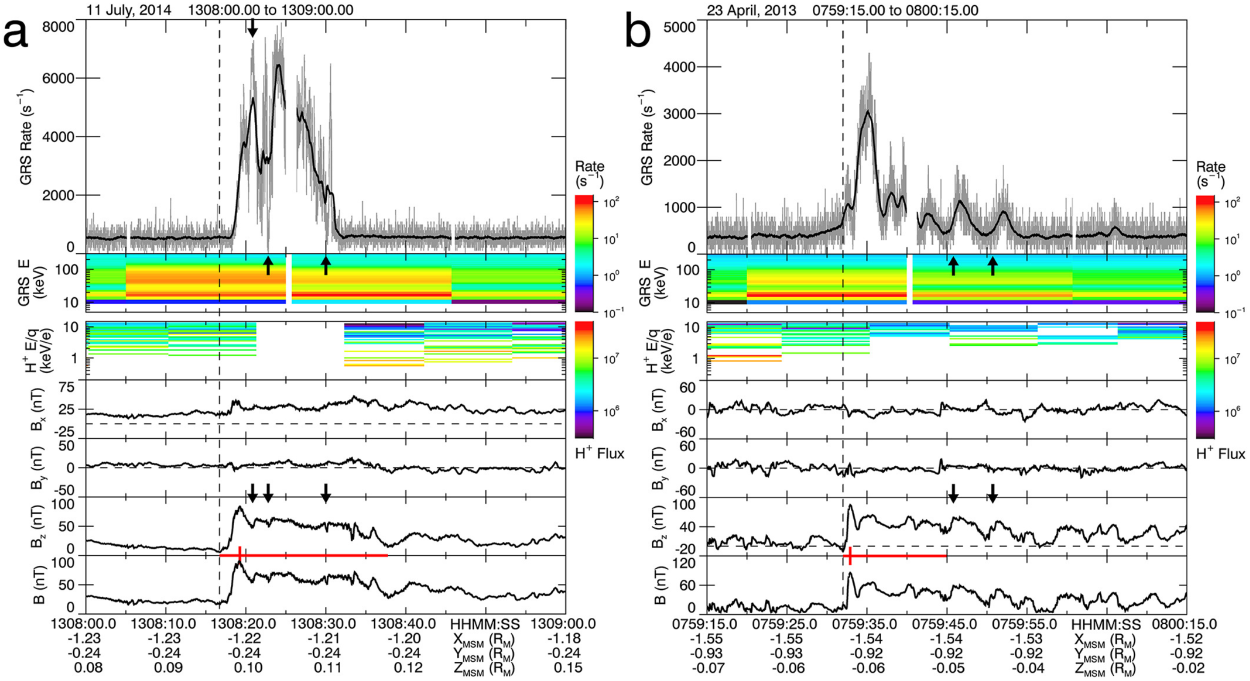

Figure 3.2. (a) A single dipolarization-injection event. (top to bottom) GRS count rate, GRS accumulated spectra, FIPS H$^+$ flux spectrogram, MAG magnetic field components (B_x, B_y, B_z), and magnetic field strength. (top) The (thick black line) GRS count rate smoothed by a 1 s moving boxcar average, as specified in the algorithm, and for comparison, the (grey) unsmoothed count rate. The upper color bar indicates count rate in the GRS spectral accumulations; the white color indicates GRS deadtime or no observed counts. The lower color bar indicates differential H$^+$ flux (s^{-1} cm^{-2} keV^{-1} Sr^{-1}); the white color indicates no observed counts in the H$^+$ spectrogram. The spacecraft position in MSM coordinates is listed at the bottom. The vertical dashed line indicates the start of the

dipolarization front, the horizontal red line spans the dipolarization event with a vertical tick at the end of the dipolarization front, the horizontal dashed lines indicate 0 nT, and the arrows denote features discussed in the text. (b) A series of dipolarization-injection events, in the same format as in Figure 3.2a.

In Figure 3.2a, a dipolarization front begins at 13:08:17 (vertical dashed line) followed by an injection of energetic electrons less than a second later. The dipolarization front is marked by the sharp increase in B_z, while the injection is marked by the sharp increase in the GRS count rate. The dipolarization front lasts until the maximum B_z at 13:08:19 (red tick), marking the beginning of the DFB that lasts until 13:08:38 (the end of the horizontal red line). The northward component of the magnetic field B_z increases by nearly a factor of 15 over the dipolarization front (from 5.5 nT to 83.8 nT; $\Delta B_z = 78.3$ nT), while the electron count rate increases by an order of magnitude during the dipolarization event, reaching a maximum near the middle of the dipolarization event at ~13:08:24 (from 550 s^{-1} to 6,470 s^{-1}; $\delta_{peak} = 5{,}920\ s^{-1}$, where δ is the background-subtracted 1 s smoothed GRS rate). During the DFB, additional magnetic field features correspond to particle signatures. Most easily seen in the unsmoothed GRS count rate (grey), the B_z depressions at ~13:08:21, ~13:08:23, and ~13:08:30 are coincident with a local maximum and two local minima in the GRS count rate, respectively, as marked by arrows. The unsmoothed GRS count rate falls to 0 s^{-1} during the second depression and falls to the background rate during the third depression. This substructure is attenuated in the 1 s smoothed GRS count rate (black). From the magnetic field signatures, this substructure could be interpreted as a series smaller dipolarizations embedded within the main event due to unsteady reconnection (e.g., Fu et al., 2011, 2013). The small, positive B_x throughout this interval and the coordinates of the spacecraft indicate that MESSENGER was located slightly north of the central current sheet and in the postmidnight sector when the dipolarization passed over it. The dipolarization front lasts $\Delta t_{DF} = 2.55$ s, the dipolarization event lasts $\Delta t_{DIP} = 21.2$ s (spanned by the horizontal red line), and the injection lasts $\Delta t_{GRS} = 13.3$ s.

Neither the GRS spectral accumulations nor the FIPS H^+ spectrogram has sufficient temporal resolution to interpret fine plasma structure within this event; however, both contain several notable features. The spectral accumulation ending at ~13:08:05 represents the GRS background; it contains no electron events and is dominated by planetary neutrons and GCRs. Enhancements above the background in the two subsequent accumulations are due to energetic electrons. Compared to the background spectra, the first event accumulation (centered at 13:08:15) is enhanced from energies ~10 keV to ~180 keV and the second accumulation (centered at 13:08:36) is enhanced from energies ~10 keV to ~150 keV. While the first event accumulation observes electrons of greater maximum energy E_{max} than the second, the second contains more counts at energies below ~15 keV. Subtracting the background spectra and normalizing the residual spectra (not shown here) accentuates these trends. The first accumulation has a greater proportion of ~90–180 keV electrons, while the second accumulation contains a greater proportion of ~10–30 keV electrons. The temporal resolution is too coarse to identify any dispersion signatures within the injection.

FIPS observations suggest some depletion and energization of thermal protons. Assuming the plasma distribution is sufficiently subsonic, we estimate the thermal plasma moments n and T (see Gershman et al., 2013). The scan centered at 13:08:05 precedes the dipolarization and observes the ambient plasma sheet with proton density $n = 1.77$ cm^{-3} and temperature T = 44.5 MK. The following scan covers the DF and notes a modest decrease in density (1.62 cm^{-3}) and increase in temperature (52.3 MK). The next scan (13:08:22 to 13:08:32) covers the DFB and observes no plasma, which could be an effect of plasma energized above the

FIPS energy range, strong planetward flows shifting the plasma outside of FIPS's field of view, and/or due to the expected decreased density within DFBs (e.g., Runov et al., 2015). Comparing the ambient thermal plasma to the plasma within the DFB, $\Delta n/n = -1.00$ and $\Delta T/T$ is undefined.

The dipolarization-injection events in Figure 3.2b display marked differences compared to the event in Figure 3.2a. The interval in Figure 3.2b is composed of three individual dipolarization-injection events, with the most significant at 07:59:32 marked by the dashed line and the other two marked by arrows. The first (main) event shows the largest change in the magnetic field and particle signatures with $\Delta B_z = 95.5$ nT, $\delta_{peak} = 2{,}670$ s^{-1}, $\Delta t_{DF} = 0.90$ s, $\Delta t_{DIP} = 13.0$ s, and $\Delta t_{GRS} = 15.6$ s. At the beginning of the dipolarization front, B_z dips briefly below 0 nT. The injection signature appears substantially different compared to the event in Figure 3.2a. The count rate rises slowly in the ~10 s preceding the dipolarization front and appears to repeatedly fall close to background levels during the dipolarization event. The GRS spectra for all three dipolarization-injection events appear similar. The two accumulations that span the three events both observe enhancements of energies to E_{max}~140 keV compared to the background spectral accumulation ending at 07:59:20. Unlike the event in Figure 3.2a, the proportion of higher/lower energy electrons after subtracting the background spectra and normalizing the residual counts remains constant across the two accumulations. In other words, despite the first accumulation recording more counts than the second, both record identical electron spectra. Similar to the event in Figure 3.2a, thermal protons increase in temperature and decrease in density throughout the series of events. Preceding the main dipolarization, $n = 1.99$ cm^{-3} and $T = 38.2$ MK in the ambient plasma sheet, followed by $n = 0.51$ cm^{-3} and $T = 67.9$ MK during the main DFB. Comparing the thermal plasma parameters, $\Delta n/n = -0.76$ and $\Delta T/T = 0.78$. The two secondary dipolarization events also observe plasma energization and depletion compared to the ambient plasma sheet but to a smaller degree; the FIPS scan centered at 07:59:51 observes $\Delta n/n = -0.70$ and $\Delta T/T = 0.14$. All three dipolarization-injection events in Figure 3.2b are located in the central plasma sheet, as noted by $B_x \sim 0$, and in the postmidnight sector.

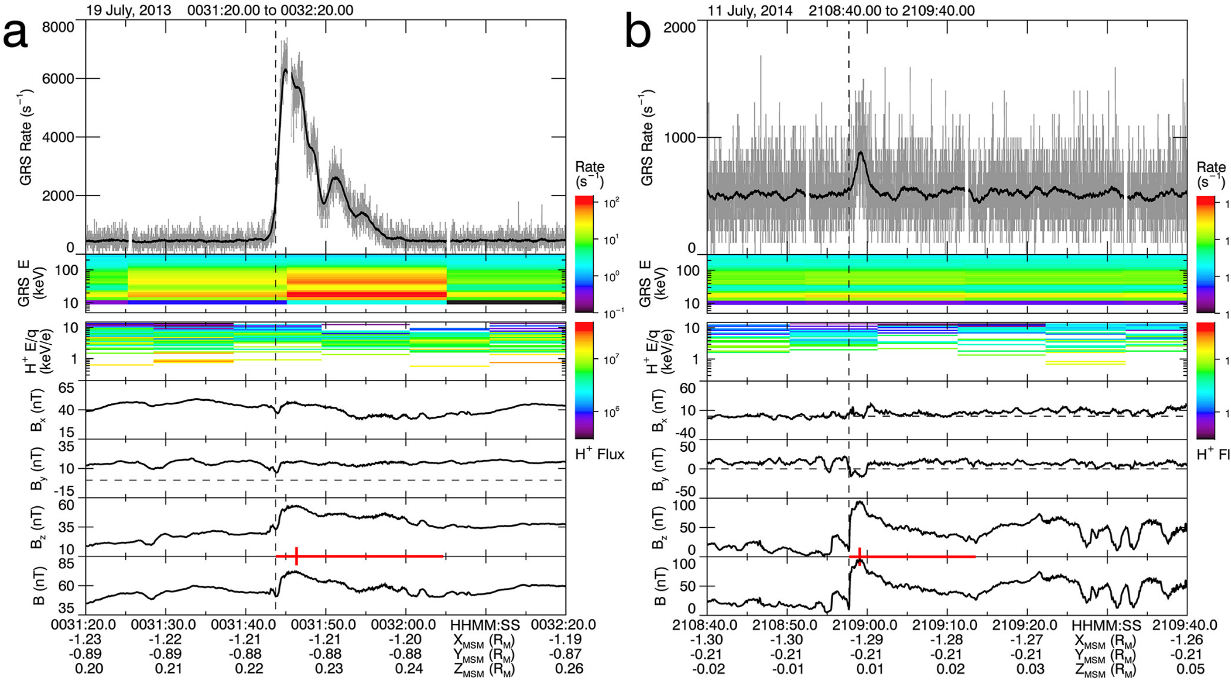

Figure 3.3. (a) A strong injection accompanied by a modest dipolarization and (b) a modest injection accompanied by a strong dipolarization in the same format as in Figure 3.2.

The dipolarization-injection event in Figure 3.3a displays an energetic electron signature similar to the Mariner 10 events (Christon et al., 1987). The rapid rise of the electron count rate is coincident with the dipolarization front; the step-like increase in GRS count rate to a local maximum is followed by a general decay with some oscillation similar to the GRS electron event in Figure 3.4 of Baker et al. (2016). The detrended count rate reaches a similar peak $\delta_{peak} = 5840\ s^{-1}$ to the event in Figure 3.2a, although the change in the northward component of the magnetic field is more modest $\Delta B_z = 20.3$ nT. The difference in magnetic field signatures is related to the spacecraft's position during this interval. MESSENGER is located in the postmidnight sector and northward of the central current sheet, as indicated by Z_{MSM} ~0.2 R_M and the background B_x ~40 nT. Compared to the background accumulation ending at 00:31:20, both accumulations spanning the injection observe electron energies to E_{max} ~170 keV. Similar to the injection in Figure 3.2a, the first accumulation during the injection observes a greater proportion of higher energy electrons (>90 keV), while the second accumulation observes a greater proportion of lower energy electrons (<20 keV) after accounting for the background GRS spectra. The thermal plasma observed during the DFB (scan centered 00:31:55) is less dense ($\Delta n/n = -0.46$) and hotter ($\Delta T/T = 0.12$) than the ambient plasma sheet (scan centered at 00:31:34). The time scales for this event are $\Delta t_{DF} = 2.60$ s, $\Delta t_{DIP} = 20.9$ s, and $\Delta t_{GRS} = 14.9$ s.

The dipolarization-injection event in Figure 3.3b displays a modest enhancement in GRS count rate ($\delta_{peak} = 370\ s^{-1}$) despite the northward component of the magnetic field increasing by $\Delta B_z = 85.8$ nT. Although smoothing the GRS count rate can attenuate substructure in injection events (e.g., Figure 3.2a), it increases the signal-to-noise ratio for low-amplitude events, such as in this event. Similar to Figure 3.2b, MESSENGER is located in the central current sheet and in the postmidnight sector during this interval but did not observe a negative B_z at the start of the dipolarization front. For this event, $\Delta t_{DF} = 1.35$ s, $\Delta t_{DIP} = 15.9$ s, and $\Delta t_{GRS} = 2.0$ s. The GRS spectral accumulation spanning the injection observes slight enhancements at ~10–20 keV and ~40–80 keV compared to the preceding background spectra. FIPS observes plasma depletion and energization during the dipolarization compared to the ambient plasma. The observed density decreases $\Delta n/n = -0.46$ and the observed temperature increases $\Delta T/T = 0.28$ within the DFB compared to the ambient plasma (scans centered at ~21:09:05 and ~21:08:45, respectively).

3.4.2 Statistical Dipolarization-Injection Analysis

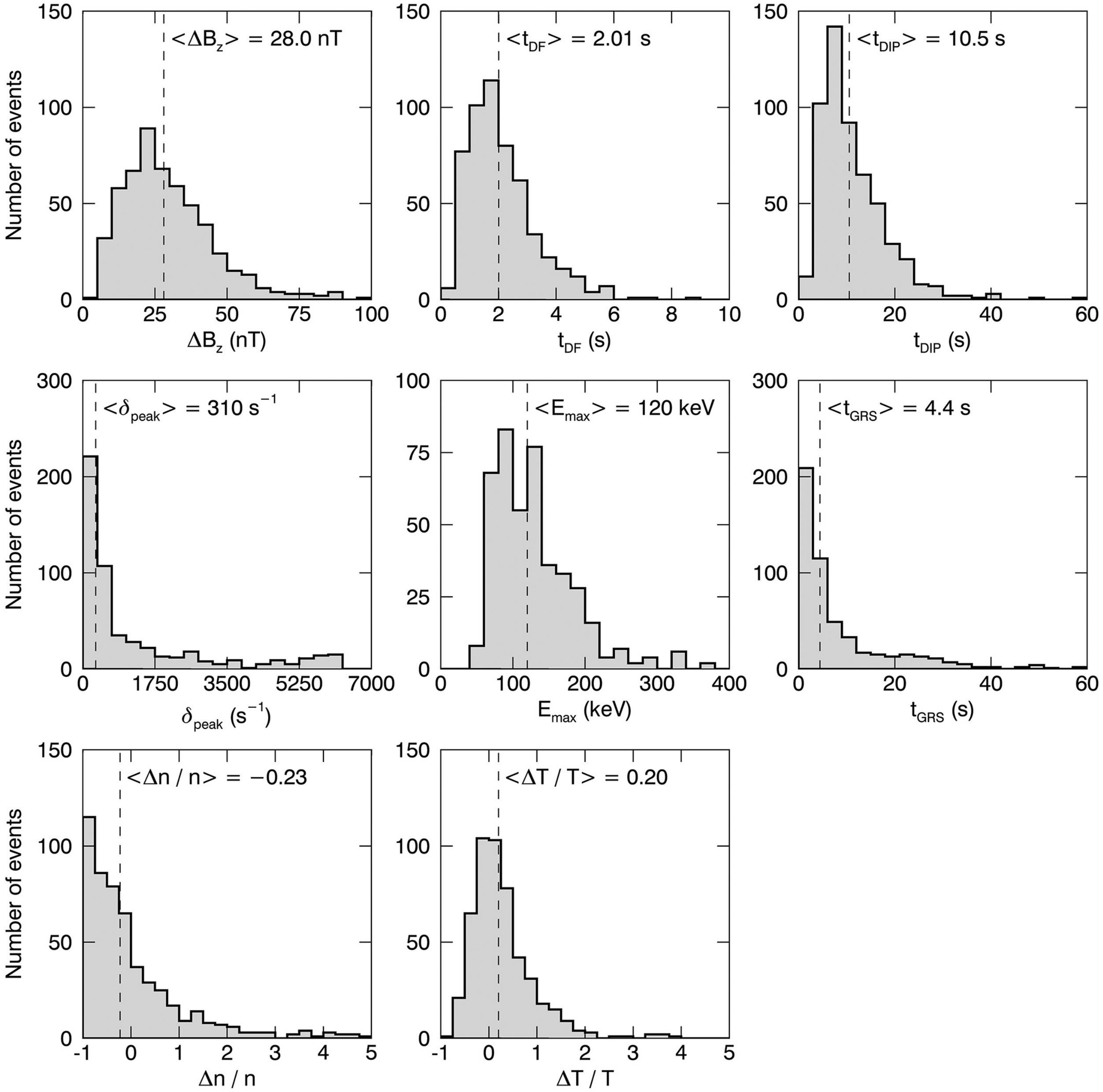

Figure 3.4. Histograms of characteristic parameters across all 538 dipolarization-injection events. (left to right) (top row) Change in B_z over the dipolarization front, duration of the dipolarization front, and duration of the dipolarization event; (middle row) peak detrended GRS count rate during the injection, maximum electron energy during the injection, and duration of the injection; (bottom row) observed changes in thermal H^+ density and temperature from the ambient plasma to the dipolarizing flux bundle. The mean of each distribution with outliers removed is marked by the dashed line and listed at the top of each panel.

To address the dipolarization-injection events statistically, Figure 3.4 displays the typical dipolarization-injection characteristics from all events. The top row contains parameters related to the dipolarization (ΔB_z, Δt_{DF}, and Δt_{DIP}), the middle row contains parameters related to the injection (δ_{peak}, E_{max} and Δt_{GRS}), and the bottom row contains parameters related to the thermal plasma ($\Delta n/n$ and $\Delta T/T$). Distributions appear to resemble decaying exponential (δ_{peak}, Δt_{GRS}, and $\Delta n/n$) or skewed unimodal functions (ΔB_z, Δt_{DF}, Δt_{DIP}, E_{max}, and $\Delta T/T$). From the histograms, the average value of each parameter and its standard deviation after excluding outliers are $\langle\Delta B_z\rangle = 28.0 \pm 13.3$ nT, $\langle\Delta t_{DF}\rangle = 2.01 \pm 1.00$ s, $\langle\Delta t_{DIP}\rangle = 10.5 \pm 5.4$ s, $\langle\delta_{peak}\rangle = 310 \pm 190\ \mathrm{s}^{-1}$, $\langle E_{max}\rangle = 120 \pm 40$ keV, $\langle\Delta t_{GRS}\rangle = 4.4 \pm 4.0$ s, $\langle\Delta n/n\rangle = -0.23 \pm 0.65$, and $\langle\Delta T/T\rangle = 0.20 \pm 0.50$. These averages are also listed in Table 3.1.

Given the substantial particle and magnetic field variability across the dipolarization-injection events, we performed superposed epoch analysis to understand better the typical characteristics, shown in Figure 3.5. We aligned each dipolarization-injection event at the midpoint of the dipolarization front and averaged the GRS, FIPS, and MAG observations. Since the GRS count rate and MAG vector field have time resolutions significantly shorter than the typical dipolarization front, both are analyzed and plotted at their native resolutions. Since the GRS spectral accumulations and FIPS scans have time resolutions significantly longer than the typical dipolarization front, both are oversampled at 1 s resolution. Time is plotted in seconds; we performed no time normalization on the MESSENGER observations. For the GRS rate and MAG vector field, the shaded regions correspond to the standard deviation of the mean multiplied by a factor of 5 for visibility, and the black horizontal dashed lines represent the preevent value, each parameter averaged over $-30 \le t \le -5$ s. The red horizontal dashed line is the propagated Poisson error from the background at the 5-sigma level, akin to the GRS event algorithm significance level (see Appendix A). For the B_x and B_y components, we averaged the absolute value of these parameters to determine the typical offset from zero. For the GRS spectral accumulation, we display the statistically significant relative change from the average GRS spectra over the range $-20 < t < -10$ s to highlight features and remove artifacts from the nonlinearity below ~50 keV. To construct the FIPS H^+ E/q spectrogram, we superposed FIPS energy-resolved pitch angle distributions at each time step and integrated the superposed distributions over pitch angle to obtain the E/q spectra. We also show the proton density as a function of time.

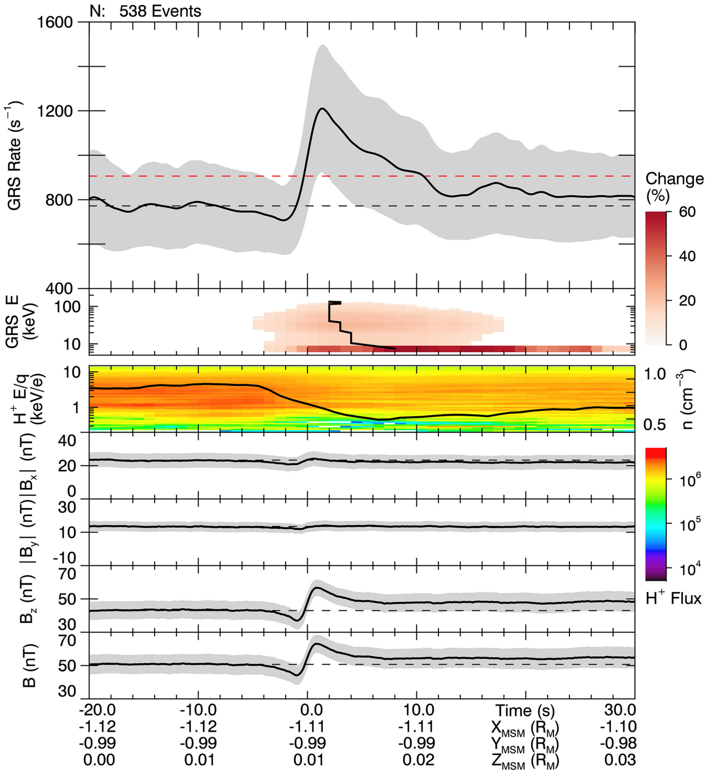

Figure 3.5. Superposed GRS, FIPS, and MAG epoch analysis in the same general format as Figure 3.2a. All 538 dipolarization events were aligned at the midpoint of the dipolarization front (t = 0 s). The second panel corresponds to the relative change in the GRS spectra from the average spectra over $-20 < t < -10$ s. Statistically significant changes are indicated by the upper color bar; relative changes below 3-sigma significance are shaded white. The black line traces the time of maximum percent change at each energy. The third panel includes the proton density, as indicated by the right axis. The fourth and fifth panels correspond to the averaged magnitudes of B_x and B_y across all

events, respectively. The horizontal black dashed lines in the GRS rate and MAG panels correspond to the mean value averaged over $-30 \leq t \leq -5$ s. The red dashed line corresponds to the algorithm significance level. The grey shaded regions correspond to the standard deviation of the mean inflated by a factor of 5. The spacecraft position below the last panel is the average spacecraft location during the dipolarization events.

The superposed epoch B_z and GRS count rate share nearly identical temporal profiles. Both B_z and the count rate begin decreasing from background levels at approximately $t = -4$ s, reaching a minimum at $t \approx -1$ s and rising to a maximum at $t \approx +1$ s. The dipolarization front lasts for $\Delta t_{DF} = 1.75$ s and results in $\Delta B_z = 19.8$ nT. The GRS count rate increases to $\delta_{peak} = 446$ s^{-1} over the background count rate. After the dipolarization front, B_z decays smoothly until reaching a constant value at $t \approx +7$ s; the entire dipolarization event lasts $\Delta t_{DIP} = 8.2$ s. The magnitude of B_z at the end of the interval (48.0 nT) is greater than at the beginning (43.2 nT), consistent with the plasma sheet thickening expected with dipolarization events. The changes in B_z are captured in the total field strength B. Throughout the interval, $|B_x|$ and $|B_y|$ remain at near-constant values (~22 nT and ~13 nT, respectively), while the average B_x and B_y (not shown here) each display no features and remain at ~0 nT.

While the magnetic field decays smoothly following the dipolarization front, the energetic electron count rate exhibits additional behavior. Following the peak at $t \approx +1$ s, the GRS count rate decays slowly to background values with $\Delta t_{GRS} = 11.0$ s but exhibits a secondary maximum at $t \approx +17$ s. This secondary maximum is not reflected in the magnetic field signature, suggesting that this peak may be due to MESSENGER interacting with either the same population of electrons as they drift about the planet or another population entirely. This peak, however, falls below the 5-sigma significance level (red) and would not be identified as an electron event by the GRS algorithm.

The GRS spectra observe a dispersionless injection with the count rate of energies <100 keV increasing nearly simultaneously at $t \approx -3$ s. In fact, the GRS spectra show a slight inverse dispersion of energies >100 keV. During the injection, we observe an increase in electron energies up to 130 keV. Energies >20 keV reach a maximum change at the end of the dipolarization front at $t \approx +2$ s, while energies <20 keV reach a maximum change during the DFB at $t \approx +8$ s, as indicated by the black line. We observe the greatest change in the spectra at these lower (<20 keV) energies. The trend of lower energies reaching a maximum change later than higher energies is similar to the dipolarization-injection events in Figures 3.2a and 3.3a. In these events, we observe the greatest proportion of lower energy electrons later in the event.

FIPS observes plasma depletion and energization during the superposed dipolarization-injection. The proton density begins decreasing from 0.85 cm^{-3} at $t \approx -4$ s to a minimum of 0.59 at $t \approx +6$ s during the DFB. Following the minimum, the density increases slowly to preevent values. To assess plasma energization in detail, we examine the superposed FIPS energy-resolved pitch angle distributions used to construct the H^+ E/q spectrum in Figure 3.5. Figure 3.6 contains the superposed energy-resolved pitch angle distributions averaged over intervals before ($-20 < t < -10$ s) and during ($0 < t < 10$ s) the superposed dipolarization-injection. Each pitch angle energy bin is sufficiently sampled for statistical analysis; the minimum number of observations in a single bin is 86, the maximum is 510, and the average is 358. Computing the plasma moments of each distribution, the H^+ density decreases from 0.87 cm^{-3} prior to the dipolarization event to 0.61 cm^{-3} during the event ($\Delta n/n = -0.30$). The decrease in density is readily noted within the black boxes. The distributions also indicate a modest energization and heating of protons; the temperature increases from 35.2 MK prior to the event to 38.0 MK during the event ($\Delta T/T = 0.08$). The change in density appears isotropic, while the changes in energy and temperature are pitch angle (Θ) dependent. Between the distributions, $\Delta n_{\parallel}/n_{\parallel} = -0.34$ and $\Delta n_{\perp}/n_{\perp} = -0.29$, while $\Delta T_{\parallel}/T_{\parallel} = +0.02$ and $\Delta T_{\perp}/T_{\perp} = +0.10$, where $n_{\perp}$ and $T_{\perp}$ are computed from pitch angles $|\Theta - 90°| < 45°$, while $n_{\parallel}$ and $T_{\parallel}$ are from $|\Theta - 90°| > 45°$. Protons experience more energization perpendicular to the local magnetic field than parallel. Finally, both distributions appear to display a plasma asymmetry between the field-aligned and antifield-aligned directions, marked approximately by the black arrows. This signature may be due to Mercury's asymmetric loss cones (estimated to be ~10° in the antifield-aligned direction and ~20° in the field-aligned direction from an offset dipole model; FIPS pitch angle uncertainty is ~10°, for contrast) and/or be an effect of strong planetward flow. Future studies will investigate this signature further.

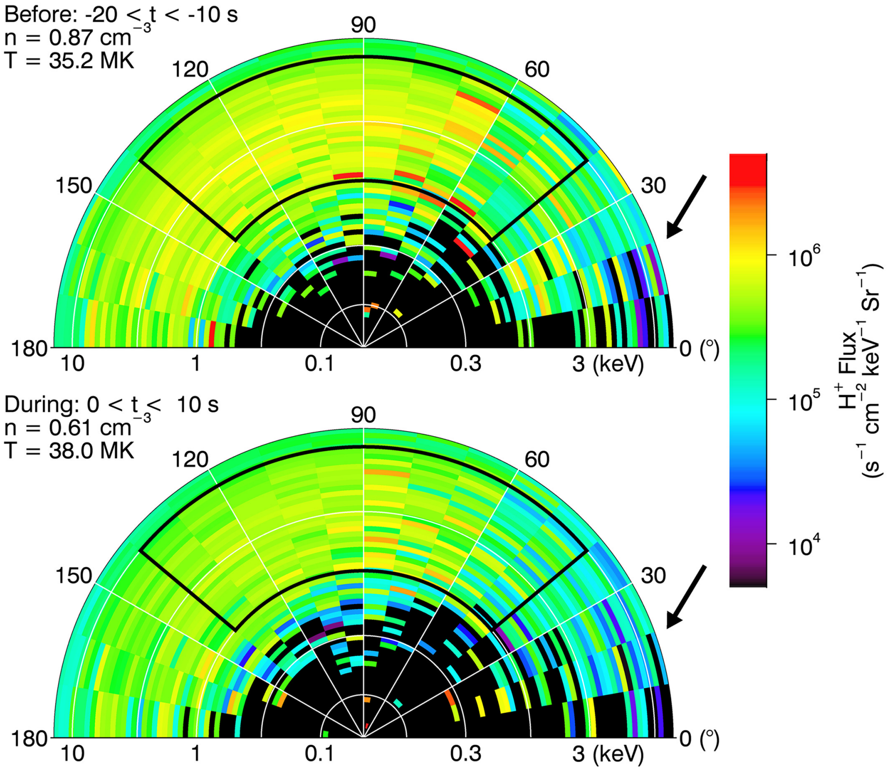

Figure 3.6. Energy-resolved pitch angle H^+ distributions from superposed FIPS analysis (top) prior to and (bottom) during the dipolarization event. The radial spokes correspond

to the pitch angle, and the concentric rings correspond to H^+ energy. The color bins have nonzero flux as indicated by the color bar. The density and energy moments are listed to the left of each distribution. The arrows and black boxes indicate features discussed in the text.

The typical dipolarization-injection characteristics from superposed epoch analysis agree well with average parameters from all individual events. Each parameter from superposed epoch analysis, save Δt_{GRS}, is within one standard deviation of the histogram means. The duration time scales agree well between the two methods; however, the superposed epoch analysis indicates that the injection typically lasts longer than the dipolarization event, whereas the histograms indicate the opposite. The close agreement between the average histogram parameters and superposed epoch analysis indicates that, although there is considerable spread in dipolarization-injection signatures, as seen in Figure 3.4, dipolarization-injection events can be well represented with single-value parameters, which may be useful to future modeling studies.

3.4.3 Spatial Frequency and Precipitation

To estimate the contribution of dipolarization events to magnetotail injections, we display the spatial fraction of electron events identified within the survey region associated with magnetic field dipolarization in Figure 3.7. In the same format and binning as Figure 3.1, Figure 3.7 examines the spatial distribution of dipolarization events, normalized to the local number of electron events. The dashed white line corresponds to the survey region. The spatial fraction ranges from 0.02 (i.e., 1 dipolarization to 50 electron events) at LT ~5.25 and Z_{MSM} ~0.35 R_M to 1.00 at LT ~0.25 and Z_{MSM} ~−0.15 R_M. The spatially averaged fraction of electron events associated with magnetic field dipolarization is 0.25, in contrast to the 538/2,976 = 0.18 fraction of electron events within the survey region identified visually with dipolarization signatures.

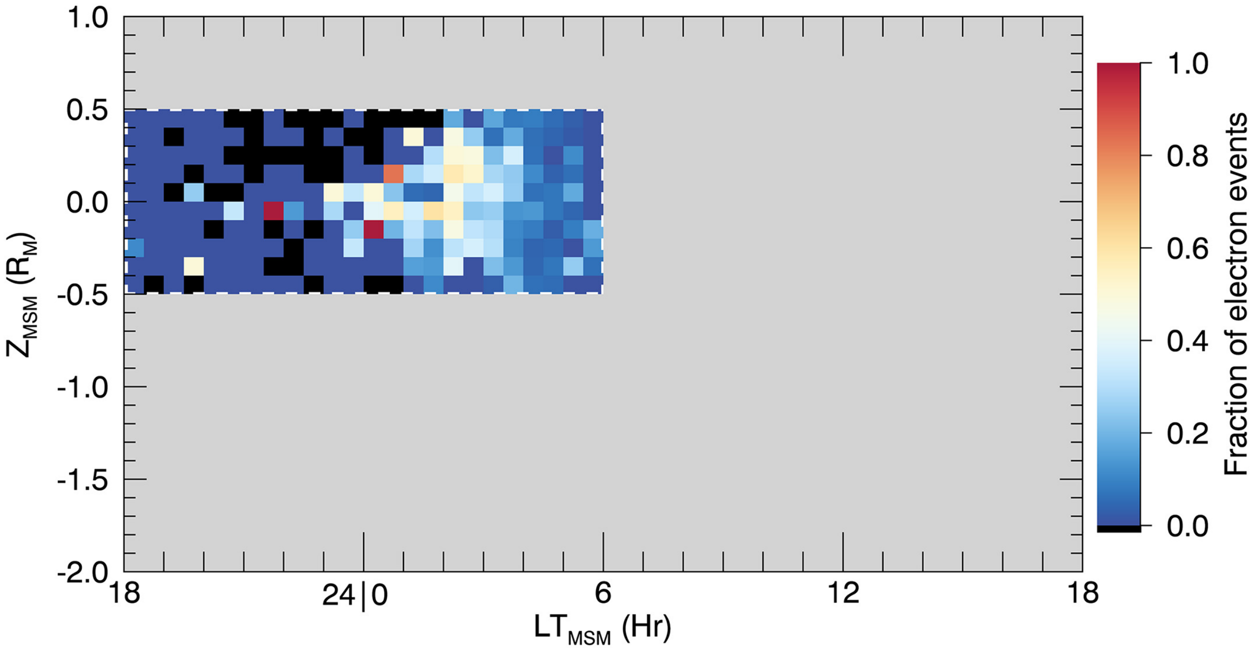

Figure 3.7. Spatial distribution of the fraction of injection events coincident with magnetic field dipolarization, in the same format as in Figure 3.1. The grey space is outside of the survey region. The color bar indicates the value within each bin. The black color indicates locations where no injections were identified (see Figure 3.1).

Compared to the peak electron event frequency in Figure 3.1, the peak ratio of dipolarizations to electron events is shifted to local times closer to midnight. The distribution of electron events in the magnetotail peak at LT ~4, while the peak fraction of electron events associated with dipolarizations occurs at LT ~ 1–2. Above LT ~2, the fraction of electron events associated with dipolarization decreases with local time, consistent with the expectation that dipolarization events are confined to the magnetotail and infrequently reach the terminator. Despite the asymmetry of electron events about local midnight, dipolarizations are more associated with events in the postmidnight sector than in the premidnight sector. In the postmidnight sector, of the 2,732 injections, there are 521 dipolarization-injection events, or approximately 1 dipolarization to 5.2 electron events (i.e., a fraction of 0.19). In the premidnight sector, of the 244 electron events, there are 17 dipolarization-injection events, or approximately 1 dipolarization to 14.4 electron events (i.e., a fraction of 0.07). The increased abundance of dipolarization events in the postmidnight sector is consistent with the observed dawn-dusk asymmetry of dipolarizations at Mercury (Sun et al., 2016).

As Mercury possesses large loss cones and lacks an appreciable atmosphere, a portion of the energetic electrons in the dipolarization-injection events is expected to precipitate directly to the planetary surface. Figure 3.8 depicts the (a) observed and (b) predicted locations of energetic electron precipitation on Mercury's nightside surface. Reproduced in Figure 3.8a, Lindsay et al. (2016) indirectly observed the energetic electron precipitation on Mercury's nightside surface; energetic electrons impinging on the surface would produce X-rays detectable by the X-Ray Spectrometer (XRS). Lindsay et al. (2016) found a strong dawn-dusk asymmetry in electron precipitation, and with the greatest precipitation occurring just equatorward of the typical open-closed field line boundary (Korth et al., 2015). In Figure 3.8b, we compare the expected precipitation from dipolarization-injection events to the precipitation map by Lindsay et al. (2016). Using a simple, azimuthally symmetric, offset-dipole model of Mercury's magnetic field, we trace MESSENGER's position during each event to Mercury's surface in both hemispheres. Despite the simplicity of the dipole model, the expected precipitation map agrees well with observations from Lindsay et al., particularly in the local time extent of the precipitation and the proximity to the open-closed field line boundary. The disagreement at LT > 4 is due to the azimuthal symmetry of our model.

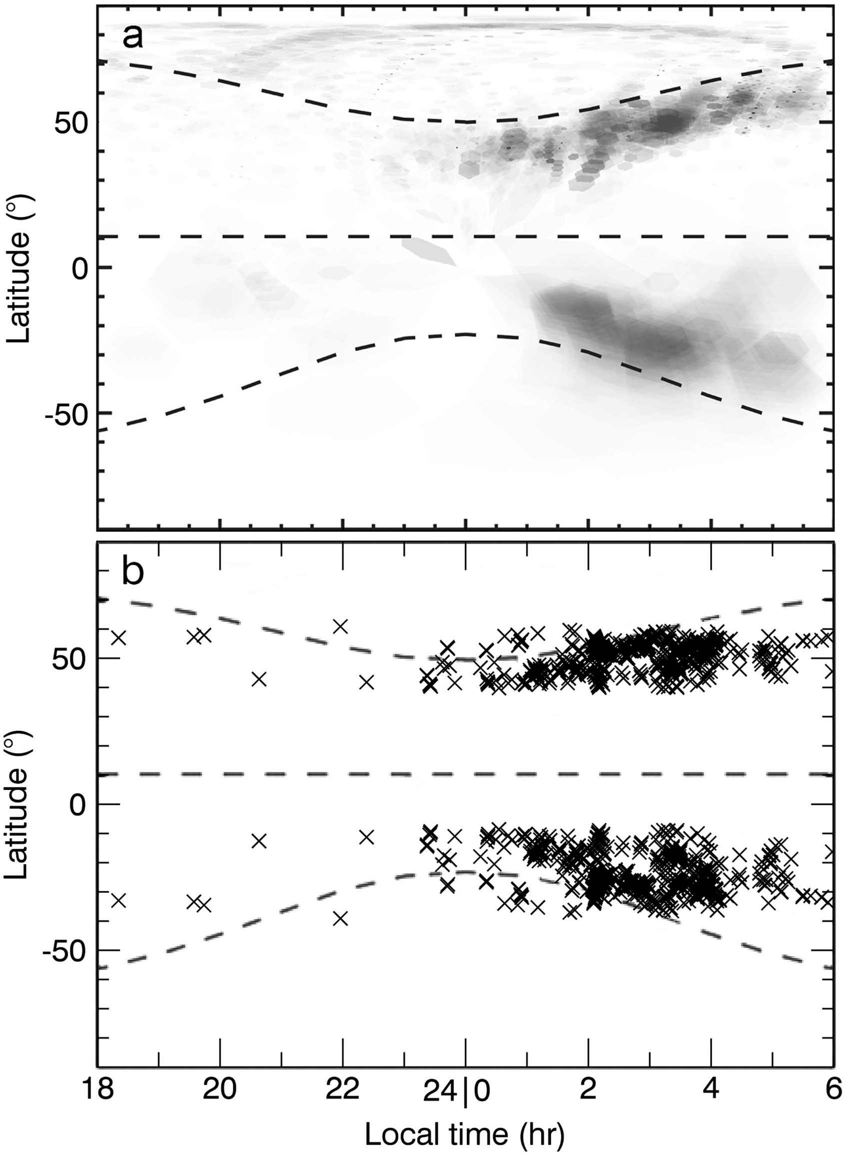

Figure 3.8. (a) XRS observations of energetic electrons precipitating to Mercury's nightside surface in geographic coordinates, adapted from Lindsay et al. (2016). The dashed lines correspond to the open-closed field line boundary and magnetic equator determined by Korth et al. (2015). (b) The predicted precipitation of energetic electrons during dipolarization-injection events.

3.4.4 Nondipolarization Electron Events

Of the 2,976 electron events within the survey region, we identified 538 to be associated with magnetic field dipolarization. From the spatial ratio of dipolarization events to electron events, ~25% of injections are directly associated with dipolarization. Compared to the remaining 2,438 electron events, the electron events associated with dipolarization tend to reach a higher count rate but last statistically similar durations. The dipolarization-associated events have $<\delta_{peak}> = 310 \pm 190\ s^{-1}$ and $<\Delta t_{GRS}> = 4.4 \pm 4.0$ s, while the remaining events have $<\delta_{peak}> = 160 \pm 60\ s^{-1}$ and $<\Delta t_{GRS}> = 3.5 \pm 5.1$ s (after removing outliers). The energy spectra of dipolarization-associated events are statistically indistinguishable from the typical spectra of the remaining events (not shown here); that is, the remaining events have the same distribution of energies but fewer counts (particles). Superposed epoch analysis of the remaining electron events, shown in Figure 3.9, suggests that magnetic field dipolarization, or at least plasma sheet thickening, may be common to most magnetotail energetic electron events. Similar to the dipolarization-injection superposed GRS and MAG epoch analysis, we aligned all remaining injection events at the event start time identified by the algorithm and averaged the particle and magnetic field properties. $|B_x|$ and $|B_y|$ show no discernible signatures; however, B_z shows a modest increase ($\Delta B_z \sim 4$ nT) coincident with the increase in GRS count rate, similar to the dipolarization-associated events. The persistent dipolarization signature in the remaining injections suggests that a larger fraction of electron events in Mercury's magnetotail are associated with dipolarization than were identified visually; that is, >25% of magnetotail electron events appear to be associated with magnetic field dipolarization.

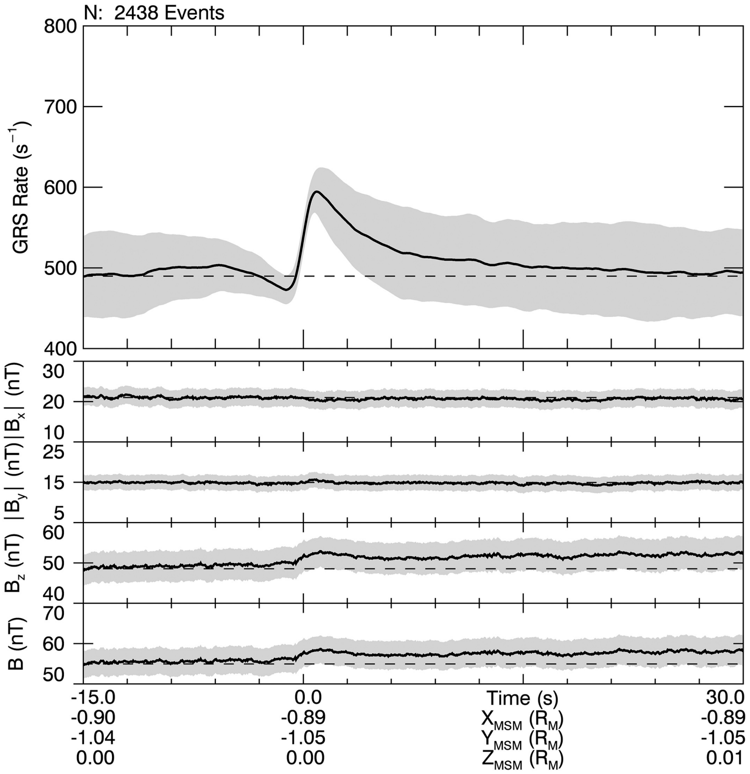

Figure 3.9. Superposed GRS and MAG epoch analysis of the remaining 2,438 electron events within the survey region, in the same format as in Figure 3.5 but with GRS spectral accumulations and FIPS observations removed.

3.5 Discussion

Using an algorithm to identify energetic electron events in Mercury's magnetotail, we identified 538 magnetic field dipolarizations associated with energetic electron injections and analyzed these events statistically. The average parameters of the dipolarization events, such as the risetime and change in the northward component of the magnetic field, agree well with previous studies of dipolarizations at Mercury. Sundberg et al. (2012) identified 24 dipolarization events and found, on average, $<\Delta B_z> = 46$ nT, $<\Delta t_{DF}> = 1.6$ s, and $<\Delta t_{DIP}> = 13$ s. We find $<\Delta B_z> = 28.0 \pm 13.3$ nT, $<\Delta t_{DF}> = 2.01 \pm 1.00$ s, and $<\Delta t_{DIP}> = 10.5 \pm 5.4$ s, each agreeing well with events identified by Sundberg et al. (2012). We find a typically smaller $<\Delta B_z>$; however, this is likely due to the small sample size and extreme events analyzed by Sundberg et al. (2012).

We also find that dipolarization events are more frequent in the postmidnight sector than the premidnight sector, despite the strong asymmetry of energetic electron events across the tail, consistent with the spatial distribution of dipolarization fronts identified by Sun et al. (2016).

In addition to agreeing well with previous studies at Mercury, the dipolarization characteristics we find at Mercury are similar to those at Earth. From superposed plasma observations, we find a decrease in plasma density within the dipolarization events compared to the ambient plasma, consistent with the interpretation of DFBs as low entropy, depleted plasma bubbles convecting planetward in the magnetotail (e.g., Pontius & Wolf, 1990; Sergeev et al., 1996). Compared to the ambient plasma sheet, we find the typical plasma density inside DFBs is a factor of 0.7 less dense than the ambient plasma, similar to the factor of 0.6 observed at Earth (Runov et al., 2015). We also find that dipolarization events at Mercury typically exhibit a dip in the magnetic field prior to the step-like increase of the dipolarization front, occasionally with the dip reaching $B_z < 0$ nT, similar to dipolarization events at Earth (e.g., Drake et al., 2014; Slavin et al., 2002; Zhou et al., 2014).

3.5.1 Particle Energization Mechanisms During Dipolarization Events

An important consequence of dipolarization events at Earth is their energization and injection of plasma into the inner magnetosphere. Observations (e.g., Gabrielse et al., 2014; Runov et al., 2009, 2013; Turner et al., 2016) and simulations (e.g., Ashour-Abdalla et al., 2011; Birn et al., 2013, 2014; Gabrielse et al., 2016) of dipolarization events indicate that betatron acceleration (conservation of the first adiabatic invariant) and Fermi acceleration (conservation of the second adiabatic invariant) are the primary acceleration mechanisms for elections. Birn et al. (2013), for example, used particle tracing through MHD fields to find that two electron populations are energized by magnetic field dipolarization and contribute to the injection event: (1) electrons drifting across the tail interact with the dipolarization region and experience betatron acceleration; (2) electrons past the magnetotail reconnection site are entrained on newly closed field lines and experience Fermi acceleration as the field line is convected planetward. Birn et al. find the first population of electrons is accelerated to greater energies and occurs earlier in the dipolarization event, while finding the second population of electrons is accelerated to relatively lower energies and arrives later during the dipolarization event. Protons, in contrast, experience only quasi-adiabatic betatron acceleration (Birn et al., 2013).

MESSENGER GRS and FIPS observations both indicate that particle acceleration occurs during dipolarization events at Mercury similar to at Earth. The dramatic increase of GRS count rate during dipolarization events suggests that electrons are accelerated into the GRS detection limit (estimated to be ~10 keV). Electron energization is corroborated by the superposed GRS spectra, which suggests that electrons are accelerated to energies E~130 keV during these events. Although the angular and temporal resolutions of the GRS spectra prevent us from directly observing betatron and Fermi acceleration, the decrease and subsequent sharp increase in GRS count rate coincident with the magnetic field during the dipolarization front suggest the presence of betatron acceleration (e.g., Runov et al., 2013) and the greater proportion of lower energy electrons later during dipolarizations may suggest the presence of Fermi acceleration (Birn et al., 2013). An additional indicator that the dipolarization events, as opposed to magnetic reconnection directly, are accelerating electrons is the location of energetic electron precipitation on Mercury's surface. Particle acceleration during dipolarization events occurs after magnetic reconnection; particles energized by the dipolarization will precipitate equatorward of the open/closed field line boundary (e.g., Birn et al., 2013). If the electrons were accelerated directly by magnetic reconnection at the reconnection site, then they would precipitate directly onto the open-closed field line boundary. The close agreement between observed and modeled precipitation in Figure 3.8 equatorward of the open-closed field line boundary indicates that the acceleration is associated with the dipolarization event, and not with magnetic reconnection itself, and that injection events from the magnetotail may be the primary contributors to the nightside energetic electron precipitation.

In contrast to the indirect observations of electron acceleration, plasma observations of H^+ exhibit more direct signatures of energization. Using superposed FIPS observations, we find that the thermal H^+ plasma contained in dipolarization events has a typical temperature 38.0 MK, compared to the 35.2 MK of the ambient thermal plasma. This increase in energy is dominated by acceleration perpendicular to the magnetic field, that is, betatron acceleration. We find little field-aligned (Fermi) acceleration. At Earth, ion temperatures observed within DFBs are typically hotter than the ambient plasma sheet by a factor of 1.3 (Runov et al., 2015) as opposed to the factor of 1.1 we find at Mercury. Two case studies analyzed by Sun et al. (2017) indicate dipolarizations may heat the plasma by a factor of ~2. While several events reach or exceed this factor (see Figure 3.4), we find a typically smaller heating factor, which is likely due to the small sample size and extreme events analyzed by Sun et al. (2017).

The modest ion acceleration compared to the dramatic electron acceleration is likely an effect of nonadiabatic ion motion. While the energy an individual particle may gain during a dipolarization is highly dependent on its trajectory and interaction with the DF(s) and DFB(s) (e.g., Gabrielse et al., 2016, 2017), we can estimate the typical adiabatic energization. From the average ratio of magnetic field strength at the end of the dipolarization front to the strength at the beginning, we estimate that the typical betatron acceleration would increase a particle's perpendicular energy by a factor of ~2.3. From the ratio of dipole field line lengths above Mercury's surface from the typical nightside X-line location at $X_{MSM} = -3\ R_M$(Poh et al., 2017) to the typical dipolarization-injection event location at L-shell ~1.5 R_M, we estimate that typical Fermi acceleration would increase a particle's parallel energy by a factor of ~2.7. We expect electrons to behave adiabatically, whereas ions behave nonadiabatically and cannot access these rates of energization fully. For a 47 nT magnetic field (the typical field at the start of the dipolarization front), the H^+ gyroperiod is 1.4 s, whereas the electron gyroperiod is 0.8 ms. With an equatorial pitch angle of 45° at an equatorial distance of 1.5 R_M in a dipole field, the 5 keV H^+ bounce period would be 13.4 s, whereas the 50 keV electron bounce period would be 0.1 s. The H^+ gyro and bounce periods are on the order of the typical dipolarization front (2.0 s) and dipolarization event (10.5 s) time scales, respectively, indicating that nonadiabatic ion motion is expected. Birn et al. (2013) found that, although proton motion is not strictly adiabatic near dipolarization events at Earth, ions drifting across the dipolarization region are accelerated akin to betatron acceleration, consistent with the acceleration we observe in FIPS observations. Both electron time scales, in contrast, are significantly shorter than either dipolarization time scale, enabling both betatron and Fermi acceleration to occur. Dipolarization events at Mercury, therefore, may typically only be a powerful source of particle acceleration for electrons.

3.5.2 Closed Drift Paths

Closed drift paths, as well as the potential for Mercury's magnetosphere to host radiation belts, have been controversial subjects since Mariner 10's flybys (e.g., Baker et al., 1986). While the large loss cones and small magnetopause standoff distance prevent permanent radiation belts like at Earth (Slavin et al., 2007), an increasing number of observations at Mercury suggest that “quasi-trapped” populations of electrons are able to execute multiple drifts about the planet before being lost to surface precipitation or magnetopause shadowing (e.g., Baker et al., 2016; Ho et al., 2016). Analytic simulations also suggest the possibility of closed drift paths at Mercury, although they appear to be more Shabansky-like in nature (Walsh et al., 2013).

The GRS superposed epoch analysis appears to have a feature indicative of a closed drift path. Following the dipolarization event, there is a second maxima in the GRS count rate without corresponding features in the magnetic field, suggesting that MESSENGER may be interacting with the injected electrons again as they drift about the planet. Assuming an equatorially mirroring electron in a dipole field, the electron’s energy would need to be ~100 keV to gradient drift about the planet in ~16 s, assuming a dipole moment of 200 nT R_M^3 and an L-shell of 1.6 (corresponding to the typical dipolarization-injection event location). While this energy is within the typical GRS electron energy spectra, the secondary peak is not significant enough to be detected by the algorithm. Additionally, the distribution of electron events about the planet (Figure 3.1) is consistent with Shabansky orbits; electrons drift near the equatorial latitudes on the nightside and pass through high latitudes in the compressed dayside magnetosphere. Future studies are required to investigate the viability and abundance of energetic electron closed drift paths at Mercury.

3.5.3 Remaining Electron Events: Near-Mercury Neutral Line

Mercury’s northward dipole moment causes electrons to gradient-curvature drift eastward about the planet; electrons injected in the magnetotail would drift to dawn and in the direction of increasing LT. The peak ratio of dipolarizations to electron events at LT ~ 1–2 and the peak electron event occurrence at LT ~4–6 are consistent with dipolarization acceleration followed by eastward drift about the planet. As electrons drift about the planet, we expect some to be lost to surface precipitation or magnetopause shadowing, consistent with the decreased counts associated with the remaining injection events compared to the dipolarization-associated events. The remaining events share statistically identical spectra to the dipolarization-associated events, suggesting that the loss process must be energy-independent (e.g., surface precipitation in the loss cone, which may be observed in the superposed FIPS spectra). As electrons continue to drift about the planet, they are expected to be continuously lost to surface precipitation and magnetopause shadowing, while a fraction of electrons may move to higher latitudes on the dayside and participate in a Shabansky orbit (e.g., Walsh et al., 2013), consistent with the global distribution of identified electron events in Figure 3.1. Without multipoint observations, the Near-Mercury Neutral Line model (e.g., Baker et al., 2016) is difficult to verify; however, the global distribution of electron events, close association of electron events with dipolarizations in the magnetotail, and energy/flux characteristics of events associated and not associated with dipolarization are all consistent with the model. Magnetotail dipolarization may be the dominant source of energetic electron acceleration in Mercury's magnetosphere.

3.6 Conclusions

We present strong evidence for Mariner 10-like energetic electron injection events associated with magnetic field dipolarization in Mercury's magnetotail. We developed an automated algorithm to identify energetic electron events in the high-time-resolution GRS count rate, and of the 2,976 events within the survey region ($X_{MSM} < 0$ R_M and $|Z_{MSM}| < 0.5$ R_M), we associate 538 such events with magnetic field dipolarization signatures. Although individual dipolarization-injection events display large variability in temporal characteristics, statistical analysis reveals a typical dipolarization risetime of ~2 s, during which the northward component of the magnetic field increases by ~30 nT and the energetic electron count rate increases by nearly an order of magnitude. Both the dipolarization and injection typically last for ~10 s. While these events are observed in the plasma sheet, often close to the central current sheet, dipolarization events occur disproportionally in the postmidnight sector. Both the energetic electron and dipolarization time scales and spatial distributions are consistent with previous studies at Mercury.

We find that >25% of magnetotail electron events are associated with magnetic field dipolarization and observe both direct and indirect electron and ion energization during these dipolarizations. Similar to dipolarization events at Earth, electrons behave adiabatically and experience both betatron and Fermi acceleration during dipolarization intervals, reaching energies ~130 keV. These electrons contribute to nightside surface precipitation and may drift about the planet in Shabansky-like orbits. Ions, in contrast, are not strictly adiabatic and appear to participate only in modest betatron acceleration. Despite the only modest energization of ions, the plasma density decreases during dipolarization intervals compared to the ambient plasma sheet, consistent with the interpretation of dipolarization events as low entropy, depleted flux tubes convecting planetward following the collapse of the inner magnetotail. Dipolarization events at Mercury, therefore, may typically only be a powerful source of particle acceleration for electrons.

While only >25% of electron events within the survey region are coincident with magnetic field dipolarization, comparisons between the dipolarization-associated electron events and the remaining events are consistent with the Near-Mercury Neutral Line model of magnetotail injection and eastward drift about the planet (e.g., Baker et al., 2016). Without multipoint observations, associating the remaining electron events with dipolarization acceleration is nontrivial. If these remaining events are indeed energized by a dipolarization upstream of the spacecraft and subsequently drift to the spacecraft's location, magnetic field dipolarization may be the dominant mechanism for energetic electron acceleration at Mercury. The substantial association between electron events and dipolarization events, the dramatic increase in energetic electron count rate during dipolarization events, the significant precipitation associated with dipolarization-accelerated electrons, and the possibility for these accelerated electrons to transport through the magnetosphere indicate that Mariner 10-like dipolarization events produce a significant component of the energetic particle environment at Mercury. As dipolarization and injection events are intimately related to substorm events at Earth, these results can provide further insight into the character and dynamics of magnetospheric substorm-like events at Mercury, the focus of our future work.

3.7 Acknowledgments

This research was supported by NASA's Discovery Data Analysis Program (NNH16ZDA001N-DDAP, NNX16AJ03G, and NNX15AL01G), Heliophysics Supporting Research Program (NNX15AJ68G), Living With a Star Program (NNX16AJ67G), Planetary Atmospheres Program (NNX14AJ46G), NASA Earth and Space Science Fellowship Program (80NSSC17K0493), and NASA grant NNX16AI98G. R. M. Dewey would like to thank S. M. Imber and W. J. Sun for valuable conversations. All MESSENGER data used in the study are available from the NASA Planetary Data System.

3.8 References

Alexeev, I. I., Belenkaya, E. S., Slavin, J. A., Korth, H., Anderson, B. J., Baker, D. N., … Solomon, S. C. (2010). Mercury's magnetospheric magnetic field after the first two MESSENGER flybys. *Icarus*, **209**(1), 23–39. https://doi.org/10.1016/j.icarus.2010.01.024

Anderson, B. J., Acuña, M. H., Lohr, D. A., Scheifele, J., Raval, A., Korth, H., & Slavin, J. A. (2007). The magnetometer instrument on MESSENGER. *Space Science Reviews*, **131**, 417–450. https://doi.org/10.1007/s11214-007-9246-7

Anderson, B. J., Johnson, C. L., Korth, H., Purucker, M. E., Winslow, R. M., Slavin, J. A., … Zurbuchen, T. H. (2011). The global magnetic field of Mercury from MESSENGER orbital observations. *Science*, **333**, 1859–1862. https://doi.org/10.1126/science.1211001

Andrews, G. B., Zurbuchen, T. H., Mauk, B. H., Malcom, H., Fisk, L. A., Gloeckler, G., … Raines, J. M. (2007). The energetic particle and plasma spectrometer instrument on the MESSENGER spacecraft. *Space Science Reviews*, **131**(1–4), 523–556. https://doi.org/10.1007/s11214-007-9272-5

Angelopoulos, V., Baumjohann, W., Kennel, C. F., Coroniti, F. V., Kivelson, M. G., Pellat, R., … Paschmann, G. (1992). Bursty bulk flows in the inner central plasma sheet. *Journal of Geophysical Research*, **97**, 4027–4039. https://doi.org/10.1029/91JA02701

Ashour-Abdalla, M., El-Alaoui, M., Goldstein, M. L., Zhou, M., Schriver, D., Richard, R., … Hwang, K.-J. (2011). Observations and simulations of non-local acceleration of electrons in magnetotail magnetic reconnection events. *Nature Physics*, **7**, 360–365. https://doi.org/10.1038/nphys1903

Baker, D. N., Dewey, R. M., Lawrence, D. J., Goldsten, J. O., Peplowski, P. N., Korth, H., … Solomon, S. C. (2016). Intense energetic electron flux enhancements in Mercury's magnetosphere: An integrated view with high-resolution observations from MESSENGER. *Journal of Geophysical Research: Space Physics*, **121**, 2171–2184. https://doi.org/10.1002/2015JA021778

Baker, D. N., Higbie, P. R., Hones, E. W. Jr., & Belian, R. D. (1978). High-resolution energetic particle measurements at 6.6 RE 3. Low-energy electron anisotropies and short-term substorm predictions. *Journal of Geophysical Research*, **83**, 4863–4868. https://doi.org/10.1029/JA083iA10p04863

Baker, D. N., Pulkkinen, T. I., Angelopoulos, V., Baumjohann, W., & McPherron, R. L. (1996). Neutral line model of substorms: Past results and present view. *Journal of Geophysical Research*, **101**, 12,975–13,010. https://doi.org/10.1029/95JA03753

Baker, D. N., Simpson, J. A., & Eraker, J. H. (1986). A model of impulsive acceleration and transport of energetic particles in Mercury's magnetosphere. *Journal of Geophysical Research*, **91**, 8742–8748. https://doi.org/10.1029/JA091iA08p08742

Birn, J., Hesse, M., Nakamura, R., & Zaharia, S. (2013). Particle acceleration in dipolarization events. *Journal of Geophysical Research: Space Physics*, **118**, 1960–1971. https://doi.org/10.1002/jgra.50132

Birn, J., Nakamura, R., Panov, E. V., & Hesse, M. (2011). Bursty bulk flows and dipolarization in MHD simulations of magnetotail reconnection. *Journal of Geophysical Research*, **116**, A01210. https://doi.org/10.1029/2010JA016083

Birn, J., Runov, A., & Hesse, M. (2014). Energetic electrons in dipolarization events: Spatial properties and anisotropy. *Journal of Geophysical Research: Space Physics*, **119**, 3604–3616. https://doi.org/10.1002/2013JA019738

Christon, S. P., Feynman, J., & Slavin, J. A. (1987). Dynamic substorm injections — Similar magnetospheric phenomena at Earth and Mercury. In A. T. Y. Lui (Ed.), *Magnetotail physics* (pp. 393–400). Baltimore, MD: Johns Hopkins University Press.

Delcourt, D. C., Moore, T. E., & Fok, M.-C. H. (2010). Ion dynamics during compression of Mercury's magnetosphere. *Annales de Geophysique*, **28**, 1467–1474. https://doi.org/10.5194/angeo-28-1467-2010

Deng, X., Ashour-Abdalla, M., Zhou, M., Walker, R., El-Alaoui, M., Angelopoulos, V., … Schriver, D. (2010). Wave and particle characteristics of earthward electron injections associated with dipolarization fronts. *Journal of Geophysical Research*, **115**, A09225. https://doi.org/10.1029/2009JA015107

Drake, J. F., Swisdak, M., Cassak, P. A., & Phan, T. D. (2014). On the 3-D structure and dissipation of reconnection-driven flow bursts. *Geophysical Research Letters*, **41**, 3710–3716. https://doi.org/10.1002/2014GL060249

Fu, H. S., Khotyaintsev, Y. V., André, M., & Vaivads, A. (2011). Fermi and betatron acceleration of suprathermal electrons behind dipolarization fronts. *Geophysical Research Letters*, **38**, L16104. https://doi.org/10.1029/2011GL048528

Fu, H. S., Khotyaintsev, Y. V., Vaivads, A., Retinò, A., & André, M. (2013). Energetic electron acceleration by unsteady magnetic reconnection. *Nature Physics*, **9**, 426–430. https://doi.org/10.1038/nphys2664

Gabrielse, C., Angelopoulos, V., Harris, C., Artemyev, A., Kepko, L., & Runov, A. (2017). Extensive electron transport and energization via multiple, localized dipolarizing flux bundles. *Journal of Geophysical Research: Space Physics*, **122**, 5059–5076. https://doi.org/10.1002/2017JA023981

Gabrielse, C., Angelopoulos, V., Runov, A., & Turner, D. L. (2014). Statistical characteristics of particle injections throughout the equatorial magnetotail. *Journal of Geophysical Research: Space Physics*, **119**, 2512–2535. https://doi.org/10.1002/2013JA019638

Gabrielse, C., Harris, C., Angelopoulos, V., Artemyev, A., & Runov, A. (2016). The role of localized inductive electric fields in electron injections around dipolarizing flux bundles. *Journal of Geophysical Research: Space Physics*, **121**, 9560–9585. https://doi.org/10.1002/2016JA023061

Gershman, D. J., Slavin, J. A., Raines, J. M., Zurbuchen, T. H., Anderson, B. J., Korth, H., … Solomon, S. C. (2013). Magnetic flux pile-up and plasma depletion in Mercury's subsolar magnetosheath. *Journal of Geophysical Research: Space Physics*, **118**, 7181–7199. https://doi.org/10.1002/2013JA019244

Goldsten, J. O., Rhodes, E. A., Boynton, W. V., Feldman,W. C., Lawrence, D. J., Trombka, J. I., … Witte, M. C. (2007). The MESSENGER gamma-ray and neutron spectrometer. *Space Science Reviews*, **131**(1–4), 339–391. https://doi.org/10.1007/s11214-007-9262-7

Ho, G. C., Krimigis, S. M., Gold, R. E., Baker, D. N., Anderson, B. J., Korth, H., … Solomon, S. C. (2012). Spatial distribution and spectral characteristics of energetic electrons in Mercury's magnetosphere. *Journal of Geophysical Research*, **117**, A00M04. https://doi.org/10.1029/2012JA017983

Ho, G. C., Krimigis, S. M., Gold, R. E., Baker, D. N., Slavin, J. A., Anderson, B. J., … Solomon, S. C. (2011). MESSENGER observations of transient bursts of energetic electrons in Mercury's magnetosphere. *Science*, **333**(6051), 1865–1868. https://doi.org/10.1126/science.1211141

Ho, G. C., Starr, R. D., Gold, R. E., Krimigis, S. M., Slavin, J. A., Baker, D. N., … Solomon, S. C. (2011). Observations of suprathermal electrons in Mercury's magnetosphere during the three MESSENGER flybys. *Planetary and Space Science*, **59**, 2016–2025.

Ho, G. C., Starr, R. D., Krimigis, S. M., Vandegriff, J. D., Baker, D. N., Gold, R. E., … Solomon, S. C. (2016). MESSENGER observations of suprathermal electrons in Mercury's magnetosphere. *Geophysical Research Letters*, **43**, 550–555. https://doi.org/10.1002/2015GL066850

Korth, H., Tsyganenko, N. A., Johnson, C. L., Philpott, L. C., Anderson, B. J., Al Asad, M. M., … McNutt, R. L. Jr. (2015). Modular model for Mercury's magnetospheric magnetic field confined within the average observed magnetopause. *Journal of Geophysical Research: Space Physics*, **120**, 4503–4518. https://doi.org/10.1002/2015JA021022

Lawrence, D. J., Anderson, B. J., Baker, D. N., Feldman, W. C., Ho, G. C., Korth, H., … Winslow, R. M. (2015). Comprehensive survey of energetic electron events in Mercury's magnetosphere with data from the MESSENGER gamma-ray and neutron spectrometer.

Journal of Geophysical Research: Space Physics, **120**, 2851–2876. https://doi.org/10.1002/2014JA020792

Lindsay, S. T., James, M. K., Bunce, E. J., Imber, S. M., Korth, H., Martindale, A., & Yeoman, T. K. (2016). MESSENGER X-ray observations of magnetosphere-surface interaction on the nightside of Mercury. *Planetary and Space Science*, **125**, 72–79. https://doi.org/10.1016/j.pss.2016.03.005

Liu, J., Angelopoulos, V., Runov, A., & Zhou, X.-Z. (2013). On the current sheets surrounding dipolarizing flux bundles in the magnetotail: The case for wedgelets. *Journal of Geophysical Research: Space Physics*, **118**, 2000–2020. https://doi.org/10.1002/jgra.50092

Peplowski, P. N., Lawrence, D. J., Feldman, W. C., Goldsten, J. O., Bazell, D., Evans, L. G., … Weider, S. Z. (2015). Geochemical terranes of Mercury’s northern hemisphere revealed by MESSENGER neutron measurements. *Icarus*, **253**, 346–363. https://doi.org/10.1016/j.icarus.2015.02.002

Poh, G., Slavin, J. A., Jia, X., Raines, J. M., Imber, S. M., Sun, W. J., … Smith, A. W. (2017). Mercury’s cross-tail current sheet: Structure, X-line location and stress balance. *Geophysical Research Letters*, **44**, 678–686. https://doi.org/10.1002/2016GL071612

Pontius, D. H., & Wolf, R. A. (1990). Transient flux tubes in the terrestrial magnetosphere. *Geophysical Research Letters*, **17**, 49–52. https://doi.org/10.1029/GL017i001p00049

Runov, A., Angelopoulos, V., Gabrielse, C., Liu, J., Turner, D. L., & Zhou, X.-Z. (2015). Average thermodynamic and spectral properties of plasma in and around dipolarizing flux bundles. *Journal of Geophysical Research: Space Physics*, **120**, 4369–4383. https://doi.org/10.1002/2015JA021166

Runov, A., Angelopoulos, V., Gabrielse, C., Zhou, X.-Z., Turner, D., & Plaschkle, F. (2013). Electron fluxes and pitch-angle distributions at dipolarization fronts: THEMIS multipoint observations. *Journal of Geophysical Research: Space Physics*, **118**, 744–755. https://doi.org/10.1002/jgra.50121

Runov, A., Angelopoulos, V., Sitnov, M. I., Sergeev, V. A., Bonnell, J., McFadden, J. P., … Auster, U. (2009). THEMIS observations of an earthward-propagating dipolarization front. *Geophysical Research Letters*, **36**, L14106. https://doi.org/10.1029/2009GL038980

Runov, A., Angelopoulos, V., & Zhou, X.-Z. (2012). Multipoint observations of dipolarization front formation by magnetotail reconnection. *Journal of Geophysical Research*, **117**, A05230. https://doi.org/10.1029/2011JA017361

Schlemm, C. E. II, Starr, R. D., Ho, G. C., Bechtold, K. E., Hamilton, S. A., Boldt, J. D., … Williams, B. D. (2007). The X-ray spectrometer on the MESSENGER spacecraft. *Space Science Reviews*, **131**(1–4), 393–415. https://doi.org/10.1007/s11214-007-9248-5

Sergeev, V. A., Angelopoulos, V., Gosling, J. T., Cattell, C. A., & Russell, C. T. (1996). Detection of localized, plasma-depleted flux tubes or bubbles in the midtail plasma sheet. *Journal of Geophysical Research*, **101**, 10,817–10,826. https://doi.org/10.1029/96JA00460

Simpson, J. A., Eraker, J. H., Lamport, J. E., & Walpole, P. H. (1974). Electrons and protons accelerated in Mercury's magnetic field. *Science*, **185**, 160–166.

Slavin, J. A., Acuna, M. H., Anderson, B. J., Baker, D. N., Benna, M., Boardsen, S. A., … Zurbuchen, T. H. (2009). MESSENGER observations of magnetic reconnection in Mercury's magnetosphere. *Science*, **324**(5927), 606–610. https://doi.org/10.1126/science.1172011

Slavin, J. A., Anderson, B. J., Baker, D. N., Benna, M., Boardsen, S. A., Gloeckler, G., … Zurbuchen, T. H. (2010). MESSENGER observations of extreme loading and unloading of Mercury's magnetic tail. *Science*, **329**(5992), 665–668. https://doi.org/10.1126/science.1188067

Slavin, J. A., Anderson, B. J., Baker, D. N., Benna, M., Boardsen, S. A., Gold, R. E., … Zurbuchen, T. H. (2012). MESSENGER and Mariner 10 flyby observations of magnetotail structure and dynamics at Mercury. *Journal of Geophysical Research*, **117**, A01215. https://doi.org/10.1029/2011JA016900

Slavin, J. A., Fairfield, D. H., Lepping, R. P., Hesse, M., Ieda, A., Tanskanen, E., Østgaard, N., & Sutcliffe, P. R. (2002). Simultaneous observations of earthward flow bursts and plasmoid ejection during magnetospheric substorms. *Journal of Geophysical Research*, **107**(A7), 1106. https://doi.org/10.1029/2000JA003501

Slavin, J. A., Krimigis, S. M., Acuña, M. H., Anderson, B. J., Baker, D. N., Koehn, P. L., … Zurbuchen, T. H. (2007). MESSENGER: Exploring Mercury's magnetosphere. *Space Science Reviews*, **131**(1–4), 133–160. https://doi.org/10.1007/s1/214-007-9154-x

Sun, W. J., Fu, S. Y., Slavin, J. A., Raines, J. M., Zong, Q. G., Poh, G. K., & Zurbuchen, T. H. (2016). Spatial distribution of Mercury's flux ropes and reconnection fronts: MESSENGER observations. *Journal of Geophysical Research: Space Physics*, **121**, 7590–7607. https://doi.org/10.1002/2016JA022787

Sun, W. J., Raines, J. M., Fu, S. Y., Slavin, J. A., Wei, Y., Poh, G. K., … Wan, W. X. (2017). MESSENGER observations of the energization and heating of protons in the near-Mercury magnetotail. *Geophysical Research Letters*, **44**, 8149–8158. https://doi.org/10.1002/2017GL074276

Sun, W.-J., Slavin, J. A., Fu, S., Raines, J. M., Zong, Q. G., Imber, S. M., … Baker, D. N. (2015). MESSENGER observations of magnetospheric substorm activity in Mercury's near magnetotail. *Geophysical Research Letters*, **42**, 3692–3699. https://doi.org/10.1002/2015GL064052

Sundberg, T., Slavin, J. A., Boardsen, S. A., Anderson, B. J., Korth, H., Ho, G. C., … Solomon, S. C. (2012). MESSENGER observations of dipolarization events in Mercury's magnetotail. *Journal of Geophysical Research*, **117**, A00M03. https://doi.org/10.1029/2012JA017756

Turner, D. L., Fennell, J. F., Blake, J. B., Clemmons, J. H., Mauk, B. H., Cohen, I. J., … Burch, J. L. (2016). Energy limits of electron acceleration in the plasma sheet during substorms: A case study with the Magnetospheric Multiscale (MMS) mission. *Geophysical Research Letters*, **43**, 7785–7794. https://doi.org/10.1002/2016GL069691

Walsh, B. M., Ryou, A. S., Sibeck, D. G., & Alexeev, I. I. (2013). Energetic particle dynamics in Mercury's magnetosphere. *Journal of Geophysical Research: Space Physics*, **118**, 1992–1999. https://doi.org/10.1002/jgra.50266

Zelenyi, L., Oka, M., Malova, H., Fujimoto, M., Delcourt, D., & Baumjohann, W. (2007). Particle acceleration in Mercury's magnetosphere. *Space Science Reviews*, **132**, 593–609. https://doi.org/10.1007/s11214-007-9169-3

Zhou, X.-Z., Angelopoulos, V., Liu, J., Runov, A., & Li, S.-S. (2014). On the origin of pressure and magnetic perturbations ahead of dipolarization fronts. *Journal of Geophysical Research: Space Physics*, **119**, 211–220. https://doi.org/10.1002/2013JA019394

CHAPTER IV. MESSENGER Observations of Fast Plasma Fows in Mercury's Magnetotail

This chapter is taken from Dewey, R. M., Raines, J. M., Sun, W., Slavin, J. A., & Poh, G. (2018). MESSENGER observations of fast plasma flows in Mercury's magnetotail. *Geophysical Research Letters*, **45**, 10,110–10,118. https://doi.org/10.1029/2018GL079056. We have performed minor edits for formatting consistency with the other chapters. The procedure to determine statistical flows that is introduced in section 4.3 is described in detail in Appendix B.

4.1 Abstract

We present the first observation of fast plasma flows in Mercury's magnetotail. Mercury experiences substorm activity phenomenologically similar to Earth's; however, field-of-view limitations of the Fast Imaging Plasma Spectrometer (FIPS) prevent the instrument from detecting fast flows in the plasma sheet. Although FIPS measures incomplete plasma distributions, subsonic flows impart an asymmetry on the partial plasma distribution, even if the flow directions are outside the field of view. We combine FIPS observations from 387 intervals containing magnetic field dipolarizations to mitigate these instrument limitations. By taking advantage of variations in spacecraft pointing during these intervals, we construct composite plasma distributions from which mean flows are determined. We find that dipolarizations at Mercury are embedded within fast sunward flows with an averaged speed of ~300 km/s compared to a typical background flow of ~50 km/s.

4.2 Introduction

The MESSENGER spacecraft has observed that Mercury's magnetosphere experiences brief, yet intense, substorm activity characteristically similar to Earth's. Mercury's magnetotail exhibits loading/unloading (Slavin et al., 2010), dipolarization (Sundberg et al., 2012), plasmoid release (Slavin et al., 2009), energetic particle injection (Dewey, Slavin, et al., 2017), auroral-like precipitation (Lindsay et al., 2016), and current wedge formation (Poh et al., 2017). Mercury's substorms are significantly shorter and relatively stronger than Earth's, a result of the differences between the two magnetospheres (Siscoe et al., 1975). Mercury has a weak global magnetic field and lacks an ionosphere but experiences stronger solar wind forcing that results in shorter temporal scales and higher magnetic reconnection rates than at Earth (e.g., DiBraccio et al., 2013; Slavin et al., 2009). The typical substorm cycle, for example, lasts ~3 min at Mercury compared to the ~1–3 hr at Earth during which Mercury's lobe magnetic field strength increases on average by ~23% compared to the ~10% at Earth (Forsyth et al., 2015; Hsu & McPherron, 2000; Imber & Slavin, 2017). While many features of Mercury's substorms have been identified and investigated, one major substorm signature has yet to be identified at Mercury — the presence of fast plasma flows in the magnetotail.

At Earth, bursty bulk flows (BBFs) are fast plasma flows within the plasma sheet, often traveling sunward with speeds >400 km/s (e.g., Angelopoulos et al., 1992) and typically accompanying magnetic field dipolarization (Ohtani et al., 2004). BBFs and dipolarizations follow the rapid reconfiguration of midtail region, $-30 < X_{GSM} < -15$ R_E (where R_E ~6,371 km is Earth's radius), where x lines drive explosive nightside energy release (e.g., Runov et al., 2012). The intense reconnection drives fast plasma flows that carry newly reconnected dipolar field lines (dipolarizing flux bundle; e.g., Liu et al., 2013) toward the inner magnetosphere. As the dipolarizing flux bundle is carried planetward, the leading edge of the flux tube steepens to form the dipolarization front (e.g., Runov et al., 2009). Force balance (e.g., Karlsson et al., 2015) and specific entropy content (e.g., Wolf et al., 2009) determine the dynamics of the BBF as it moves planetward, resulting in rapid braking of the flow between $-15 < X_{GSM} < -10$ R_E (e.g., Fu et al., 2012; Shiokawa et al., 1997) and in the generation of the substorm current wedge (e.g., Birn et al., 1999; Liu et al., 2013; Sergeev et al., 2014; Sun et al., 2013; Yao et al., 2012). During substorm intervals, BBFs contribute significantly to the mass, energy, and magnetic flux transport in the magnetotail (e.g., Angelopoulos et al., 1992; Liu et al., 2014; Schmid et al., 2016). Similar to Earth, fast plasma flows are expected in Mercury's magnetotail (e.g., Poh et al., 2017; Slavin et al., 2009; Sun et al., 2015) in coincidence with dipolarizations (e.g., Dewey, Slavin, et al., 2017; Sundberg et al., 2012), which are a consistent signature of substorm activity at Mercury (e.g., Sun et al., 2015).

Due to limitations imposed on the plasma instrument, MESSENGER cannot directly resolve plasma flows at Mercury. The spacecraft is three-axis stabilized so the thermal ion sensor, the Fast Imaging Plasma Spectrometer (FIPS; Andrews et al., 2007), cannot measure complete plasma distributions from which to determine flows. Furthermore, the FIPS sensor never observes the sunward or antisunward directions since the spacecraft's sunshade must continuously point sunward. Although bulk flow cannot be determined unambiguously from an incomplete plasma distribution, a subsonic flow would impart asymmetry on the distribution even with the flow direction outside the field of view (FOV). In this study, we apply statistical techniques to identify flows in Mercury's magnetotail by combining multiple intervals to construct more complete plasma distributions. We find that similar to Earth, dipolarizations at

Mercury are typically embedded in fast sunward flows. These are the first plasma flows measured at Mercury and illustrate the new capability of measuring statistical flows with FIPS.

4.3 Data Sources and Methodology

FIPS measures thermal and low-energy ions with energy per charge ratio (E/q) between 46 eV/e and 13 keV/e with a nominal energy scan time of 10 s. FIPS is comprised of an electrostatic analyzer and a time-of-flight chamber, in the latter of which ions stop by encountering a position-sensing microchannel plate (MCP). The stop MCP consists of an array of 64 by 64 pixels, each of which map to a location in the FIPS FOV, enabling the ions' incident direction to be determined. Combined, the MCP pixels allow for an instantaneous FOV imaging of ~1.4π sr about FIPS's boresight direction (the central axis of the FOV cone), although spacecraft obstructions reduce this to an effective ~1.15π sr. We also use magnetic field vector measurements collected by the Magnetometer (Anderson et al., 2007) at 20-Hz resolution. We display all MESSENGER observations in the Mercury solar magnetospheric (MSM) coordinate system, which is centered at Mercury's dipole center with X_{MSM} pointing sunward, Z_{MSM} pointing northward, and Y_{MSM} completing the right-handed system.

To identify fast flows, we analyze intervals containing dipolarizations selected by Dewey, Slavin, et al. (2017). Dewey, Slavin, et al. (2017) identified 538 dipolarizations coincident with energetic electron injections in Mercury's magnetotail from March 2013 to April 2015. An example of such an interval is shown in Figure 4.1a. During this 1-min interval, two dipolarizations are present: one beginning at ~08:26:12 and another at ~08:26:40. Both dipolarizations are coincident with enhancements in the Gamma-Ray Spectrometer count rate, corresponding to energetic electron injections (e.g., Baker et al., 2016; Lawrence et al., 2015).

The FIPS scan shaded in gray spans from the end of the first dipolarization to the beginning of the second. Figure 4.1b contains the scan's angular flux map: proton flux accumulated during this scan as a function of MSM angular direction. Figure 4.1c contains the scan's angular FOV map: the number of MCP pixels observing each direction of MSM-space. Examining this scan's angular maps, the FIPS FOV limitations are apparent. The sensor surveys only a fraction of the sky and cannot observe plasma traveling in neither the sunward (+X_{MSM}) nor antisunward (–X_{MSM}) directions. While the sensor cannot unambiguously determine bulk plasma flow from the incomplete plasma distribution of this single scan, there is more flux traveling in +X_{MSM} than −X_{MSM} (see guiding arrows), suggestive of a sunward plasma flow. There are several high-flux bins near −Z_{MSM}; however, these bins have high uncertainty as they are observed by few MCP pixels and correspond each to single proton counts.

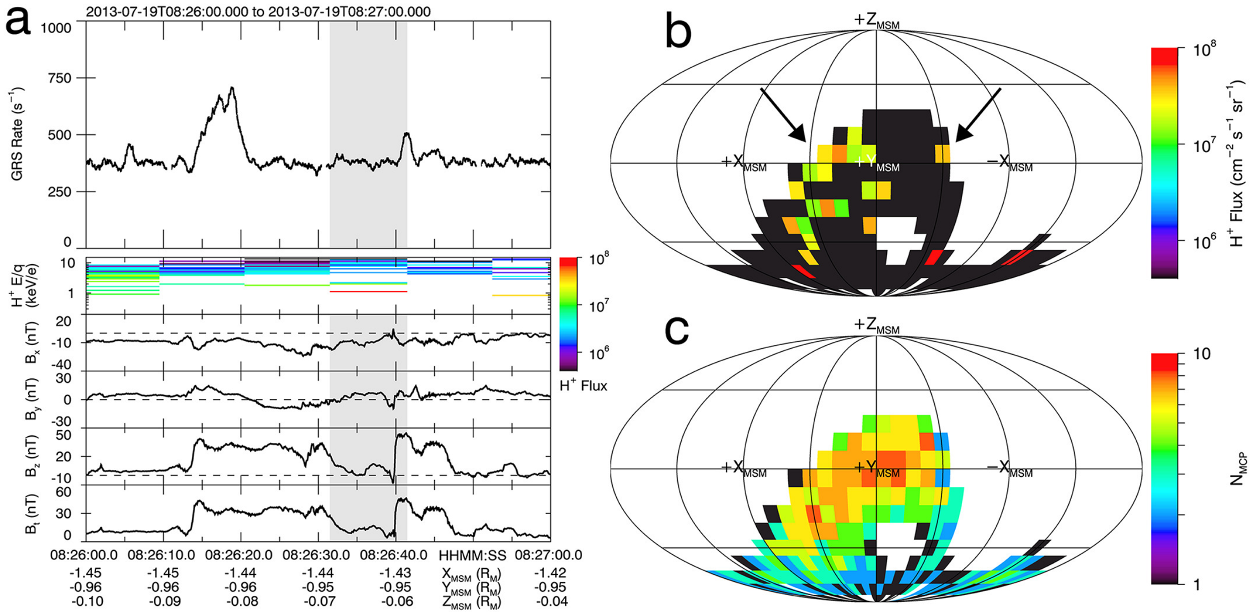

Figure 4.1. (a) Magnetic field dipolarizations and energetic electron injections identified by Dewey, Slavin, et al. (2017). (top) Gamma-Ray Spectrometer (GRS) count rate, (middle) Fast Imaging Plasma Spectrometer (FIPS) H$^+$ flux spectrogram, and (bottom) magnetic field components B_x, B_y, B_z, and B_t. Spacecraft position is listed below the bottom panel. (b) FIPS angular flux map corresponding to the energy scan shaded in gray in (a). Color bins have nonzero flux as indicated by the upper color bar. (c) Angular field-

of-view (FOV) map of the same scan. The number of microchannel plate (MCP) pixels sampling each region of Mercury solar magnetospheric space (MSM) is indicated by the lower color bar. For both maps, the white color indicates regions outside the FOV.

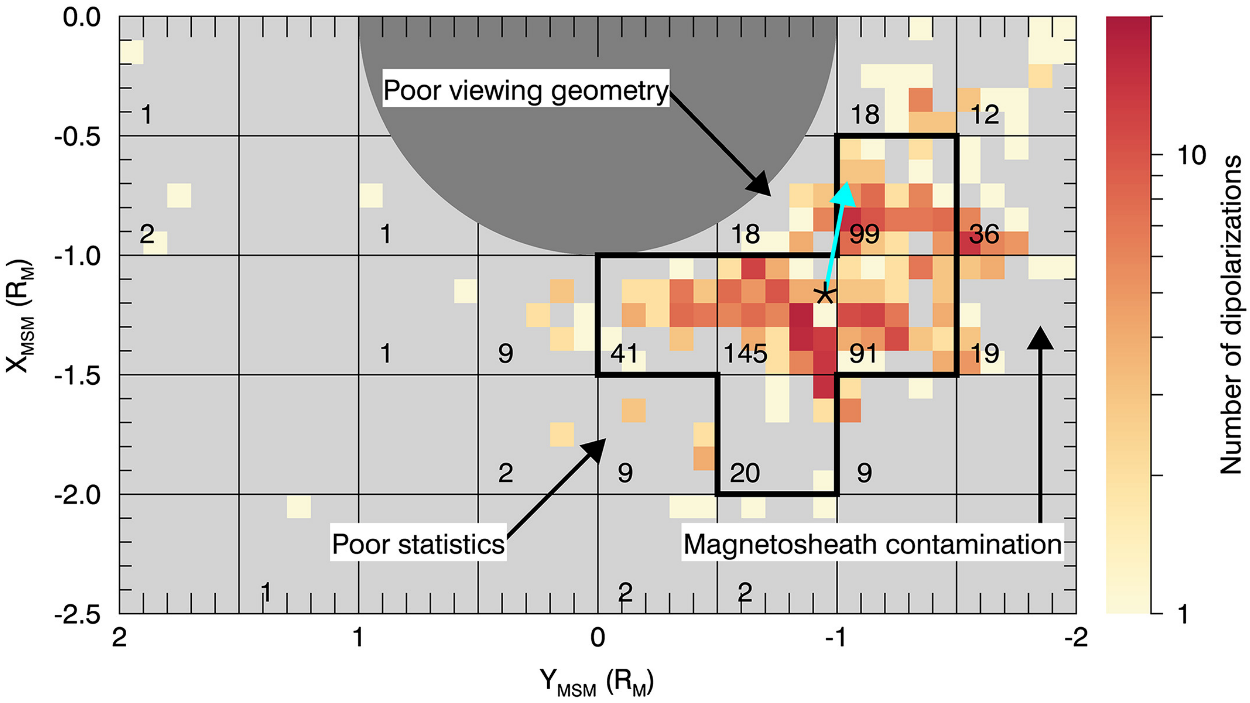

Figure 4.2. Equatorial distribution of dipolarizations identified by Dewey, Slavin, et al. (2017). The color bar indicates the number of dipolarizations within each (0.1 R_M)^2 bin; the light gray color corresponds to no dipolarizations. The number of dipolarizations within each (0.5 R_M)^2 box is listed in the box's lower-left corner. The thick black line outlines the region used for statistical analysis. For the selected dipolarizations, the star denotes the average spacecraft location and the cyan arrow points in the statistical equatorial flow direction. The dark gray region marks Mercury's surface. Annotations are discussed in the text.

Since a single FIPS scan has insufficient FOV coverage to determine plasma flows unambiguously, we construct composite plasma distributions by combining multiple FIPS measurements. Of the 538 Dewey, Slavin, et al. (2017) dipolarizations, we select 387 for statistical analysis. Figure 4.2 contains the equatorial distribution of all dipolarizations. For our analysis, we exclude regions near the magnetopause ($Y_{MSM} < -1.5$ R_M, where R_M ~2,440 km is Mercury's radius) to avoid contamination from the magnetosheath, regions close to the planet with poor viewing geometry (i.e., boresight pointing does not vary significantly across these events) to avoid biasing the composite distribution, and regions with too few events (<10 dipolarizations) to avoid introducing outliers due to small geographic sample size. Of the 396 dipolarizations within the resulting region of interest (outlined by a thick black line), we exclude nine during which FIPS operated outside of its nominal mode.

To combine multiple FIPS scans into a composite plasma distribution, we (1) construct a three-dimensional spherical velocity phase space in MSM coordinates, (2) select all protons from the scans with corresponding MCP pixel location, (3) determine the velocity space location of each proton, (4) weigh each proton's phase space density (PSD) by the ratio of the solid angle of the MCP pixel that recorded it to the accumulated solid angle of all MCP pixels during that scan that observed that velocity space location, (5) add the weighted PSDs to velocity space, and (6) normalize the accumulated PSD at each velocity space location by the number of scans that observed that location. This procedure can be written as

$$F(v,\theta,\phi) = \frac{1}{N(\theta,\phi)} \sum_{i=1}^{N(\theta,\phi)} \left[\sum_{j} \left(\Omega_{ij}(\theta,\phi) \sum_{k} f_{ijk}(v) \right) \Big/ \sum_{j} \Omega_{ij}(\theta,\phi) \right]$$

where (v,θ,ϕ) are typical spherical coordinates; $F(v,\theta,\phi)$ is the averaged PSD at velocity space location (v,θ,ϕ); $N(\theta,\phi)$ is the number of scans that observed (θ,ϕ), indexed by i; $\Omega_{ij}(\theta,\phi)$ is the solid angle of MCP pixel number j that observed (θ,ϕ) during scan i; and $f_{ijk}(v)$ is the PSD of proton number k that has velocity (v) recorded by MCP pixel j during scan i. Combining many FIPS scans with variable boresight pointing will generate a complete three-dimensional plasma distribution except for the sunshade-blocked conic regions near ±X_{MSM}. Plasma flows along ±Y_{MSM} and ±Z_{MSM} can be determined unambiguously from this composite distribution, while flows along ±X_{MSM} can be determined so long as they are sufficiently subsonic.

A composite plasma distribution from the 387 dipolarizations is shown in Figure 4.3. For this distribution, we combine all FIPS scans that occur in the 1 s before each dipolarization front midpoint. With a 1-s selection window, most dipolarizations contribute one FIPS scan to the composite distribution; however, ~10% contribute two as one scan ends and another begins within the window, for a total of 424 scans. Clear anisotropies are observed in the angular flux map (Figure 4.3a). While $\pm X_{MSM}$ are not observed directly, there is greater flux traveling in $+X_{MSM}$ (yellow/orange) than $-X_{MSM}$ (blue) surrounding the unobserved regions. There are bins with low flux (black) about both $+X_{MSM}$ and $-X_{MSM}$; however, these bins have high uncertainty as they are observed by few MCP pixels (Figure 4.3b). The $\pm X_{MSM}$ anisotropy is also observed away from the X_{MSM}-Y_{MSM} plane. In the region between the X_{MSM}-Y_{MSM} plane and $-Z_{MSM}$, for example, greater flux is traveling in $+X_{MSM}$ (green) than $-X_{MSM}$ (blue). There is also clear anisotropy between $\pm Z_{MSM}$.

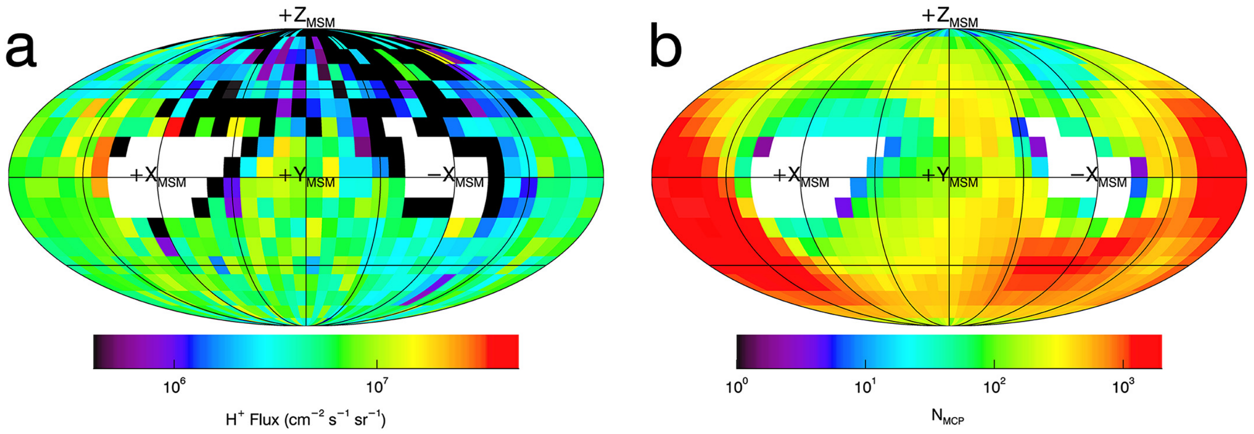

Figure 4.3. Composite plasma distribution of the 387 dipolarizations. (a) Angular flux map in the same format as Figure 4.1b. (b) Angular field-of-view map in the same format as Figure 4.1c. The white color indicates unobserved regions.

Since the $\pm X_{MSM}$ anisotropy is observed at all Z_{MSM} in the composite plasma distribution, sunward plasma flows are sufficiently subsonic to determine numerically. Calculating the moments (e.g., Paschmann et al., 1998) yields a proton density n_p of 0.60 ± 0.03 cm^{-3}, a sunward velocity v_x of 136 ± 14 km/s, a duskward velocity v_y of−60 ± 25 km/s, a northward velocity v_z of −140 ± 18 km/s, and a proton temperature T_p of 38.6 ± 0.9 MK. We evaluate uncertainties using both Monte Carlo and subsampling techniques. In the former, we perturb the PSD at each velocity space location by a random value from a normal distribution multiplied by that location's propagated Poisson error. In the latter, we randomly select 10% of the scans and construct a new composite plasma distribution. After generating new plasma distributions, we compute the new plasma moments. We repeat each technique with 5,000 iterations to form probability distributions for each plasma moment for each technique. For Monte Carlo, a distribution's spread represents that moment's instrument error, while for subsampling, it represents that moment's sampling error. We find that sampling error dominates instrument error.

We use a software model of the FIPS sensor (Dewey, Raines, & Tracy, 2017) to correct the plasma moments for the unobserved regions of the composite plasma distribution. The model simulates the sensor's response to a drifting Maxwellian plasma distribution. The model uses an input proton density, bulk velocity, temperature, and time-accurate pointing information to determine the PSD at each MCP pixel. Following the same procedure as for the composite plasma distribution, multiple intervals are combined and the plasma moments are calculated. Using this technique, we estimate that the in situ plasma in Figure 4.3 is most likely $n_p = 0.74 \pm 0.05$ cm^{-3}, $v_x = 225 \pm 25$ km/s, $v_y = -58 \pm 27$ km/s, $v_z = -147 \pm 18$ km/s, and $T_p = 46.4 \pm 1.7$ MK. The moments determined directly from the composite plasma distribution underestimate n_p by only ~20%, v_x by ~40%, and T_p by ~17% while capturing v_y and v_z well. At a temperature of T_p = 46.4 MK, the thermal proton speed is ~875 km/s, indicating the flow is subsonic with a Mach number of ~0.3.

4.4 Results

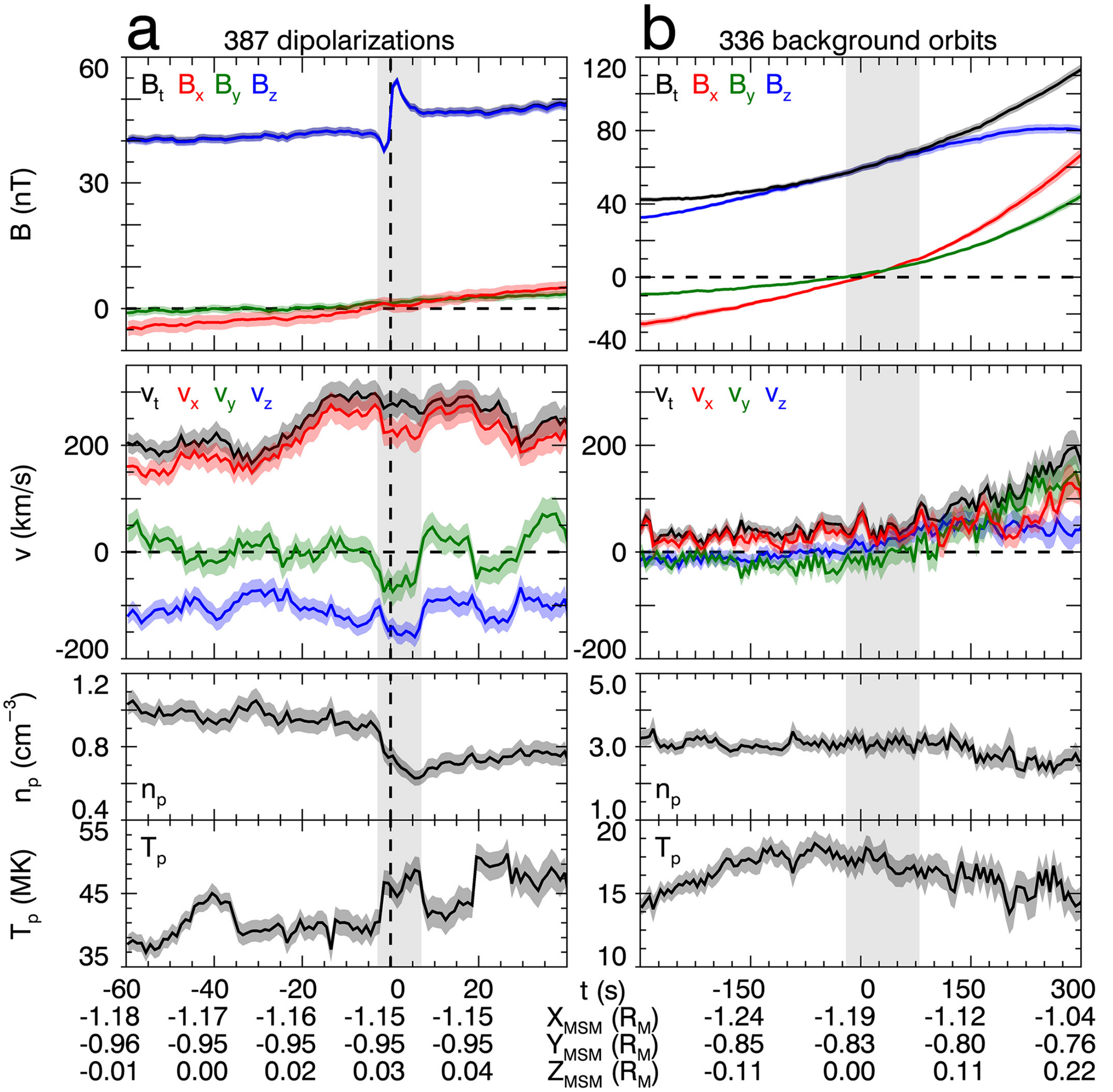

Figure 4.4. (a) Statistical plasma and magnetic field observations from the 387 dipolarization intervals. (top) Magnetic field components, (middle) plasma flow components, and (bottom) proton density and temperature. Average spacecraft location is listed below the bottom panel. The light gray shaded region spans the statistical dipolarization. (b) Statistical observations from 336 background orbits, in the same format as (a). The light gray shaded region corresponds to the same range of Z_{MSM} as in (a).

To examine the evolution of the plasma flows about the 387 selected dipolarizations, we perform superposed epoch analysis on the plasma and magnetic field observations, displayed in

Figure 4.4a. Each dipolarization is aligned at the midpoint of its dipolarization front (defined to be $t = 0$). For each 1-s time step $-60 < t < +40$ s, we collect the magnetic field, spacecraft location, and FIPS scans within the time window for each dipolarization. For each step, the average magnetic field and spacecraft location are calculated, and the plasma density, flow, and temperature are determined using the statistical technique described in section 4.3. The composite plasma distribution from Figure 4.3 corresponds to the time of the dashed vertical line in Figure 4.4a.

Typical dipolarization signatures are immediately apparent. In B_z, a decrease in the magnetic field beginning at $t = -3$ s followed by a sharp, step-like increase to $t = +2$ s marks the dipolarization front, while afterward, the decaying B_z to a near-constant value ($+2 < t < +7$ s) marks the dipolarizing flux bundle. The gray shaded region spans from the start of the dipolarization front to the end of the dipolarizing flux bundle. During this interval, the proton density decreases ~30% and the proton temperature increases ~20%. The spacecraft is located, on average, in the postmidnight sector at local time ~2.7 hr and radial distance ~1.5 R_M, and its northward motion through the plasma sheet can be seen in the magnetic field components. B_x and B_y have small amplitudes throughout the interval but both reverse sign, consistent with the averaged spacecraft motion from $-Z_{MSM}$ to $+Z_{MSM}$, indicating a current sheet crossing. These composite plasma and magnetic field signatures are similar to previous studies at Mercury (Sun et al., 2017; Sundberg et al., 2012), which is not surprising given the use of dipolarization intervals from Dewey, Slavin, et al. (2017).

A flow enhancement is observed coincident with the statistical dipolarization. Throughout the interval, v_x dominates the total flow speed v_t, while v_y remains near 0 km/s and $v_z$remains negative. Prior to the dipolarization ($-60 < t < -30$ s), each velocity component remains steady with $v_x \sim 160 \pm 22$ km/s, $v_y \sim 0 \pm 25$ km/s, $v_z \sim -100 \pm 20$ km/s, and $v_t \sim 200 \pm 18$ km/s. From $-30 < t < -15$ s, v_x increases steadily to 276 ± 26 km/s bringing v_t to 294 ± 25 km/s. The flow speed remains at ~300 km/s until after the dipolarization ($t > +25$ s). During the dipolarization, the flow diverts azimuthally with v_t remaining constant while the magnitude of v_x decreases (228 ± 25 km/s) and the magnitude of v_y increases (-74 ± 27 km/s). The cyan arrow in Figure 4.2 marks the equatorial direction of the flow during the statistical dipolarization. Throughout the interval, v_z remains negative, reaching a maximum absolute value of -159 ± 20 km/s within the dipolarization at $t \sim +6$ s.

For comparison, we perform the same statistical analysis on quiescent intervals, shown in Figure 4.4b. We select 336 orbits between 1 March 2013 and 30 April 2015 that cross the magnetic equator within the region of interest (see Figure 4.2), contain no dipolarization-injection events (Dewey, Slavin, et al., 2017), and during which FIPS operated nominally. We align each orbit at the current sheet crossing ($t = 0$) and determine plasma and magnetic field parameters at 5-s resolution for times $-300 < t < +300$ s. We select this time interval as it corresponds to the typical time required for the spacecraft to traverse $|Z_{MSM}| < 0.5\ R_M$, the region Dewey, Slavin, et al. (2017) used to identify dipolarizations. The shaded gray interval ($-20 < t < +80$ s) corresponds to the same averaged Z_{MSM} traveled by the spacecraft as in Figure 4.4a. During this interval, plasma conditions remain constant to within uncertainty. The plasma sheet is denser ($n_p \sim 3.10 \pm 0.26$ cm^{-3}), colder ($T_p \sim 17.0 \pm 0.9$ MK), and more stagnant ($v_x \sim 38 \pm 16$ km/s, $v_y \sim -7 \pm 23$ km/s, $v_z \sim 20 \pm 16$ km/s, $v_t \sim 47 \pm 17$ km/s) compared to the averaged dipolarization and agrees well with previous typical plasma sheet proton densities and temperatures (e.g., Gershman et al., 2014). While the plasma moments show no significant trends within the shaded interval, the magnetic field is dominated by the spacecraft's motion through the planetary dipole field.

4.5 Discussion and Conclusions

We use statistical techniques to determine mean proton flows in the plasma sheet during substorm and quiescent intervals using the FIPS data. We combine plasma observations from 387 dipolarization intervals and 336 background intervals to produce composite plasma distributions from which flows are inferred. During dipolarizations, the flow is ~300 km/s and predominately in the $+X_{MSM}$ direction. By comparison, the convection speed during more quiescent intervals is ~50 km/s. The dipolarization-associated flows are similar to those during dipolarizations at Earth. Liu et al. (2014), for example, found v_x to be typically ~100 km/s greater during a dipolarization than the interval preceding it.

While v_x is enhanced during dipolarizations, it increases in magnitude steadily prior to the dipolarizations, which may be associated with enhanced convection during the substorm growth phase. During the growth phase at Earth, enhanced convection driven by reconnection at the magnetopause pulls closed flux from the inner tail to the dayside reconnection region (Hsieh & Otto, 2014), which results in tail current sheet thinning (e.g., Gordeev et al., 2017; Sun et al., 2017). Alternatively, this signature could be due protons reflected by the dipolarization front (e.g., Zhou et al., 2010) or an effect of averaging successive dipolarizations, as in Figure 4.1a. Nevertheless, an increase in v_x prior to a dipolarization is typically observed at Earth (e.g., Runov et al., 2011). Finally, the negative v_z during dipolarizations may be combination of effects. It could be related to the spacecraft (located at $Z_{MSM} \gtrsim 0$) observing current sheet thinning or the contraction of stretched field lines. It could also be related to the asymmetry between Mercury's loss cones, in which more particles are lost in the southern hemisphere, resulting in a net southward streaming and indicating particle loss. Sampling bias is unlikely to cause the v_z signature since the statistical composite technique accounts for FOV bias.

Given an average plasma sheet $B_z \sim 45$ nT and $v_x \sim 250$ km/s, the implied electric field during dipolarizations is ~11 ± 1 mV/m. If we assume a single cross-tail flow channel width of ~0.2 R_M (scaled from the ~1–2 R_E at Earth), the additional cross-magnetospheric potential due to a dipolarization would be ~5.4 ± 0.5 kV and the typical flux transported by a dipolarization would be ~0.06 ± 0.01 MWb. In contrast, from the statistical background observations, the typical cross-tail electric field is ~2.4 ± 1.2 mV/m, corresponding to a cross-tail potential of ~23 kV, which is consistent with previous estimates at Mercury (DiBraccio et al., 2015; Jasinski et al., 2017; Slavin et al., 2010). For substorm intervals, Imber and Slavin (2017) found that loading typically increases the lobe magnetic content by ~0.6 MWb over a period of ~100 s. This rate of loading corresponds to a difference in the dayside and tail reconnection rates of ~6 kV. While a single dipolarization can account for the reconnection rate difference, numerous dipolarizations (~10) are required to unload the magnetotail. Dipolarizations at Mercury, therefore, are associated with strong convection and transport, although multiple are expected to occur during Mercury's substorm cycle.

Without reliable spatial gradients, the flow braking of the statistical dipolarization cannot be determined. As the dipolarization continues to move sunward, however, it is expected to encounter strong braking due to increased magnetic pressure gradients from the planetary dipole field (e.g., Shiokawa et al., 1997) where the flow's rapid braking and flux pile-up develop the substorm current wedge (e.g., Kepko et al., 2015). Using the magnetic field strength of the statistical dipolarization and a dipole description of Mercury's inner magnetotail (appropriate for radial distances $\lesssim 1.5\ R_M$; Rong et al., 2018), we estimate substantial braking to occur at radial distances $<1.3\ R_M$. If the negative v_z signature indicates particle loss as discussed above, the reduction in specific entropy of the dipolarizing flux tube would result in a braking region even closer to the planet (e.g., Wolf et al., 2009), with some fast flows possibly reaching Mercury's nightside surface. However, observations suggest that the typical dipolarization diverts about the planet (cyan arrow in Figure 4.2) such that it may not encounter steep gradients in the field and may instead propagate some distance before stopping. Without observations within the braking region, we cannot reliably estimate the typical dipolarization's contribution to the substorm current wedge, although the expectation that multiple dipolarizations are required to unload the magnetotail is similar to the wedgelet model at Earth (Liu et al., 2013). Interestingly, and requiring future investigation, a sustained series of dipolarizations compressing the nightside inner magnetosphere could produce induction effects in Mercury's core, similar to those induced on the dayside during strong solar wind forcing conditions (Slavin et al., 2014), which would cause the braking region to move tailward and possibly divert flows. Understanding the dipolarization flow speed as a function of downtail distance (e.g., Baumjohann et al., 1990) will help to refine these estimates; future observations from BepiColombo will be of particular value.

4.6 Acknowledgments

This research is supported by NASA's Discovery Data Analysis Program (NNX16AJ03G and NNX15AL01G), Living With a Star Program (NNX16AJ67G), Heliophysics Supporting Research Program (NNX15AJ68G), and Earth and Space Science Fellowship Program (80NSSC17K0493). All MESSENGER data used in this study are available from the NASA Planetary Data System.

4.7 References

Anderson, B. J., Acuña, M. H., Lohr, D. A., Scheifele, J., Raval, A., Korth, H., & Slavin, J. A. (2007). The magnetometer instrument on MESSENGER. *Space Science Reviews*, **131**(1-4), 417–450. https://doi.org/10.1007/s11214-007-9246-7

Andrews, G. B., Zurbuchen, T. H., Mauk, B. H., Malcom, H., Fisk, L. A., Gloeckler, G., et al. (2007). The energetic particle and plasma spectrometer instrument on the MESSENGER spacecraft. *Space Science Reviews*, **131**(1-4), 523–556. https://doi.org/10.1007/s11214-007-9272-5

Angelopoulos, V., Baumjohann, W., Kennel, C. F., Coroniti, F. V., Kivelson, M. G., Pellat, R., et al. (1992). Bursty bulk flows in the inner central plasma sheet. *Journal of Geophysical Research*, **97**(A4), 4027–4039. https://doi.org/10.1029/91JA02701

Baker, D. N., Dewey, R. M., Lawrence, D. J., Goldsten, J. O., Peplowski, P. N., Korth, H., et al. (2016). Intense energetic electron flux enhancements in Mercury's magnetosphere: An integrated view with high-resolution observations from MESSENGER. *Journal of Geophysical Research: Space Physics*, **121**, 2171–2184. https://doi.org/10.1002/2015JA021778

Baumjohann, W., Paschmann, G., & Luhr, H. (1990). Characteristics of high-speed ion flows in the plasma sheet. *Journal of Geophysical Research*, **95**, 3801–3809. https://doi.org/10.1029/JA095iA04p03801

Birn, J., Hesse, M., Haerendel, G., Baumjohann, W., & Shiokawa, K. (1999). Flow braking and the substorm current wedge. *Journal of Geophysical Research*, **104**(19), 19,895–19,904. https://doi.org/10.1029/1999JA900173

Dewey, R. M., Raines, J. M., & Tracy, P. J. (2017). Interpreting FIPS density, temperature, and pressure, NASA Planetary Data System, MESS-E/V/H/SW-EPPS-3-FIPS-DDR-V2.0.

Dewey, R. M., Slavin, J. A., Raines, J. M., Baker, D. N., & Lawrence, D. J. (2017). Energetic electron acceleration and injection during dipolarization events in Mercury's magnetotail. *Journal of Geophysical Research: Space Physics*, **122**, 12,170–12,188. https://doi.org/10.1002/2017JA024617

DiBraccio, G. A., Slavin, J. A., Boardsen, S. A., Anderson, B. J., Korth, H., Zurbuchen, T. H., et al. (2013). MESSENGER observations of magnetopause structure and dynamics at Mercury. *Journal of Geophysical Research: Space Physics*, **118**, 997–1008. https://doi.org/10.1002/jgra.50123

DiBraccio, G. A., Slavin, J. A., Raines, J. M., Gershman, D. J., Tracy, P. J., Boardsen, S. A., et al. (2015). First observations of Mercury's plasma mantle by MESSENGER. *Geophysical Research Letters*, **42**, 9666–9675. https://doi.org/10.1002/2015GL065805

Forsyth, C., Rae, I. J., Coxon, J. C., Freeman, M. P., Jackman, C. M., Gjerloev, J., & Fazakerley, A. N. (2015). A new technique for determining substorm onsets and phases from indices of the electrojet (SOPHIE). *Journal of Geophysical Research: Space Physics*, **120**, 10,592–10,606. https://doi.org/10.1002/2015JA021343

Fu, H. S., Khotyaintsev, Y. V., Vaivads, A., André, M., & Huang, S. Y. (2012). Occurrence rate of earthward-propagating dipolarization fronts. *Geophysical Research Letters*, **39**, L10101. https://doi.org/10.1029/2012GL051784

Gershman, D. J., Slavin, J. A., Raines, J. M., Zurbuchen, T. H., Anderson, B. J., Korth, H., et al. (2014). Ion kinetic properties in Mercury's premidnight plasma sheet. *Geophysical Research Letters*, **41**, 5740–5747. https://doi.org/10.1002/2014GL060468

Gordeev, E., Sergeev, V., Merkin, V., & Kuznetsova, M. (2017). On the origin of plasma sheet reconfiguration during the substorm growth phase. *Geophysical Research Letters*, **44**, 8696–8702. https://doi.org/10.1002/2017GL074539

Hsieh, M.-S., & Otto, A. (2014). The influence of magnetic flux depletion on the magnetotail and auroral morphology during the substorm growth phase. *Journal of Geophysical Research: Space Physics*, **119**, 3430–3443. https://doi.org/10.1002/2013JA019459

Hsu, T.-S., & McPherron, R. L. (2000). The characteristics of storm-time substorms and non-storm substorms, Proceedings of the International Conference on Substorms (ICS-5), Eur. Space Agency, Spec. Publ., ESA SP-443, 439.

Imber, S. M., & Slavin, J. A. (2017). MESSENGER observations of magnetotail loading and unloading: Implications for substorms at Mercury. *Journal of Geophysical Research: Space Physics*, **122**, 11,402–11,412. https://doi.org/10.1002/2017JA024332

Jasinski, J. M., Slavin, J. A., Raines, J. M., & DiBraccio, G. A. (2017). Mercury's solar wind interaction as characterized by magnetospheric plasma mantle observations with MESSENGER. *Journal of Geophysical Research: Space Physics*, **122**, 12,153–12,169. https://doi.org/10.1002/2017JA024594

Karlsson, T., Hamrin, M., Nilsson, H., Kullen, A., & Pitkänen, T. (2015). Magnetic forces associated with bursty bulk flows in Earth's magnetotail. *Geophysical Research Letters*, **42**, 3122–3128. https://doi.org/10.1002/2015GL063999

Lawrence, D. J., Anderson, B. J., Baker, D. N., Feldman, W. C., Ho, G. C., Korth, H., et al. (2015). Comprehensive survey of energetic electron events in Mercury's magnetosphere with data from the MESSENGER gamma-ray and neutron spectrometer. *Journal of Geophysical Research: Space Physics*, **120**, 2851–2876. https://doi.org/10.1002/2014JA020792

Lindsay, S. T., James, M. K., Bunce, E. J., Imber, S. M., Korth, H., Martindale, A., & Yeoman, T. K. (2016). MESSENGER X-ray observations of magnetosphere-surface interaction on the nightside of Mercury. *Planetary and Space Science*, **125**, 72–79. https://doi.org/10.1016/j.pss.2016.03.005

Liu, J., Angelopoulos, V., Runov, A., & Zhou, X.-Z. (2013). On the current sheets surrounding dipolarizing flux bundles in the magnetotail: The case for wedgelets. *Journal of Geophysical Research: Space Physics*, **118**, 2000–2020. https://doi.org/10.1002/jgra.50092

Liu, J., Angelopoulos, V., Zhou, X.-Z., & Runov, A. (2014). Magnetic flux transport by dipolarizing flux bundles. *Journal of Geophysical Research: Space Physics*, **119**, 909–926. https://doi.org/10.1002/2013JA019395

Ohtani, S., Shay, M. A., & Mukai, T. (2004). Temporal structure of the fast convective flow in the plasma sheet: Comparison between observations and two-fluid simulations. *Journal of Geophysical Research*, **109**, A03210. https://doi.org/10.1029/2003JA010002

Paschmann, G., Fazakerley, A. N., & Schwartz, S. J. (1998). Moments of plasma velocity distributions, Analysis Methods for Multi-Spacecraft Data, ISSI Scientific Report, SR-001.

Poh, G., Slavin, J. A., Jia, X., Raines, J. M., Imber, S. M., Sun, W. J., et al. (2017). Coupling between Mercury and its nightside magnetosphere: Cross-tail current sheet asymmetry and substorm current wedge formation. *Journal of Geophysical Research: Space Physics*, **122**, 8419–8433. https://doi.org/10.1002/2017JA024266

Rong, Z. J., Ding, Y., Slavin, J. A., Zhong, J., Poh, G., Sun, W. J., et al. (2018). The magnetic field structure of Mercury's magnetotail. *Journal of Geophysical Research: Space Physics*, **123**, 548–566. https://doi.org/10.1002/2017JA024923

Runov, A., Angelopoulos, V., Sitnov, M. I., Sergeev, V. A., Bonnell, J., McFadden, J. P., et al. (2009). THEMIS observations of an earthward propagating dipolarization front. *Geophysical Research Letters*, **36**, L14106. https://doi.org/10.1029/2009GL038980

Runov, A., Angelopoulos, V., & Zhou, X.-Z. (2012). Multipoint observations of dipolarization front formation by magnetotail reconnection. *Journal of Geophysical Research*, **117**, A05230. https://doi.org/10.1029/2011JA017361

Runov, A., Angelopoulos, V., Zhou, X. Z., Zhang, X. J., Li, S., Plaschke, F., & Bonnell, J. (2011). A THEMIS multicase study of dipolarization fronts in the magnetotail plasma sheet. *Journal of Geophysical Research*, **116**, A05216. https://doi.org/10.1029/2010JA016316

Schmid, D., Nakamura, R., Volwerk, M., Plaschke, F., Narita, Y., Baumjohann, W., et al. (2016). A comparative study of dipolarization fronts at MMS and Cluster. *Geophysical Research Letters*, **43**, 6012–6019. https://doi.org/10.1002/2016GL069520

Sergeev, V. A., Chernyaev, I. A., Angelopoulos, V., Runov, A. V., & Nakamura, R. (2014). Stopping flow bursts and their role in the generation of the substorm current wedge. *Geophysical Research Letters*, **41**, 1106–1112. https://doi.org/10.1002/2014GL059309

Shiokawa, K., Baumjohann, W., & Haerendel, G. (1997). Braking of high-speed flows in the near-Earth tail. *Geophysical Research Letters*, **24**(10), 1179–1182. https://doi.org/10.1029/97GL01062

Siscoe, G. L., Ness, N. F., & Yeates, C. M. (1975). Substorms on Mercury? *Journal of Geophysical Research*, **80**(31), 4359–4363. https://doi.org/10.1029/JA080i031p04359

Slavin, J. A., Acuna, M. H., Anderson, B. J., Baker, D. N., Benna, M., Boardsen, S. A., et al. (2009). MESSENGER observations of magnetic reconnection in Mercury's magnetosphere. *Science*, **324**(5927), 606–610. https://doi.org/10.1126/science.1172011

Slavin, J. A., Anderson, B. J., Baker, D. N., Benna, M., Boardsen, S. A., Gloeckler, G., et al. (2010). MESSENGER observations of extreme loading and unloading of Mercury's magnetic tail. *Science*, **329**(5992), 665–668. https://doi.org/10.1126/science.1188067

Slavin, J. A., DiBraccio, G. A., Gershman, D. J., Imber, S. M., Poh, G. K., Raines, J. M., et al. (2014). MESSENGER observations of Mercury's dayside magnetosphere under extreme solar wind conditions. *Journal of Geophysical Research: Space Physics*, **119**, 8087–8116. https://doi.org/10.1002/2014JA020319

Sun, W. J., Fu, S. Y., Parks, G. K., Liu, J., Yao, Z. H., Shi, Q. Q., et al. (2013). Field-aligned currents associated with dipolarization fronts. *Geophysical Research Letters*, **40**, 4503–4508. https://doi.org/10.1002/grl.50902

Sun, W. J., Fu, S. Y., Wei, Y., Yao, Z. H., Rong, Z. J., Zhou, X. Z., et al. (2017). Plasma sheet pressure variations in the near-Earth magnetotail during substorm growth phase: THEMIS observations. *Journal of Geophysical Research: Space Physics*, **122**, 12,212–12,228. https://doi.org/10.1002/2017JA024603

Sun, W. J., Raines, J. M., Fu, S. Y., Slavin, J. A., Wei, Y., Poh, G. K., et al. (2017). MESSENGER observations of the energization and heating of protons in the near-Mercury magnetotail. *Geophysical Research Letters*, **44**, 8149–8158. https://doi.org/10.1002/2017GL074276

Sun, W.-J., Slavin, J. A., Fu, S., Raines, J. M., Sundberg, T., Zong, Q. G., et al. (2015). MESSENGER observations of Alfvénic and compressional waves during Mercury's substorms. *Geophysical Research Letters*, **42**, 6189–6198. https://doi.org/10.1002/2015GL065452

Sun, W.-J., Slavin, J. A., Fu, S., Raines, J. M., Zong, Q. G., Imber, S. M., et al. (2015). MESSENGER observations of magnetospheric substorm activity in Mercury's near magnetotail. *Geophysical Research Letters*, **42**, 3692–3699. https://doi.org/10.1002/2015GL064052

Sundberg, T., Slavin, J. A., Boardsen, S. A., Anderson, B. J., Korth, H., Ho, G. C., et al. (2012). MESSENGER observations of dipolarization events in Mercury's magnetotail. *Journal of Geophysical Research*, **117**, A00M03. https://doi.org/10.1029/2012JA017756

Wolf, R. A., Wan, Y., Xing, X., Zhang, J.-C., & Sazykin, S. (2009). Entropy and plasma sheet transport. *Journal of Geophysical Research*, **114**, A00D05. https://doi.org/10.1029/2009JA014044

Yao, Z. H., Pu, Z. Y., Fu, S. Y., Angelopoulos, V., Kubyshkina, M., Xing, X., et al. (2012). Mechanism of substorm current wedge formation: THEMIS observations. *Geophysical Research Letters*, **39**, L13102. https://doi.org/10.1029/2012GL052055

Zhou, X.-Z., Angelopoulos, V., Sergeev, V. A., & Runov, A. (2010). Accelerated ions ahead of earthward propagating dipolarization fronts. *Journal of Geophysical Research*, **115**, A00I03. https://doi.org/10.1029/2010JA015481

CHAPTER V. MESSENGER Observations of Flow Braking and Flux Pileup of Dipolarizations in Mercury's Magnetotail: Evidence for Current Wedge Formation

This chapter is taken from Dewey, R. M., Slavin, J. A., Raines, J. M., Azari, A. R., & Sun, W. (2020). MESSENGER observations of flow braking and flux pileup of dipolarizations in Mercury's magnetotail: Evidence for current wedge formation. *Journal of Geophysical Research: Space Physics,* (submitted). We have performed minor edits for formatting consistency with the other chapters.

5.1 Abstract

Similar to Earth, Mercury's magnetotail experiences frequent dipolarization of the magnetic field. These rapid (~2 s) increases in the northward component of the tail field (ΔB_z ~ 30 nT) at Mercury are associated with fast sunward flows (~200 km/s) that enhance local magnetic field convection, similar to dipolarizations in Earth's magnetotail. Differences between the two magnetospheres, namely Mercury's smaller spatiotemporal scales and lack of an ionosphere, result in differences in the dynamics of dipolarizations in these magnetotails. At Earth, for example, the braking of these fast flows as they approach the inner magnetosphere accumulates magnetic flux and plays an important role in developing the substorm current wedge. At Mercury, flow braking and flux pileup in the near magnetotail remain open questions. We develop an automated algorithm to identify dipolarizations in the magnetic field time series, allowing for statistical examination of flow braking and flux pileup in Mercury's magnetotail.

We find that near the inner edge of the plasma sheet, steep magnetic pressure gradients cause substantial braking of the fast dipolarization flows. The dipolarization frequency and sunward flow speed decrease significantly within a region ~500 km thick located at ~900 km altitude above Mercury's local midnight surface. Due to the close proximity of the braking region to the planet, we estimate ~10-20% of dipolarizations may reach the nightside surface of the planet. The remaining dipolarizations exhibit prolonged statistical flux pileup within the braking region similar to large-scale dipolarization of Earth's inner magnetosphere. The existence of flow braking and flux pileup at Mercury indicates a current wedge may form, although the limitations imposed by the small magnetospheric scales and the resistive regolith that covers Mercury's conducting core require the braking of multiple, continuous dipolarizations for current wedge formation.

5.2. Introduction

Dipolarizations are common to the magnetotails of both Earth and Mercury. A product of intense nightside reconnection, dipolarizations represent newly-closed, more dipolar field lines that are carried planetward by fast reconnection outflows (e.g., Sitnov et al., 2009; Runov et al., 2012; Fu et al., 2013). Observed in situ, dipolarizations are identified by the sharp, step-like increase in the northward component of the magnetic field (known as the dipolarization front, e.g., Nakamura et al., 2002) that precedes the newly-reconnected flux tube (known as the dipolarizing flux bundle, Liu et al., 2013). Since dipolarizations are a result of reconnection between the low-density magnetotail lobes, they tend to be depleted in thermal plasma and embedded within fast sunward flows (e.g., Angelopoulos et al., 1992; Sergeev et al., 1996; Runov et al., 2015). Additional signatures of dipolarizations include an enhanced cross-tail electric field, enhanced thermal plasma temperature, and enhanced energetic particle flux compared to the surrounding plasma sheet (e.g., Runov et al., 2009; Runov et al. 2013).

At Earth, dipolarizations contribute major roles in mass and magnetic flux transport, particle acceleration, and substorm current wedge formation. Although individual dipolarizations are localized in their cross-tail extent (~1-3 R_E, where R_E is Earth's mean radius, 6,371 km), their faster sunward flow, stronger northward magnetic field, and enhanced cross-tail electric field compared to the surrounding plasma sheet result in dipolarizations transporting the majority of magnetic flux from the mid-tail to the near-tail, particularly during geomagnetically active intervals (Liu et al., 2014). As a dipolarization travels planetward, particles interacting with its magnetic structure, particularly those trapped by the local magnetic field gradients about the dipolarization front, can experience betatron and Fermi acceleration (e.g., Ashour-Abdalla et al., 2011; Birn et al., 2013; Gabrielse et al., 2016; Ukhorskiy et al., 2018). Only a small fraction of dipolarizations penetrate into the inner magnetosphere, with the majority of dipolarizations stopping near the inner edge of the plasma sheet (Shiokawa et al., 1997, Dubyagin et al., 2011; Ohtani et al., 2006). Near this boundary, dipolarizations brake due to steep magnetic pressure gradients, and their magnetic flux accumulates (or piles up) (Birn et al., 2011; Karlsson et al., 2015). As additional dipolarizations brake and accumulate, this flux pileup region can expand both azimuthally and downtail, resulting in a large-scale dipolarization of the near-tail region (e.g., Baumjohann et al., 1999; Birn et al., 2011; Birn et al., 2019; Merkin et al., 2019). The flux pileup structure is supported by the substorm current wedge, which diverts the cross-tail current into the ionosphere via field-aligned currents of the Region 1-sense (e.g., McPherron et al., 1973; Birn et al., 1999; Kepko et al., 2015a). While the exact mechanics by which dipolarizations (both small- and large-scale) establish and maintain the substorm current wedge, it has been the subject of considerable interest and debate. A current understanding is the “wedgelet” conceptual model in which the individual field-aligned current systems of many small-scale dipolarizations manifest into the substorm current wedge as the dipolarizations brake near the inner magnetosphere (e.g., Liu et al., 2013; Sun et al., 2013; Birn et al., 2019). In this understanding, the current wedge is not a single, monolithic current loop, but that its trending structure emerges from the complex interaction between individual dipolarization current systems.

Mercury possesses a terrestrial-like magnetosphere, but it operates at substantially smaller spatiotemporal scales, experiences stronger effects from magnetic reconnection, and couples to a different type of inner magnetospheric boundary than Earth’s magnetosphere. Mercury’s magnetosphere contains many of the same regions as Earth’s, including a closed dayside region and an extended magnetotail (see Korth et al., 2018 and Slavin et al., 2018 for comprehensive reviews). Mercury’s planetary magnetic field, however, is only ~1% the strength of Earth’s (e.g., Anderson et al., 2011), which when combined with the stronger upstream solar wind dynamic pressure at Mercury’s orbital location, results in a magnetosphere substantially smaller in both absolute and relative scales. For example, Mercury’s subsolar magnetopause stands at ~0.5 $R_M \approx$ 1,200 km altitude above the planet’s dayside surface (Winslow et al., 2013), where R_M is Mercury’s mean radius (2,440 km). By contrast, Earth’s subsolar magnetopause stands at ~10 $R_E \approx$ 64,000 km altitude (e.g., Shue et al., 1998). Furthermore, the cross-tail extent of Mercury’s magnetotail is ~4 $R_M \approx$ 10,000 km compared to Earth’s of ~40 $R_E \approx$ 255,000 km (Slavin et al., 2012; Rong et al., 2018; Kaymaz et al., 1992). Consequences of the small dimensions of Mercury’s magnetosphere include increased finite gyroradius effects (particularly for heavy ions of planetary origin), increased loss due to surface precipitation, and an increased fraction of the magnetosphere occupied by the planet (e.g., Ogilvie et al., 1997; Delcourt et al., 2003; Delcourt, 2013; Raines et al., 2014). Mercury's plasmapause, for example, would be located below the planet's surface due to the planet occupying a large fraction of the magnetosphere and the planet's slow ~59-day rotation. Mercury's magnetosphere also experiences stronger effects from magnetic reconnection. The lower solar wind Alfvén Mach number at Mercury's orbital location results in the formation of thick plasma depletion layers within Mercury's magnetosheath adjacent to the magnetopause (Gershman et al., 2013). These depletion layers allow for more frequent and stronger subsolar magnetopause reconnection that is less sensitive to the direction of the interplanetary magnetic field than at Earth (DiBraccio et al., 2013). Dayside reconnection powers Mercury's ~3 min Dungey cycle and many of the observed dynamics within the magnetosphere (e.g., Slavin et al., 2009; Slavin et al., 2010; Imber & Slavin, 2017; Slavin et al., 2018). Finally, Mercury's large conducting core plays a unique role in magnetospheric dynamics by acting as the magnetosphere's innermost boundary. Mercury lacks an ionosphere so it is expected that its large core (~2,000 km in radius) provides current-closure for static and/or large-scale field-aligned current systems (e.g., Jahunen & Kallio, 2004; Anderson et al., 2014). These current systems pass radially through the thin (~400 km) layer of resistive regolith to connect over the surface of the conducting core. Mercury's core also influences the magnetosphere's interaction with the solar wind. Changes in the solar wind dynamic pressure induce currents on the core's surface that modify the planet's magnetic moment to resist these changes (e.g., Slavin et al., 2014; Jia et al., 2015; Johnson et al., 2016; Jia et al., 2019). Although similar responsive currents may also be induced on the surface of Earth's core, these currents are substantially stronger at Mercury due to Mercury's relatively larger core and the core's close proximity to the magnetopause.

Given the similar topology between Mercury and Earth's magnetospheres and the dominance of magnetic reconnection in Mercury's dynamics, it is not surprising that dipolarizations are frequent to Mercury's magnetotail. Similar to those identified at Earth, dipolarizations at Mercury are characterized by a rapid (~2 s) increase in the northward component of the magnetic field (~30 nT) that persists for a short time (~10 s) (Sundberg et al., 2012). Observations from the MESSENGER spacecraft have associated dipolarizations in Mercury's magnetotail with thermal plasma depletion and heating, fast sunward flows, and energetic electron acceleration and injection (Dewey et al., 2017; Dewey et al., 2018; Sun et al., 2018). While Mercury's dipolarizations share many similar features to those at Earth, they also display curious differences. Dipolarizations, for example, are more frequent to Mercury's post-midnight magnetotail, opposite to that of Earth (Sun et al., 2016). Studies of dipolarizations at Mercury have made considerable progress in understanding the signatures and characteristics of these events, yet the dynamics and consequences of Mercury's dipolarizations remain less well understood. One such topic is that of flow braking. Mercury's near-planet reconnection site, located at or planetward of $X_{MSM'} = -3\ R_M$, is only ~5,000 km above the planet's nightside surface (e.g., Slavin et al., 2009; DiBraccio et al., 2015; Poh et al., 2017a; Smith et al., 2017). Even smaller yet is the distance between the inner edge of Mercury's current sheet and the planet's surface (~500-750 km) (Poh et al., 2017a). Over these distances, the magnetic field increases by a factor of only ~10-100, due to Mercury's weak planetary magnetic field and the large volume of the magnetosphere that the planet occupies. By contrast, the magnetic field at Earth's surface is ~10,000 times greater than in the magnetotail. Is Mercury's magnetic field strong enough to brake dipolarizations and their fast flows? Or do dipolarizations stream directly into the planet's nightside surface unencumbered by the relatively weak magnetic gradients? The answers to these questions carry significance for mass and magnetic flux transport, but are also interdisciplinary, with consequences for exospheric generation and space weathering.

Initial investigations suggest that braking is likely to occur although the mechanism and location of braking are poorly unconstrained. Sun et al. (2015) provided the first evidence for flow braking in Mercury's magnetotail by analyzing case studies of Alfvén and compressional waves associated with dipolarizations near the planet, interpreting them to be similar to the waves generated by the braking of flows in Earth's magnetotail (e.g., Panov et al., 2014). At that time, however, the association of Mercury's dipolarizations with fast sunward flows was only speculated. Dewey et al. (2018) established the connection between fast flows and dipolarizations at Mercury by developing a technique to determine average flows by combining together plasma observations of many individual dipolarizations. On the basis of pressure balance, Dewey et al. (2018) hypothesized that these fast flows would break at or planetward of $X_{MSM'} = -1.3$ R_M, near the expected inner edge of the current sheet (e.g., Poh et al., 2017a). Due to the limited sample size of dipolarizations, however, Dewey et al. (2018) was unable to examine the behavior of flows as a function of location in Mercury's magnetotail and could not support their hypothesis of braking directly. Finally, Poh et al. (2017b) investigated a signature suggestive of magnetic flux pileup within Mercury's midnight current sheet. Poh et al. (2017b) selected current sheet crossings on their ability to be fit by a one-dimensional Harris current sheet and noticed an enhancement of B_z local to midnight between $-1.4 < X_{MSM'} < -1.7$ R_M. The authors interpreted the B_z enhancement as being due to a current wedge similar to Earth's, however, their work does not connect such a signature to dipolarizations, fast flows, or substorm dynamics. These studies have provided valuable foundational observations and discussions into the topics of flow braking and flux pileup in Mercury's magnetotail but leave the topic largely unconstrained.

In this study, we expand upon previous observations and discussions of flow braking and flux pileup in Mercury's magnetotail. We develop an automated algorithm to identify dipolarizations in the magnetic field time series to expand the sample size of events to over an order of magnitude previously examined. Such a large sample size allows us to employ statistical techniques and form a statistical description of flow braking in lieu of multi-point spacecraft observations. We find that the majority (~80-90%) of dipolarizations brake within a thin (~500 km) region located close to Mercury's surface (~900 km altitude) due to magnetic pressure gradients from the planet's dipole magnetic field. As these flows brake, we observe statistically that their magnetic flux accumulates to form a pileup region that may be associated with an Earth-like current wedge. In Section 5.4, we describe our data sources and briefly introduce the dipolarization identification algorithm (described in detail in Appendix C). In Section 5.4, we present both statistical and case study analysis of flow braking and flux pileup, followed by a discussion of these results and the possibility of current wedge formation at Mercury in Section 5.5. We conclude this investigation in Section 5.6 with avenues for further research.

5.3. Methodology and Data Sources

For this investigation, we rely on observations from MESSENGER's Magnetometer (MAG; Anderson et al., 2007) and Fast Imaging Plasma Spectrometer (FIPS; Andrews et al., 2007). The MAG instrument measures the local vector magnetic field at 50 ms time resolution. The FIPS sensor measures thermal and low-energy ions with energy-per-charge (e/q) spanning 50 eV/e to 13 keV/e and mass-per-charge (m/q) spanning 1 amu/e to 40 amu/e. FIPS completes a nominal sweep of its energy steps in 10 s. While FIPS has a large instantaneous field of view (~1.1π sr), it is unable to measure bulk plasma flows at its native resolution since the spacecraft is three-axis stabilized. To estimate flows, we rely on a statistical reconstruction technique developed by Dewey et al. (2018). This technique assumes plasma flows are subsonic, and utilizes variable field of view pointing across many FIPS scans to construct a more complete velocity space distribution from which bulk plasma moments (including vector flow) can be determined. We display all MESSENGER observations in the aberrated Mercury solar magnetospheric (MSM') coordinate system, which is centered at Mercury's dipole center with $X_{MSM'}$ pointing anti-parallel to the solar wind (a radial solar wind speed of 400 km/s is assumed), $Z_{MSM'}$ pointing northward, and $Y_{MSM'}$ completing the right-handed system.

To identify dipolarizations, we rely exclusively on the MAG observations. While several dipolarization signatures are related to the thermal plasma, a complete FIPS scan has time resolution comparable to the typical duration of a dipolarization (Dewey et al., 2017) and therefore cannot resolve these signatures for all dipolarizations. MAG observations, in contrast, are able to resolve the magnetic field structure of the dipolarization at native resolution. Of the magnetic field signatures of a dipolarization, the sharp, step-like increase in B_z of the dipolarization front is the easiest to detect (e.g., Liu et al. 2013; Sun et al., 2016). We develop an automated algorithm to identify dipolarization fronts in the B_z time series. The algorithm, described in detail in Appendix C, evaluates each point in the time series for a strong, positive, coherent, local gradient in B_z and applies a series of physical tests to determine if such a slope is representative of a dipolarization front or not.

We apply our dipolarization selection procedure to 1,946 magnetotail intervals that satisfy several criteria. First, to ensure that we are examining the plasma sheet rather than the adjacent magnetotail lobes, we require the 1-minute running average $B_z/|B| > 0.5$ and $\beta > 0.1$, where β is the proton plasma beta. These criteria estimate that the spacecraft samples the closed, mass-loaded magnetic field lines characteristic of the plasma sheet. Other studies of Mercury's magnetotail have used β to identify plasma sheet intervals (e.g., Sun et al., 2017; Poh et al., 2018), but they typically use a higher β threshold. We use a lower threshold since FIPS may underestimate the local plasma beta in the presence of the fast flows associated with dipolarizations (e.g., Dewey et al., 2018) due to the sensor's limited field of view. Second, we exclude intervals contaminated by solar energetic particle events. Third, we limit our survey to the spatial region $-2.5 < X_{MSM'} < 0$, $|Y_{MSM'}| < 1.5$, and $|Z_{MSM'}| < 0.2$ R_M. Finally, to prevent biasing from short intervals, we require that the criteria above must be met for longer than three minutes (the nominal Dungey cycle duration). Together, these 1,946 magnetotail intervals represent an accumulated 14,022 minutes of observation.

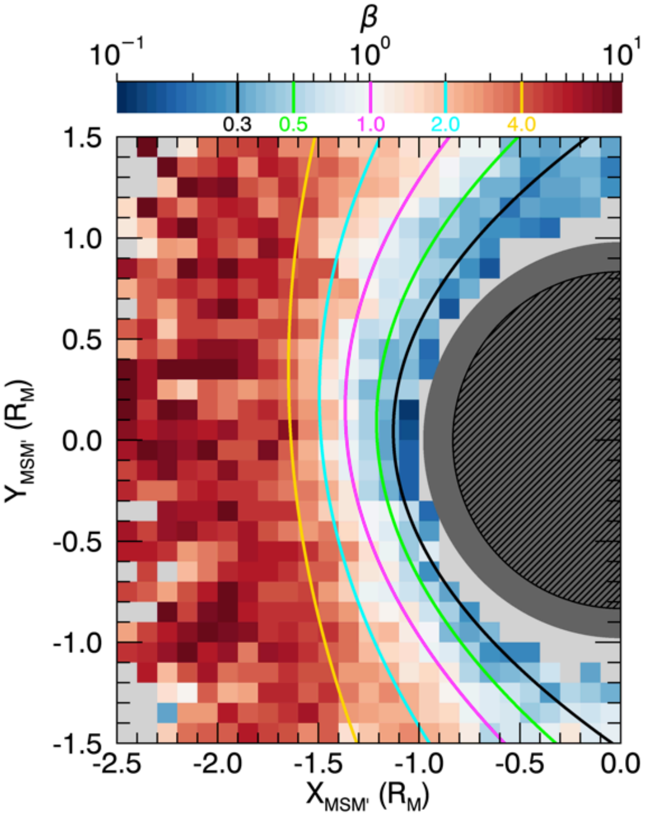

Figure 5.1. Equatorial distribution of proton plasma beta (β) as indicated by the color bar. Light grey bins indicate regions of insufficient sampling. The dark grey indicates

Mercury's nightside surface and the black-hatched region denotes its conducting core. The five color polynomials (black, lime, magenta, cyan, and gold) are contours of specific β, as indicated by the vertical lines of the corresponding color in the color bar.

To provide context to the dipolarization observations described in later sections, we determine the average proton plasma beta (β) as a function of spatial location in Mercury's magnetic equatorial plane, as shown in Figure 5.1. To construct this distribution, we compute the average magnetic field, proton density, and proton temperature under the assumption of isotropy (e.g., Gershman et al., 2013) for each FIPS scan within the 1,946 intervals (84,187 scans total). We then use the spacecraft's location at the center of each scan to sort scans into a two dimensional ($X_{\mathrm{MSM'}}$, $Y_{\mathrm{MSM'}}$) histogram. Within each histogram bin, we determine the mean proton density, proton temperature, and magnetic field strength from the scans assigned to that bin, from which plasma beta is then calculated. For five specific values of β (0.3, 0.5, 1.0, 2.0, and 4.0) we determine contours within the spatial distribution and display polynomial fits to those contours (black, lime, magenta, cyan, and gold, respectively). Each contour is well represented by a second-order polynomial (χ^2 values of 0.045, 0.049, 0.029, 0.033, and 0.019, respectively). As expected for the plasma sheet, $\beta >> 1$ far from the center of the planetary dipole with contours nearly parallel to $Y_{\mathrm{MSM'}}$. Approaching the planet, β decreases and contours bow about the planetary magnetic field, with $\beta << 1$ close the dipole center. For reference, at local midnight, $\beta = 1$ (magenta line) at $X_{\mathrm{MSM'}} \approx -1.36\ R_M$, approximately 900 km in altitude above the nightside surface. Plasma beta also displays a cross-tail asymmetry, with systematically greater values in the post-midnight plasma sheet. This asymmetry can be observed by noticing that the β contours in the post-midnight plasma sheet are located at greater $X_{\mathrm{MSM'}}$ values than those in the pre-midnight plasma sheet. For example, at $Y_{\mathrm{MSM'}} = -1\ R_M$ the $\beta = 1$ contour is located at $X_{\mathrm{MSM'}} \approx -0.98\ R_M$ while at $Y_{\mathrm{MSM'}} = +1\ R_M$ the same contour is located at $X_{\mathrm{MSM'}} \approx -1.16\ R_M$. This cross-tail asymmetry is among other asymmetries noted in plasma and magnetic field parameters in

Mercury's central plasma sheet (e.g., Raines et al., 2013; Korth et al., 2014; Poh et al., 2017b; Rong et al., 2018).

5.4. Results

5.4.1 Observations of Flow Braking

To determine if dipolarizations impact Mercury's nightside surface directly or if they brake/divert before then, we begin by examining the distribution of dipolarization occurrence as a function of location within Mercury's magnetotail. Figure 5.2a displays the number of dipolarizations identified by the automated procedure of Section 5.3 as a function of equatorial ($X_{MSM'}$, $Y_{MSM'}$) location. As a function of $Y_{MSM'}$, dipolarizations display a strong cross-tail asymmetry with over an order of magnitude more dipolarizations observed post-midnight than pre-midnight similar to the findings of other studies (Sun et al., 2016; Dewey et al., 2018). The range $-1.5 < Y_{MSM'} < 0.5$ R_M contains 90.7% of the identified dipolarizations. As a function of $X_{MSM'}$, the number of dipolarizations drops sharply planetward of the $\beta = 1$ contour (magenta line), particularly in the post-midnight magnetotail. Few dipolarizations are observed tailward of $X_{MSM'} = -2$ R_M.

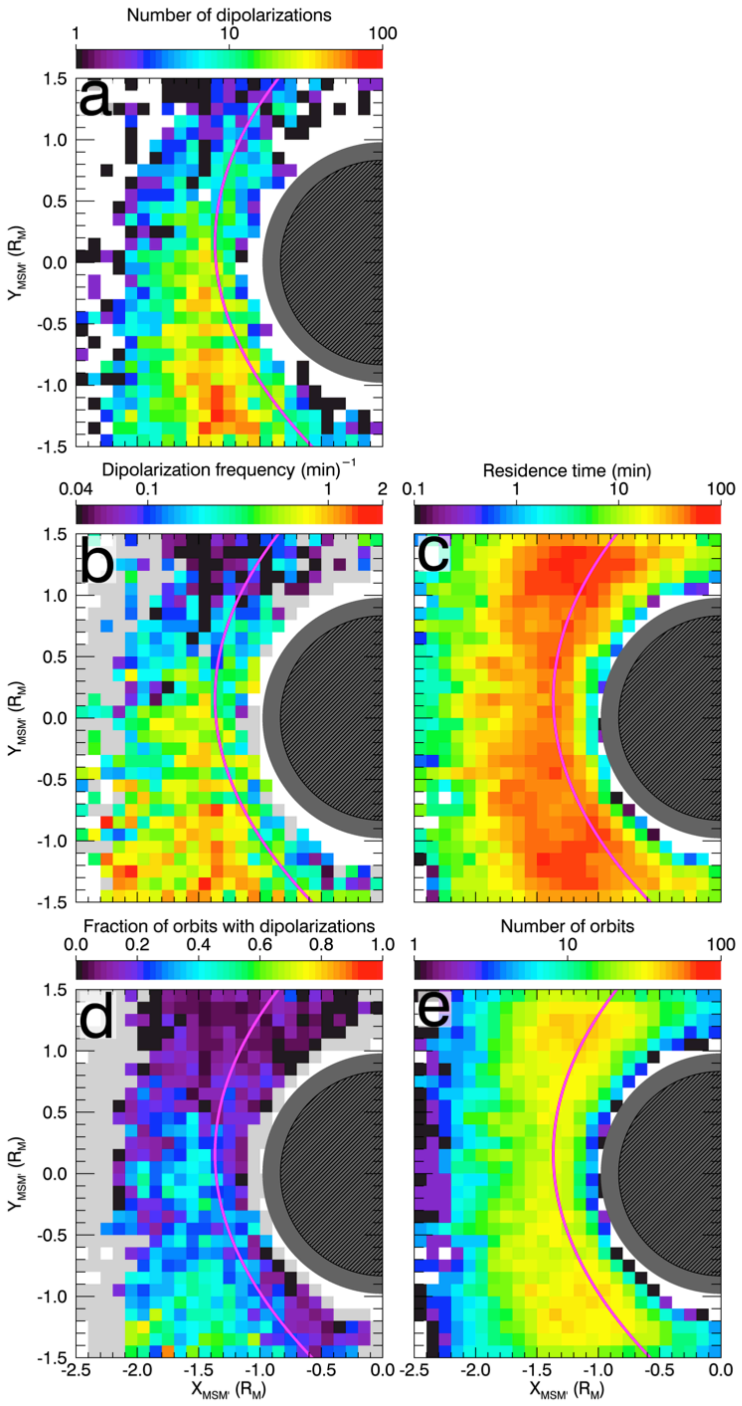

Figure 5.2. Equatorial distributions in the same format as Figure 5.1. (a) Number of dipolarizations, where white indicates no dipolarizations observed. (b) Frequency of dipolarizations, where light grey indicates no dipolarizations observed and white indicates insufficient sampling time (<1 min). (c) Spacecraft sampling time, where white indicates regions of no samples. (d) Fraction of orbits that contain dipolarizations within that spatial bin, where light grey indicates insufficient sampling (<3 orbits) and white indicates regions of no sampling. (e) Number of orbits, where white indicates regions of

no samples. The magenta polynomial in each panel corresponds to the β = 1 contour from Figure 5.1.

To account for effects from non-uniform spacecraft sampling, we display the frequency of dipolarizations within Figure 5.2b. To produce this distribution, we divide the number of dipolarizations observed within each spatial bin (Figure 5.2a) by the total time the spacecraft searched for dipolarizations at that location (Figure 5.2c). Examining the frequency of dipolarizations, the strong cross-tail asymmetry persists. The apparent decease in dipolarizations tailward of $X_{MSM'} = -2\ R_M$, however, is removed after correcting for spacecraft sampling. Dipolarizations possess an approximately uniform frequency tailward of the β = 1 contour for $Y_{MSM'} < -0.5\ R_M$. The decrease in number of dipolarizations sunward of β = 1 does not appear to be an artifact of spacecraft sampling. Where dipolarizations are most frequent ($-1.5 < Y_{MSM'} < 0.5\ R_M$), the frequency decreases by an order of magnitude about β = 1. For $Y_{MSM'} < -0.5\ R_M$, the frequency tailward of β = 1 is ~1-2 dipolarizations per minute, falling to ~0.1-0.2 closer to the planet. The trend is less clear at local midnight ($-0.5 < Y_{MSM'} < 0.5\ R_M$). The frequency tailward of β = 1 is ~1 dipolarization per minute, and while there are several bins planetward of β = 1 that reach similar frequencies, there is considerable scatter, with many bins observing dipolarizations at a rate of ~0.2 per minute and many others observing no dipolarizations at all (light grey).

As will be described in further detail below (Figure 5.7), when dipolarizations are observed, they tend to be observed in series with other dipolarizations. This trend has been anecdotally described in other studies involving dipolarizations at Mercury (e.g., Sundberg et al., 2012; Dewey et al., 2017; Dewey et al., 2018; Sun et al., 2020). An effect of dipolarizations typically appearing in groups is that it can skew event frequency. We therefore use the fraction of orbits that contain dipolarizations (Figure 5.2d) as a metric complementary to event frequency. To produce this distribution, for each spatial bin, we determine the number of orbits that contain one or more dipolarizations within that bin and divide it by the total number of orbits that sampled that bin (Figure 5.2e). Similar to conventional frequency (Figure 5.2b), the cross-tail asymmetry in dipolarization occurrence persists. Post-midnight, a greater fraction of orbits (~0.4-0.7) contain dipolarizations than pre-midnight (~0.1). About $\beta = 1$, the fraction of orbits that contain dipolarizations also drops substantially. Where dipolarizations are most common ($-1.5 < Y_{MSM'} < 0.5$ R_M), the fraction of orbits with dipolarizations decreases from ~0.4-0.5 just tailward of $\beta = 1$ to ~0.1 planetward of the contour. The only location within this $Y_{MSM'}$ range that does not appear to follow this trend is at $Y_{MSM'} = -0.5$ R_M where the fraction of orbits with dipolarizations (~0.4) remains unchanged about $\beta = 1$.

Taken together, these trends in dipolarization occurrence imply that they do not typically reach Mercury's nightside surface. If dipolarizations usually impacted the planet, we should expect the rate at which dipolarizations are observed to remain approximately constant up to the planet's surface. Rather, we observe that the rate of dipolarization occurrence (interpreted either as the frequency of dipolarizations or as the fraction of orbits that contain dipolarizations) decreases sharply about the $\beta = 1$ contour, ~900 km altitude above the nightside surface. If dipolarizations do indeed divert or brake before reaching the nightside surface, these signatures should be apparent in the flows associated with dipolarizations. In Figure 5.3, we examine the typical flows associated with dipolarizations as a function of spatial location. Since the FIPS sensor cannot determine flows at its nominal resolution, we use the statistical technique developed by Dewey et al. (2018) to construct typical flow vectors. The technique combines multiple FIPS scans together and takes advantage of the variable FIPS field of view pointing between scans to construct a (more) complete velocity space distribution from which flows can be determined. Dewey et al. (2018) applied this technique to 386 dipolarizations spread throughout Mercury's post-midnight magnetotail to determine a single flow vector. With the increased sample size from our automated procedure (Section 5.3 and Appendix C), we have sufficient number of events to apply the flow-determination technique to dipolarizations as a function of spatial location. Within each spatial bin of Figure 5.3, we apply the Dewey et al. (2018) procedure to the FIPS scans that cover the dipolarization fronts of that bin's events. Figure 5.3a displays V_x, 3b displays V_y, 3c displays V_z, and 3d displays the number of dipolarizations within each bin used to construct typical flows. While some bins in Figure 5.3d reach ~400 dipolarizations, many have only ~50-100. As a result, the composite velocity space distributions of some bins still have missing regions that affect the determination of one or more flow vector components. Grey bins in Figures 5.3a-c denote locations where vector components cannot be reliably determined. Finally, we expect proton flows to be representative of dipolarization transport. Dipolarizations have dimensions ~2,000 km in $X_{MSM'}$ and ~750 km in $Y_{MSM'}$ (see Section 5.4.3), which are greater than the typical proton gyroradius about dipolarizations (~300 km for a 4 keV proton in a 30 nT magnetic field), indicating that the frozen-in condition is valid.

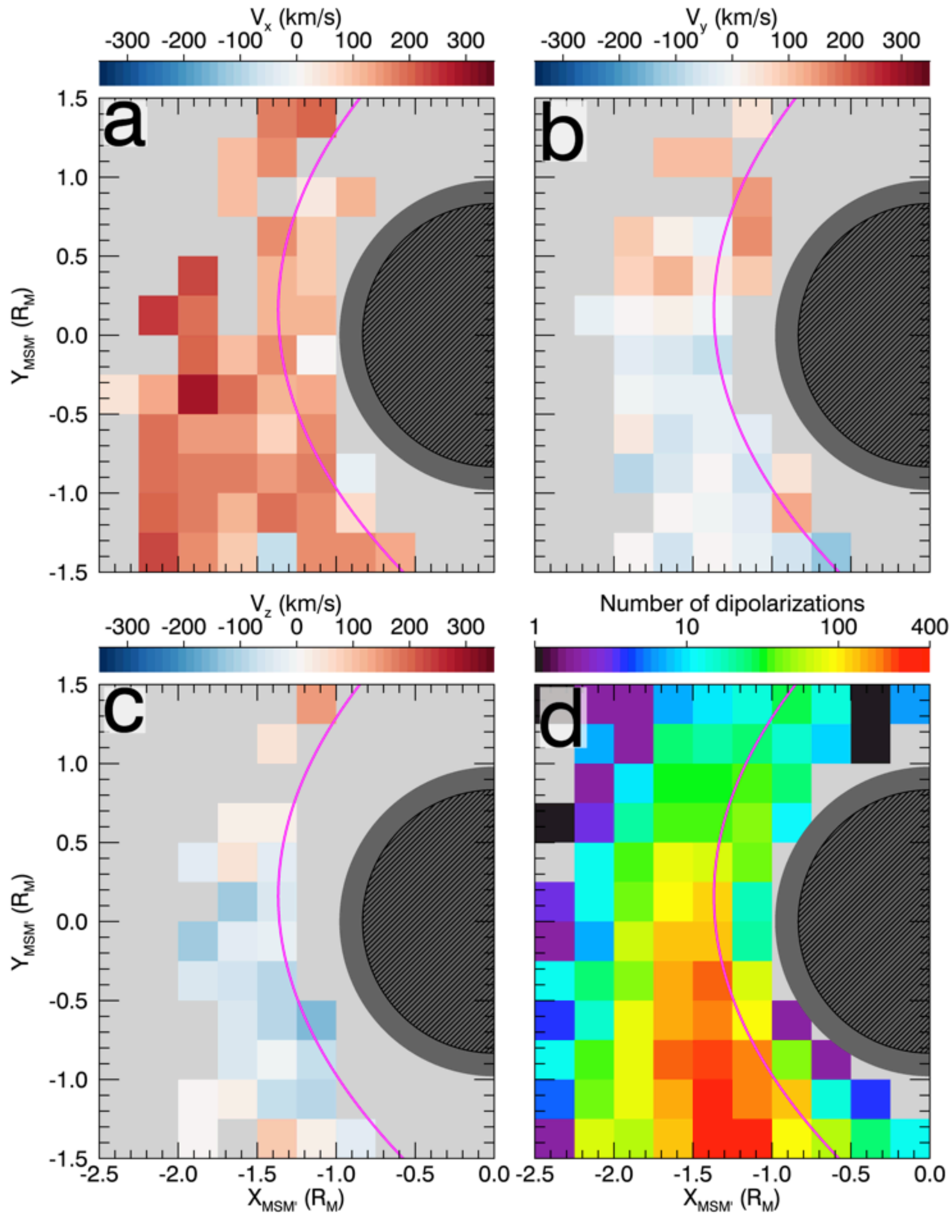

Figure 5.3. Typical dipolarization flow components as a function of equatorial location in the same format as Figure 5.2. (a) Sunward component (V_x), (b) duskward component (V_y), (c) northward component (V_z), and (d) number of dipolarizations used to determine these flows. Light grey bins in (a)-(c) indicate spatial locations whose flow component in that direction could not be determined reliably (see text). Light grey bins in (d) indicate regions with no dipolarizations.

The flows in Figure 5.3 are indicative of both flow braking and diversion. Tailward of $\beta = 1$, V_x is dominant with speeds ~200 km/s in the sunward direction, similar to the dipolarization flow determined by Dewey et al. (2018). Post-midnight, these flows have a slightly negative V_y

(~ –50 km/s) component, while the V_y is stronger and positive (~ +75 km/s) pre-midnight. Flows along $Z_{MSM'}$ are generally negative about local midnight and positive closer to the flanks of the magnetotail, and are of the same approximate strength as V_y. Planetward of $\beta = 1$, the sunward component decreases in magnitude. This trend is most apparent for $-1 < Y_{MSM'} < 0$ R_M, where V_x decreases from ~100-200 km/s to ~0-50 km/s about $\beta = 1$. While the northward flow component cannot be reliably determined planetward of $\beta = 1$, the dawn-dusk component appears to become systematically positive (duskward). These V_x and V_y flow signatures are indicative of both flow braking and diversion.

Figure 5.4 displays trends along $X_{MSM'}$ more clearly. Each panel examines average parameter(s) within $-1.5 < Y_{MSM'} < 0.5$ R_M (where dipolarizations are most common) as a function of $\Delta X_{MSM'}$. $\Delta X_{MSM'}$ is the distance along $X_{MSM'}$ from the $\beta = 1$ contour (i.e., $\Delta X_{MSM'} = 0$ lies on the $\beta = 1$ contour, with $\Delta X_{MSM'} > 0$ planetward of the contour). Figure 5.4a examines the frequency of dipolarizations organized by $\Delta X_{MSM'}$. Similar to the observations discussed with Figure 5.2, the frequency of dipolarizations remains approximately constant until $\beta = 1$. For $-1.5 < \Delta X_{MSM'} < 0$ R_M, the dipolarization frequency fluctuates but remains about 0.6 min^{-1} (shaded grey region) until decreasing significantly at $\Delta X_{MSM'} \approx 0$. By the $\beta = 0.5$ contour (lime), the frequency has dropped to half its downtail value. Further planetward, the frequency continues to drop to ~0.1 min^{-1}, suggesting that only a small fraction (~10-20%) of dipolarizations may impact the nightside surface directly. The sunward flow component V_x in Figure 5.4b displays a similar trend. For $-1.5 < \Delta X_{MSM'} < 0$ R_M, the sunward flow speed fluctuates but remains about 200 km/s before beginning to decrease meaningfully at $\Delta X_{MSM'} \approx 0$. By the $\beta = 0.5$ contour, the sunward flow has decreased to approximately half its downtail value. The dipolarization frequency and flow speed decreasing to half their respective downtail values by $\Delta X_{MSM'} \approx 0.15$

R_M suggests the braking region has a downtail extent of ~500 km and begins at $\beta = 1$ (an altitude of ~900 km at local midnight).

To understand the mechanism causing braking to occur in Mercury's magnetotail, Figure 5.4c examines proton plasma pressure (P_{NKT}) and magnetic pressure (P_{MAG}) as functions of $\Delta X_{MSM'}$. We follow the same general procedure in determining these pressures as for the proton plasma beta within Section 5.3. In order to examine conditions that dipolarizations encounter, we use only FIPS and MAG measurements belonging to orbits that contain one or more dipolarization. For $\Delta X_{MSM'} < 0$, both plasma and magnetic pressures remain small (<1 nPa) with the plasma pressure dominating magnetic pressure (consistent with $\beta > 1$). At $\Delta X_{MSM'} = 0$, both pressures are within uncertainty of each other ($\beta = 1$). For $\Delta X_{MSM'} > 0$, magnetic pressure dominates plasma pressure ($\beta < 1$) as we move closer to Mercury's dipole center. Using these one-dimensional pressure profiles, we can estimate the pressure gradient forces in the sunward direction. For both $\Delta X_{MSM'} < 0$ and $\Delta X_{MSM'} > 0$, we apply linear fits to both the magnetic and plasma pressure profiles with the slope of the fit indicating the force density. For $\Delta X_{MSM'} < 0$, both magnetic and plasma pressure gradients are small (~0.1-0.2 nPa R_M^{-1}) and are within uncertainty of each other. At $\Delta X_{MSM'} = 0$, the magnetic pressure gradient increases by a factor of 60 ± 20 and the plasma pressure gradient increases by a more modest factor of 16 ± 7. The strong pressure gradients, particularly in magnetic pressure, coincident with the decreases in dipolarization occurrence and flow speed suggest dipolarizations and their associated fast flows brake as a result of the strong magnetic pressure gradients of Mercury's dipole magnetic field. Finally, Figure 5.4d displays the local Alfvén speed (V_A) as a function of $\Delta X_{MSM'}$. We will use V_A in the discussion of current wedge formation in Section 5.5. For now, we illustrate that dipolarizations far downtail of the braking region ($\Delta X_{MSM'} < -1\ R_M$) typically travel near the Alfvén speed.

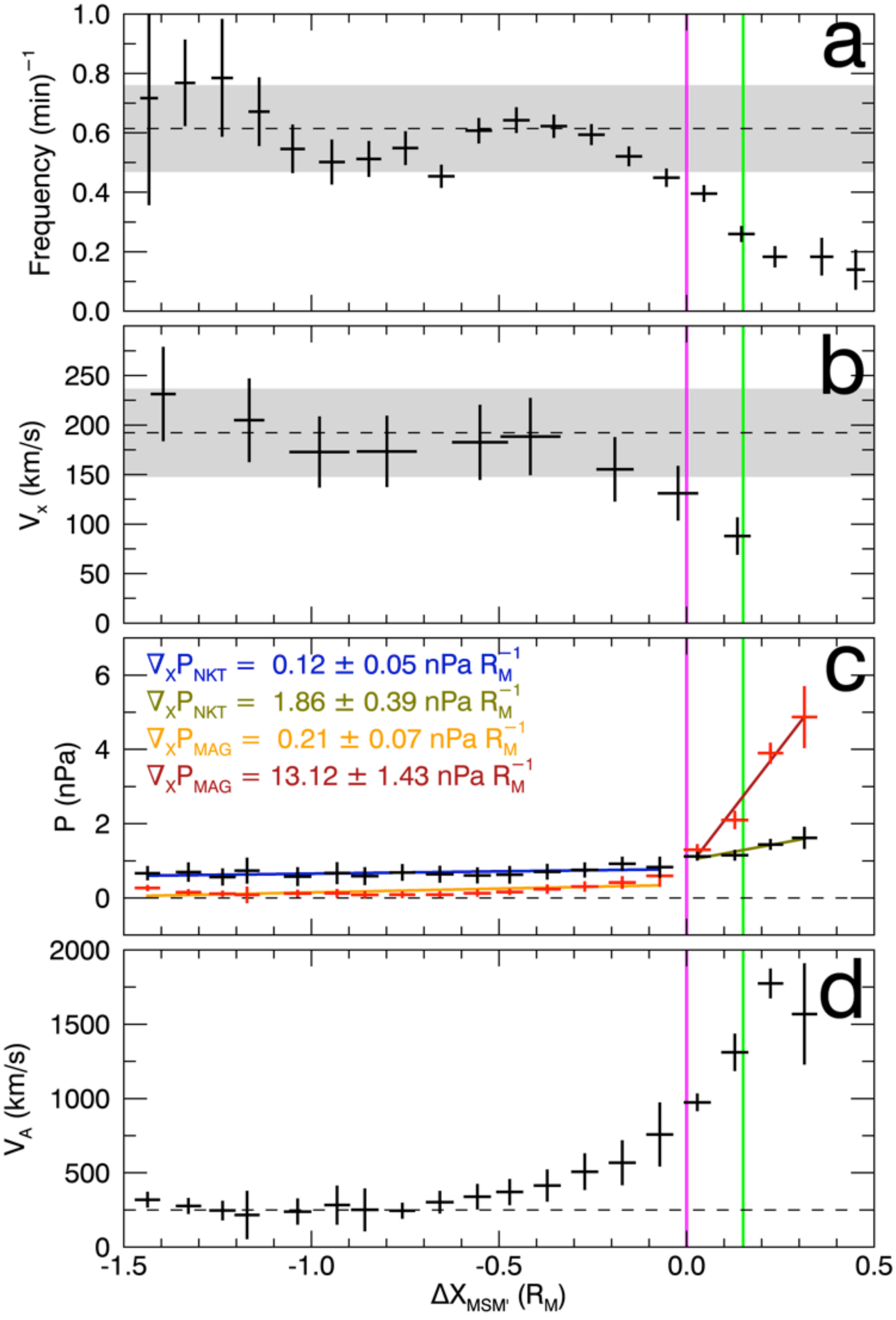

Figure 5.4. (a) Dipolarization frequency, (b) typical dipolarization sunward flow, (c) magnetic and thermal proton pressures, and (d) Alfvén speed as functions of $\Delta X_{MSM'}$

(defined in the text). The vertical magenta line corresponds to the location of the β = 1 contour and the vertical lime line corresponds to the location of the β = 0.5 contour (see Figure 5.1). In (a) and (b), the horizontal dashed lines and grey boxes correspond to the average and uncertainty of dipolarization frequency and sunward flow speed for $-1.5 < \Delta X_{MSM'} < 0$ R_M. In (c), the horizontal dashed line corresponds to a pressure of zero, while the colored lines correspond to linear fits whose slopes are listed. In (d), the horizontal dashed line corresponds to a speed of 250 km/s.

5.4.2 Observations of Flux Pileup

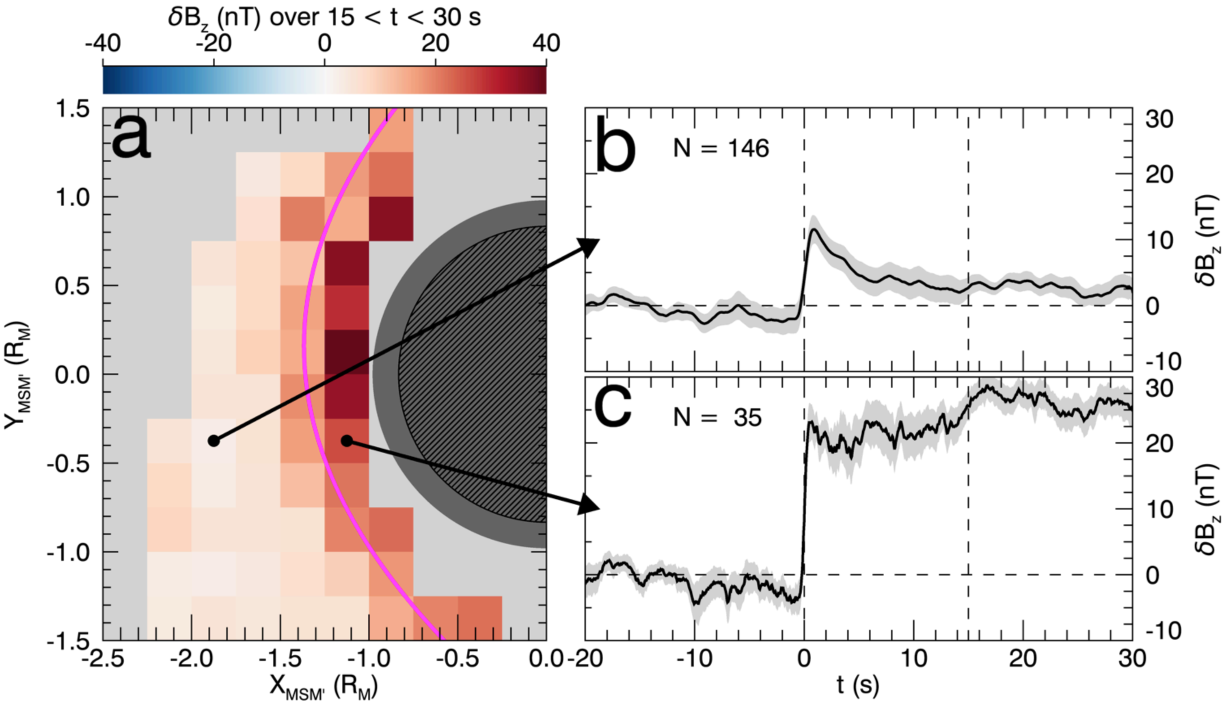

Figure 5.5. (a) Equatorial distribution of the average detrended, background-subtracted northward magnetic field component (δB_z) following dipolarizations in the same format as Figure 5.3. The color bar indicates the average δB_z of the superposed dipolarization profiles over $15 < t < 30$ s. Light grey regions have insufficient number of dipolarizations for statistical analysis (<15 dipolarizations, see Figure 5.3d). The black arrows indicate corresponding spatial locations in (a) for the two example profiles in (b) and (c). For (b) and (c), the thick black line indicates the mean δB_z over the N-dipolarizations at each time step and the light grey indicates the standard error. The vertical dashed lines correspond to $t = 0$ s (the midpoint of dipolarization fronts that the profiles are organized by) and $t = 15$ s. The horizontal dashed lines correspond to 0 nT.

Observations of dipolarization frequency and flow speed in Section 5.4.1 establish that dipolarizations typically brake before reaching Mercury's nightside surface. Within this section, we investigate whether the flow braking of dipolarizations is associated with magnetic flux pileup. We begin by first examining dipolarization profiles as a function of location within Mercury's magnetotail, similar to the frequency maps of Figure 5.2 and the flow maps of Figure 5.3. In Figure 5.5, we examine the northward component of the magnetic field (B_z) following dipolarizations. We standardize dipolarizations by converting to new time and magnetic field coordinates. For time, we use t, which is the time in seconds local to the midpoint of a dipolarization's dipolarization front (i.e., the midpoint of a dipolarization front is defined to be $t = 0$ s). For the magnetic field, we are interested in how the field changes after the dipolarization compared to before it, so we define $\delta\mathbf{B}$, the background-subtracted, detrended magnetic field. To construct $\delta\mathbf{B}$, we first remove the effects of the spacecraft's motion through Mercury's dipole magnetic field after which we subtract the average magnetic field over $-20 < t < -10$ s. Using the same spatial gridding as in Figure 5.3, we examine the superposed epoch profiles of dipolarizations in the new (t, δB_z) coordinates as a function of equatorial location.

The average δB_z over $15 < t < 30$ s from each spatially-resolved superposed dipolarization profile is shown in Figure 5.5a, while Figures 5.5b and 5.5c show two example profiles, one tailward and one planetward of the $\beta = 1$ contour, respectively. Tailward of $\beta = 1$, dipolarizations do not exhibit large, prolonged enhancements of the magnetic field following the initial dipolarization. In Figure 5.5b, for example, the magnetic field decreases slightly prior to the sharp, step-like increase of the dipolarization front (centered at $t = 0$) after which the northward component of the magnetic field remains enhanced for several seconds before falling to near pre-dipolarization values. The average δB_z over $15 < t < 30$ s remains close to within uncertainty of the value over $-20 < t < -10$ s. Correspondingly, the average δB_z over $15 < t < 30$ s for regions tailward of $\beta = 1$ in Figure 5.5a is small, $\lesssim 5$ nT. In contrast, dipolarizations at and planetward of $\beta = 1$ display substantial, prolonged increases in the magnetic field. The superposed dipolarization profile in Figure 5.5c, for example, shares similar features as the profile in Figure 5.5b, however, after the initial dipolarization front, the magnetic field remains enhanced by ~25 nT for a substantial duration of time (i.e., greater than the typical dipolarizing flux bundle duration of ~10 s, see Dewey et al., 2017). Correspondingly, the average post-dipolarization δB_z at and planetward of the $\beta = 1$ contour in Figure 5.5a has values ~10-40 nT, with a median value of 29 nT. Planetward of $\beta = 1$, the post-dipolarization δB_z is asymmetric about local midnight, with greater strength pre-midnight (~36 nT) than post-midnight (~26 nT). Synoptically, the prolonged δB_z enhancement planetward of $\beta = 1$ appears to be a large-scale dipolarization of Mercury's near-tail region.

These spatially-resolved superposed dipolarization profiles indicate flux pileup occurs in Mercury's magnetotail alongside flow braking. Tailward of $\beta = 1$, superposed dipolarization profiles exhibit only transient increases in the magnetic field consistent with dipolarizations travelling rapidly sunward and passing quickly over the spacecraft and resulting in a small δB_z over $15 < t < 30$ s. Planetward of $\beta = 1$, coincident with where substantial braking occurs, the superposed dipolarization profile indicate a more permanent increase in the magnetic field with magnetic flux pileup resulting in a large average δB_z over $15 < t < 30$ s. To determine if the synoptic pileup (i.e., large-scale dipolarization) signature across Mercury's near-tail region is physical, we turn to magnetic flux budget analysis in Section 5.4.3 and examine a case study in Section 5.4.4.

5.4.3 Flux Budget of Statistical Pileup Signature

To determine if the statistical, synoptic flux pileup signature (i.e., large-scale dipolarization) is physical, we first look to determine if dipolarizations could supply sufficient magnetic flux to establish it. From the distribution of δB_z planetward of $\beta = 1$ in Figure 5.5a, we estimate that the large-scale flux pileup contains 0.28 ± 0.08 MWb magnetic flux. We wish to determine if it is possible for dipolarizations to supply this flux to the inner magnetotail.

The typical magnetic flux transported by a dipolarization can be estimated by

$$\Phi \approx 2\Delta Y V_x \int B_z \, dt$$

where ΔY is the half-width of the dipolarization, assumed to be approximately constant. We can use superposed dipolarization profiles and typical dipolarization flows to estimate these terms, however, the cross-tail half-width remains unknown. Determining the width of dipolarizations is challenging, even when multi-spacecraft observations available (e.g., Sergeev et al., 1996; Nakamura et al., 2004). However, taking advantage of our expanded dipolarization event list, we can employ statistical techniques to provide some insight into their cross-tail width. Similar to determining dipolarization flows, we will not be able to determine the cross-tail width of dipolarizations on an event-by-event basis, but rather, we can use the following statistical analysis to determine a representative value.

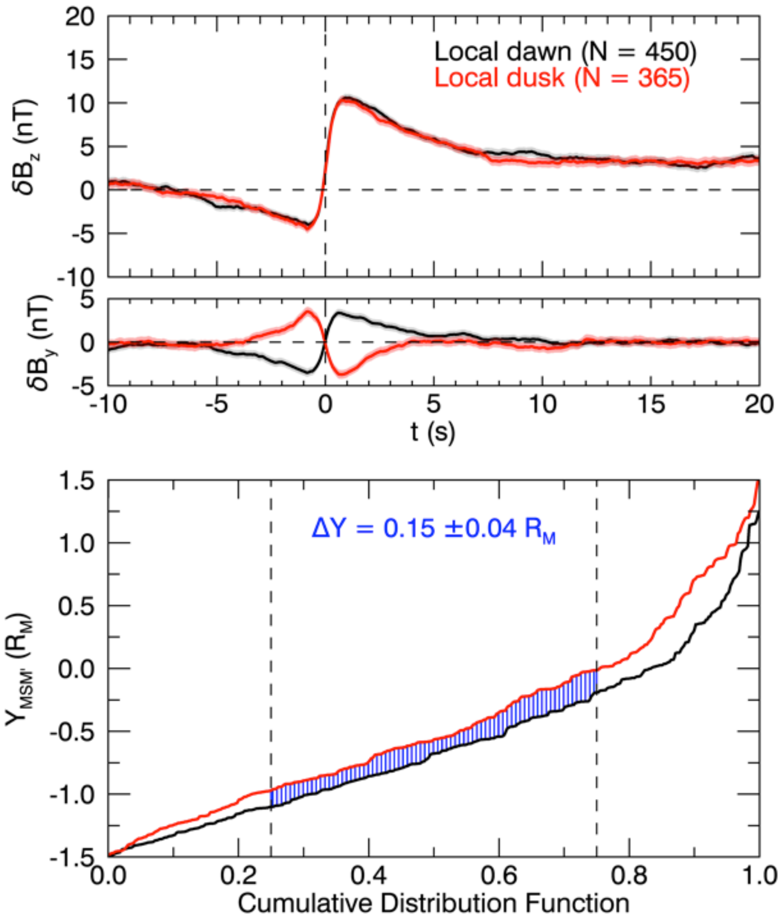

Figure 5.6. (top) Superposed dipolarization profiles of δB_z and δB_y for dipolarizations observed at their local dawn (black) and local dusk (red) sides in the same format as Figure 5.5b and 5.5c. (bottom) Cumulative distribution function of the spacecraft $Y_{MSM'}$ location when it encountered a dipolarization on the dipolarization's local dawn (black) or local dusk (red) side. The separation between the curves (vertical blues lines) indicates the typical cross-tail half-width of dipolarizations. The dashed vertical black lines indicate the 25th and 75th percentiles.

Dipolarizations possess several current structures (e.g., Sun et al., 2013). At the dipolarization front, a dawn-to-dusk current separates the surrounding plasma from the enhanced B_z within the dipolarization. While some of this current closes about the dipolarization, most is expected to close as field-aligned currents of the Region-2 sense (e.g., Birn et al., 2019). These field-aligned currents produce perturbations in the magnetic field that we can use to determine if the spacecraft observed the local dawn or dusk flank of the dipolarization. For example, for spacecraft observations of the local dawn side of dipolarizations whose field-aligned current closes into the northern hemisphere, we expect a negative-then-positive perturbation in B_y (i.e., $\delta B_y < 0$ followed by $\delta B_y > 0$) at the dipolarization front. By examining the distribution of where the spacecraft observed the local dawn versus local dusk sides of dipolarizations, we can determine the characteristic cross-tail width. For example, consider if dipolarizations at Mercury typically encompass the entire width of the magnetotail ($-2 < Y_{MSM'} < 2$ R_M). Observing the local dawn side would only occur when the spacecraft is post-midnight ($Y_{MSM'} < 0$), and observing the local dusk side would only occur when the spacecraft is pre-midnight ($Y_{MSM'} > 0$). The typical separation between observations of local dawn (on average, $Y_{MSM'} \approx -1$ R_M) and of local dusk (on average, $Y_{MSM'} \approx 1$ R_M) would be 2 R_M, the half-width of the full structure (4 R_M).

We implement this methodology to determine the typical dipolarization half-width ΔY in Figure 5.6. We select dipolarizations in the $\beta > 1$ region (to avoid contamination from braking dipolarizations) that possess significant bipolar signatures in δB_y at the dipolarization front. We use the polarity of the δB_y signature and the spacecraft's $Z_{MSM'}$ location to estimate if the spacecraft observed the local dawn or local dusk side of the event. A total of 815 dipolarizations met these criteria, with the spacecraft observing local dawn for 450 of these events, and local dusk for the remaining 365. The top panels of Figure 5.6 display the superposed epoch δB_z and δB_y profiles of these events. We invert the sign of δB_y for events when $Z_{MSM'} < 0$ to produce clear signals in the superposed δB_y profiles (i.e., for events with $Z_{MSM'} < 0$, we display $-\delta B_y$ in Figure 5.6). The profiles look nearly identical in magnitude and timing, with just the polarity of the δB_y bipolar signature reversed. The bottom panel displays the cumulative distribution function of the spacecraft's $Y_{MSM'}$ position for both local dawn (black) and local dusk (red) observations. As expected, the spacecraft position is systematically shifted to greater $Y_{MSM'}$

when it observed dipolarizations' local dusk side. The separation between the two distribution functions indicates the typical dipolarization half-width. To avoid outliers, we use the 25th to 75th percentiles (dashed vertical lines) to estimate $\Delta Y = 0.15 \pm 0.4\ R_M$. Equipped with the dipolarization half-width, we use B_z profiles and typical V_x flows to estimate that a single dipolarization typically transports 0.053 ± 0.019 MWb. To supply the magnetic flux observed in the flux pileup region would therefore require 5 ± 2 dipolarizations.

The number of dipolarizations required to build the flux pileup signature is supported observationally, shown in Figure 5.7. Figure 5.7a displays the number of dipolarizations identified during an orbit versus the median time between those dipolarizations (time between successive dipolarization fronts). We include the time between dipolarizations as it suggests a causal link; dipolarizations separated by >2-3 min, for instance, may not be considered to be of the same substorm. Figure 5.7b shows the marginal distribution of the number of dipolarizations observed per orbit, while Figure 5.7c shows the time between individual dipolarization fronts (as opposed to the median separation time per orbit in 7a). From Figure 5.7b, nearly half of orbits (818/1946 ~ 0.4) contain no dipolarizations. Of the remaining orbits, more orbits contain more than one dipolarization than a single dipolarization. Approximately ~18% of all orbits (345/1946) contain 5 or more dipolarizations, with the most extreme containing 32. Examining the time between dipolarizations (Figure 5.7c), most dipolarizations are observed in series with one followed soon by another. The typical time between dipolarization fronts is between 5-20 s while the typical dipolarization duration is ~10 s (Dewey et al., 2017). Combining these distributions together in Figure 5.7a, only ~6% of orbits contain a sufficient number of dipolarizations (5) with median time between dipolarizations < 20 s. While this is a small fraction of orbits, this determination is sensitive to the number of active reconnection sites in

Mercury's magnetotail (e.g., if two reconnection sites are active we may require the spacecraft to observe 2-3 dipolarizations for the orbit to qualify). We do not intend this fraction of orbits to communicate how common large-scale pileup may occur, but rather that the flux pileup signature identified statistically in Figure 5.5 is indeed possible to establish via multiple dipolarizations.

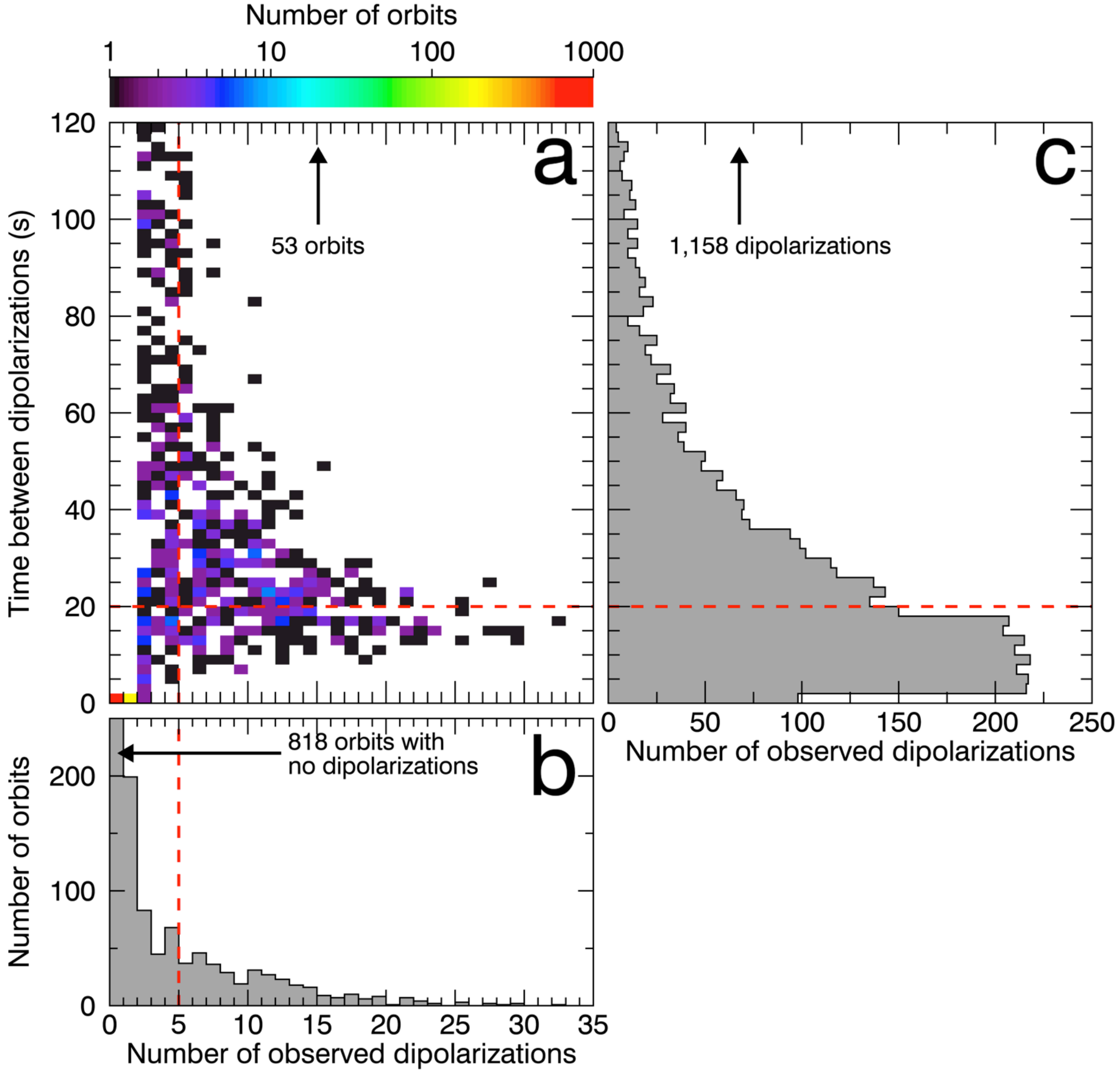

Figure 5.7. (a) Distribution of the number of dipolarizations observed per orbit versus the median time between dipolarizations during that orbit, where the color bar indicates the number of occurrences. White indicates no occurrences. (b) The marginal distribution of the number of dipolarizations per orbit. (c) The distribution of the time between

successive dipolarization fronts. The dashed red lines correspond to thresholds discussed in the text.

5.4.4 Flow Braking and Flux Pileup Example

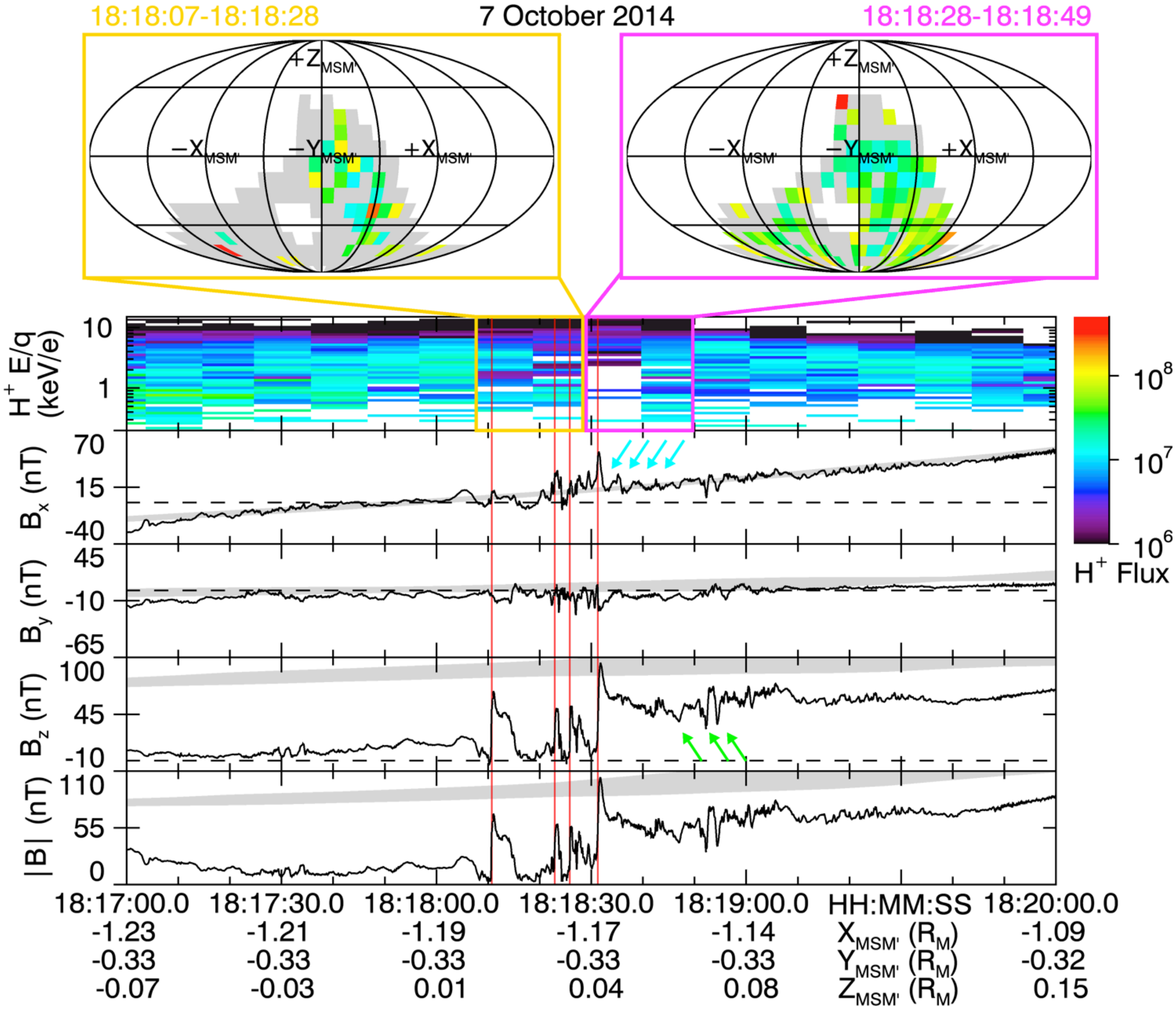

Figure 5.8. FIPS and MAG observations over 18:17:00 to 18:20:00 on 10-07-2014. The panels from top to bottom are FIPS proton flux (values indicated by the color bar, units of s^{-1} cm^{-2}), B_x, B_y, B_z, and magnetic field strength |B|. Below the bottom panel, the time and spacecraft position are listed. The vertical red lines indicate dipolarization fronts as identified by the selection algorithm (see Section 5.3 and Appendix C). The cyan and lime arrows correspond to magnetic fluctuations described in the text. The grey shaded regions in each magnetic field panel indicate typical magnetic field conditions at this location in Mercury's magnetotail. In the FIPS proton flux spectrogram, the gold and magenta boxed scans correspond to the integrated proton flux maps above the panels. Each flux map indicates the proton flux observed by FIPS as a function of direction in a

Mollweide projection. The color bins correspond to the same color bar (units of s^{-1} cm^{-2} sr^{-2}), light grey regions are those within the FIPS field of view but with no observed plasma, and the white regions are those outside the FIPS field of view. Direction labels (e.g., $+X_{MSM'}$) indicate the direction the protons are travelling towards.

Thus far, our investigation into flow braking and flux pileup at Mercury has been statistical in focus. To ground these statistical results, we conclude this section by presenting an example of flow braking and flux pileup in Mercury's magnetotail, demonstrating that the statistical results described above are representative of Mercury's magnetosphere. Figure 5.8 displays MAG and FIPS observations on 07 October 2014 from 18:17:00 to 18:20:00. During this interval, the spacecraft was located in Mercury's post-midnight magnetotail ($Y_{MSM'} = -0.33$ R_M) close to Mercury's nightside surface (altitude of ~700 km). At these coordinates, we expect the spacecraft to be within the typical braking region identified in Section 5.4.1. The spacecraft crossed Mercury's central current sheet, as evidenced by the change in sign of both B_x and the $Z_{MSM'}$. During this crossing, MESSENGER encountered several dipolarizations, marked by vertical red lines, and observed multiple magnetic and plasma signatures of flow braking and flux pileup.

To provide context to the magnetic field signatures observed during this interval, we include the typical magnetic field conditions at the spacecraft's location as shaded grey regions in each of the magnetic field panels. To determine these conditions, for each point in the magnetic field time series within this interval, we select the 10,000 magnetic field measurements taken closest to the spacecraft's current position that do not belong to the current orbit. We perform a weighted average on these measurements, using the squared distance from each measurement to the current spacecraft position as that measurement's weight, and evaluate variance. These statistical magnetic field conditions not only reflect typical or background observations but also reveal effects of the spacecraft's orbit. For example, the crossing of the central current sheet marked by the reversal in B_x agrees well with the statistical magnetic field description, confirming that this crossing is a result of spacecraft motion rather than current sheet motion.

Prior to the arrival of the dipolarizations, the northward component of the magnetic field (B_z) is weak at ~10 nT. At this location, B_z is typically ~70 nT indicating that the current sheet is substantially thinned compared to nominal conditions. Each dipolarization increases the northward component and total field strength, however, the first three dipolarizations represent only transient increases (i.e., local plasma sheet thickening). The dipolarization fronts of the first three dipolarizations increase the northward component (ΔB_z) by 68.2 nT, 38.6 nT, and 45.6 nT over a time of 0.75 s, 0.45 s, and 0.45 s, respectively. Although each of these three dipolarizations reach field strengths of ~40-50 nT following their dipolarization fronts, the enhancements are short-lived, with the magnetic field returning to pre-dipolarization values 5.50 s, 1.65 s, and 4.55 s after the start of each dipolarization, respectively. The final, and largest, dipolarization is associated with a prolonged enhancement of the magnetic field. The final dipolarization front increases B_z by 83.4 nT over 0.90 s, reaching the statistically-observed B_z for the only time during this interval. The final dipolarization front reaches a local maximum in B_z (95 nT), but unlike the other dipolarizations, the magnetic field does not return to pre-dipolarization values. Instead, B_z remains enhanced at ~55 nT with fluctuations of ±13 nT through the remainder of the interval. This magnetic field is still weaker than what is normally observed at this location (~100 nT) but is notably enhanced above the field at the beginning of the interval, representing a more permanent dipolarization of the field.

In addition to these B_z signatures, the dipolarizations within this interval are also associated with B_x and B_y perturbations. The first dipolarization is associated with intensification of both B_x and B_y, while the final three dipolarizations display larger-amplitude quasi-periodic fluctuations in both B_x and B_y. These quasi-periodic structures are most readily observed with the third and fourth dipolarizations. Between the third and fourth dipolarizations, the enhancements in B_x last for ~1 s over which B_x changes by ~13 nT. The largest B_x perturbation is associated with the final dipolarization front, with $\Delta B_x = 30$ nT. This large B_x perturbation is associated with a bipolar B_y perturbation, consistent with the structure of an electromagnetic pulse (e.g., Parks et al., 2007). Following the final dipolarization front, additional fluctuations in B_x and B_y are observed. These perturbations (marked by cyan arrows) are perpendicular to the magnetic field direction, have amplitudes ~6 nT, and period ~3.5 s. Near ~18:18:55, additional fluctuations are observed in the magnetic field (marked by lime arrows), although these are predominately parallel to the magnetic field (primarily along B_z). These perturbations are similar to those analyzed at higher latitudes by Sun et al. (2015). The perpendicular fluctuations following the final dipolarization front are consistent with Alfvén waves, while the later parallel fluctuations are consistent with compressional wave modes. Following the interpretation of Sun et al. (2015), these waves are suggestive of flow braking.

To determine if these dipolarizations are associated with strong flows, we examine FIPS proton flux maps. The two FIPS scans that cover the first three dipolarizations correspond to the gold-boxed flux map, while the scans that cover the final dipolarization correspond to the magenta-boxed flux map. For both ranges, the FIPS field of view is oriented such that it most readily detects protons traveling in $-Y_{MSM'}$ and $-Z_{MSM'}$ directions. While the missing regions of velocity space are too large to unambiguously determine flow direction and magnitude, the FIPS scans that cover the first three dipolarizations (18:18:07 to 18:18:28) are indicative of a strong sunward flow with more plasma traveling in $+X_{MSM'}$ than in $-X_{MSM'}$. In contrast, the final dipolarization does not appear to be associated a strong sunward flow, with its flux map (18:18:28 to 18:18:49) appearing substantially more isotropic.

Taken together, these magnetic field and plasma observations are indicative of flow braking and flux pileup in Mercury's magnetotail. In the span of ~30 s, the spacecraft observed four dipolarizations. The first three are associated with fast sunward flow and pass over the spacecraft, resulting in temporary, transient increases in the magnetic field. The final dipolarization, in contrast, displays no meaningful flow along $X_{MSM'}$, and is instead associated with a prolonged magnetic field enhancement, characteristic of flow braking and flux pileup. Additionally, perturbations in the magnetic field following the final dipolarization are consistent with Alfvén and compressional waves expected to be associated with flow braking at Mercury (Sun et al., 2015). From the first dipolarization to the last in this time series, the spacecraft moved only 40 km sunward, 3 km duskward, and 60 km northward. For the spacecraft to observe a series of sunward-traveling dipolarizations followed by an approximately stagnant flux pileup region while moving only a small distance in Mercury's magnetotail, it is possible that the final dipolarization may in fact be the piled-up signature of the first three dipolarizations after they experienced intense flow braking.

5.5. Discussion

Using an algorithm to identify magnetotail dipolarizations in the magnetic field time series, we have presented both statistical and case study evidence for the flow braking and subsequent magnetic flux pileup associated with dipolarizations in Mercury's magnetotail. We find that downtail of the braking region, the frequency of dipolarizations and the typical sunward flow speed of these structures remains approximately constant. As dipolarizations approach

Mercury's near-tail region, as indicated by where the proton plasma beta (β) reaches unity, both the frequency and flow speed of dipolarizations decrease substantially. These observations are analogous to the earliest evidence for the existence of a flow-braking region at Earth (e.g., Shiokawa et al., 1997). While Mercury's braking region is thinner (~500 km) and situated closer to the planet (~900 km in altitude) than Earth's, the intense magnetic pressure gradients at both planets appear responsible for flow braking and deflection. Coincident with the decrease in dipolarization frequency and flow speed, the magnetic pressure gradient in Mercury's near-tail region increases by a factor of 60 ± 20. The proton plasma pressure gradient also increases at this location, but it increases by a more modest factor (16 ± 7).

We find that as these dipolarization flows brake, they accumulate magnetic flux in Mercury's near-tail region. Within the braking region, dipolarizations are associated with prolonged enhancements in the magnetic field, as opposed to transient enhancements observed with dipolarizations traveling quickly over the spacecraft upstream of the braking region. We examine the magnetic flux budget of both this pileup region and of individual dipolarizations to determine that spacecraft observations support these statistical findings. Indeed, although building the synoptic flux pileup signature requires several dipolarizations (5 ± 2), dipolarizations are typically observed in series, such that the spacecraft has observed this number or more of dipolarizations in sequence. More simply, we estimate that the flux pileup region contains 0.28 ± 0.08 MWb. Loading of Mercury's magnetotail increases the magnetic flux content of the lobes by 0.69 ± 0.38 MWb (Imber & Slavin, 2017), so there is sufficient magnetic flux loaded into the magnetotail during a typical substorm at Mercury to develop the flux pileup region (i.e., large-scale dipolarization).

5.5.1 Westward Expansion of Magnetic Flux Pileup

We find that the synoptic signature of magnetic flux pileup associated with dipolarizations in Mercury's magnetotail exhibits an asymmetry about local midnight, with a stronger dipolarized field pre-midnight than post-midnight. This asymmetry in pileup is likely related to the asymmetry in dipolarization occurrence and westward expansion of the pileup region. Consistent with previous studies of Mercury's dipolarizations (Sun et al., 2016; Dewey et al., 2018), we find that dipolarizations are more common to Mercury's post-midnight magnetotail as measured both by frequency and by fraction of orbits that possess them. Without the ability to constrain the magnetic flux transported by each dipolarization independently, the increased rate of dipolarizations post-midnight indicates more magnetic flux is usually transported to the post-midnight inner magnetosphere than that pre-midnight, such that we expect pileup to initiate more commonly post-midnight. We observe that dipolarization-related V_y flows within the braking region are consistently duskward suggesting that the pre-midnight pileup signature could be the westward expansion of post-midnight pileup. At Earth, azimuthal expansion occurs after substantial pileup. If this is true for Mercury, then we expect to observe only the strongest instances of pileup pre-midnight, which could explain the cross-tail asymmetry in pileup strength. Furthermore, the greater rate of dipolarizations post-midnight could average down the statistical pileup signature there if not all dipolarizations within the braking region exhibit local pileup. For example, the case study examined in Section 5.4.4 contains four dipolarizations, only the last of which exhibits pileup. Since the four dipolarizations are observed close to each other spatially, they each map to the same spatial bin for determining the statistical pileup signature in Figure 5.5. The first three dipolarizations dilute the pileup signature of the forth in our statistical examination of large-scale pileup. Therefore, the pre-midnight pileup signature could be biased by stronger, less frequent instances of pileup resulting from westward expansion while the post-midnight signature could be averaged down by non-pileup events.

5.5.2 Substorm Current Wedge Formation

At Earth, flux pileup is associated with the substorm current wedge: could a current wedge exist at Mercury? Without ground magnetometers or multi-point spacecraft observations, it may be difficult to determine unambiguously. However, the results described in Section 5.4 suggest it may be possible, if not common, to Mercury's substorms. Alfvén waves, and the field-aligned currents they carry, communicate motion of magnetic field lines of the magnetosphere to the inner conducting boundary in which they are rooted (Southwood & Kivelson, 1991). For Earth, this boundary is the ionosphere, while at Mercury, it is its large conducting core. For a static field-aligned current system like the substorm current wedge to establish, it requires multiple bounces of the current-carrying Alfvén waves (see, e.g., Kepko et al., 2015b). At Mercury's braking region, we find a typical Alfvén speed of ~1,000 km/s (see Figure 5.4d). We estimate, by assuming dipole field line geometry, that field lines are ~2 R_M in length above Mercury's conducting core at local midnight within the braking region. For such locations close to the planet, the assumption of dipole field line geometry is expected to be valid (see, e.g., Rong et al., 2018). To execute a complete round-trip bounce would therefore require ~10 s for an Alfvén wave assuming the Alfvén speed remains constant along the field line. If we assume the magnetic field strength along the field line scales like that of a dipole field line, then the round-trip time would be ~6 s. The typical substorm unloading time at Mercury is ~100 s (Imber & Slavin, 2017), allowing for many bounces of Alfvén waves within the braking region.

Although the typical substorm unloading duration allows for many (~10-16) bounces of Alfvén waves to attempt to establish a static current system, the resistive regolith that covers Mercury conductive core presents additional restraints on establishing a current wedge. To communicate with the core, the skin depth of the Alfvén wave must be greater than the depth of the regolith. With a period of ~6-10 s and a height-integrated regolith conductivity of ~1 siemen (Anderson et al., 2014), the skin depth of these Alfvén waves would be between 750-960 km, which is greater than the regolith layer (~400 km). While these Alfvén waves reach the conductive core, their passage through the resistive regolith reduces their current density. In a round-trip bounce, the waves pass through an accumulated ~1,600 km of regolith, such that the amplitude (i.e., current density) of the waves after a complete bounce would only be ~12-19% the initial value. Therefore, while a single Alfvén wave within the braking region may complete a sufficient number of bounces during a typical substorm unloading to establish a static field-aligned current system, the resulting current density would be negligible. Furthermore, while the bounce time is substantially smaller than the substorm unloading time at Mercury, it is on the similar time scale as an individual dipolarization. As observed by dipolarizations passing over the spacecraft, the transient increase in the magnetic field associated with individual dipolarizations last for ~10 s (see Dewey et al., 2017 and Figure 5.5b above). Dipolarizations are expected to interact with the braking region for about this duration as well. This timescale allows for only ~1-2 round-trip bounces of an Alfvén wave, an insufficient number to prevent the dipolarization structure from dissipating. Both the damping of Alfvén waves and the dissipation of an individual dipolarization structure before a static field-aligned system can be established point towards a common solution: continuous supply of dipolarizations.

When observed, dipolarizations are more commonly observed in series with other dipolarizations than as isolated events (see Figure 5.7b). A series of dipolarizations, one after another, would supply new Alfvén waves to the braking region (e.g., Sun et al., 2015 and Section 5.4.4 above) and allow existing Alfvén waves to maintain the magnetic shear about incoming dipolarizations that separate them from the surrounding plasma (i.e., prevent dissipation). Indeed, from flux budget analysis of a typical dipolarization compared with the flux loaded into the magnetotail (Imber & Slavin, 2017), we expect multiple (13 ± 9) dipolarizations during a substorm unloading phase. With most dipolarizations observed ~5-20 s apart (Figure 5.7c), these dipolarizations would arrive at the braking region within 1-2 Alfvén bounce times of another. Therefore, despite the limitations imposed by the conducing core, the resistive regolith, and the Alfvén bounce times, observations of dipolarizations at Mercury suggest a current wedge structure appears possible to form in Mercury's magnetotail. With the expectation that such a current wedge at Mercury would require the interaction between the field-aligned current systems (i.e., Alfvén waves) of multiple, successive dipolarizations, it is surprisingly similar to the "wedgelet" conceptual model of Earth's substorm current wedge.

With the formation of a current wedge possible at Mercury, we determine its characteristics by examining the synoptic flux pileup signature (i.e., large-scale dipolarization) of Figure 5.5. Using a simple current wedge line model (e.g., Poh et al., 2017b), we estimate that the current consistent with this enhanced δB_z would need to be ~14.6 ± 5.0 kA in the plasma sheet. This current is ~20 times weaker than that at Earth (e.g., Kepko et al., 2015b; Birn et al., 2019). From the weak sunward flow in the braking region (~50-100 km/s), we estimate that the potential drop across the current wedge in the equatorial plane would be ~12.2 ± 3.4 kV, indicating a height-integrated electrical conductance of ~0.8 ± 0.4 siemens, which is consistent with recent estimates from Mercury's Region-1 static current system (Anderson et al., 2014).

5.5.3 Core Induction and Surface Precipitation

The substorm current wedge may not be the only means by which dipolarizations and the magnetotail couple to Mercury's conducting core. Mercury's core responds to compression of the magnetosphere by inducing currents on its surface to resist these changes. Although most thoroughly studied with regards to changes in solar wind dynamic pressure (e.g., Slavin et al., 2014; Jia et al., 2015; Johnson et al., 2016; Jia et al., 2019), studies of Mercury's magnetotail have discussed the possibility of inducing currents on the core's nightside surface in response to compression of the planet's nightside inner magnetosphere (e.g., Dewey et al., 2018). Based on our findings, we expect that dipolarizations are unlikely to elicit a strong inductive response from the planetary core. Dipolarizations provide only small increases in dynamic pressure with which to compress Mercury's nightside magnetic field. Given the characteristics of dipolarizations described in Section 5.4 and by Dewey et al. (2018), the typical dynamic pressure of a dipolarization is of order ~0.1 nPa. Mercury's inner magnetosphere has magnetic pressure of order ~5 nPa (see Figure 5.4) so individual dipolarizations are unlikely to substantially compress the nightside inner magnetosphere and generate inductive currents in the core. By comparison, changes in dynamic pressure along Mercury's highly eccentric orbit (~11 nPa at aphelion to ~26 nPa at perihelion, Slavin & Holzer, 1981) result in induction currents that change Mercury's magnetic moment by only ~5% (Johnson et al., 2016). To reach similar dynamic pressures in Mercury's magnetotail, dipolarizations would need to be associated with extreme density (> 5 cm^{-3}) and flow speeds (>1,000 km/s). Even then, dipolarizations are localized in cross-tail extent so they would only compress the nightside inner magnetosphere regionally. Increases in solar wind dynamic pressure compress the dayside magnetosphere globally so any nightside inductive currents would be much smaller in spatial extent on the core than the dayside equivalents.

Dipolarizations also interact with Mercury's surface. There is some evidence that a small fraction of dipolarizations may reach Mercury's low latitude nightside surface. The occurrence maps of dipolarizations (Figure 5.2) indicate that some dipolarizations are observed at < 200 km altitude. Furthermore, organizing dipolarization frequency about $\beta = 1$ (Figure 5.4) indicates that far downstream of the braking region (e.g., $\Delta X_{MSM'} = 0.5\ R_M$) dipolarizations are still observed even if at a low rate. At these locations, the rate of dipolarizations (~0.1-0.2 min^{-1}) is much lower than the downtail occurrence (~0.6 min^{-1}) implying that no more than ~10-20% of dipolarizations travel far beyond the braking region. At the flanks of the magnetotail, dipolarizations traveling this far beyond $\beta = 1$ may return their magnetic flux to the dayside directly, while those behind the planet may impact the low latitude surface (or approach within a gyroradius of the surface). As most precipitation in Mercury's plasma sheet is expected at mid- or high-latitudes (e.g., Korth et al., 2014), the opportunity for dipolarizations to transport plasma and magnetic flux directly to the low latitude surface may have consequences for exospheric generation and space weathering (e.g., Raines et al., 2016). Aside from dipolarizations reaching the low-latitude nightside surface, the close proximity of the braking region to the planet's surface (altitude of ~900 km) results in large expected loss cones (~25-40°) such that substantial plasma precipitation may occur with most dipolarizations in the braking region already. The mass transport of dipolarizations in Mercury's magnetotail deserves further dedicated study.

5.6. Conclusions

We present strong evidence for flow braking and magnetic flux pileup associated with dipolarizations in Mercury's magnetotail. We summarize our findings in Figure 5.9, a schematic representation of flow braking, flux pileup, and current wedge formation. Dipolarizations first begin in the mid-tail as a product of reconnection and are transported sunward by the fast reconnection outflows. As dipolarizations and their associated flows approach Mercury's inner magnetosphere, the flows encounter steep magnetic pressure gradients from Mercury's planetary dipole field, causing the flows to brake and deflect. A small fraction (no more than ~10-20%) of dipolarizations may be able to reach the dayside magnetosphere or Mercury's nightside surface while the remainder typically brake within a region ~500 km in thickness located ~900 km in altitude above Mercury's local midnight surface as evidenced by substantial and significant decreases in dipolarization frequency and sunward flow speed. As dipolarizations brake, their transported magnetic flux accumulates. Current-carrying Alfvén waves generated by the motion and braking of the dipolarization field lines communicate these changes to Mercury's conductive core. As additional dipolarizations brake and pileup, the large-scale dipolarization near the inner magnetosphere expands westward into the pre-midnight magnetotail. Simultaneously, the interaction of the Alfvén waves from the braking of multiple, continuous dipolarizations may be able to establish a large-scale current system to support the enhanced magnetic field within the pileup region, akin to Earth's substorm current wedge. Despite the differences between Mercury and Earth's magnetospheres, namely the smaller spatiotemporal scales, enhanced effects of magnetic reconnection, and lack of ionosphere at Mercury, the dynamics of dipolarizations are surprisingly similar. While we have presented both statistical analysis and a case study in support of our conclusions, observations from the en route BepiColombo spacecraft mission and global modeling simulations of Mercury's magnetosphere will be of particular value to continue to investigate and constrain these results.

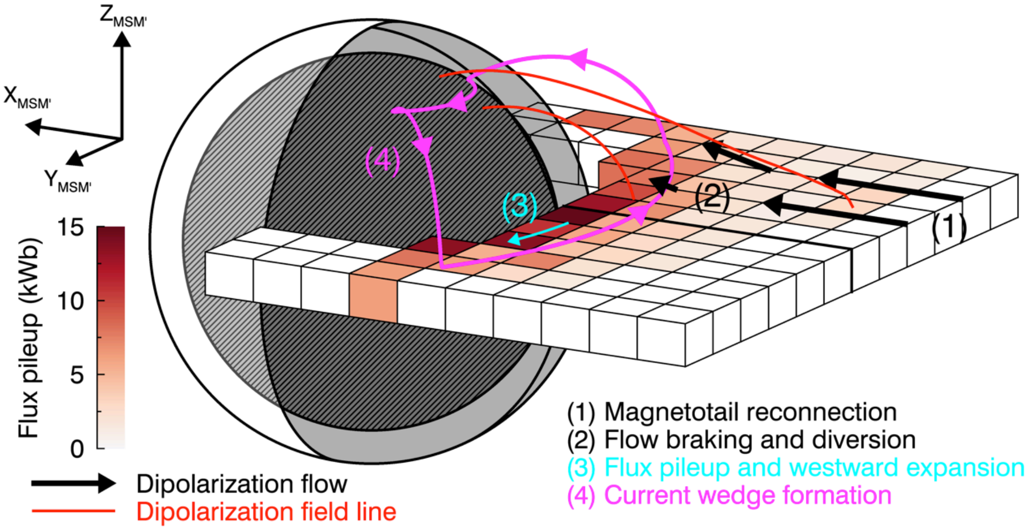

Figure 5.9. Schematic of flow braking, flux pileup, and current wedge formation from dipolarizations within Mercury's magnetotail. The colored boxes are the pileup observations from Figure 5.5. Features are at accurate scaling with respect to each other.

5.7 Acknowledgements

NASA's Earth and Space Science Fellowship Program (80NSSC17K0493) supported R. M. Dewey. NASA Grants NNX16AJ67G and 80NSSC18K1137 supported W. Sun and J. A. Slavin. R. M. Dewey would like to thank A. Runov, A. Artemyev, C. Gabrielse, V. Angelopoulos, and T. Nishimura for valuable conversations. All MESSENGER data used in this study are available from the NASA Planetary Data System.

5.8 References

Anderson, B. J., Acuña, M. H., Lohr, D. A., Scheifele, J., Raval, A., Korth, H., & Slavin, J. A. (2007). The Magnetometer instrument on MESSENGER. *Space Science Reviews,* **131**(1-4), 417–450. https://doi.org/10.1007/s11214-007-9246-7

Anderson, B. J., Johnson, C. L., Korth, H., Purucker, M. E., Winslow, R. M., Slavin, J. A., et al. (2011). The global magnetic field of Mercury from MESSENGER orbital observations. *Science,* **333**(6051), 1859–1862. https://doi.org/10.1126/science.1211001

Anderson, B. J., Johnson, C. L., Korth, H., Slavin, J. A., Winslow, R. M., Phillips, R. J., Solomon, S. C., & McNutt Jr., R. L. (2014). Steady-state field-aligned currents at Mercury. *Geophysical Research Letters,* **41**, 7444–7452. https://doi.org/10.1002/2014GL061677

Andrews, G. B., Zurbuchen, T. H., Mauk, B. H., Malcom, H., Fisk, L. A., Gloeckler, G., et al. (2007). The Energetic Particle and Plasma Spectrometer instrument on the MESSENGER spacecraft. *Space Science Reviews,* **131**(1-4), 523–556. https://doi.org/10.1007/s11214-007-9272-5

Angelopoulos, V., Baumjohann, W., Kennel, C. F., Coroniti, F. V., Kivelson, M. G., Pellat, R., et al. (1992). Bursty bulk flows in the inner central plasma sheet. *Journal of Geophysical Research,* **97**(A4), 4027–4039. https://doi.org/10.1029/91JA02701

Ashour-Abdalla, M., El-Alaoui, M., Goldstein, M. L., Zhou, M., Schriver, D., Richard, R., …Hwang, K.-J. (2011). Observations and simulations of non-local acceleration of electrons in magnetotail magnetic reconnection events. *Nature Physics,* **7**, 360 365. https://doi.org/10.1038/nphys1903

Baumjohann, W., Hesse, M., Kokubun, S., Mukai, T., Nagai, T., & Petrukovich, A. A. (1999). Substorm dipolarization and recovery. *Journal of Geophysical Research*, **104**, 24995–25000. https://doi.org/10.1029/1999JA900282

Birn, J., Hesse, M., Haerendel, G., Aumjohann, W. B., & Shiokawa, K. (1999). Flow braking and the substorm current wedge. *Journal of Geophysical Research: Space Physics,* **114**(A), 19895–19904.

Birn, J., Nakamura, R., Panov, E., & Hesse, M. (2011). Bursty bulk flows and dipolarization in MHD simulations of magnetotail reconnection. *Journal of Geophysical Research*, **116**, A01210. https://doi.org/10.1029/2010JA016083

Birn, J., Hesse, M., Nakamura, R., & Zaharia, S. (2013). Particle acceleration in dipolarization events. *Journal of Geophysical Research: Space Physics,* **118**, 1960–1971. https://doi.org/10.1002/jgra.50132

Birn, J., Liu, J., Runov, A., Kepko, L., & Angelopoulos, V. (2019). On the contribution of dipolarizing flux bundles to the substorm current wedge and to flux and energy transport. *Journal of Geophysical Research: Space Physics,* **124**, 5408–5420. https://doi.org/10.1029/2019JA026658

Delcourt, D. C., Grimald, S., Leblanc, F., Berthelier, J.-J., Millilo, A., Mura, A., et al. (2003). A quantitative model of planetary Na+ contribution to Mercury's magnetosphere. *Annales Geophysicae*, **21**(8), 1723–1736. https://doi.org/10.5194/angeo-21-1723-2003

Delcourt, D. (2013). On the supply of heavy planetary material to the magnetotail of Mercury. *Annales Geophysicae,* **31**(10), 1673–1679. https://doi.org/10.5194/angeo-31-1673-2013

Dewey, R. M., Slavin, J. A., Raines, J. M., Baker, D. N., & Lawrence, D. J. (2017). Energetic electron acceleration and injection during dipolarization events in Mercury's magnetotail. *Journal of Geophysical Research: Space Physics,* **122**, 12,170–12,188. https://doi.org/10.1002/2017JA024617

Dewey, R. M., Raines, J. M., Sun, W., Slavin, J. A., & Poh, G. (2018). MESSENGER observations of fast plasma flows in Mercury's magnetotail. *Geophysical Research Letters,* **45**, 10,110–10,118. https://doi.org/10.1029/2018GL079056

DiBraccio, G. A., Slavin, J. A., Boardsen, S. A., Anderson, B. J., Korth, H., Zurbuchen, T. H.,…Solomon, S. C. (2013). MESSENGER observations of magnetopause structure and dynamics at Mercury. *Journal of Geophysical Research: Space Physics,* **118**, 997–1008. https://doi.org/10.1002/jgra.50123

DiBraccio, G. A., Slavin, J. A., Imber, S. M., Gershman, D. J., Raines, J. M., Jackman, C. M., et al. (2015). MESSENGER observations of flux ropes in Mercury's magnetotail. *Planetary and Space Science,* **115**, 77–89. https://doi.org/10.1016/j.pss.2014.12.016

Dubyagin, S., Sergeev, V., Apatenkov, S., Angelopoulos, V., Runov, A., Nakamura, R., … Larson, D. (2011). Can flow bursts penetrate into the inner magnetosphere? *Geophysical Research Letters,* **38**, L08102. https://doi.org/10.1029/2011GL047016

Fu, H. S., Cao, J. B., Khotyaintsev, Y. V., Sitnov, M. I., Runov, A., Fu, S. Y., … Huang, S. Y. (2013). Dipolarization fronts as a consequence of transient reconnection: In situ evidence. *Geophysical Research Letters,* **40**, 6023–6027. https://doi.org/10.1002/2013GL058620

Gabrielse, C., Harris, C., Angelopoulos, V., Artemyev, A., & Runov, A. (2016). The role of localized inductive electric fields in electron injections around dipolarizing flux bundles. *Journal of Geophysical Research: Space Physics,* **121**, 9560–9585. https://doi.org/10.1002/2016JA023061

Gershman, D. J., Slavin, J. A., Raines, J. M., Zurbuchen, T. H., Anderson, B. J., Korth, H.,…Solomon, S. C. (2013). Magnetic flux pileup and plasma depletion in Mercury's subsolar magnetosheath. *Journal of Geophysical Research: Space Physics,* **118**, 7181–7199. https://doi.org/10.1002/2013JA019244

Imber, S. M., & Slavin, J. A. (2017). MESSENGER observations of magnetotail loading and unloading: Implications for substorms at Mercury. *Journal of Geophysical Research: Space Physics,* **122**, 11,402–11,412. https://doi.org/10.1002/2017JA024332

Janhunen, P., & Kallio, E. (2004). Surface conductivity of Mercury provides current closure and may affect magnetospheric symmetry. *Annals of Geophysics,* **22**(5), 1829–1837. https://doi.org/10.5194/angeo-22-1829-2004

Jia, X., Slavin, J. A., Gombosi, T. I., Daldorff, L. K. S., Toth, G., & van der Holst, B. (2015). Global MHD simulations of Mercury's magnetosphere with coupled planetary interior: Induction effect of the planetary conducting core on the global interaction. *Journal of Geophysical Research: Space Physics,* **120**, 4763–4775. https://doi.org/10.1002/2015JA021143

Jia, X., Slavin, J. A., Poh, G., DiBraccio, G. A., Toth, G., Chen, Y., et al. (2019). MESSENGER observations and global simulations of highly compressed magnetosphere events at Mercury. *Journal of Geophysical Research: Space Physics,* **124**, 229–247. https://doi.org/10.1029/2018JA026166

Johnson, C. L., Philpott, L. C., Anderson, B. J., Korth, H., Hauck, S. A. II, Heyner, D., et al. (2016). Messenger Observations Of Induced Magnetic Fields In Mercury's Core. *Geophysical Research Letters,* **43**, 2436–2444. https://doi.org/10.1002/2015GL067370

Karlsson, T., Hamrin, M., Nilsson, H., Kullen, A., & Pitkänen, T. (2015). Magnetic forces associated with bursty bulk flows in Earth’s magnetotail. *Geophysical Research Letters,* **42**, 3122–3128. https://doi.org/10.1002/2015GL063999

Kaymaz, Z., Siscoe, G. L., & Luhmann, J. G. (1992). IMF draping around the Geotail: IMP 8 observations. *Journal of Geophysical Research*, **19**, 829– 832.

Kepko, L., McPherron, R., Amm, O., Apatenkov, S., Baumjohann, W., Birn, J., & Sergeev, V. (2015a). Substorm current wedge revisited. *Space Science Reviews,* **190**, 1–46. https://doi.org/10.1007/s11214-014-0124-9

Kepko, L., Glassmeier, K.-H., Slavin, J. A., & Sundberg, T. (2015b). Substorm current wedge at Earth and Mercury. In A. Keiling, C. M. Jackman, & P. A. Delamere (Eds.), *Magnetotails in the solar system*. Hoboken, NJ: John Wiley. https://doi.org/10.1002/9781118842324.ch21

Korth, H., Anderson, B. J., Gershman, D. J., Raines, J. M., Slavin, J. A., Zurbuchen, T. H., et al. (2014). Plasma distribution in Mercury's magnetosphere derived from MESSENGER magnetometer and fast imaging plasma spectrometer observations. *Journal of*

Geophysical Research: Space Physics, **119**, 2917–2932. https://doi.org/10.1002/2013JA019567

Korth, H., Anderson, B. J., Johnson, C. L., Slavin, J. A., Raines, J. M., & Zurbuchen, T. H. (2018). Structure and configuration of Mercury's magnetosphere. In S. C. L. R. Nittler, & B. J. Anderson (Eds.), *Mercury: The view after MESSENGER* (Chapter 16, pp. 430–460). London: Cambridge Univ. Press. ISBN: 978-1107154452

Liu, J., Angelopoulos, V., Runov, A., & Zhou, X.-Z. (2013). On the current sheets surrounding dipolarizing flux bundles in the magnetotail: The case for wedgelets. *Journal of Geophysical Research: Space Physics,* **118**, 2000–2020. https://doi.org/10.1002/jgra.50092

Liu, J., Angelopoulos, V., Zhou, X.-Z., & Runov, A. (2014). Magnetic flux transport by dipolarizing flux bundles. *Journal of Geophysical Research: Space Physics,* **119**, 909–926. https://doi.org/10.1002/2013JA019395

McPherron, R. L., Russell, C. T., & Aubry, M. A. (1973). Satellite studies of magnetospheric substorms on August 15, 1968, 9, Phenomenological model for substorms. *Journal of Geophysical Research,* **78**, 3131.

Merkin, V. G., Panov, E. V., Sorathia, K., & Ukhorskiy, A. Y. (2019). Contribution of bursty bulk flows to the global dipolarization of the magnetotail during an isolated substorm. *Journal of Geophysical Research: Space Physics,* **124**, 8647–8668. https://doi.org/10.1029/2019JA026872

Nakamura, M. S., Matsumoto, H., & Fujimoto M. (2002). Interchange instability at the leading part of reconnection jets. *Geophysical Research Letters,* **29**(8), 1247. https://doi.org/10.1029/2001GL013780

Nakamura, R., Baumjohann,W.,Mouikis, C., Kistler, L. M., Runov, A., Volwerk, M., & Balogh, A. (2004). Spatial scale of high-speed flows in the plasma sheet observed by Cluster. *Geophysical Research Letters,* **31**, L09804. https://doi.org/10.1029/2004GL019558

Ogilvie, K. W., Scudder, J. D., Vasyliunas, V. M., Hartle, R. E., & Siscoe, G. L. (1977). Observations at the planet Mercury by the plasma electron experiment, Mariner 10. *Journal of Geophysical Research,* **82**(13), 1807–1824. https://doi.org/10.1029/JA082i013p01807

Ohtani, S., Singer, H. J., & Mukai, T. (2006). Effects of the fast plasma sheet flow on the geosynchronous magnetic configuration: Geotail and GOES coordinated study. *Journal of Geophysical Research,* **111**, A01204. https://doi.org/10.1029/2005JA011383

Panov, E. V., Baumjohann, W., Nakamura, R., Kubyshkina, M. V., Glassmeier, K.-H., Angelopoulos, V., Petrukovich, A. A., & Sergeev, V. A. (2014). Period and damping factor of Pi2 pulsations during oscillatory flow braking in the magnetotail. *Journal of*

Geophysical Research: Space Physics, **119**, 4512–4520. https://doi.org/10.1002/2013JA019633

Parks, G. K., Lee, E., Lin, N. Mozer, F., Wilber, M., Dandouras, I., … Décréau, P. (2007). Solitary electromagnetic pulses detected with super-Alfvénic flows in Earth's geomagnetic tail. *Physical Review Letters,* **98**. https://doi.org/10.1103/PhysRevLett.98.265001

Poh, G., Slavin, J. A., Jia, X., Raines, J. M., Imber, S. M., Sun, W.-J., et al. (2017a). Mercury's cross-tail current sheet: Structure, X-line location and stress balance. *Geophysical Research Letters,* **44**, 678–686. https://doi.org/10.1002/2016GL071612

Poh, G., Slavin, J. A., Jia, X., Raines, J. M., Imber, S. M., Sun, W.-J., et al. (2017b). Coupling between Mercury and its nightside magnetosphere: Cross-tail current sheet asymmetry and substorm current wedge formation. *Journal of Geophysical Research: Space Physics,* **122**, 8419–8433. https://doi.org/10.1002/2017JA024266

Poh, G., Slavin, J. A., Jia, X., Sun, W.-J., Raines, J. M., Imber, S. M., et al. (2018). Transport of mass and energy in Mercury's plasma sheet. *Geophysical Research Letters,* **45**, 12,163–12,170. https://doi.org/10.1029/2018GL080601

Raines, J. M., Gershman, D. J., Zurbuchen, T. H., Sarantos, M., Slavin, J. A., Gilbert, J. A., et al. (2013). Distribution and compositional variations of plasma ions in Mercury's space environment: The first three Mercury years of MESSENGER observations. *Journal of Geophysical Research: Space Physics,* **118**, 1604–1619. https://doi.org/10.1029/2012JA018073

Raines, J. M., Gershman, D. J., Slavin, J. A., Zurbuchen, T. H., Korth, H., Anderson, B. J., … Solomon, S. C. (2014). Structure and dynamics of Mercury's magnetospheric cusp: MESSENGER measurements of protons and planetary ions. *Journal of Geophysical Research: Space Physics,* **119**, 6587–6602. https://doi.org/10.1002/2014JA020120

Raines, J. M., Slavin, J. A., Tracy, P., Gershman, D. J., Zurbuchen, T., Dewey, R. M., & Sarantos, M. (2016). Plasma precipitation on Mercury's nightside and its implications for magnetospheric convection and exosphere generation. *AGU Fall Meeting 2016*, paper #SM53B-08, San Francisco, CA.

Rong, Z. J., Ding, Y., Slavin, J. A., Zhong, J., Poh, G., Sun, W. J., … Shen, C. (2018). The magnetic field structure of Mercury's magnetotail. *Journal of Geophysical Research: Space Physics,* **123**, 548–566. https://doi.org/10.1002/2017JA024923

Runov, A., Angelopoulos, V., Sitnov, M. I., Sergeev, V. A., Bonnell, J., McFadden, J. P., … Auster, U. (2009). THEMIS observations of an earthward-propagating dipolarization front. *Geophysical Research Letters,* **36**, L14106. https://doi.org/10.1029/2009GL038980

Runov, A., Angelopoulos, V., & Zhou, X.-Z. (2012). Multipoint observations of dipolarization front formation by magnetotail reconnection. *Journal of Geophysical Research,* **117**, A05230. https://doi.org/10.1029/2011JA017361

Runov, A., Angelopoulos, V., Gabrielse, C., Zhou, X.-Z., Turner, D., & Plaschkle, F. (2013). Electron fluxes and pitch-angle distributions at dipolarization fronts: THEMIS multipoint observations. *Journal of Geophysical Research: Space Physics,* **118**, 744–755. https://doi.org/10.1002/jgra.50121

Runov, A., Angelopoulos, V., Gabrielse, C., Liu, J., Turner, D. L., & Zhou, X.-Z. (2015). Average thermodynamic and spectral properties of plasma in and around dipolarizing flux bundles. *Journal of Geophysical Research: Space Physics,* **120**, 4369 4383. https://doi.org/10.1002/2015JA021166

Sergeev, V. A., Angelopoulos, V., Gosling, J. T., Cattell, C. A., & Russell, C. T. (1996). Detection of localized, plasma-depleted flux tubes or bubbles in the midtail plasma sheet. *Journal of Geophysical Research,* **101**, 10,817–10,826. https://doi.org/10.1029/96JA00460

Shiokawa, K., Baumjohann, W., & Haerendel, G. (1997). Braking of high-speed flows in the near-Earth tail. *Geophysical Research Letters,* **24**, 1179–1182. https://doi.org/10.1029/97GL01062

Shue, J.-H., Song, P., Russell, C. T., Steinberg, J. T., Chao, J. K., Zastenker, G.,…Kawano, H. (1998). Magnetopause location under extreme solar wind conditions. *Journal of Geophysical Research, 103*, 17,691–17,700. https://doi.org/10.1029/98JA01103

Sitnov, M. I., Swisdak, M., & Divin, A. V. (2009). Dipolarization fronts as a signature of transient reconnection in the magnetotail. *Journal of Geophysical Research*, **114**, A04202. https://doi.org/10.1029/2008JA013980

Slavin, J. A., & Holzer R. E. (1981). Solar wind flow about the terrestrial planets, 1. Modeling bow shock position and shape. *Journal of Geophysical Research*, **86**, 11,401–11,418. doi:10.1029/JA086iA13p11401.

Slavin, J. A., Acuna, M. H., Anderson, B. J., Baker, D. N., Benna, M., Boardsen, S. A., et al. (2009). MESSENGER observations of magnetic reconnection in Mercury's magnetosphere. *Science,* **324**(5927), 606–610. https://doi.org/10.1126/science.1172011

Slavin, J. A., Anderson, B. J., Baker, D. N., Benna, M., Boardsen, S. A., Gloeckler, G., … Zurbuchen, T. H. (2010). MESSENGER observations of extreme loading and unloading of Mercury's magnetic tail. *Science*, **329**(5992), 665–668. https://doi.org/10.1126/science.1188067

Slavin, J. A., Anderson, B. J., Baker, D. N., Benna, M., Boardsen, S. A., Gold, R. E., et al. (2012). MESSENGER and Mariner 10 flyby observations of magnetotail structure and dynamics at Mercury. *Journal of Geophysical Research,* **117**, A01215. https://doi.org/10.1029/2011JA016900

Slavin, J. A., DiBraccio, G. A., Gershman, D. J., Imber, S., Poh, G. K., Raines, J., et al. (2014). MESSENGER observations of Mercury's dayside magnetosphere under extreme solar wind conditions. *Journal of Geophysical Research: Space Physics,* **119**, 8087–8116. https://doi.org/10.1002/2014JA020319

Slavin, J. A., Baker, D. N., Gershman, D. J., Ho, G., Imber, S. M., Krimigis, S. M., & Sundberg, T. (2018). Mercury's dynamic magnetosphere. In S. C. L. R. Nittler, & B. J. Anderson (Eds.), *Mercury: The view after MESSENGER* (Chapter 17, pp. 461–496). London: Cambridge Univ. Press. ISBN: 978-1107154452

Smith, A.W., Slavin, J. A., Jackman, C.M., Poh,G.-K., & Fear, R. C. (2017). Flux ropes in the Hermean magnetotail: Distribution, properties, and formation. *Journal of Geophysical Research: Space Physics,* **122**, 8136–8153. https://doi.org/10.1002/2017JA024295

Sun, W. J., Fu S. Y., Parks, G. K., Liu, J., Yao, Z. H., Shi, Q. Q., Zong, Q. G., Huang, S. Y., Pu, Z. Y., & Xiao, T. (2013). Field-aligned currents associated with dipolarizations fronts. *Geophysical Research Letters*, **40**(17), 4503–4508. https://doi.org/10.1002/grl.50902

Sun, W.-J., Slavin, J. A., Fu, S., Raines, J. M., Sundberg, T., Zong, Q. G., et al. (2015). MESSENGER observations of Alfvénic and compressional waves during Mercury’s substorms. *Geophysical Research Letters,* **42**, 6189–6198. https://doi.org/10.1002/2015GL065452

Sun, W. J., Fu, S. Y., Slavin, J. A., Raines, J. M., Zong, Q. G., Poh, G. K., & Zurbuchen, T. H. (2016). Spatial distribution of Mercury’s flux ropes and reconnection fronts: MESSENGER observations. *Journal of Geophysical Research: Space Physics,* **121**, 7590–7607. https://doi.org/10.1002/2016JA022787

Sun, W. J., Raines, J. M., Fu, S. Y., Slavin, J. A., Wei, Y., Poh, G. K., et al. (2017). MESSENGER observations of the energization and heating of protons in the near-Mercury magnetotail. *Geophysical Research Letters,* **44**, 8149–8158. https://doi.org/10.1002/2017GL074276

Sun, W. J., Slavin, J. A., Dewey, R. M., Raines, J. M., Fu, S. Y., Wei, Y., et al. (2018). A comparative study of the proton properties of magnetospheric substorms at Earth and Mercury in the near magnetotail. *Geophysical Research Letters,* **45**, 7933–7941. https://doi.org/10.1029/2018GL079181

Sun, W. J., Slavin, J. A., Dewey, R. M., Chen, Y., DiBraccio, G. A., Raines, J. M., Jasinski, J. M., Jia, X., Akhavan-Tafti, M. (2020). MESSENGER observations of Mercury’s nightside magnetosphere under extreme solar wind conditions: reconnection-generated structures and steady convection. *Journal of Geophysical Research: Space Physics*. https://doi.org/10.1029/2019JA027490

Sundberg, T., Slavin, J. A., Boardsen, S. A., Anderson, B. J., Korth, H., Ho, G. C., et al. (2012). MESSENGER observations of dipolarization events in Mercury's magnetotail. *Journal of Geophysical Research,* **117**, A00M03. https://doi.org/10.1029/2012JA017756

Ukhorskiy, A. Y., Sorathia, K. A., Merkin, V. G., Sitnov, M. I., Mitchell, D. G., & Gkioulidou, M. (2018). Ion trapping and acceleration at dipolarization fronts: High-resolution MHD and test-particle simulations. *Journal of Geophysical Research: Space Physics,* **123***,* 5580–5589. https://doi.org/10.1029/2018JA025370

Winslow, R. M., Anderson, B. J., Johnson, C. L., Slavin, J. A., Korth, H., Purucker, M. E., … Solomon, S. C. (2013). Mercury's magnetopause and bow shock from MESSENGER Magnetometer observations. *Journal of Geophysical Research: Space Physics,* **118**, 2213–2227. https://doi.org/10.1002/jgra.50237

CHAPTER VI. Conclusions and Future Work

Within this chapter, we return to the guiding science questions introduced in Chapter 1.6. We summarize and synthesize the scientific findings of Chapters 3-5 to shed new light on Mercury's magnetosphere and its substorm dynamics. Scientific understanding is a process, so we conclude with an eye towards future studies to further refine and interrogate the results presented here.

6.1 Guiding Science Questions Revisited

Mercury's magnetosphere shares many similar features with Earth's, including the presence of substorm dynamics. We seek to understand how differences between Mercury and Earth's magnetospheres, namely Mercury's weaker planetary magnetic field, lack of ionosphere, and stronger upstream solar wind forcing affect substorm dynamics between these two planets. Using in situ observations from the MESSENGER spacecraft we focus on Mercury's magnetotail dipolarizations, a feature common to both planets and an integral component of substorm dynamics at Earth (and expected to be at Mercury). We frame our investigation about the three following guiding questions that we will now revisit and discuss in light of our investigations (Chapters 3-5).

1. **How characteristically similar are dipolarizations in Mercury's magnetotail to those at Earth?**

Compared to their surrounding plasma, dipolarizations at Earth are associated with: (1) an enhanced northward magnetic field that exhibits a sharp rise followed usually by a slower decay; (2) an enhanced flow in the sunward direction; (3) an enhanced duskward electric field; (4) thermal plasma depletion and heating; (5) an enhancement of energetic particle flux; (6) increased magnetic pressure and decreased plasma pressure; and (7) current structure (e.g., strong duskward current at the dipolarization front that connects to the ionosphere via field-aligned currents). In addition to these characteristic signatures, dipolarizations at Earth are observed more frequently in the pre-midnight magnetotail.

We find many of the same signatures of dipolarizations at Mercury. An analysis of 538 dipolarizations indicate they exhibit the sharp, step-like increase of the magnetic field at the dipolarization front (ΔB_z ~ 28 nT over Δt_{DF} ~ 2 s) that persists for some time (~10 s), consistent with an increase in magnetic pressure. Within the dipolarization, we find that the thermal proton density decreases by ~20-30% while the thermal proton temperature increases by ~10-30%, consistent with a net decrease in plasma pressure. We find that energetic electrons are closely associated with dipolarizations, typically observing energetic electrons of maximum estimated energy ~120 keV associated with these events. Due to limitations in spacecraft instrumentation, we cannot quantify this enhancement of energetic electrons in terms of flux. Developing and applying a novel technique to determine statistical plasma flows at Mercury, we find that these dipolarizations are associated with strong sunward flow, and correspondingly, an enhanced duskward electric field. When we expand our search for dipolarizations using a new automated technique, we identify dipolarizations with perturbations in the perpendicular components of the magnetic field consistent with field-aligned currents about the dipolarization front. Taken together, these characteristics are surprisingly Earth-like. The most significant difference we observe with dipolarizations between these magnetospheres is that while dipolarizations at Earth are more common to the pre-midnight magnetotail the opposite is true for Mercury.

2. What are the consequences of dipolarizations at Mercury?

Dipolarizations in Earth's magnetotail are important for magnetic flux transport, plasma energization, and substorm current wedge formation. We identify similar importance at Mercury. We find that dipolarizations correspond to local enhancements in magnetic flux transport. The cross-tail electric field of dipolarizations is ~11 mV/m compared to a background convective electric field of ~3 mV/m. A single dipolarization transports ~0.08 MWb, requiring only several (~10) dipolarizations to transport the additional magnetic flux loaded into the magnetotail lobes during a substorm. Without multipoint observations, we cannot directly observe the number active reconnection sites in Mercury's magnetotail during a substorm expansion phase so we are unable to measure the number of dipolarizations typically produced during a substorm. However, when dipolarizations are observed, they are typically observed in series with other dipolarizations (i.e., dipolarizations are infrequently observed in isolation). Dipolarizations observed in series and each associated with strong local convective electric fields indicate that these events contribute substantially to magnetic flux transport during Mercury's substorm process.

Next, dipolarizations at Mercury are not only associated with energetic electrons, but may be the dominant source of these particles in Mercury's magnetosphere. We find direct and indirect association between energetic electron bursts and dipolarizations within the magnetotail. Directly associating these two phenomena, we find approximately 25% of magnetotail energetic electron bursts are coincident with dipolarization of the magnetic field. During these dipolarizations, we find signatures of betatron and Fermi acceleration of electrons to typical maximum energies of ~120 keV. These are the typical maximum energies of electrons observed within Mercury's magnetosphere (Ho et al., 2011; Ho et al., 2012) indicating that dipolarizations are a powerful source of local energetic electron acceleration. Indirect association of energetic electron bursts with dipolarizations suggests the 25% listed above may be substantially underestimating the connection between these two phenomena. Superposed profiles of energetic electron events that are not coincident with a clear dipolarization still exhibit an increase in B_z coincident with the start of the electron burst indicating that some fraction of these events are associated with dipolarization. Furthermore, electrons may have been energized and injected by dipolarizations and have since drifted away from these magnetic structures by the time/location they are observed by the spacecraft allowing energetic electron bursts to be associated with dipolarizations even though they are not coincident with an increase in B_z when observed. Therefore, even events with no increase in B_z may be associated with energization at dipolarizations. Recent evidence (Nikoukar et al., 2018) supports the hypothesis that energetic electrons in the dawnside and dayside magnetosphere originate in the magnetotail (e.g., Baker et al., 2016), so as dipolarizations contribute substantially to energetic electron acceleration in the magnetotail, dipolarizations are likely a major source of Mercury's energetic electron environment.

Finally, dipolarizations at Mercury exhibit flow braking and flux pileup, and suggest the formation of a substorm current wedge structure. Organized by the inner edge of Mercury's plasma sheet ($\beta = 1$), dipolarizations tailward of this point (i.e., $\beta > 1$) display nearly uniform frequency and fast sunward flow speed as a function of downtail distance. Planetward of the inner plasma sheet edge (i.e., $\beta < 1$), the frequency and flow speed of dipolarizations decrease substantially, indicative of flow braking in Mercury's magnetotail. Associated with the same spatial region as flow braking, profiles of dipolarizations' magnetic field exhibit enhanced, persistent increase in B_z long after the typical dipolarization duration, indicative of magnetic flux pileup. We examine the magnetic flux budget of both individual dipolarizations and the pileup region and find that dipolarizations are capable of supplying the necessary flux to develop this synoptic pileup signature, indicative that this pileup structure is physically possible. Finally, we find the synoptic pileup signature is consistent with a current wedge structure. Confirmation of such a temporally variable, large-scale, field-aligned current system may not be possible without multipoint spacecraft and/or ground-based observations. Nevertheless, signatures of flow braking and flux pileup of dipolarizations in Mercury's magnetotail suggest it is possible for a current wedge to form.

3. How do differences between Earth and Mercury's magnetospheres manifest in dipolarizations?

Previous studies have indicated some difference between dipolarizations at Mercury and at Earth, namely that they occur most commonly on different sides of their respective magnetotails. We find additional differences in dipolarization characteristics and consequences between the two planets, stemming from differences between their magnetospheres. Dipolarizations at Mercury are of smaller absolute size, but similar in relative size, to those at Earth. The cross-tail width of Mercury's dipolarizations are ~0.3 R_M = 750 km compared to ~1-3 $R_M \approx$ 10,000 km at Earth. Normalizing the dipolarization width to the cross-tail width of their respective magnetospheres, they represent similar scales (i.e., aspect ratio) of ~0.1. The smaller absolute size results from the smaller spatiotemporal scales at Mercury, while the similar relative sizes hints at something more intrinsic to dipolarizations and perhaps magnetic reconnection in magnetotails.

The smaller absolute size of Mercury's dipolarizations appears to limit particle acceleration at Mercury. While energetic electrons are associated with dipolarizations, Mercury's magnetosphere is absent of energetic ions (see, e.g., Ho et al., 2011; Delcourt, 2013) implying that dipolarizations are not strong energetic ion sources. This is likely a finite gyroradius effect. Protons possess the smallest gyroradii of all ion species (at fixed energy) but their gyroradii are substantially larger than those of electrons. For example, a 120 keV electron has gyroradius ~50 km compared to a 10 keV proton gyroradius of ~750 km in Mercury's magnetotail (~20 nT field). As dipolarization cross-tail width is only ~750 km at Mercury, ions cannot access the betatron and Fermi acceleration that electrons can. Indeed, estimating particle energization with dipolarizations in Chapter 3.5 indicates mild acceleration of superthermal protons far below adiabatic rates (see, additionally, Sun et al., 2018).

While the magnetic field strength of dipolarizations is similar between the magnetospheres, their flow speeds are different. Mercury's dipolarizations travel at ~200 km/s compared to Earth's ~400 km/s. This difference likely stems from the upstream solar wind conditions at Mercury. The greater solar wind density at Mercury's orbital location results in a greater plasma sheet density at Mercury than at Earth, corresponding to a smaller Alfvén speed at Mercury that sets the theoretical limit of dipolarization flow speed. Self-consistently, dipolarizations at Mercury exhibit weaker cross-tail electric field than those at Earth.

In addition to differences in characteristics, consequences of dipolarizations between the magnetospheres stem from the differences in magnetosphere structure. The potential for substorm current wedge formation, in particular, is affected by magnetospheric differences. Discussed in greater detail in Chapter 5.5, Mercury's short substorm duration combined with its lack of ionosphere and smaller Alfvén speed limit the ability for a current wedge structure to form. The conducting core is the most likely avenue for near-planet current closure, but the resistive regolith that surrounds the core is expected to cause severe dissipation of the current-carrying Alfvén waves in addition to limiting the frequencies of waves that can interact with the core. The strong wave damping is exacerbated by the substorm timescales at Mercury. A typical unloading lasts for only ~100 s and a round-trip bounce of an Alfvén wave near the planet is expected to be ~5-10 s, allowing for a smaller number of bounces during substorm expansion/recovery compared to Earth that has an unloading duration of ~1 hr and bounce times of seconds to minute. For current wedge formation, Mercury's spatiotemporal scales and core current-closure require the braking and pileup of multiple, continuous dipolarizations to establish this large-scale field-aligned current system. Additional differences of the current wedge include the reduced current magnitude estimated at Mercury and the direction of azimuthal pileup expansion. Mercury's potential current wedge is expected to carry less current than Earth's, likely due to differences in the height-integrated electrical conductance and the magnetic flux content within the pileup regions of the two planets. For azimuthal pileup expansion, pileup expands eastward at Earth and westward at Mercury, likely due to the preference of dipolarizations on different sides of the magnetotails.

The difference in current wedge formation is particularly notable considering that mechanisms of braking and flux pileup between the two magnetospheres closely resemble each other. At both planets, the strong pressure gradients in the magnetic field associated with the inner edge of the plasma sheet decelerate flows and prevent them from typically traveling deep into the inner magnetosphere. While at Earth ~30% of dipolarizations may reach geosynchronous orbit (Liu et al., 2016), approximately 10-20% of dipolarizations reach the equivalent location at Mercury by impacting Mercury's nightside surface directly. Finally, while each planet observes only a small fraction of dipolarizations propagating into the inner magnetosphere, the consequences of these few dipolarizations are substantially different. At Earth, dipolarizations that make it to the inner magnetosphere can transport and inject energetic particle flux to the radiation belts. At Mercury, the planetary body occupies the equivalent inner magnetosphere to that of Earth so dipolarizations that make it to the inner magnetosphere likely impact the nightside surface directly, corresponding to sources of plasma loss from the magnetosphere, space weathering of the surface, and exospheric generation from the interaction of this plasma with the planet's surface.

Taken together, our investigations into the dynamics of Mercury's dipolarizations as led by our guiding science questions highlight not only the importance of dipolarizations to Mercury's magnetotail, but also the broader importance of comparative magnetospheric studies.

Comparing this aspect of substorm dynamics between the two planetary magnetospheres indicates that while differences between the magnetospheres result in differences in the character and consequences of dipolarizations, these phenomena remain strikingly similar between the two systems. Although Mercury lacks an atmosphere and ionosphere, its large conducting core fills the role as the magnetosphere's conducting inner boundary, allowing for the possibility of substorm current wedge formation. Although Mercury and Earth's magnetospheres represent only two cases of global, planetary magnetic fields driven by external solar wind forcing, the similarities in dipolarization characteristics and consequences suggest the substorm process may be common to similar magnetospheres throughout the universe. As we continue to identify and investigate planets outside of our own solar system, these results highlight some of the likely dynamics of their magnetospheres, whether the planet possesses an atmosphere or not. Scientific inquiry is a process that demands continued and evolving investigation. Therefore, while we may hypothesize how dipolarizations behave throughout the universe, future work can help constrain these ideas.

6.2 Future Work

We highlight several avenues of future research for the topics related to our work, suggesting both areas of study and methods involved. Foremost, the work represented by this thesis rests predominately on analysis of spacecraft-collected data. In our investigations, we do not employ modeling of Mercury's magnetosphere. Several global numerical models of Mercury's magnetosphere exist (e.g., Trávníček et al., 2010; Schriver et al., 2011; Müller et al., 2012; Jia et al., 2015; Fatemi et al., 2018; Exner et al., 2018; Chen et al., 2019; Echterling et al., 2019) and they can each provide valuable insight into the dynamics of dipolarizations in

Mercury’s magnetosphere. Of particular interest will be the topic of flow braking, flux pileup, and current wedge formation as the topic of current wedge formation at Mercury has been long-speculated and much debated (e.g., Kepko et al., 2015; Poh et al., 2017). In addition to modeling Mercury’s system, observations from the BepiColombo mission (e.g., Balogh et al., 2007) will continue to improve our understanding of Mercury and its space environment. For topics related to dipolarizations, the dual spacecraft nature of the BepiColombo mission will provide valuable multipoint observations of dipolarizations in the magnetotail, allowing us to constrain dipolarization evolution and braking directly. Finally, examining other magnetospheres and their dynamics will provide valuable insights. Jupiter and Saturn’s magnetospheres, for example, are substantially larger than Mercury or Earth’s and are internally driven by the fast rotation of these gas giants. Understanding if or how the substorm process manifests in these large, internally driven magnetospheres will highlight how the size and forcing of magnetospheres plays a role in substorm dynamics. In addition, the moon Ganymede stands out for particular interest. Similar to Mercury, Ganymede possesses a global magnetic field and lacks an atmosphere (Kivelson et al., 1996). Different to both Earth and Mercury, however, Ganymede does not interact with the supersonic solar wind, but rather Jupiter’s subsonic magnetosphere resulting in a different type of magnetosphere interaction as well as steadier upstream conditions (Jia et al., 2010). The upcoming JUICE spacecraft (Grasset et al., 2013) that will collect in situ observations of Ganymede’s space environment will be of particular use. Understanding if Ganymede can possess substorm activity, particularly dipolarizations, enables us to refine our estimates of how common dipolarizations, their characteristics, and their consequences are to the universe.

6.3 References

Baker, D. N., Dewey, R. M., Lawrence, D. J., Goldsten, J. O., Peplowski, P. N., Korth, H., … Solomon, S. C. (2016). Intense energetic electron flux enhancements in Mercury's magnetosphere: An integrated view with high-resolution observations from MESSENGER. *Journal of Geophysical Research: Space Physics*, **121**, 2171–2184. https://doi.org/10.1002/2015JA021778

Balogh, A., Grard, R., Solomon, S. C., Schulz, R., Langevin, Y., Kasaba, Y., & Fujimoto, M. (2007). Missions to Mercury. *Space Science Reviews*, **132**, 611–645. https://doi.org/10.1007/s11214-007-9212-4

Chen, Y., Tóth, G., Jia, X., Slavin, J. A., Sun, W., Markidis, S., et al. (2019). Studying dawn-dusk asymmetries of Mercury's magnetotail using MHD-EPIC simulations. *Journal of Geophysical Research: Space Physics*, **124**, 8954–8973. https://doi.org/10.1029/2019JA026840

Delcourt, D. (2013). On the supply of heavy planetary material to the magnetotail of Mercury. *Annales Geophysicae,* **31**(10), 1673–1679. https://doi.org/10.5194/angeo-31-1673-2013

Echterling, N., Schriver, D., Travnicek, P. M., Lapenta, G., Amaya, J., Richard, R. L., Berchem, J., El-Alaoui, M., & Walker, R. J. (2019). Understanding multi-scale plasma energization in Mercury's magnetosphere using global kinetic simulations and MESSENGER data. *AGU Fall Meeting 2019*, paper #SM51A-06, San Francisco, CA.

Exner, X., Heyner, D., Liuzzo, L., Motschmann, U., Shiota, D., Kusano, K., & Shibayama, T. (2018). Coronal mass ejection hits mercury: A.I.K.E.F. hybrid-code results compared to MESSENGER data. *Planetary and Space Science*, **153**, 89–99. https://doi.org/10.1016/j.pss.2017.12.016

Fatemi, S., Poirier, N., Holmström, M., Lindkvist, J., Wieser, M., & Barabash, S. (2018). A modelling approach to infer the solar wind dynamic pressure from magnetic field observations inside Mercury's magnetosphere. *Astronomy and Astrophysics*, **614**, A132. https://doi.org/10.1051/0004-6361/201832764

Grasset, O., Dougherty, M. K., Coustenis, A., Bunce, E. J., Erd, C., Titov, D., Bunce, E., Coustenis, A., Blanc, M., Coates, A., Drossart, P., Fletcher, L., Hussmann, H., Jaumann, R., Krupp, N., Prieto-Ballesteros, O., Tortora, P., Tosi, F., & Van Hoolst, T. (2013). JUpiter ICy moons Explorer (JUICE): An ESA mission to orbit Ganymede and to characterise the Jupiter system. *Planetary and Space Science*, **78**, 1– 21. https://doi.org/10.1016/j.pss.2012.12.002

Ho, G. C., Krimigis, S. M., Gold, R. E., Baker, D. N., Anderson, B. J., Korth, H., … Solomon, S. C. (2012). Spatial distribution and spectral characteristics of energetic electrons in

Mercury’s magnetosphere. *Journal of Geophysical Research*, **117**, A00M04. https://doi.org/10.1029/2012JA017983

Ho, G. C., Krimigis, S. M., Gold, R. E., Baker, D. N., Slavin, J. A., Anderson, B. J., … Solomon, S. C. (2011). MESSENGER observations of transient bursts of energetic electrons in Mercury’s magnetosphere. *Science*, **333**(6051), 1865–1868. https://doi.org/10.1126/science.1211141

Jia, X., Walker, R. J., Kivelson, M. G., Khurana, K. K., & Linker, J. A. (2010). Dynamics of Ganymede's magnetopause: Intermittent reconnection under steady external conditions. *Journal of Geophysical Research*, **115**, 12202. https://doi.org/10.1029/2010JA015771

Jia, X., Slavin, J. A., Gombosi, T. I., Daldorff, L. K. S., Toth, G., & van der Holst, B. (2015). Global MHD simulations of Mercury's magnetosphere with coupled planetary interior: Induction effect of the planetary conducting core on the global interaction. *Journal of Geophysical Research: Space Physics*, **120**, 4763–4775. https://doi.org/10.1002/2015JA021143

Kepko, L., Glassmeier, K.-H., Slavin, J. A., & Sundberg, T. (2015). Substorm current wedge at Earth and Mercury. In A. Keiling, C. M. Jackman, & P. A. Delamere (Eds.), *Magnetotails in the solar system*. Hoboken, NJ: John Wiley. https://doi.org/10.1002/9781118842324.ch21

Kivelson, M. G., Khurana, K. K., Russell, C. T., Walker, R. J., Warnecke, J., Coroniti, F. V., Polanskey, C., Southwood, D. J., & Schubert, G. (1996). Discovery of Ganymede's magnetic field by the Galileo spacecraft. *Nature*, **384**, 537– 541. https://doi.org/10.1038/384537a0

Liu, J., Angelopoulos, V., Zhang, X.-J., Turner, D. L., Gabrielse, C., Runov, A., Li, J., Funsten, H. O., & Spence, H. E. (2016). Dipolarizing flux bundles in the cis-geosynchronous magnetosphere: Relationship between electric fields and energetic particle injections. *Journal of Geophysical Research: Space Physics*, **121**, 1362–1376. https://doi.org/10.1002/2015JA021691

Müller, J., Simon, S., Wang, Y.-C., Motschmann, U., Heyner, D., Schüle, J., Ip, W.-H., Kleindienst, G., & Pringle, G. J. (2012). Origin of Mercury's double magnetopause: 3D hybrid simulation study with A.I.K.E.F. *Icarus*, **218**, 666–687. https://doi.org/10.1016/j.icarus.2011.12.028

Nikoukar, R., Lawrence, D. J., Peplowski, P. N., Dewey, R. M., Korth, H., Baker, D. N., & McNutt, R. L. Jr. (2018). Statistical study of Mercury's energetic electron events as observed by the Gamma-Ray and Neutron Spectrometer instrument onboard MESSENGER. *Journal of Geophysical Research: Space Physics*, **123**, 4961–4978. https://doi.org/10.1029/2018JA025339

Poh, G., Slavin, J. A., Jia, X., Raines, J. M., Imber, S. M., Sun, W.-J., et al. (2017). Coupling between Mercury and its nightside magnetosphere: Cross-tail current sheet asymmetry and substorm current wedge formation. *Journal of Geophysical Research: Space Physics,* **122**, 8419–8433. https://doi.org/10.1002/2017JA024266

Schriver, D., Trávníček, P. M., Anderson, B. J., Ashour-Abdalla, M., Baker, D. N., Benna, M., et al. (2011). Quasi-trapped ion and electron populations at mercury. *Geophysical Research Letters*, **38**, L23103. https://doi.org/10.1029/2011GL049629

Sun, W. J., Slavin, J. A., Dewey, R. M., Raines, J. M., Fu, S. Y., Wei, Y., et al. (2018). A comparative study of the proton properties of magnetospheric substorms at Earth and Mercury in the near magnetotail. *Geophysical Research Letters,* **45**, 7933–7941. https://doi.org/10.1029/2018GL079181

Trávníček, P. M., Schriver, D., Hellinger, P., Herčík, D., Anderson, B. J., Sarantos, M., & Slavin, J. A. (2010). Mercury's magnetosphere–solar wind interaction for northward and southward interplanetary magnetic field: Hybrid simulations. *Icarus*, **209**(1), 11–22. https://doi.org/10.1016/j.icarus.2010.01.008

APPENDICES

APPENDIX A. Energetic Electron Event Identification Algorithm

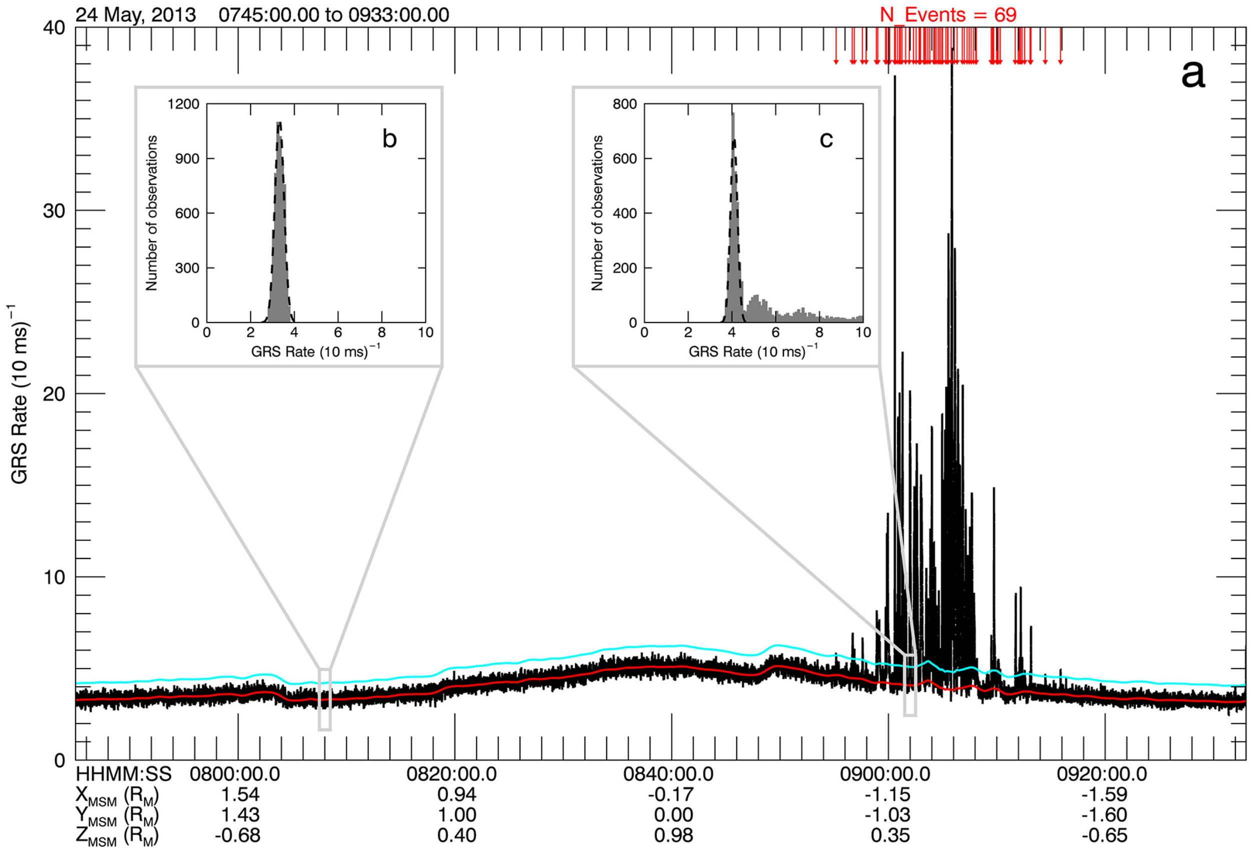

Figure A1. (a) Example of the identification algorithm determining the background count rate (red) and level of significance (cyan) from the GRS observations (black). The GRS count rate has been smoothed by a 1 s moving boxcar average. During this interval, the algorithm successfully adapts to changes in the count rate due to spacecraft pointing and altitude and identifies 69 electron events (red arrows). Inserted are two examples of the sliding window and Gaussian fitting used to determine the background count rate during (b) an interval with no electron events and (c) an interval with electron events. The dashed black line corresponds to the final Gaussian fit used to determine the background count rate and significance.

The energetic electron detection technique is described briefly in Section 3.3. In this appendix, we discuss the identification procedure in detail. Figure A1a displays an example of the algorithm background (red) determined from the GRS count rate (black) during the 24 May 2013 07:45 magnetospheric pass. The algorithm identified 69 electron events (red arrows) as intervals when the GRS rate exceeds the level of significance (cyan). The two inserts depict the local GRS distribution used to generate the background during two windows, one without electron events (Figure A1b) and one with electron events (Figure A1c).

At native resolution and in the absence of energetic electron events, the (background) GRS count rate is well described by a Poisson distribution with mean and variance λ, dominated by GCRs and planetary neutrons interacting with the anticoincidence shield (see Section 2.1). Smoothing the background count rate with a moving boxcar average, by the central limit theorem, causes the background rate to be approximated by a Gaussian distribution with mean $\bar{x}$ = λ and variance σ^2 = λ/N_s, where N_s is the number of points used in the boxcar filter. From Gaussian statistics, knowing $\bar{x}$ and σ allows us to determine significant observations, interpreted as energetic electron events. To complicate this procedure, the background Gaussian distribution is time-dependent (i.e., $\bar{x} = \bar{x}(t)$ and $\sigma = \sigma(t)$) as it responds to both changes in spacecraft altitude and in boresight pointing. While changes in altitude often have timescales of several minutes (e.g., 08:20 to 08:40 in Figure A1a), changes in spacecraft pointing can change the background rate on the timescale of a minute (e.g., 08:49). By contrast, electron events appear as sharp, localized (timescales of seconds) peaks superposed on the background (e.g., 08:56 to 09:16). To accommodate the time-variable nature of the background, we use a sliding window to find the local background Gaussian distribution and construct the background count rate from the time series of the local Gaussian parameters.

To identify electron events within each MESSENGER orbit, we applied the following procedure to each interval of continuous GRS observations:

1. Smooth the GRS count rate with a moving boxcar average ($N_s = 100$, i.e., a 1-s smoothing filter).
2. Construct the background count rate in sliding windows of duration $t_{\text{window}} = 1$ min and with a time step between windows $\Delta t_{\text{step}} = 0.1$ min. Within each window (e.g., as depicted in Figure A1b and Figure A1c), use an iterative Gaussian fit to find the local $\bar{x}$ and σ:
    a. Construct the GRS histogram of counts.
    b. Identify the lowest-count peak within the histogram (e.g., the peak at ~4.2 (10 ms)$^{-1}$ in Figure A1c).
    c. Determine the cumulative number of observations to the left of this peak.
    d. Find the bin to the right of this peak that, between the peak and the bin, contains the same cumulative number of observations as found in step 2c.
    e. Fit a Gaussian to the subset of the histogram spanning the leftmost bin to the bin selected in step 2d. This initial fit returns $\bar{x}_{\text{temp}}$ and σ_{temp}.
    f. Using the fit in step 2e as an initial guess, select all histogram bins less than $\bar{x}_{\text{temp}} + 2\sigma_{\text{temp}}$ and fit a Gaussian to this subset of the histogram, returning a new $\bar{x}_{\text{temp}}$ and σ_{temp}. Iteratively repeat this step until the Gaussian fit converges.
    g. Return the local mean $\bar{x} = \bar{x}_{\text{temp}}$ and variance $\sigma^2 = \bar{x}_{\text{temp}}/\mathrm{N_s}$. The black dashed line in Figure A1b and 1c correspond to a Gaussian with mean $\bar{x}$ and variance σ^2. We found the propagated Poisson variance $\sigma^2 = \bar{x}_{\text{temp}}/\mathrm{N_s}$ to be a more accurate and reliable measure of uncertainty than the returned Gaussian $\sigma^2{}_{\text{temp}}$.
3. From all local $\bar{x}$ and σ construct the background time series, $\bar{x}(t)$ and $\sigma(t)$. To ensure a continuous background, apply a 1-min moving boxcar average to $\bar{x}(t)$ and $\sigma(t)$.

4. Find all GRS points that fall above $\bar{x}(t) + 5\sigma(t)$ (cyan in Figure A1a). Aggregate any significant points within 1 s of another (to reduce the total number of events), and record the start and stop times of each bundle of significant points as an electron event.

Over the 1 March 2013 to 30 April 2015 period of our study, the algorithm identified 11756 energetic electron events over 2139 orbits. We removed 214 orbits from our analysis due to high solar energetic particle count rates in the detector. We estimate 1190 (~10%) of the events are false positives, due to anomalously low background fitting. Since the algorithm identifies the lowest count peak in the GRS histogram (e.g., the leftmost peak in Figure A1c), an anomalously low number of counts will skew the local background low and produce a series of false positive events. Visually checking each orbit and the low rate of false positives suggest the algorithm accurately identified energetic electron events. We validated the algorithm by comparing the duration and amplitude of identified GRS events against synthetic GRS events identified by the algorithm (not shown here) and found no significant systematic bias in the algorithm. The algorithm is validated further by the similarities the spatial distribution of events in Figure 3.1 shares with previous studies of electron events at Mercury (Lawrence et al., 2015; Baker et al., 2016; Ho et al., 2016).

References

Baker, D. N., Dewey, R. M., Lawrence, D. J., Goldsten, J. O., Peplowski, P. N., Korth, H., … Solomon, S. C. (2016). Intense energetic electron flux enhancements in Mercury's magnetosphere: An integrated view with high-resolution observations from MESSENGER. *Journal of Geophysical Research: Space Physics*, **121**, 2171–2184. https://doi.org/10.1002/2015JA021778

Ho, G. C., Starr, R. D., Krimigis, S. M., Vandegriff, J. D., Baker, D. N., Gold, R. E., … Solomon, S. C. (2016). MESSENGER observations of suprathermal electrons in

Mercury’s magnetosphere. *Geophysical Research Letters*, **43**, 550–555. https://doi.org/10.1002/2015GL066850

Lawrence, D. J., Anderson, B. J., Baker, D. N., Feldman, W. C., Ho, G. C., Korth, H., … Winslow, R. M. (2015). Comprehensive survey of energetic electron events in Mercury’s magnetosphere with data from the MESSENGER gamma-ray and neutron spectrometer. *Journal of Geophysical Research: Space Physics*, **120**, 2851–2876. https://doi.org/10.1002/2014JA020792

APPENDIX B. Statistical FIPS Bulk Flow Determination

Within this appendix, we describe in detail the philosophy and methodology in determining statistical flows from FIPS observations as used in Chapters 4 and 5. This technique involves combining multiple FIPS scans together to construct (more) complete velocity space distributions from which bulk flows can be determined. We evaluate uncertainty associated with this calculation and correct for the effects from missing regions of velocity space.

Bulk motion of plasma (i.e., plasma flows) are ubiquitous to space plasmas, and measuring and interpreting them are critical to understanding dynamics in space physics. Flows transport mass and magnetic flux, generate electric fields and currents, compress and rarify magnetic fields, and accelerate particles. Measuring flows are also of practical use. Knowing the local flow, for example, can allow for the approximate transformation of the temporal domain to the spatial domain (in other words, converting a time series into a spatial series).

Plasma flows describe the collective motion of individual particles and are therefore a fluid (macroscopic) description of the kinetic (microscopic) plasma. Consider the particles of a given species (e.g., H^+) moving through a point in space at a given time. Ions of different energies will be traveling through this point in different directions. In the absence of plasma flow, the motion of particles through this point is random (thermal) such that the flux of particles traveling in any given direction will be the same as the flux traveling against that direction. With the introduction of a plasma flow, however, these ions will travel systematically along the flow direction in addition to their thermal motion. If the flow speed is much smaller than the thermal speed (i.e., Mach number << 1), then the difference between the flux in the direction along the plasma flow and the flux against that direction will be small. If the flow speed is much greater than the thermal speed (i.e., Mach number >> 1), then this difference will be large, such that as the Mach number tends toward infinity, no flux will be observed in the direction against the flow. In other words, the difference in flux along one direction and the flux antiparallel to that direction defines a plasma flow, or lack thereof.

This qualitative description of plasma flows is expressed numerically by the phase space distribution function $f(\boldsymbol{v})$. This distribution indicates the number of particles traveling through our point in space as a function of velocity. Bulk plasma flows are defined by asymmetries within velocity space, and can be determined by calculating the moments of the phase space distribution. The first three moments of $f(\boldsymbol{v})$ are:

$$n = \iiint_{-\infty}^{\infty} f(\boldsymbol{v})\, d^3v$$

$$\boldsymbol{u} = \frac{1}{n} \iiint_{-\infty}^{\infty} \boldsymbol{v} f(\boldsymbol{v})\, d^3v$$

$$3k_bT = \frac{m}{n} \iiint_{-\infty}^{\infty} (\boldsymbol{v} - \boldsymbol{u})^2 f(\boldsymbol{v})\, d^3v$$

where k_b is Boltzmann's constant, m is the mass of the species, n is the density, $\boldsymbol{u}$ is the vector bulk flow, and T is the temperature. These moments connect the behavior and identity of individual particles (as expressed by $f(\boldsymbol{v})$) to macroscopic, bulk parameters (n, $\boldsymbol{u}$, T).

In situ, spacecraft use particle detectors to construct velocity space distributions from which to determine flows. Since velocity space is three-dimensional, spacecraft must measure plasma traveling in all directions to construct such a distribution. To accomplish this, spacecraft use either a combination of multiple plasma detectors each looking in a different direction and/or spin, such that in a short period of time even a single plasma detector can observe the entire sky. The Magnetospheric Multiscale (MMS) Mission is an example that utilizes both methods. Each of the four MMS spacecraft are equipped with four thermal ion detectors that each look in different directions (e.g., Pollock et al., 2016). While an individual ion spectrometer cannot observe the entire sky instantaneously, combining the field of views of the four sensors creates a complete velocity space distribution. Additionally, each MMS spacecraft spin at a rate of three revolutions per minute so in the course of ~20 s, an individual sensor has observed the entire sky (e.g., Burch et al., 2016). Equipped with both multiple ion spectrometers and utilizing its spin, each MMS spacecraft has multiple avenues to which it can construct velocity space distributions and determine ion flows.

The Fast Imaging Plasma Spectrometer (FIPS, Andrews et al., 2007) sensor aboard MESSENGER faces more severe limitations on determining bulk flows. FIPS measures thermal and low-energy ions with energy per charge ratio (E/q) between 46 eV/e and 13 keV/e with a nominal energy scan time of 10 s. FIPS is comprised of an electrostatic analyzer and a time-of-flight chamber, in the latter of which ions stop by encountering a position-sensing micro-channel plate (MCP). The stop MCP consists of an array of 64 by 64 pixels, each of which map to a location in the FIPS field of view (FOV), enabling the ions' incident direction to be determined. Combined, the MCP pixels allow for an instantaneous FOV imaging of ~1.4π sr about FIPS's boresight direction (the central axis of the ~70° FOV cone), although spacecraft obstructions reduce this to an effective ~1.15π sr. Figure B1 illustrates the spacecraft obstructions to the FIPS FOV and how those obstructions affect the sensor's response to local plasma flows.

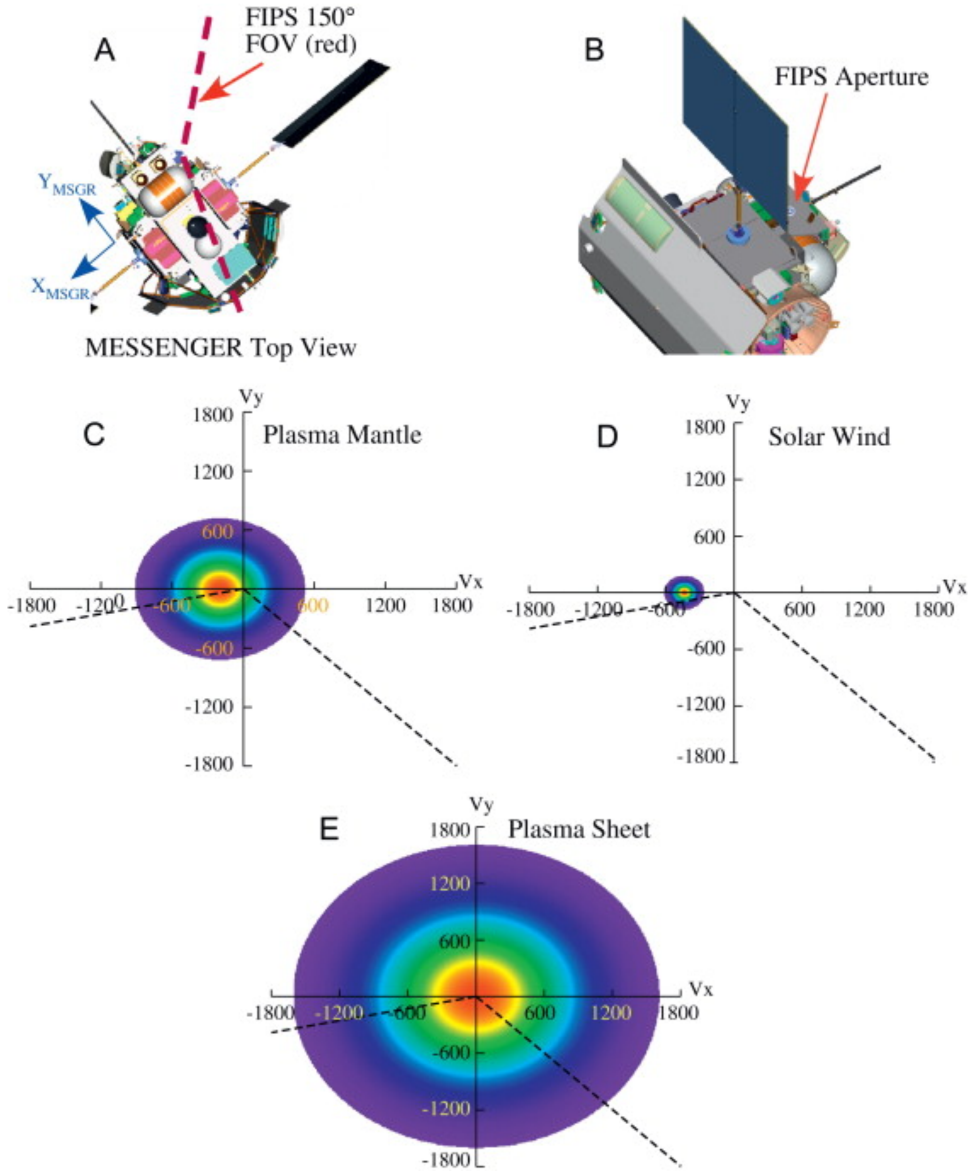

Figure B1. FIPS field of view (FOV), obstructions, and placement on the spacecraft from Raines et al. (2011). (a) A view of the MESSENGER spacecraft along the Z_{sc} axis with the full FIPS FOV cone marked by dashed red lines. (b) A view of FIPS along its boresight vector illustrating obstructions from the spacecraft body, sunshade, and a solar panel. (c-e) Diagrams of FIPS response in velocity space to different local plasma conditions. The observed region of velocity space in these examples is the region along –V_y bounded by the dashed black lines. The color corresponds to phase space density (red is greatest). Local plasma conditions that have subsonic flows (e.g., e) allow for more accurate determination of ion density and temperature than supersonic flows (e.g., c). The limited region of observed velocity space limit the ability of the FIPS sensor to determine local plasma flows (see text).

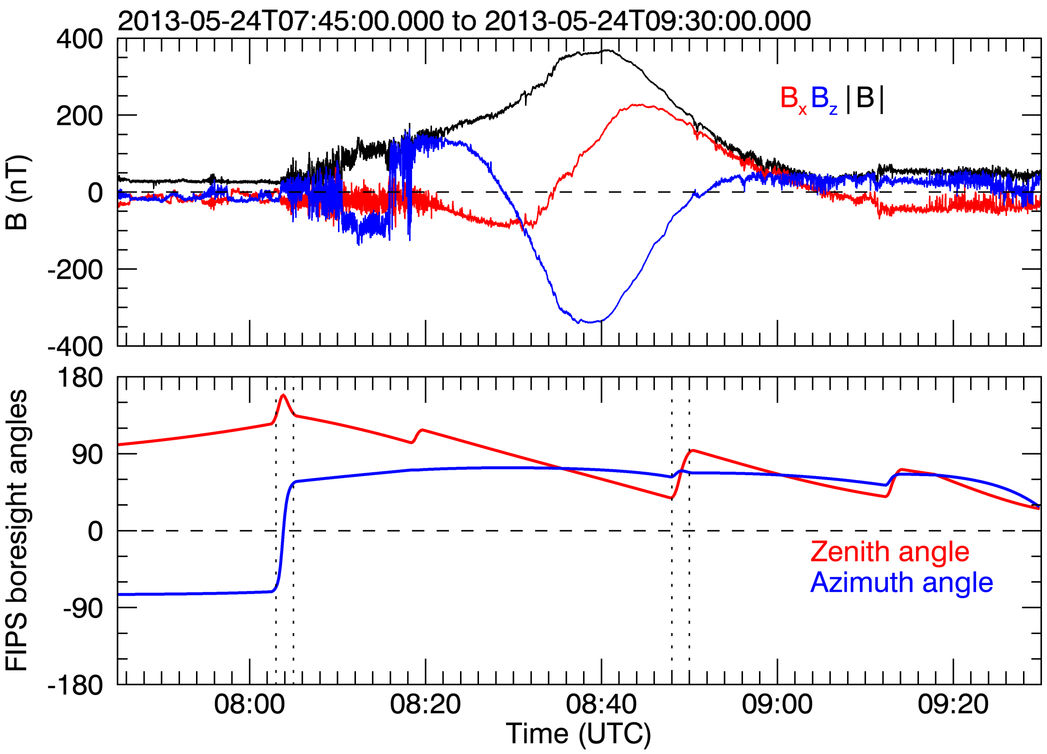

Figure B2. (top) Magnetic field observations and (bottom) angles between FIPS boresight and MSM coordinate vectors for the magnetosphere pass on 24 May 2013 between 07:45 and 09:30.

Although FIPS has a large instantaneous field of view it cannot determine flows at its native resolution because there is only the single sensor and the spacecraft does not spin. To allow for imaging of the planetary surface and exosphere, the spacecraft is three-axis stabilized and rotates on timescales of minutes to hours, as opposed to seconds for spinning spacecraft (e.g., MMS). Figure B2 illustrates the timescales over which the FIPS FOV changes. The magnetic field observations demonstrate a pass through Mercury's magnetosphere, with MESSENGER encountering the dayside magnetosphere and passing over the northern hemisphere before crossing the magnetotail's central current sheet at ~09:00. Over this time, we include information on FIPS pointing, expressed as angles between the boresight direction and MSM coordinates. The zenith angle (red) is the angle between FIPS boresight and $+Z_{MSM}$ and the azimuth angle (blue) is the angle of the boresight vector about $+Z_{MSM}$. During this magnetosphere pass, FIPS FOV evolves on timescales of minutes to hours. At its longest timescales, FIPS pointing changes smoothly over the course of the orbit (e.g., between 08:20 and 08:40). Interrupting this smooth, long-wavelength variation are short intervals of quick spacecraft rotation. These periods of quick rotation are on the timescales on minutes, with the two most extreme rotations as indicated by the pairs of vertical dotted lines each lasting two minutes. While FIPS FOV evolves with time, these timescales are longer than many of the dynamics within the magnetosphere and therefore do not allow FIPS to resolve flows associated with these features. For example, dipolarizations in the magnetotail possess durations ~10 s (e.g., Dewey et al., 2017a) so even the fastest spacecraft rotation in this example interval is too long to allow FIPS to construct a complete velocity space distribution to resolve flows associated with these events. Additionally, these changes in spacecraft pointing are often insufficient for construction of a complete velocity space distribution. Take, for example, the rotation spanned by the first two vertical dotted lines. While the azimuth angle changes from approximately –70° (near $-Y_{MSM}$) to +60° (near $+Y_{MSM}$), the zenith angle remains near 180° ($-Z_{MSM}$). Although there is substantial rotation in the X_{MSM}-Y_{MSM} plane, the boresight remaining near $-Z_{MSM}$ results in only a small increase in velocity space coverage. Even the long-duration FOV changes result in only a fractional increase in velocity space coverage. For example, between 08:20 and 08:40, the azimuthal pointing remains fixed while the zenith pointing changes by ~75°. Since the azimuth pointing does not change substantially over this interval, the majority of velocity space remains unobserved. Finally, there are regions of velocity space that are never observed. As a result of the spacecraft's sunshade always needing to be pointed towards the Sun, FIPS never observes within ~20° of the $\pm X_{MSM}$ directions (e.g., see Figure 4.3). When aberrating the coordinates to account for Mercury's orbital motion about the Sun, there are chances for FIPS to observe along

$–X_{MSM'}$ or $+X_{MSM'}$, however, these require intervals of extreme aberration (typical aberration at Mercury's orbital location is ~7° assuming a radial solar wind speed of ~400 km/s). Since FIPS is a single sensor, the limitations imposed on it by the spacecraft prevent it from constructing velocity space distributions on relevant magnetospheric timescales.

While FIPS cannot readily construct complete velocity space distributions to determine flows, its partial velocity space observations are still sensitive to ion flows and the asymmetries they impart. Consider Figure B2, reproduced from Chapter 4, which consists of MAG, GRS, and FIPS observations of a series of dipolarizations in Mercury's magnetotail. During the 1-min interval in Figure B3a, two dipolarizations are present: one beginning at ~08:26:12 and another at ~08:26:40. Both dipolarizations are coincident with enhancements in the Gamma-Ray Spectrometer (GRS) count rate, corresponding to energetic electron injections (e.g., Baker et al., 2016). The FIPS scan shaded in grey spans from the end of the first dipolarization to the beginning of the second. Figure B3b contains the scan's angular flux map: proton flux accumulated during this scan as a function of MSM angular direction. Figure B3c contains the scan's angular FOV map: the number of microchannel plate (MCP) pixels observing each direction of MSM-space. Examining this scan's angular maps, the FIPS FOV limitations are apparent. The sensor surveys only a fraction of the sky and cannot observe plasma traveling in neither the sunward ($+X_{MSM}$) nor antisunward ($–X_{MSM}$) directions. While the sensor cannot unambiguously determine bulk plasma flow from the incomplete plasma distribution of this single scan, there is more flux traveling in $+X_{MSM}$ than $–X_{MSM}$ (see guiding arrows), suggestive of a sunward plasma flow. There are several high-flux bins near $–Z_{MSM}$, however, these bins have high uncertainty as they are observed by few MCP pixels and correspond each to single proton counts.

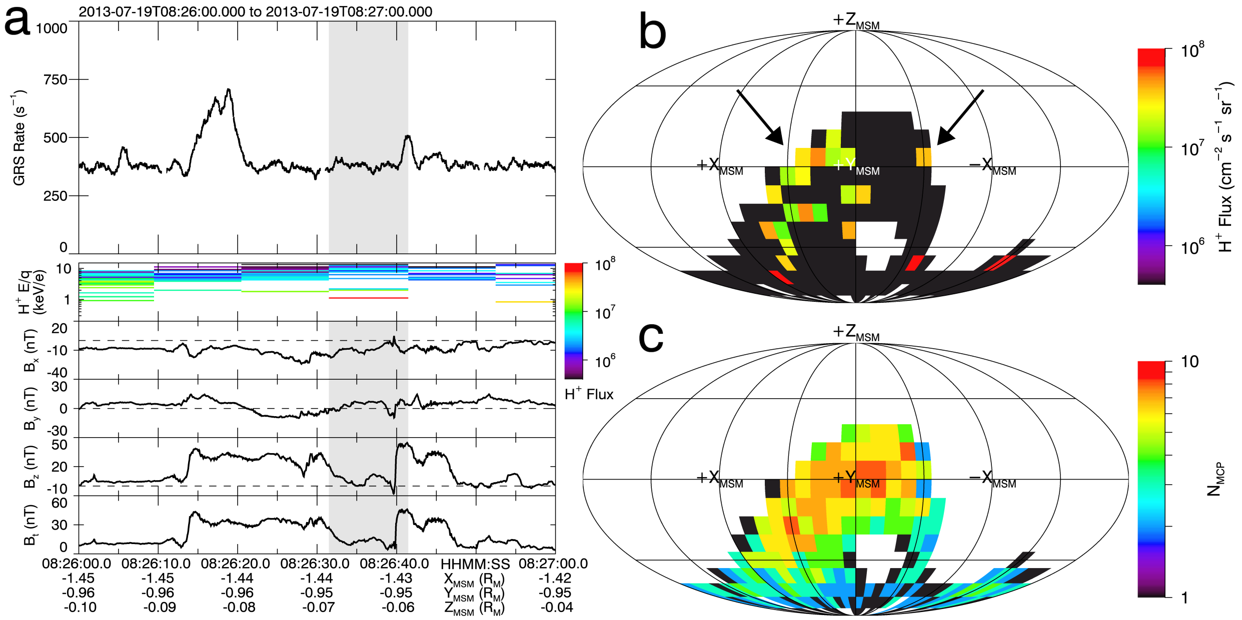

Figure 3B. (a) Magnetic field dipolarizations and energetic electron injections identified by Dewey et al. (2018). From top to bottom: GRS count rate; FIPS H$^+$ flux spectrogram; and magnetic field components B_x, B_y, B_z, |B|. Spacecraft position is listed below the bottom panel. (b) FIPS angular flux map corresponding to the energy scan shaded in grey in (a). Color bins have nonzero flux as indicated by the upper color bar. (c) Angular FOV map of the same scan. The number of MCP pixels sampling each region of MSM space is indicated by the lower color bar. For both maps, white indicates regions outside the FOV.

Asymmetries in the partial velocity space distributions can become more apparent by accumulating multiple FIPS scans. Figure B4 shows accumulation of FIPS observations for two different plasma sheet intervals from Sun et al. (2020). For each interval, FIPS observations are combined to produce integrated flux maps in the same format as Figure B3b, angular FOV maps in the same format as Figure B3c, and angular count maps. The first interval (top), spans 22:29 to 22:47 on 11 May 2012, corresponding to an accumulation of 103 FIPS scans. Despite the long accumulation, large regions of velocity space are unobserved (white). In the angular flux map, while ±X_{MSM} are not observed directly the strong difference in flux in regions observed about +X_{MSM} and –X_{MSM} indicate a sunward (+X_{MSM}) flow. Unfortunately, the lack of observations about +Y_{MSM} and +Z_{MSM} prevent estimation of duskward (Y_{MSM}) and northward (Z_{MSM}) flows. In the second interval (09:23 to 09:27 on 23 November 2011), fewer FIPS scans are accumulated that result in a greater fraction of unobserved velocity space but the asymmetry in flux about $\pm X_{MSM}$ is more apparent. During this interval, the spacecraft is located tailward of the magnetotail's reconnection site and is observing fast tailward reconnection outflows. During this second interval, the difference in coverage about $\pm Y_{MSM}$ is too great to reliably determine duskward flow and the strong asymmetries in coverage between $\pm Z_{MSM}$ leave northward flows entirely unconstrained.

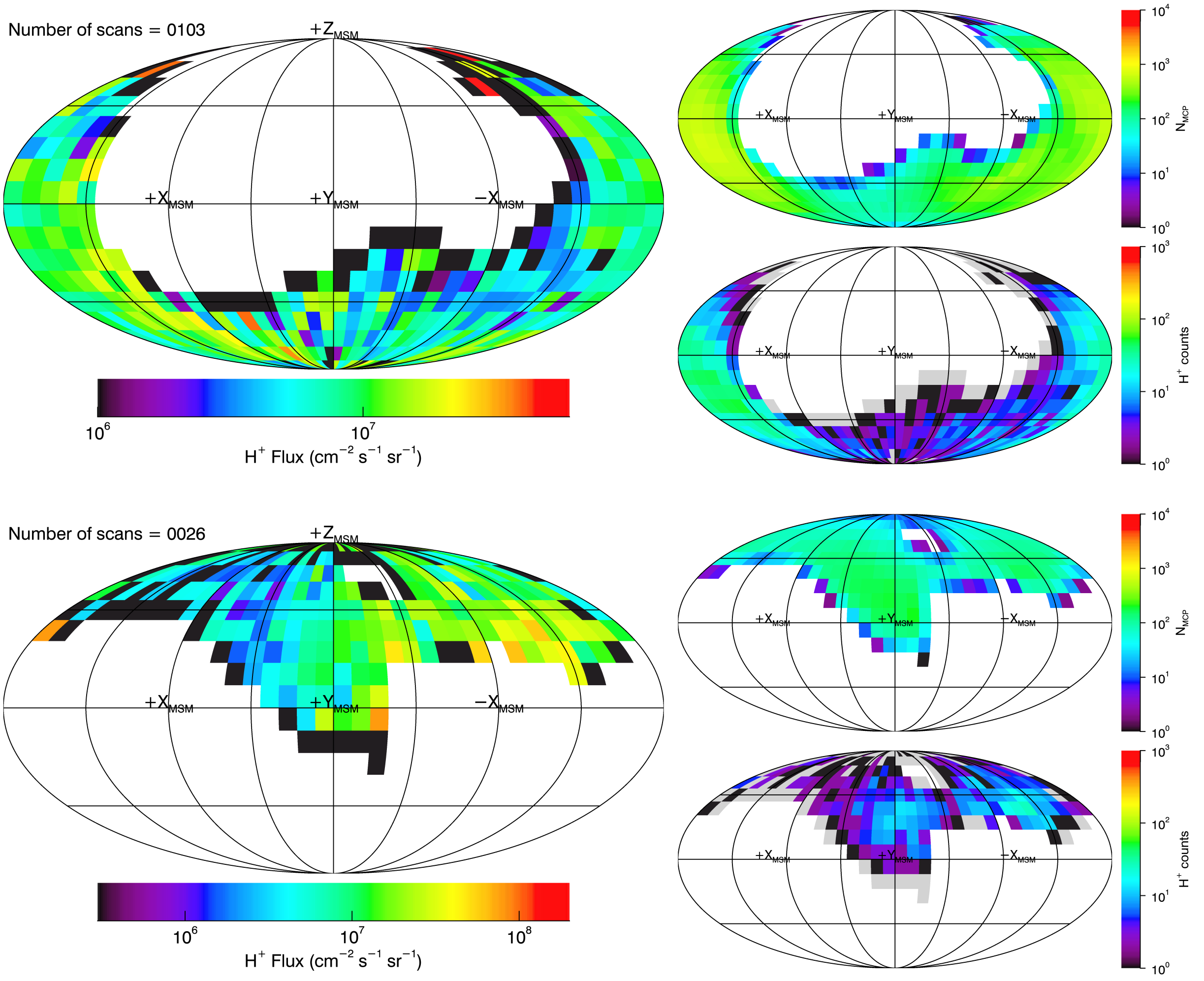

Figure B4. Accumulated FIPS observations from two intervals from Sun et al. (2020).

FIPS is responsive to plasma flows, however, it cannot determine them unambiguously since it cannot construct complete velocity space distributions on relevant magnetospheric timescales. Therefore, we developed a technique to construct a complete velocity space distribution statistically from which flows can be calculated directly. Below we describe, in detail, the procedure to combine FIPS observations, determine ion flows, and evaluate uncertainties.

1. Select FIPS scans.

   For a given magnetospheric phenomena (e.g., magnetotail dipolarizations) or for a given spatial region (e.g., southern lobe), the first step in determining statistical ion flows is deciding which FIPS scans to include. The method to deciding which scans to use varies substantially based on scientific objective but we encourage readers to avoid intervals contaminated by Solar Energetic Particle (SEP) events or intervals of unusual FIPS scan type (we recommend using either survey mode or burst mode scans).

2. Construct native FIPS velocity space distributions.

   For each scan selected in Step 1, we construct FIPS velocity space distributions at native resolution. For each scan, we determine the phase space density (i.e., $f(\boldsymbol{v})$ described above), counts, and number of MCP pixels at each location within velocity space. Since FIPS measures 64 E/q steps during a single scan, spherical coordinates for velocity space are the most appropriate. Considering the size of these distributions and the angular resolution of the FIPS instrument, we recommend 10° angular resolution in both angular coordinates. Each distribution will therefore contain 64 (energy) by 36 (azimuth) by 18 (zenith) bins.

   To construct these distributions, we first acquire the relevant pulse-height analyzed (PHA) event words. PHA words are detector counts for which the complete record was telemetered to the ground, and after acquisition, need to be filtered by the desired ion species. The FIPS “rates” product is also available, but since it does not contain directionality information for each individual count, we cannot directly use this product to determine flows. The phase space density at each velocity space location is described as:

$$f(v_i, \phi_j, \theta_k) = \left[\sum_{l}\left[\sum_{m} \not{f}_{lm}(v_i, \phi_j, \theta_k)\right]\Omega_l(v_i, \phi_j, \theta_k)\right] \Bigg/ \left[\sum_{l}\Omega_l(v_i, \phi_j, \theta_k)\right]$$

where v_i, ϕ_j, and $\theta_k$indicate the respective energy, azimuth, and zenith bins; Ω_l is the solid angle of MCP l; and $\not{f}_{lm}$ is the phase space density of PHA m that was recorded by MCP pixel l. Qualitatively, at each location of velocity space, determine which MCP pixels observe that location, then determine the weighted average of PHA phase space density (weighted by MCP solid angle). Determining which velocity space bin a given MCP pixel observed depends on FIPS pointing and is therefore time-dependent. Using SPICE kernels, the FIPS pointing during any scan can be determined, allowing for the transformation of MCP pixel look direction in spacecraft coordinates to MSM (or MSM’) coordinates. For an MCP pixel looking along unit vector $\boldsymbol{a}_{sc}$ in spacecraft coordinates, the transformation to MSM coordinates is:

$$\boldsymbol{a}_{MSM} = -\underline{\boldsymbol{R}}\boldsymbol{a}_{sc}$$

where $\underline{\boldsymbol{R}}$ is the time-specific rotation matrix. The minus sign indicates the transformation of the direction the MCP pixel looks in to the direction particles recorded by the MCP pixel are moving in (e.g., if an MCP pixel looks along $+Z_{MSM}$ then the particles it detects will be moving along $-Z_{MSM}$). The value of using spherical coordinates is now clear:

during the course of a scan, an MCP pixel observes the same angular bin (ϕ_j, θ_k) at all energy steps (v_i).

The counts distribution $c(\boldsymbol{v})$ is simpler to construct:

$$c(v_i, \phi_j, \theta_k) = \sum_l \left[\sum_m 1\right]$$

Similarly, the MCP pixel distribution:

$$n(v_i, \phi_j, \theta_k) = \sum_l 1$$

3. Combine observations into composite velocity space distributions.

With the distributions for each individual scan on hand, we can now combine them statistically into (more) complete velocity space distributions. To accumulate the counts distributions:

$$C(v_i, \phi_j, \theta_k) = \sum_p c_p(v_i, \phi_j, \theta_k)$$

where $C(v, \phi, \theta)$ is the combined distribution, i.e., counts summed across each scan p. Next, we determine the FOV distribution, a modified accumulation of individual MCP pixel distributions:

$$N(v_i, \phi_j, \theta_k) = \begin{cases} 1 \text{ for } n_p(v_i, \phi_j, \theta_k) \geq 1 \\ 0 \text{ for } n_p(v_i, \phi_j, \theta_k) = 0 \end{cases}$$

The FOV distribution indicates the number of scans at each velocity space location that observed that location with one or more MCP pixels. The composite phase space density distribution is:

$$F(v_i, \phi_j, \theta_k) = \left[\sum_p f_p(v_i, \phi_j, \theta_k)\right] \Big/ N(v_i, \phi_j, \theta_k)$$

i.e., the phase space density averaged across the scans that observed that velocity space location.

4. Computing plasma moments from the composite velocity space distributions.

With a (nearly) complete velocity space distribution $F(v, \phi, \theta)$, we can determine the plasma moments. While fitting $F(v, \phi, \theta)$ to a known distribution (e.g., drifting Maxwellian) can be done to determine moments, the process of fitting is computationally expensive considering the number of velocity space bins (~41,500) and the number of free parameters (5+). Rather, we recommend computing the moments analytically (see above). Although we do not discuss it thoroughly here, readers should be aware of potential effects from the finite FIPS energy range (e.g., Gershman et al., 2012; Gershman et al., 2013). These effects, as well as those of remaining missing regions of velocity space (e.g., about $\pm X_{MSM}$), are mitigated by incorporating a software model of the FIPS sensor (Dewey et al., 2017b). The software model uses the time-accurate pointing of the instrument and user-inputted plasma moments to model the phase space density each MCP pixel would measure ideally. We can therefore use this model to determine how moments calculated analytically would be affected by the finite FIPS energy range and any remaining missing velocity space regions.

We first calculate the plasma moments from $F(v,\phi,\theta)$ and represent them as vector $\boldsymbol{M}=\left(n,u_x,u_y,u_z,T\right)$. We denote the phase space density distribution and calculated moments from the FIPS observations as $F_0(v,\phi,\theta)$ and $\boldsymbol{M}_0$. We then iteratively follow:

(1) Set $\boldsymbol{M}_0$ as the input moments ($\boldsymbol{I}$) to the FIPS software model.

(2) Construct a new phase space distribution, $F_1(v,\phi,\theta)$, by repeating Step 3 but instead of using FIPS observations use the modeled phase space density determined from the FIPS software model and input moments $\boldsymbol{I}$.

(3) Calculate the new moments, $\boldsymbol{M}_1$, from $F_1(v,\phi,\theta)$.

(4) Compare the original moments to the new moments by determining the root-mean square error. If the error is large (>1%) then define a new input to the software model $\boldsymbol{I}_{new}=\boldsymbol{I}_{old}-\boldsymbol{M}_1+\boldsymbol{M}_0$ and repeat steps (2)-(4) with the new input. If the error is small, we end the iterations.

The result of this back-modeling is a new set of moments $\boldsymbol{I}$ that more accurately reflect the characteristic plasma conditions observed in the composite velocity space distribution. Using the moments $\boldsymbol{I}$ as input to the FIPS software model, we follow the same combination procedure as in Step 3 and result in a phase space distribution with calculated (output) moments equal to $\boldsymbol{M}_0$. Therefore, $\boldsymbol{I}$ represents the characteristic plasma conditions before limitations of the spacecraft affect their determination ($\boldsymbol{M}_0$). For the composite distribution described in Chapter 4, the combined 424 FIPS scans result in a near-complete distribution, with just regions about $\pm X_{MSM}$ missing (Figure 4.3). One of the results of these missing regions is underestimation of u_x. The sunward flow calculated directly from the distribution is ~140 km/s. If we use this as the input sunward flow speed to the FIPS software model and follow the combination procedure of Step 3, the new sunward flow speed is ~80 km/s, suggesting that our input flow speed (~140 km/s) has been underestimated. To recover output sunward flow of ~140 km/s, we need an input flow speed of ~230 km/s. This example qualitatively illustrates the value of using the software FIPS model to correct the calculated plasma moments for missing regions of velocity space and for the finite FIPS energy range.

5. Estimate statistical and sampling uncertainties.

There are two main sources of uncertainty associated with this FIPS statistical flow determination method. The first is statistical uncertainty associated with Poisson error (counting error) and represents uncertainty of the instrument. Following a Poisson distribution, if FIPS collects $c(v,\phi,\theta)$ counts at a location in velocity space during a scan, then the associated uncertainty is $\sqrt{c(v,\phi,\theta)}$. We propagate this uncertainty to the composite distribution. We also consider the uncertainty from the number of scans that observe each location of velocity space, $N(v,\phi,\theta)$. If many scans observe the same location, we have higher confidence in the average phase space density there compared to regions with few scans. We therefore define the composite phase space density uncertainty as:

$$\delta F(v_i,\phi_j,\theta_k) = \frac{F(v_i,\phi_j,\theta_k)}{\sqrt{C(v_i,\phi_j,\theta_k)N(v_i,\phi_j,\theta_k)}}$$

which is proportional to Poisson uncertainty from the number of counts and is modified by the number of scans at that location (i.e., converting the standard error to the standard error of the mean). To determine how this uncertainty affects the plasma moments determined in Step 4, we follow a Monte Carlo procedure:

(1) Define a new, perturbed phase space density distribution $D(v, \phi, \theta)$ by:

$$D\left(v_i, \phi_j, \theta_k\right) = \left(F\left(v_i, \phi_j, \theta_k\right) + \eta\left(v_i, \phi_j, \theta_k\right)\delta F\left(v_i, \phi_j, \theta_k\right)\right) > 0$$

where $\eta\left(v_i, \phi_j, \theta_k\right)$ is a distribution in velocity space of numbers generated at random from a normal distribution with a mean of zero and standard deviation of one. We include the final equality statement since phase space density cannot be negative by definition.

(2) Calculate moments of $D(v, \phi, \theta)$, including the model correction, as described in Step 4.

(3) Record these new moments and repeat (1)-(2) for some number of iterations (>1,000).

The result of this Monte Carlo procedure is a distribution for each moment. If the number of iterations is sufficiently large, then by the central limit theorem, the distribution for each moment should be distributed normally where the center of each distribution should reflect the value of the moment determined from Step 4 and the width of each distribution indicates statistical uncertainty of that moment.

In addition to statistical uncertainty, we also evaluate sampling uncertainty. This uncertainty represents how our choice of FIPS scans, and the variability across them, influences the moments we determine in Step 4. To evaluate this uncertainty quantitatively, we perform repetitive subsampling analysis:

(1) Select, at random and without replacement, a fraction (~0.1-0.2) of the scans identified in Step 1.

(2) Using just these scans, repeat Steps 3 and 4, determining new model-correction moments.

(3) Record these new moments and repeat (1)-(2) for some number of iterations (>1,000).

Similar to the Monte Carlo statistical uncertainty evaluation, this sampling uncertainty evaluation will result in a distribution for each moment. If the number of iterations is sufficiently large, then by the central limit theorem, the distribution for each moment should be distributed normally where the center of each distribution should reflect the value of the moment determined from Step 4 and the width of each distribution indicates sampling uncertainty of that moment. Since we use a smaller number of samples then the population available to use in Step 1, the width of the distribution needs to be corrected by a factor $\sqrt{N_{subsample}/N_{total}}$ where $N_{subsample}$ is the number of scans used in each subsample iteration and N_{total} is the total number of scans available. The final uncertainty in each moment is the statistical and sampling uncertainties combined in quadrature.

Following Steps 1 through 5 above, we can determine typical (or statistical) plasma flows. This procedure requires many FIPS scans and given the number of iterations in Step 5, can also be computationally expensive. However, the result is a set of plasma moments (including plasma flow) that have been corrected by instrument limitations and have uncertainties evaluated. Since plasma flows are ubiquitous to space plasmas and are critical in understanding space physics dynamics, this technique represents a powerful new capability for the FIPS instrument to not only enhance its science return, but revolutionize our understanding of Mercury's space environment.

This technique is not without its limitations, which deserve as much attention as the technique's capabilities. The method described is statistical by nature and therefore performs best with many FIPS observations. We cannot prescribe a minimum number of scans needed since that depends on the pointing across the selected scans as well as the scientific objective. Correspondingly, one may perform Steps 1 to 3 only to find that the composite velocity space distributions still have large regions of velocity space missing (e.g., see Figure B4). We have yet to set explicit criteria on how much missing velocity space is too much to determine plasma moment(s). Next, this technique may miss super or hypersonic flows. Consider a supersonic flow such as the solar wind (at Mercury Mach number ~2-5). If the flow direction is not within FIPS FOV, then as a result of the small thermal speed compared to the flow speed, no asymmetries may be imparted on the partial velocity space distribution (i.e., no plasma is observed). Combining many similar scans will yield a statistical flow speed of zero if no scans capture the supersonic flow direction directly. Therefore, this technique is best applied to subsonic flows. Next, this technique in its current form does not account for seasonal effects. As a result of Mercury's highly eccentric orbit, solar wind conditions at Mercury's orbital location vary dramatically over a Mercury year, not to mention the hour-to-hour or day-to-day variability associated with solar wind transients. As the seasonal effects of Mercury's orbit on the magnetosphere are poorly constrained, they cannot be corrected for yet. However, we may be able to estimate some of them. For example, solar wind density falls off sharply as a function of distance from the Sun. As the solar wind supplies Mercury's magnetosphere with the majority of its plasma, when Mercury is at aphelion, we may expect lower plasma sheet densities than at perihelion. Examining flows within the magnetotail will therefore be biased towards the perihelion description as they represent observations of greater typical densities (i.e., greater typical phase space densities). Finally, we wish to remind readers than this technique should only be applied to magnetospherically similar scans. Scans, for example, belonging to similar phenomena (e.g., dipolarizations) or belonging to a well-defined region of the magnetosphere (e.g., central current sheet). Nevertheless, this technique and its careful application empower new discoveries of Mercury's space environment.

References

Andrews, G. B., Zurbuchen, T. H., Mauk, B. H., Malcom, H., Fisk, L. A., Gloeckler, G., et al. (2007). The energetic particle and plasma spectrometer instrument on the MESSENGER spacecraft. *Space Science Reviews*, **131**(1-4), 523–556. https://doi.org/10.1007/s11214-007-9272-5

Baker, D. N., Dewey, R. M., Lawrence, D. J., Goldsten, J. O., Peplowski, P. N., Korth, H., et al. (2016). Intense energetic electron flux enhancements in Mercury's magnetosphere: An integrated view with high-resolution observations from MESSENGER. *Journal of Geophysical Research: Space Physics*, **121**, 2171–2184. https://doi.org/10.1002/2015JA021778

Burch, J. L., Moore, T. E., Torbert, R. B, & Giles, B. L. (2016). Magnetospheric Multiscale Overview and Science Objectives. *Space Science Reviews*, **199**, 5–21. https://doi.org/10.1007/s11214-015-0164-9

Dewey, R. M., Slavin, J. A., Raines, J. M., Baker, D. N., & Lawrence, D. J. (2017a). Energetic electron acceleration and injection during dipolarization events in Mercury's magnetotail. *Journal of Geophysical Research: Space Physics*, **122**, 12,170–12,188. https://doi.org/10.1002/2017JA024617

Dewey, R. M., Raines, J. M., & Tracy, P. J. (2017b). Interpreting FIPS density, temperature, and pressure, NASA Planetary Data System, MESS-E/V/H/SW-EPPS-3-FIPS-DDR-V2.0.

Dewey, R. M., Raines, J. M., Sun, W., Slavin, J. A., & Poh, G. (2018). MESSENGER observations of fast plasma flows in Mercury's magnetotail. *Geophysical Research Letters,* **45**, 10,110–10,118. https://doi.org/10.1029/2018GL079056

Gershman, D. J., Zurbuchen, T. H., Fisk, L. A., Gilbert, J. A., Raines, J. M., Anderson, B. J., Smith, C. W., Korth, H., & Solomon, S. C. (2012). Solar wind alpha particles and heavy ions in the inner heliosphere observed with MESSENGER. *Journal of Geophysical Research: Space Physics*, **117**, A00M02. https://doi.org/10.1029/2012JA017829

Gershman, D. J., Slavin, J. A., Raines, J. M., Zurbuchen, T. H., Anderson, B. J., Korth, H., … Solomon, S. C. (2013). Magnetic flux pile-up and plasma depletion in Mercury's subsolar magnetosheath. *Journal of Geophysical Research: Space Physics*, **118**, 7181–7199. https://doi.org/10.1002/2013JA019244

Pollock, C., Moore, T., Jacques, A., Burch, J., … (2016). Fast Plasma Investigation for Magnetospheric Multiscale. *Space Science Reviews*, **199**, 33–406. https://doi.org/10.1007/s11214-016-0245-4

Raines, J. M., Slavin, J. A., Zurbuchen, T. H., Gloeckler, G., Anderson, B. J., Baker, D. N., Korth, H., Krimigis, S. M., & McNutt Jr., R. L. (2011). MESSENGER observations of the plasma environment near Mercury. *Planetary and Space Science*, **59**(15), 2004–2015. https://doi.org/10.1016/j.pss.2011.02.004

Sun, W. J., Slavin, J. A., Dewey, R. M., Chen, Y., DiBraccio, G. A., Raines, J. M., Jasinski, J. M., Jia, X., Akhavan-Tafti, M. (2020). MESSENGER observations of Mercury's nightside magnetosphere under extreme solar wind conditions: reconnection-generated structures and steady convection. *Journal of Geophysical Research: Space Physics*. https://doi.org/10.1029/2019JA027490

APPENDIX C. Dipolarization Identification Algorithm

The dipolarization identification technique is described briefly in Section 5.3. In this appendix, we describe the procedure in greater detail. Previous approaches to determining dipolarizations via autonomous algorithm have focused on identifying the leading edge of the event (dipolarization front) using a sliding window (e.g., Liu et al., 2013; Sun et al., 2016). We follow a similar, but modified approach, first identifying potential dipolarization fronts within the magnetic field time series and then applying a series of physical tests to determine if these signals represent dipolarizations or not. We take advantage of the initial statistical characterization of dipolarizations at Mercury from Sundberg et al. (2012), Sun et al. (2016), and Dewey et al. (2017) to set several empirical limits in identifying events.

To identify potential dipolarization fronts, we examine each point in the $B_z(t)$ time series for a strong, local, coherent, positive gradient. At point i in the time series (i.e., $t = t_i$), we determine the minimum time (Δt) by which B_z increases by ΔB_z, i.e., $B_z(t_i + \Delta t) = B_z(t_i) + \Delta B_z$. The parameter ΔB_z will therefore be the minimum increase in B_z of an identified dipolarization front. We use $\Delta B_z = 10$ nT, which corresponds the 5th percentile of dipolarization fronts identified by Dewey et al. (2017). For the interval of t_i to $t_i + \Delta t$ to qualify as a potential dipolarization front, we require:

1. $\Delta B_z / \Delta t \geq 5\ \mathrm{nT/s}$;

2. $\mathrm{minimum}\big(B_z(t_i < t < t_i + \Delta t)\big) \geq B_z(t_i)$; and

3. $\mu\big(\partial B_z(t_i < t < t_i + \Delta t)\big) > \sigma\big(\partial B_z(t_i < t < t_i + \Delta t)\big)$

where $\partial B_z(t)$ is the point-to-point change in $B_z(t)$, μ is the mean function, and σ is the standard deviation function. The first criterion requires local gradients to be both strong and positive, while the last two criteria require local gradients to be coherent. We set the threshold of the first criterion empirically by examining dipolarizations of Dewey et al. (2017) and the distribution of $\Delta B_z(\Delta t)$ across the 1,946 dipolarization-search intervals. Each group of sequential points in the time series that meet these three criteria is determined to be potential dipolarization front. We require that each potential dipolarization front have a minimum duration of 0.4 s (eight or more sequential MAG observations) to ensure the dipolarization front is well resolved. For comparison, Dewey et al. (2017) found a minimum dipolarization front duration of 0.7 s.

To determine if a potential dipolarization front corresponds to a dipolarization or not, a series of tests are applied. These tests include physical and statistical considerations and are designed to mimic signals that one's eye would use to select dipolarizations. Because the duration of dipolarization fronts can vary substantially (i.e., from < 1 s to > 5 s, see Dewey et al., 2017), these tests use time durations standardized by the potential dipolarization front's duration Δt_{DF}. The first test evaluates if the increase in B_z across the potential dipolarization front is meaningful and takes the form of a Student's t-test:

$$\frac{\mu\big(B_z(t_2 < t < t_2 + \gamma \Delta t_{DF})\big) - \mu\big(B_z(t_1 - \alpha \Delta t_{DF} < t < t_1)\big)}{\sqrt{\sigma\big(B_z(t_2 < t < t_2 + \gamma \Delta t_{DF})\big)^2 + \sigma\big(B_z(t_1 - \alpha \Delta t_{DF} < t < t_1)\big)^2}} > \eta$$

where t_1 is the start time of the potential dipolarization front, t_2 is the end time of the potential dipolarization front, and therefore $\Delta t_{\mathrm{DF}} = t_2 - t_1$. The parameters α, γ, and η are determined from optimization, described below. The second test evaluates if the potential dipolarization has sufficient duration:

$$\tau_2 > \varepsilon \Delta t_{DF}$$

where

$$\tau_2 = t\big(B_z = \tilde{\mu}\big(B_z(t_1 < t < t_2)\big); t > t_2\big) - t_2$$

and $\tilde{\mu}$ is the median function. The parameter τ_2 reflects the duration of time following the end of the potential dipolarization front that B_z is elevated above the median B_z during the potential front. The parameter ε is determined from optimization. The third test evaluates if the potential dipolarization stands above the preceding magnetic field for sufficient time:

$$t_1 - t_0 - \tau_2 > \zeta \Delta t_{DF}$$

where

$$\int_{t_0}^{t_1} \lambda(t)\, dt = \tau_2$$

and

$$\lambda(t) = \begin{cases} 1 \text{ for } B_z(t) \geq \tilde{\mu}\big(B_z(t_1 < t < t_2)\big) \\ 0 \text{ for } B_z(t) < \tilde{\mu}\big(B_z(t_1 < t < t_2)\big) \end{cases}$$

and ζ is determined from optimization. This third test is similar to the second in that it determines the duration of time before the potential dipolarization front that the magnetic field was below the median level during the potential front, but with the addition that it allows for short intervals of time (relative to the duration of the potential dipolarization) that the field was above the median level. We find that dipolarizations often occur in series with other dipolarizations (e.g., see Figure 5.7 within Section 5.4.3 or Figure 2 of Sundberg et al., 2012) and that without allowing for an interval of B_z greater than the median level, many dipolarizations in series would be disqualified. The final test evaluates how the change in B_z across the dipolarization front compares in magnitude to the preceding field:

$$\frac{B_z(t_2) - B_z(t_1)}{\mu\big(B_z(t_1 - \zeta \Delta t_{DF} < t < t_1)\big)} > \nu$$

where ν is determined by optimization. We experimented with additional tests and tests with different functional forms, and found that these four tests provide the minimum yet sufficient criteria to determine which potential dipolarization fronts indeed correspond to dipolarizations.

To optimize the six (α, γ, η, ε, ζ, and ν) free parameters, we developed a training set of dipolarizations to determine algorithm performance. We selected, at random, 196 of the 1,946 intervals (~10%) and for each potential dipolarization front within these selected intervals, evaluated by eye whether it corresponds to a dipolarization or not. The 196 intervals contain 1,775 potential dipolarization fronts, of which 623 correspond to dipolarizations and 1,152 do not. By systematically varying the six free parameters, we evaluated algorithm performance on this training set. We follow the optimization technique outlined by Azari et al. (2018), which focuses on the Heidke Skill Score (HSS) for evaluating and optimizing algorithm performance. HSS ranges from $-\infty$ (perfect anti-prediction) to 1 (perfect prediction), with HSS = 0 representing prediction as good as random change. For a discussion of the advantages of using HSS for identification algorithms in space physics, see Azari et al. (2018) and references therein. For our algorithm, maximizing HSS to determine free parameter values led to a large fraction of false positives identified as events. At the maximum HSS (0.806), 13.0% of events identified by the algorithm to be dipolarizations were false positives, and 7.1% of all 1,152 non-dipolarizations were detected as events. We therefore modified the Azari et al. (2018) approach by limiting the maximum fraction of false positives to 5%. Setting this limit, the maximum qualifying HSS is 0.764, corresponding to free parameter values of

$$\alpha = 1.75$$

$$\gamma = 1.50$$

$$\eta = 1.75$$

$$\varepsilon = 1$$

$$\zeta = 2$$

$$\nu = 0.3$$

With these parameters, the rate of dipolarization detection is 73.7%, the rate of non-dipolarizations being detected as events is 2.1%, and the fraction of algorithm-identified events that are false positives is 5.0%. The HSS of 0.76 indicates this algorithm identifies dipolarizations much better than random chance. For comparison, semi-autonomous identification of injection events at Saturn by Azari et al. (2018) has an HSS of 0.56, while space weather models typically have HSS < 0.5 for predicting magnetic perturbations at ground magnetometer stations (Pulkkinen et al., 2013).

References

Azari, A. R., Liemohn, M. W., Jia, X., Thomsen, M. F., Mitchell, D. G., Sergis, N., et al. (2018). Interchange injections at Saturn: Statistical survey of energetic H+ sudden flux intensifications. *Journal of Geophysical Research: Space Physics,* **123**, 4692–4711. https://doi.org/10.1029/2018JA025391

Dewey, R. M., Slavin, J. A., Raines, J. M., Baker, D. N., & Lawrence, D. J. (2017). Energetic electron acceleration and injection during dipolarization events in Mercury's magnetotail. *Journal of Geophysical Research: Space Physics,* **122**, 12,170–12,188. https://doi.org/10.1002/2017JA024617

Liu, J., Angelopoulos, V., Runov, A., & Zhou, X.-Z. (2013). On the current sheets surrounding dipolarizing flux bundles in the magnetotail: The case for wedgelets. *Journal of Geophysical Research: Space Physics,* **118**, 2000–2020. https://doi.org/10.1002/jgra.50092

Pulkkinen, A., Rastätter, L., Kuznetsova, M., Singer, H., Balch, C., Weimer, D., et al. (2013). Community-wide validation of geospace model ground magnetic field perturbation predictions to support model transition to operations. *Space Weather,* **11**, 369–385. https://doi.org/10.1002/swe.20056

Sun, W. J., Fu, S. Y., Slavin, J. A., Raines, J. M., Zong, Q. G., Poh, G. K., & Zurbuchen, T. H. (2016). Spatial distribution of Mercury's flux ropes and reconnection fronts:

MESSENGER observations. *Journal of Geophysical Research: Space Physics, 121*, 7590–7607. https://doi.org/10.1002/2016JA022787

Sundberg, T., Slavin, J. A., Boardsen, S. A., Anderson, B. J., Korth, H., Ho, G. C., et al. (2012). MESSENGER observations of dipolarization events in Mercury's magnetotail. *Journal of Geophysical Research,* **117**, A00M03. https://doi.org/10.1029/2012JA017756